

Physik-Department  
der Technischen Universität München  
Lehrstuhl für Biophysik E22 - Univ.-Prof. Dr. M. Rief

*Nano-mechanics of biomimetic models  
of the actin based cytoskeleton  
From single molecules to complex composite structures*

**Alexander Roth**

Vollständiger Abdruck der von der Fakultät für Physik der Technischen Universität München zur Erlangung des akademischen Grades eines Doktors der Naturwissenschaften (Dr. rer. nat.) genehmigten Dissertation.

Vorsitzender: Univ. Prof. Dr. Manfred Kleber

Prüfer der Dissertation:

1. Univ. Prof. Dr. Matthias Rief (schriftliche Beurteilung)  
Univ. Prof. Dr. Erich Sackmann (mündliche Prüfung)
2. Univ. Prof. Dr. Michael Schleicher  
(Ludwigs-Maximilians-Universität München)

Die Dissertation wurde am 8. 7. 2004 bei der Technischen Universität München eingereicht und durch die Fakultät für Physik am 2. 8. 2004 angenommen.

# Contents

Abstract . . . . .	8
<b>1 Introduction</b>	<b>12</b>
1.1 Motor proteins . . . . .	15
1.2 Dissociation of single specific bonds . . . . .	17
1.2.1 Thermal bond dissociation . . . . .	18
1.2.2 Force induced bond dissociation . . . . .	18
1.3 Introduction to semi-flexible polymers . . . . .	20
1.3.1 Oscillations of semi-flexible polymers . . . . .	22
1.3.2 Solutions of semi-flexible actin polymers . . . . .	23
1.4 Linear viscoelastic theory . . . . .	23
1.4.1 Linear viscoelastic models . . . . .	25
<b>2 Materials and Methods</b>	<b>28</b>
2.1 Biochemical Materials . . . . .	28
2.1.1 Proteins . . . . .	28
2.1.2 Phospholipids . . . . .	37
2.1.3 Chemicals . . . . .	38
2.2 Sample Preparation . . . . .	39
2.2.1 Surface coating with thin polymer layers . . . . .	39
2.2.2 Pillar array preparation . . . . .	40
2.2.3 Giant phospholipid vesicle preparation . . . . .	41
2.2.4 Magnetic bead functionalization . . . . .	42
2.3 Experimental Techniques . . . . .	42
2.3.1 Optical Microscopy . . . . .	42
2.3.2 Image analysis and processing . . . . .	48
2.3.3 Magnetic colloidal force transducer (Magnetic Tweezers) . . . . .	55

<b>3</b>	<b>Results and Discussion</b>	<b>63</b>
3.1	Myosin V single molecule experiments . . . . .	63
3.1.1	Particle transport by myosin V . . . . .	63
3.1.2	Average step size . . . . .	65
3.1.3	Force spectroscopy of the actin binding potential of moving myosin V molecules . . . . .	68
3.1.4	Myosin V movement under forward and backward forces . . . . .	83
3.2	Actin cortex models on micro pillar arrays . . . . .	91
3.2.1	Self assembly of a freely suspended quasi two dimensional actin network . . . . .	92
3.2.2	Mechanical properties of the quasi two dimensional actin network . . . . .	98
3.2.3	Elastic properties of actin filaments . . . . .	101
3.2.4	Elastic properties of actin - filamin bundles . . . . .	107
3.3	Structure and mechanics of actin cortex vesicles . . . . .	112
3.3.1	Structure of the actin cortex . . . . .	113
3.3.2	Data acquisition . . . . .	119
3.3.3	Analysis of the creep compliance . . . . .	120
3.3.4	Calculation of the strain relaxation function $G(t)$ . . . . .	126
3.3.5	Photochemical alternation of the actin cortex . . . . .	129
3.3.6	Work hardening . . . . .	131
3.3.7	Analysis of thermal bead fluctuations . . . . .	132
3.3.8	Strain field mapping . . . . .	134
3.4	Drop evaporation of entangled actin solutions . . . . .	139
3.4.1	Reconstruction of the droplet shape . . . . .	139
3.4.2	Filament bending under hydrodynamic pressure . . . . .	143
3.5	Contraction forces in active actin-myosin networks . . . . .	152
3.5.1	Active actin-myosin networks . . . . .	152
3.5.2	Percolation and viscoelastic properties . . . . .	154
3.5.3	Three dimensional reconstruction of vesicles . . . . .	160
3.5.4	Contraction forces . . . . .	163
<b>4</b>	<b>Conclusion and Outlook</b>	<b>170</b>
<b>A</b>	<b>Appendix</b>	<b>177</b>
A.1	Chemicals . . . . .	177
A.1.1	Ascorbic acid . . . . .	177

A.1.2	Glucose Oxidase . . . . .	177
A.1.3	Catalase . . . . .	177
A.2	Buffer composition . . . . .	178
A.2.1	A buffer . . . . .	178
A.2.2	B buffer . . . . .	178
A.2.3	G* buffer . . . . .	178
A.2.4	F buffer . . . . .	179
A.3	Abbreviations . . . . .	179
	<b>Bibliography</b>	<b>180</b>

# List of Figures

1.1	Images of the actin cytoskeleton inside cells . . . . .	14
1.2	Electron micrographs of motor proteins . . . . .	16
1.3	Hypothetic binding potential of a molecular bond . . . . .	19
1.4	Geometry of a schematic semi-flexible polymer . . . . .	21
1.5	Models for viscoelastic materials . . . . .	26
2.1	Actin . . . . .	29
2.2	The process of actin polymerization . . . . .	30
2.3	Structure of myosin V . . . . .	32
2.4	Electron micrograph and schematics of smooth muscle . . . . .	34
2.5	formation of pillar array substrates from silicon . . . . .	40
2.6	SEM images of pillar array substrates made from silicon and PDMS . . . . .	41
2.7	Schematics of the principle of a fluorescence microscope. . . . .	45
2.8	Principle of the Reflection Interference Contrast Microscope . . . . .	46
2.9	Three dimensional tracking algorithm . . . . .	50
2.10	Calibration curve for the three dimensional particle tracking algorithm . . . . .	51
2.11	Resolution of the particle tracking algorithm as function of the velocity of the particle . . . . .	52
2.12	Actin filament shape tracing . . . . .	53
2.13	Order analysis of an actin assembly . . . . .	55
2.14	Electron micrographs of super-paramagnetic colloidal particles . . . . .	56
2.15	Vertical magnetic tweezers . . . . .	58
2.16	Vertical magnetic tweezers calibration . . . . .	59
2.17	Vertical magnetic tweezers magnetization . . . . .	60
2.18	Horizontal force transducer . . . . .	61
2.19	Horizontal force transducer magnetic field and field gradient . . . . .	61

2.20	Horizontal force transducer magnetization and calibration curve	62
3.1	Movement of a myosin V coated bead along an actin filament	65
3.2	Histograms of the image to image displacement of a moving bead.	66
3.3	Snapshots of a force induced bond rupture of a myosin V molecule moving along an actin filament	70
3.4	Rupture process a of single myosin V molecule from an actin filament	71
3.5	Rupture forces of single myosin V molecules from actin filaments	73
3.6	Force - time relation of a moving motor molecule	75
3.7	Rupture forces of single myosin V molecules with a least square fit	78
3.8	The probability $N(F)$ of an intact bond and the bond rupture distribution $-\frac{N(F)}{dF}$	79
3.9	Stochastic deviations of the rupture forces	80
3.10	Combined probability density $P_g(f_0, k_0)$ for a myosin V bond rupture as a function of the parameters $k_0$ and $f_0$ .	81
3.11	Movement of a magnetic bead transported by a single myosin V molecule under increasing backward load	85
3.12	Displacement of myosin V along actin under backward load	85
3.13	Schematics of the geometry when myosin V is examined under a load parallel to its direction of movement.	86
3.14	Displacement of myosin V along actin under forward load	88
3.15	Electron micrographs of moving myosin V molecules	89
3.16	Fluorescence micrograph of actin filaments attached to a silicon pillar array substrate	93
3.17	Fluorescence micrograph of a cross-linked quasi two dimensional actin network on a silicon pillar array substrate	94
3.18	Actin network cross linked with filamin on a flat patterned substrate.	96
3.19	A 40 nm polystyrene bead being transported by myosin V on an quasi two dimensional actin network.	97
3.20	Probing the elastic properties of a freely suspended quasi two dimensional actin network on a pillar array substrate.	99
3.21	Thermally undulating filament on a photo resin pillar substrate	101
3.22	Fit of the first four Eigenmodes for the contour of an undulating actin filament	103

3.23	Bending stiffness of an actin filament determined from the first four undulation Eigenmodes . . . . .	104
3.24	Principle of the superposition mechanism to determine the bending rigidity of an actin filament . . . . .	107
3.25	Actin - filamin bundles immobilized on pillar array substrates .	108
3.26	persistence length of actin-filamin bundles . . . . .	109
3.27	Fluorescence micrographs of an actin cortex vesicle with a magnetic bead attached . . . . .	114
3.28	Structure of the actin cortex inside a vesicle . . . . .	115
3.29	Actin cortex vesicle with a magnetic bead attached . . . . .	116
3.30	Schematics of a parallel filament arrangement and actin bundles on micro film balance . . . . .	118
3.31	In plane force and displacement of a magnetic bead on the surface of an actin cortex vesicle. . . . .	120
3.32	Creep compliance and zero frequency shear modulus of actin cortex vesicles . . . . .	121
3.33	Fit functions of the creep compliance of an actin vesicle with different numbers of parameters . . . . .	123
3.34	Mechanical representation model used to analyze the creep compliance of actin cortex vesicles . . . . .	123
3.35	Dependence of the fit parameters of the actin vesicle creep compliance on the actin density . . . . .	125
3.36	Creep compliance and stress relaxation function of an actin cortex vesicle . . . . .	127
3.37	Stress relaxation curve of an entangled actin network . . . . .	129
3.38	Comparison of creep compliance and stress relaxation for intact and photochemically damaged actin cortex vesicles . . . . .	130
3.39	Strain field mapping on the upper half sphere of an actin cortex vesicle. . . . .	135
3.40	Displacements of different non magnetic beads used as strain field sensors on the outer surface of an actin cortex vesicle . . .	136
3.41	Spherical cap geometry of a droplet deposited onto a solid surface . . . . .	140
3.42	An actin filament moving radially outward in an evaporating droplet. . . . .	141
3.43	Evaporation process of an actin filament solution droplet deposited on a glass slide. . . . .	142

3.44	Snapshots of an actin filament being compressed against the dense actin structure close to the triple interface line of an evaporating actin droplet. . . . .	144
3.45	Characteristic bending length of an actin filament, which is compressed in a flow against an obstacle. . . . .	146
3.46	Time evolution of the bending energy per length (circles) of an actin filament, which is compressed against an obstacle . . . . .	150
3.47	Electron micrographs of myosin mini-filaments and an actin - myosin network . . . . .	154
3.48	Snapshots from a movie taken during a sol-gel percolation transition in an actin myosin network . . . . .	155
3.49	Time correlation between the damping of a magnetic bead oscillation and the deformation of an embedded vesicle in a percolating network. . . . .	156
3.50	Fluorescence micrographs of deformed vesicles in an actin - myosin gel. . . . .	157
3.51	Time evolution of $G'$ and $G''$ of an actin myosin network during the percolation transition. . . . .	158
3.52	Trajectory of the oscillating magnetic bead in the percolating actin - myosin network . . . . .	159
3.53	Curvature of a deformed vesicle in an actin myosin network after the percolation transition . . . . .	160
3.54	Schematics of the three dimensional shape reconstruction algorithm for a deformed vesicle . . . . .	162
3.55	Evolution of the surface area and volume of a vesicle being deformed in a percolating actin network . . . . .	163
3.56	Characteristic dynamic parameters for the deformation of the vesicle in the percolating network . . . . .	164
3.57	Superposition of vesicle contours at different moments during the percolation transition . . . . .	166
3.58	Force acting on the vesicle in the actin network during the percolation transition . . . . .	168

## 0.1 Abstract

In this work the mechanical properties of model cellular and subcellular processes have been studied using self-assembled biomimetic systems of the actin cortex of the cytoskeleton. For this purpose, microscopy based magnetic colloidal force transducers (magnetic tweezers) were designed and image analysis algorithms developed. The first part examines the transport properties of the processive motor protein myosin V. In single molecule experiments, an average step size of 36.5 nm of the molecule is calculated from a statistical analysis of the movement data. This value coincides with the helix pseudo repeat of the actin filament myosin V moves along. Using magnetic colloidal force transducers, the detachment forces of single actively moving myosin V molecules from actin filaments could be measured for forces parallel and perpendicular to the movement direction. For forces applied perpendicular to the movement direction, the unbinding forces show an increase with increasing force rate, for which a general theoretical model for the dynamic unbinding of a moving motor protein was developed. This model yields an analytic relation of unbinding force and force rate, which was used to compute an internal length of 11 nm of the binding potential and an equilibrium dissociation constant of  $0.3 \text{ s}^{-1}$  of the predominant kinetic state of the motor protein. To estimate an error for the values for the two potential parameters from the limited data set, a Monte carlo like method of fitting a randomly modified data set was developed. For comparison, a second method to determine the internal length of the binding potential and the equilibrium dissociation constant, from a combined rupture force probability density of all rupture events, was developed. This yielded equivalent results. The determined dissociation constant is remarkably smaller than expected from the duty ratio of the individual binding sites of the molecule. This leads to the conclusion, that a strain mediated interaction between the two actin binding sites exists, which results in longer movements of the molecule and a super-processive behavior. Additionally the movement of single myosin V molecules under forward and backward load was observed. The result that the velocity of myosin V does not change up to a load of 900 fN can be combined with previous studies to the picture that in an apparent

internal strain coupling between the two active domains during the movement of the molecule, the leading head is blocked by the stress the trailing head imposes on it.

The second part of this work deals with self-assembled actin networks on three dimensionally micro-structured surfaces. The structures used were arrays of micro pillars made by photo lithography and etching techniques from Silicon, photo resin or PDMS. Actin filaments could selectively be polymerized from the tops of these pillars, so that after cross linking of the filaments a freely suspended quasi two dimensional actin network was obtained on top of the pillar array. This network structure served as biomimetic model for the quasi two dimensional membrane-associated actin cortex in cells. The motor protein myosin V was used to transport polystyrene nano-beads on the network structure and thus mimic inner-cellular transport processes. With magnetic colloidal force transducers local elastic properties of the actin network were measured and an approximate Young modulus of  $1 \text{ N/m}^2$  for the network was determined. The micro pillar arrays were also used to immobilize single actin filaments and bundles on them and calculate their elastic properties from the observation of their thermal undulations. Two different methods for the data analysis were used which both yielded equivalent values for the persistence length of  $15 - 17 \mu\text{m}$ . The Young modulus of actin as a material property was calculated taking into account the helical structure of the filament, which leads to a value of  $3.1 \cdot 10^8 \text{ N/m}^2$ . Using quantitative fluorescence analysis, the number of actin filaments in actin - filamin bundles could be determined. The persistence length of these bundles was analyzed in dependence on the number of filaments in the bundle. This showed a quadratic dependence, as for a homogeneous rigid rod with the same Young modulus as actin.

In the third part of this work, the viscoelastic properties of vesicles that contained a self assembled internal actin cortex were examined. Actin filaments that were polymerized inside phospholipid vesicles form a thin cortex structure of mostly parallel filaments bound to the phospholipid bilayer membrane when electrostatically attracted to it. Magnetic beads were placed

from the outside onto substrate adhered vesicles and pulled perpendicular to the substrate. To observe the movement of beads in three dimensions, a three dimensional particle tracking algorithm was established. The bead movement in response to a periodic step force of 0.3 up to 5 pN was analyzed as the creep compliance function  $J(t)$ , parallel and perpendicular to the vesicle surface, in the time domain. Using a numeric procedure the creep data  $J(t)$  was converted into the stress relaxation function  $G(t)$ . This procedure showed the existence of separated time scales in the stress relaxation so that a phenomenological viscoelastic model could be used to fit the creep compliance data. The use of two response times yielded good fit results and a set of four parameters (two viscous and two elastic) was used to describe the creep response of the system. The two response times were separated by one order of magnitude. All four parameters showed a linear dependence on actin surface density. Furthermore the influence of photochemically induced damage on the actin filaments and a work hardening of the cortex of actin vesicles are discussed. The analysis of membrane fluctuations, using the magnetic bead as a marker, led to the determination of a bending rigidity of roughly  $1000 k_B T$  and the shear rigidity of  $0.1 \mu N/m$  the vesicles. The comparison of these two elastic parameters leads to the conclusion that in the anisotropic actin cortex deformation modes longitudinal to the filament orientation are preferred over transverse ones. To visualize the strain field in the vesicle surface, small non-magnetic beads were additionally attached to the outside of the vesicles. By simultaneously observing the movement of a magnetic and many non-magnetic beads, the strain field inside the membrane-cortex composite sheet could be mapped. From this strain field in the two dimensional actin cortex the Young modulus of the actin - membrane composite sheet was determined to be  $179 N/m^2$

In a fourth part evaporating droplets of entangled actin networks have been studied. At certain wetting conditions of actin solutions on glass, the triple interface line between glass, actin solution and air is pinned during a first period of the evaporation process. This leads to a radially outward flow. At the triple line, actin is accumulated in a dense structure. When outward flowing filaments encounter this structure, they are compressed against it and show

bending and folding with characteristic bending contour length. To analyze these bending contour length, a filament contour tracing algorithm was developed. Observed bending contours differ significantly from buckling contours expected from calculations of buckling under hydrodynamic forces. Comparison of the network mesh size with the thermal undulation amplitudes and the characteristic buckling time with the relaxation time of the thermal modes show that the bending process observed is rather a amplification of accessible thermal modes than a classical Euler buckling instability. The dominant amplified mode is determined by the characteristic time of the bending process and the mode relaxation time of the filament.

In the last part phospholipid vesicles, embedded in actin-myosin networks, have been used as force sensors. Motor active actin-myosin networks have been shown to exhibit a sol-gel transition, due to a percolation, and internal movements of filaments in the moment of ATP depletion. Vesicles embedded in and electrostatically coupled to such actin myosin networks show strong deformations from their initial shape during the sol-gel transition. This deformation happens simultaneously to a drastic increase in the viscoelastic moduli of the network, which were measured simultaneously in the same sample using magnetic bead micro-rheometry. An image processing algorithm to analyze shapes of deforming vesicles was established. Thus the local deformation energy of the actin myosin network contraction was calculated. A three dimensional reconstruction method of the vesicle shape showed that the surface area of the vesicle stays constant during the transition, but the volume decreases by 25 %. The comparison of the vesicle shapes during the transition with phase diagrams of vesicle equilibrium shapes show that although the obtained shape seems to have the form of a stomatocyte, the deformation can not be described in terms of a area - volume shape transformation of vesicles. This leads to the assumption that the vesicle is deformed by locally percolating actin structures in the network. An approximate deformation force acting on a small part of the vesicle is calculated for the entire deformation process. The maximum force exerted on the vesicle during the percolation is shown to be around 100 pN, which is a reasonable value for myosin assemblies.

# Chapter 1

## Introduction

Cells are the unique building blocks of life. Since all living beings are made up from cells, it seems that the compartmentation of organisms into cells is a vital criterion for the evolutionary development of all complex living structures. In brief, understanding cells means understanding life. From a physics point of view, cells are highly complex, many parameter systems, which can hardly be described with existing theories. A common approach is therefore to investigate the function of simple model systems of cellular substructures, such as vesicles, biopolymer networks, or individual proteins in single molecule experiments. All these approaches mimic a partial function of cells, have few and well controllable parameters and may add up to a better understanding of real cellular function. Furthermore, results of these kind of experiments can be analyzed within such well established frameworks as statistical mechanics, thermodynamics, the theory of elasticity and complex fluids. In order to retrieve results from an experimental model system, which can be interpreted in comparison with cellular function, the model system has to mimic the cellular system as closely as possible. However, the model system has to be as simple as possible, keeping the number of components and parameters small and still allow a numeric analysis and interpretation. Since self-assembly is thought to play key role for the formation of cellular structures, all biomimetic model system used were established through self-assembly of its components, while the boundary conditions of the assembly process determined the developing structures. The functional unit of the cell which was tried to study in the context of this work through biomimetic model experiments is the membrane

associated part of the cytoskeleton. The cell cytoskeleton is a self-assembled, rigid yet flexible network of bio-polymers inside the cell body. Its strength and dynamics determine the mechanic properties of the cell. It can roughly be divided into a bulk cytoskeleton, which is mostly made up of microtubuls and intermediate filaments, such as vimentin, and a membrane associated part. The latter is mostly made up of actin microfilaments and actin binding proteins. It spans the whole inside of the cell plasma membrane like a thin sheet of several tens to a few hundred nanometer thickness. The cellular role of this actin cortex is to control and regulate the mechanical stability of the cell [1], to serve as a driving force in cell locomotion [2][3], to develop cell protrusions [4][5] and to serve as a guiding system along which cell organelles can be transported by motor proteins [6]. The local geometry of the actin cytoskeleton can show, according to its function, different structures, of which several are shown in the fluorescence micrograph of the actin cytoskeleton of a fibroblast in figure 1.1a. Filopodia and microspikes are elongated cylindrical protrusions, that contain oriented and bundled actin filaments and different actin cross-linking proteins. They can extend several tens of micrometers from the cell and show a co-localization of motor proteins with the actin in the filopodia [9]. The most prominent role of filopodia is in neuronal growth cones, but they also exist in most motile cells. The lamellipodium is a flat protrusive sheet at the leading edge of many motile cells, such as fibroblasts or keratinocytes. When motile cells crawl over a flat surface, the lamellipodium is pushed forward by the polymerization pressure of a crosslinked actin network, which due to the polar structure of the actin filaments has a preferred orientation for its extension. Figure 1.1d shows the actin network in the lamellipodium of a crawling fish keratinocyte. Stress fibers are thick actin bundle structures, which often span over nearly the whole cell. They are linked to the cell membrane via focal contacts, adhesion spots of the cell on a substrate. Stress fibers ensure the stability of the cell shape and can exert contractile forces of the cell to its adhesion points [10]. Besides actin cross-linking proteins like filamin or  $\alpha$ -actinin, stress fibers usually contain motor proteins, which are needed to produce the contractile forces. The local structure of the actin cytoskeleton is closely linked to its cellular function. For this reason, if biomimetic experi-

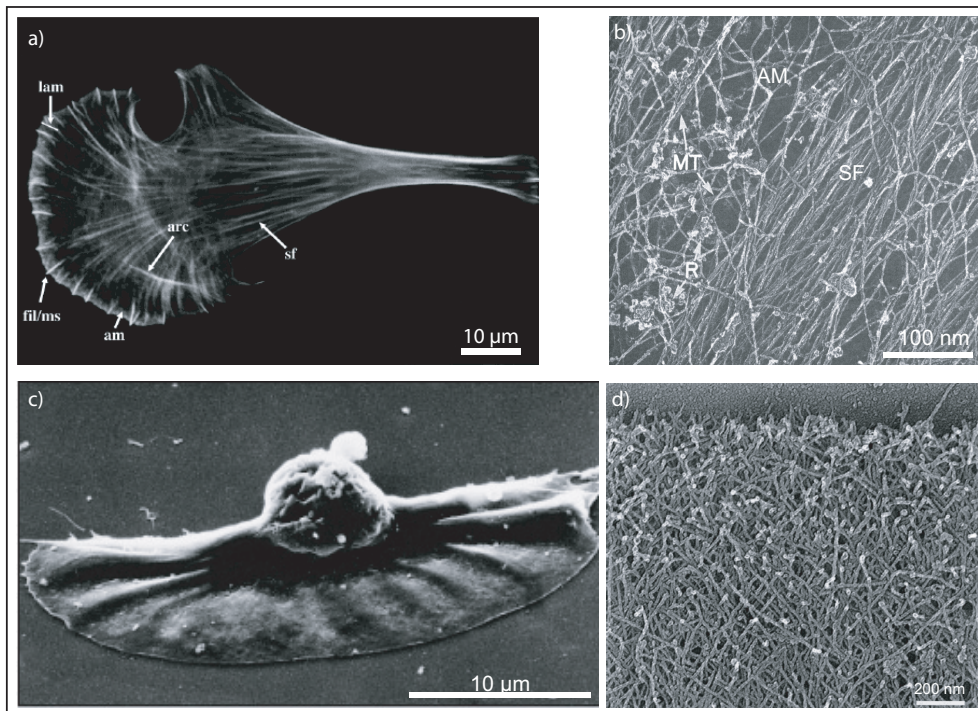


Figure 1.1: Images of the actin cytoskeleton inside cells

a) Fluorescence micrograph of a chick heart fibroblast. Actin is labelled with Rhodamine - Phalloidin. The abbreviations of the indicated structures are: am: actin meshwork; arc: dorsal arc; fil/ms: filopodium/microspike; lam: lamellipodium; sf: stress fiber. (source Small et al [7]) b) Typical electron micrograph of the cytoskeleton. Abbreviations: MT: microtubules; AM: actin meshwork; SF: stress fiber. (source: Alberts et al [8]) c) Scanning Electron micrograph of a crawling fish keratinocyte. The large lamellipodium is spread in the direction of its movement. (source: Alberts et al [8]) d) Electron micrograph of the leading edge of the lamellipodium of a crawling fish keratinocyte. The cross-weave and branching of the actin filaments and their orientation in an angle to the direction of the protrusion can nicely be observed. (source Small et al [7])

ments shall be related to the function of sub-cellular units of the cytoskeleton, the structure of this units has to be modelled as closely as possible.

## 1.1 Motor proteins

Motor proteins are biochemical machines that transform energy stored in nucleotides (ATP or GTP) into directed motion along thread-like tracks, the bio-polymers of the cytoskeleton. The motor proteins therefore interact via a specific binding site with the bio-polymers relative to which the translation is achieved. Prominent motor protein-polymer pairs are; myosin-actin, kinesin-microtubuls or dynein-microtubuls. Since these track forming bio-polymer filaments are polar structures, their polarity defines the direction of the motor proteins' movement. Most motor proteins share common basic structural features. They are fork-like homo-dimeric molecules. Each monomer has a globular domain, that contains the nucleotide binding site and the binding site for the bio-polymer and a long, mostly  $\alpha$ -helical stalk. With the exception of myosin I, two monomers are assembled into dimers with their stalk regions forming a coiled-coil structure. Figure 1.2 shows electron microscopy images of different motor proteins.

Each of the globular binding domains works in a cyclic manner; in it' s biochemical pathway of binding nucleotide, hydrolyzing it and releasing the products, as well as in it' s mechanical process of unbinding from the bio-polymer, moving forward and rebinding to it. This biochemical and mechanical cycle both have a characteristic cycle time  $\tau_c$ . The percentage of time, one binding domain remains bound to the bio-polymer during one cycle is called the duty ratio  $r_d$  of the molecule. Depending on this duty ratio, motor proteins can be roughly divided into two classes. Processive motors can work on a single molecule basis and have high duty ratios (e.g. Myosin V,  $r_d=0.7$  [12]) . This means that one individual molecule is able to perform continuous movement along a bio-polymer chain for several work cycles. These classes of motor proteins are mostly involved in particle transport processes inside cells [13]. Non-processive motor proteins, such as muscle myosin II, have to work together in large ensembles to perform continuous movement, or exert contin-

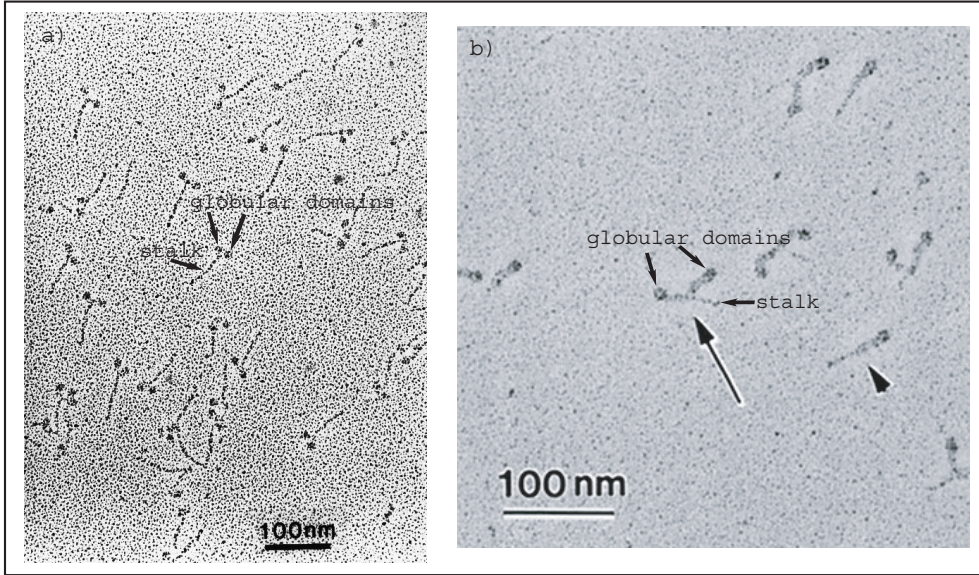


Figure 1.2: Electron micrographs of motor proteins

a) **Truncated muscle myosin II fragments. Image made on a Phillips CM 120 transmission electron microscope.** b) **Class V myosin molecules (image from: Wang et al, [11], p.4331)**

ous large forces as needed for cell locomotion [14] or the extension of cellular protrusions [4]. Their duty ratio is very low e.g. muscle myosin II,  $r_d = 0.01 - 0.02$  [15]). From the duty ratio of a binding domain of a motor molecule, the dissociation constant of the dimeric molecule can be calculated, if no stress mediated interaction exists between the two binding domains of the molecule. For independent binding domains, the probability that both unbind during one cycle time  $\tau_c$  is  $(1 - r_d)^2$ . In terms of a dissociation constant  $k_0$  for the entire moving molecule, the same probability is  $1 - e^{-k_0 \cdot \tau_c}$ . By setting these two expressions equal, the dissociation constant can be determined as

$$k_0 = \frac{1}{\tau_c} \cdot \ln \left( \frac{1}{2r_d - r_d^2} \right) \quad (1.1)$$

Looking at the cycle times  $\tau_c$  for processive myosin V ( $\approx 60ms$ ) and non-processive myosin II ( $\approx 8ms$ ) one retrieves dissociation constants of  $1.57 s^{-1}$  for myosin V and  $\approx 400 - 500 s^{-1}$  for myosin II. This clearly illustrates the difference between processive ( $k_0 \cdot \tau_c \ll 1$ ) and non-processive behavior ( $k_0 \cdot \tau_c > 1$ ). Recent experiments hint that a strain interaction between the two binding domains of some motor proteins exist, which may enable a coordination of the

biochemical reactions at these domains [16].

The forward movement of motor proteins does not occur in a continuous way, but rather in discrete steps with dwelling intervals in between. The step sizes of many motor proteins have been measured [17] [18][19], with optical trap or micro-needle experiments. Interestingly, many motor proteins, especially processive ones, show step size distributions with average values that coincide with repeat periods of the bio-polymers they move along [20][21]. High resolution tracking of the movement of motor proteins has even shown characteristic sub steps within the movement between two repeat motives of the bio-polymer, which must stem from the internal mechanics of the motor molecule [16][22].

If all reactions of the biochemical cycle of the motor molecule are irreversible, which can roughly be assumed, the distribution of dwelling intervals shows an exponential decay for each of the reaction rates [21][23]. In practice, most reaction rates are so high, that due to time resolution only the slowest rates can be determined. Nevertheless those are the most important rates for the motor protein, since they serve to identify the rate limiting step of the molecule's kinetics. When a load is applied to the molecule in parallel to its movement direction, most motor proteins will stall at a characteristic force, denoted as their specific stall force. Stall forces for many molecules have been measured [23][19] and are found in the range of a few piconewtons.

## 1.2 Dissociation of single specific bonds

Biological macromolecules interact via specific binding sites of their tertiary structure. The specific bond between two molecules is characterized by its binding potential  $U(\vec{r})$ . Bonds between biological molecules are relatively weak, compared to covalent bonds. The yield forces of biological bonds are in the range of a few to tens of piconewtons [24][25], whereas yield forces of covalent bonds can exceed by far 1 nN [26]. This weakness of bonds between biological macromolecules has an important role for the cellular system, since cells are highly dynamic and flexible and bonds that cannot easily be ruptured

would be dangerous obstacles for the adaptability of a cell to its changing environment. Furthermore, the natural turnover of all cellular material (proteins, lipids, etc.) would be inhibited by bonds with long lifetimes ( $> 1$  day).

### 1.2.1 Thermal bond dissociation

The binding potential  $U(\vec{r})$  of a single bond between two molecules, has a minimum at the average bond length. When the bond is broken, the binding partners are assumed to move through the potential along a one dimensional transition pathway  $\vec{x}$  of minimum energy barriers. The binding potential of the bond can thus be characterized through the highest energy barrier  $\Delta G$  that has to be overcome to break the bond and the length  $l$  of the transition pathway between the average bond length and the position of the barrier (figure 1.3) [27]. Thus already in the absence of external forces, any bond can rupture through thermal fluctuation and any bond will rupture if one waits long enough. The probability  $N_0$  that a bond observed is not ruptured yet obeys the equation

$$\frac{dN_0}{dt} = -k_0 \cdot N_0 \quad (1.2)$$

where  $k_0$  is the equilibrium dissociation constant [28]. It depends on the height of the energy barrier  $G_0$  as a Boltzmann factor [27].

$$k_0 \propto e^{\frac{G_0}{k_b \cdot T}} \quad (1.3)$$

### 1.2.2 Force induced bond dissociation

If an external force is applied to the bond, the binding potential is distorted in a way that the work  $E_{el}$ , performed by the external force on the bond, has to be included in the binding potential. For small forces<sup>1</sup> one can assume that the binding enthalpy does not change<sup>2</sup> and the entire potential is simply a superposition of the undisturbed potential and the elastic energy along the reaction pathway  $E_{el} = \vec{F} \cdot \vec{x}$ . Thus the energy barrier is lowered by  $\Delta G = \vec{F} \cdot \vec{l}$

---

<sup>1</sup>the force applied must be much smaller than the gradient of the binding potential

<sup>2</sup>the structure of the binding partners is not changed

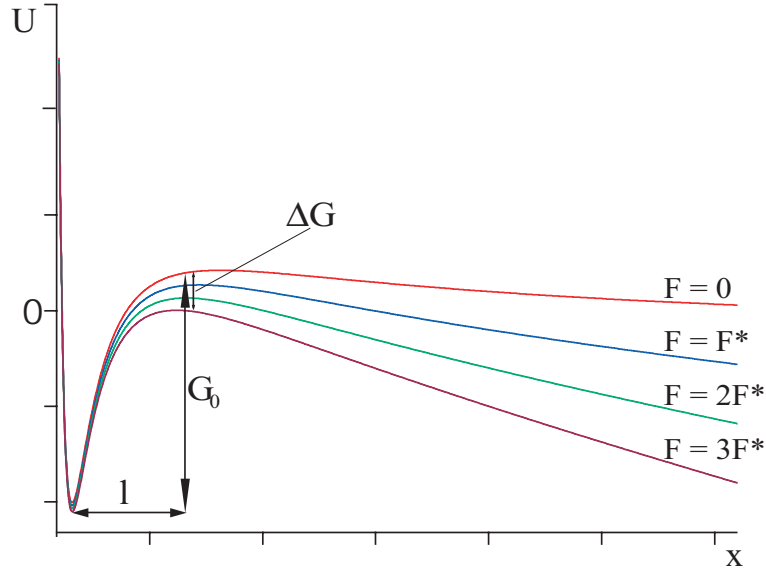


Figure 1.3: Hypothetic binding potential of a molecular bond **The hypothetical binding potential is shown for an undisturbed bond ( $F=0$ ) and for externally applied forces. The energy barrier for a thermal escape, which for an undisturbed bond is  $G_0$  is lower by the applied force.**

and the dissociation rate  $k$  changes to

$$k(F) = k_0 \cdot e^{\frac{F \cdot l}{k_b \cdot T}} = k_0 \cdot e^{\frac{F}{f_0}} \quad (1.4)$$

$f_0 = \frac{k_b \cdot T}{l}$  is a typical force for the rupture of the bond [29]. For the calculation of the distribution of rupture forces it is assumed that once the bond is broken, the two binding partners are separated fast to a large distance so that rebinding can be neglected. By solving equation 1.2 one retrieves the probability  $N(t)$  that a bond that existed at time zero still exists at time  $t$ . Transforming the coordinates of integration from the time to the force domain, using a force-time relation  $F(t)$  one retrieves the probability  $N(F)$  that a bond that existed at force 0 still exists at force  $F$ .

$$N(F) = \exp\left(\int_0^F -k(F)\left(\frac{dt}{dF}\right)dF\right) \quad (1.5)$$

$N_r(F) = 1 - N(F)$  therefore is the probability that the bond is ruptured. The force derivative  $\frac{d}{dF}(N_r(F))$  represents a distribution of rupture forces. This shows that weak bonds, such as the ones between biological macromolecules

do not have a yield force but a distribution of yield forces. Therefore the bond is not characterized by a minimum force to rupture it, but by the potential parameters  $k_0$  and  $l$ .

### 1.3 Introduction to semi-flexible polymers

Semi-flexible polymers can be seen as rod-like objects that show, due to thermal motion, shape oscillations around their minimum energy shape of a straight rod. The energy associated with their shape oscillations is the bending energy  $E_b$ . For a thin rod <sup>3</sup> of length  $l$  and Young modulus  $E$  the bending energy for small bending amplitudes<sup>4</sup> is

$$E_b = \frac{E}{2} \cdot \int_0^l I_x \left( \frac{\partial^2 \vec{x}}{\partial z^2} \right)^2 + I_y \left( \frac{\partial^2 \vec{y}}{\partial z^2} \right)^2 dz \quad (1.6)$$

Here the  $z$ -axis is the connecting axis between the points 0 and  $l$  and  $I_x$  and  $I_y$  are the moments of inertia in  $x$  and  $y$  direction. For  $I_x = I_y = I$ , which can be assumed for polymers due to their rotational symmetry, equation 1.6 simplifies to

$$E_b = \frac{E \cdot I}{2} \cdot \int_0^l \frac{1}{R^2(z)} dz = \frac{\kappa}{2} \cdot \int_0^l \frac{1}{R^2(z)} dz \quad (1.7)$$

Here  $R$  denotes the radius of curvature and  $\kappa = E \cdot I$  is the bending rigidity. The bending rigidity is a geometric and material property of the polymer.

An intuitive measure for the shape or the stiffness of the polymer is the vector correlation  $C(\Delta s, t)$  between the tangential vectors  $\vec{T}(s, t)$  at two different points on the contour  $s$  of the polymer, which are separated by the contour length  $\Delta s$ .

$$C(\Delta s, t) = \langle \vec{T}(s, t), \vec{T}(s + \Delta s, t) \rangle \quad (1.8)$$

This is equivalent to the time average of the absolute cosine of the angle  $\alpha$  between the tangents at two points on the fluctuating polymer, which are separated by a contour length  $\Delta s$ . (See figure 1.4) The polymer section between 0 and  $\Delta s$  is, for simplicity, shown with a constant radius of curvature. The

---

<sup>3</sup>the diameter of the rod must be substantially smaller than the length of the rod

<sup>4</sup>the change in position of a point relative to any other point must be small compared to their distance

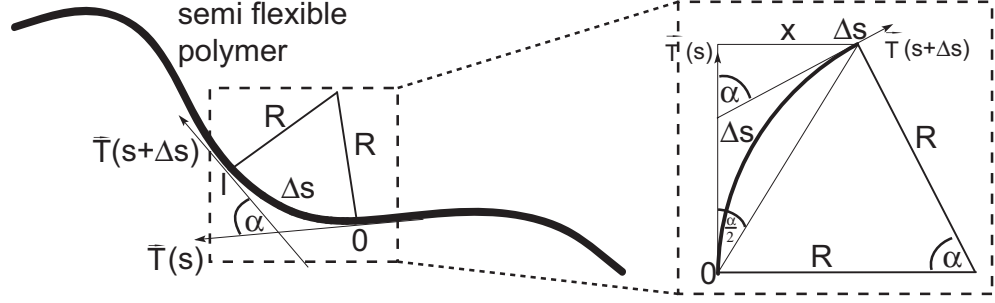


Figure 1.4: Geometry of a schematic semi-flexible polymer  
**The semi flexible polymer is represented by its contour (thick line), with two tangent vectors  $\vec{T}$  separated by a length of  $\Delta s$  along the polymer contour. )**

end point of the polymer fluctuates in an harmonic potential  $\frac{k}{2}x^2$ , which is determined by the bending energy. The corresponding equation of motion is

$$m\ddot{x} + kx = F(t) \quad (1.9)$$

with a rapidly oscillating thermal force  $F(t)$ . The inertia term is very small compared to the restoring harmonic potential force, such that following all terms containing the mass of the polymer are neglected. Thus the equation has the probability density  $P(x)$  for the amplitude  $x$  of [30]

$$P(x) = \sqrt{\frac{2\pi \cdot k_b T}{k}} \cdot e^{-\frac{k \cdot x^2}{2k_b T}} \quad (1.10)$$

Using geometric relations, which can be seen in figure 1.4, this density function is transformed into a probability density of the angle  $\alpha$  between the tangents at points 0 and  $\Delta s$ . The necessary transformations are:

$$R = \frac{\Delta s}{\alpha} \quad (1.11)$$

$$x = R(1 - \cos\alpha) \approx \frac{R\alpha^2}{2} = \Delta s \cdot \frac{\alpha}{2} \quad (1.12)$$

The bending energy (equation 1.7) thus becomes

$$E_b = \frac{k}{2} \cdot x^2 = \frac{\kappa}{4 \cdot \Delta s} \cdot \alpha^2 \quad (1.13)$$

and the probability density for  $\alpha$

$$P(\alpha) = \sqrt{\frac{4\pi \cdot k_b T \Delta s}{\kappa}} \cdot e^{-\frac{\kappa \cdot \alpha^2}{4k_b T \Delta s}} \quad (1.14)$$

the average value for the absolute cosine of  $\alpha$ , which is the tangent correlation function  $C(\Delta s, t)$  is

$$C(\Delta s, t) = \langle |\cos(\alpha)| \rangle = \int_{-\infty}^{\infty} \cos(\alpha) \cdot P(\alpha) d\alpha = e^{-\frac{\Delta s \cdot \kappa_b T}{\kappa}} =: e^{-\frac{\Delta s}{l_p}} \quad (1.15)$$

The parameter  $l_p = \frac{\kappa}{\kappa_b T}$  has the unit of a length and is called persistence length of the polymer. The correlation function  $C(\Delta s, t)$  of two tangents to the contour of a semi-flexible polymer thus shows an exponential decay with increasing distance from an original point with a characteristic length  $l_p$ . Determining for the shape of a polymer is the ratio  $r_p$  of the length of the polymer to its persistence length,  $r_p = \frac{l}{l_p}$ . For large ratios as e.g. for DNA ( $r_p > 10$ ), the polymer appears as a coil. The shape of polymers like actin ( $r_p \approx 1$ ) appears like a curved line, whereas polymers like microtubules, ( $r_p < 0.1$ ), appear like straight rigid rods. The parameter  $r_p$  thus serves as a classification criterion for polymers into flexible, semi-flexible and rigid polymers.

### 1.3.1 Oscillations of semi-flexible polymers

Like all elastic systems, semi-flexible polymers possess a series of Eigenmodes which are preferably excited. The entire fluctuations of the polymer can be therefore simply described in terms of a superposition of its Eigenmodes. The mathematical form of the individual mode depends on the bending stiffness, the length of the polymer and its boundary conditions, and can be calculated as the oscillations of an elastic rod subjected to fluctuating forces. The wave equation for small oscillations  $x = x_0 \cos(\omega t)$  of a rotational symmetric homogeneous rod is

$$\frac{d^4 x_0}{dz^4} = k^4 x_0 \quad (1.16)$$

where  $k$  has the units of a wave number. The complete solution of the equation is

$$x_0 = A \cos(kz) + B \sin(kz) + C \cosh(kz) + D \sinh(kz) \quad (1.17)$$

in which the boundary conditions at the two limiting points have to be inserted. The easiest is the case when at both points (separated by the length  $l$ ) the filament is fixed ( $x_0(0) = x_0(l) = 0$ ) but exhibits free rotational degree of freedom ( $\frac{dx_0}{dz}(0) \neq 0$ ;  $\frac{dx_0}{dz}(l) \neq 0$ ). For this case, the Eigenmodes have a pure

sinusoidal form  $x = A \cdot \sin(kz) \cdot \cos(\omega t)$  with wave numbers  $k = \frac{n}{2l}$ , where  $n$  is a positive integer.

### 1.3.2 Solutions of semi-flexible actin polymers

In concentrated solutions of actin polymers, the individual filaments are entangled and interact in a steric repulsion potential. An empiric formula for the relation of the mesh size  $\xi$ , which is the average distance between two polymers, to the molar concentration<sup>5</sup> of actin filament solutions  $c_{actin}$  is [31]

$$\xi = 1.66 \cdot (c_{actin}(\mu M))^{-\frac{1}{2}} [\mu m] \quad (1.18)$$

An important condition for an entanglement is that the mesh size is much smaller than the length and persistence length of the filaments. The entanglement of the filaments leads to a mechanical response of actin solutions to external forces that are not purely viscous, but show a mixture of viscous and elastic behavior depending on the time scale on which the response is observed. In entangled actin solutions, for each filament, the surrounding filaments can be accounted for by a tube, which limits its lateral motion perpendicular to the diameter of the tube [32]. A diffusion out of the tube is only possible along the filament and tube axis and can take up to hours [33]. The diffusion is called reptation [34] and its characteristic time is called disengagement time, which is proportional to  $l^{\frac{3}{2}}$  [33] of the length of the filament. The self-diffusion of filaments out of their reptation tubes determines the viscous response of actin solutions at long time scales. The elastic behavior on shorter time scales stems from the deformation of filaments inside their reptation tubes and the damping of internal modes of the filaments.

## 1.4 Linear viscoelastic theory

Viscoelasticity is the phenomena that some materials show time dependent restoring forces, internal stresses and deformations as response to externally applied forces. When two points of a material, which are separated by the

---

<sup>5</sup>of initial actin monomers

vector  $\vec{x}$ , are displaced, due to an externally applied force  $F$ , by the vector  $\vec{u}$ , the strain tensor  $\epsilon_{ij}$  for small deformations<sup>6</sup> is

$$\epsilon_{ij} = \frac{1}{2} \left( \frac{\partial u_i}{\partial x_j} + \frac{\partial u_j}{\partial x_i} \right) \quad (1.19)$$

Due to the externally applied force and the deformation of the material, the whole system is in mechanical equilibrium. Nevertheless internal stresses exist, which have the form of a tensor  $\sigma_{ij}$ , which is defined through the force components in the volume of the material.

$$F_i = \sum_j \frac{\sigma_{ij}}{x_j} \quad (1.20)$$

The linearity of the viscoelastic response leads to the superposition principle, that the internal stress of the system at time  $t$  is determined by the sum (or integral) over all strains at previous times  $\tau$  introducing a linear response function  $Q(t - \tau)$ .

$$\sigma(t) = \int_0^t Q(t - \tau) \epsilon(\tau) d\tau \quad (1.21)$$

An equivalent relation yields for the strain

$$\epsilon(t) = \int_0^t U(t - \tau) \sigma(\tau) d\tau \quad (1.22)$$

$U(t - \tau)$  and  $Q(t - \tau)$  are also called memory functions of the material since they link its mechanical state to all its previous mechanical states. Equations 1.21 and 1.22 are the constituting equations for the behavior of viscoelastic materials. If a step stress<sup>7</sup> is applied to the system equation 1.22 can be used to calculate the viscoelastic response of the system. The Laplace transform  $\mathcal{L}(\sigma(t))$  of the stress is

$$\mathcal{L}(\sigma(t)) = \sigma(\omega) = \frac{\sigma_0}{\omega} \quad (1.23)$$

Since like for the Fourier transform, the Laplace transform of a convolution integral is the product of the transforms of the two convolution functions, equation 1.22 can be Laplace transformed and leads, using equation 1.23 to

$$\epsilon(\omega) = U(\omega) \sigma(\omega) = \frac{\sigma_0}{\omega} U(\omega) \quad (1.24)$$

---

<sup>6</sup>  $\|\vec{u}\| \ll \|\vec{x}\|$

<sup>7</sup>  $\sigma(t) = 0$  for  $t < 0$ ;  $\sigma(t) = \sigma_0$  for  $t \geq 0$

Inversely Laplace transforming equation 1.24 yields

$$\mathcal{L}^{-1}(\epsilon(\omega)) = \epsilon(t) = \sigma_0 \mathcal{L}^{-1} \left( \frac{U(\omega)}{\omega} \right) \quad (1.25)$$

By defining a new function  $J(\omega) = \frac{U(\omega)}{\omega}$  the inverse transformation yields

$$\epsilon(t) = \sigma_0 \mathcal{L}^{-1} J(\omega) = \sigma_0 J(t) \quad (1.26)$$

Thus for a step force applied to a viscoelastic system, the strain of the system is proportional to the amplitude of the step stress with a relating function  $J(t)$ , called creep compliance. Using the definition of  $J(\omega)$  one can write  $J(t)$  as

$$J(t) = \mathcal{L}^{-1} \left( \frac{U(\omega)}{\omega} \right) = \int_0^t U(\tau) d\tau \quad (1.27)$$

This formula states that the creep compliance  $J(t)$  is the viscoelastic response function of a material to a step stress. In the same way one can introduce a function  $G(t)$  for a suddenly introduced step strain with amplitude  $\epsilon_0$ ,

$$G(t) = \mathcal{L}^{-1} \left( \frac{Q(\omega)}{\omega} \right) = \int_0^t Q(\tau) d\tau \quad (1.28)$$

which is the stress relaxation function of the material.

$$G(t) = \frac{\sigma(t)}{\epsilon_0} \quad (1.29)$$

For a given strain or stress function, the two characteristic material functions  $J(t)$  and  $G(t)$  are linked through a convolution integral.

$$\int_0^t J(\tau) G(t - \tau) d\tau = \int_0^t G(\tau) J(t - \tau) d\tau = t \quad (1.30)$$

In creep experiments, a constant force is induced and the deformation of the sample observed, in relaxation experiments, the sample is held under constant deformation and the relaxation of the internal stress is measured.

### 1.4.1 Linear viscoelastic models

As recognized for the first time by Maxwell, the one dimensional viscoelastic behavior of a materials can be represented through a idealized scheme as a combination of constitutive elements. In analogy to capacitors and coils in

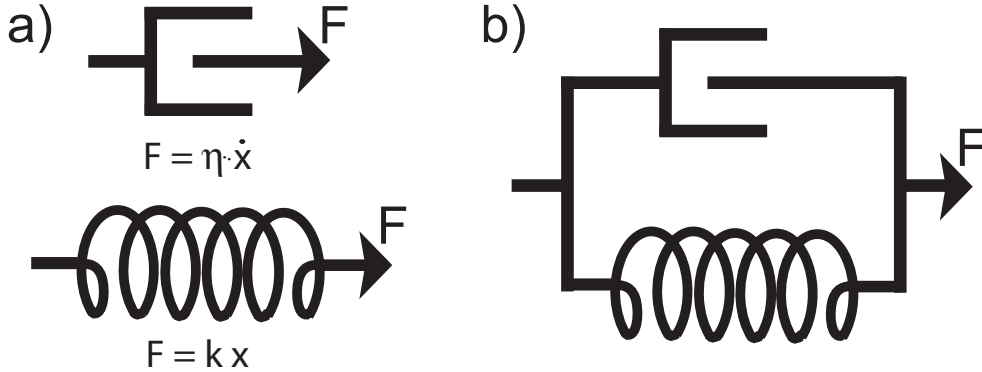


Figure 1.5: Models for viscoelastic materials

a) The two basic units of linear viscoelastic models are purely elastic (spring) and purely viscous (dashpot) elements. b) The Voigt model is a basic unit of viscoelastic modelling. Its creep compliance and strain relaxation are given by equations 1.31 and 1.32 respectively.

electric circuits, sets of elastic elements, which obey Hook's law, and viscous elements, which obey Newton's law of viscous friction, model the viscoelastic behavior. Strains  $\epsilon$  are replaced with displacements  $x$  and stresses  $\sigma$  with forces  $F$ . In circuit representation springs and dashpots are used as symbols representing the mechanical behavior of an element. The number and combination of elastic and viscous elements determine  $J(t)$  and  $G(t)$  of the model. One very basic model, which is often used as base unit for more complex ones is the Voigt model, which is a parallel combination of a spring and a dashpot (figure 1.5b). To calculate the creep compliance of a viscoelastic model system, the set of coupled equations of motion, which is given by the constituting units, has to be solved for  $x(t)$  and a constant force  $F$ . Boundary conditions are equal forces in serial arrangements and equal displacements in parallel arrangements. The creep compliance function of a Voigt unit is given by

$$J(t) = \frac{1}{k} \left( 1 - e^{-\frac{kt}{\eta}} \right) \quad (1.31)$$

The calculation of  $G(t)$  is done in an equivalent way by computing  $F(t)$  for a constant displacement  $x$ . The strain relaxation function of a Voigt unit is

$$G(t) = k \left( e^{-\frac{kt}{\eta}} \right) \quad (1.32)$$

The Voigt model represents a viscoelastic material with one simple strain relaxation process. A general model for a viscoelastic material is a infinite series

of Voigt models, which signifies a linear superposition of all possible relaxation mechanisms. This approach can be used when the exact composition and structure of a material is not known [35]. Nevertheless, most materials have a small number of dominant relaxation mechanisms and can therefore be modelled with a limited number of Voigt models in serial arrangement. In order to describe the viscoelastic behavior of complex materials without a well defined structure, these mechanical circuit representations are often used to model the mechanical behavior of cells [36][37].

# Chapter 2

## Materials and Methods

### 2.1 Biochemical Materials

This section describes the most important proteins and biochemical agents used in the experiments. Further chemicals used, buffer solutions and abbreviations are described in the appendix.

#### 2.1.1 Proteins

##### Actin

Actin is a globular 43 kD protein of 375 amino acids, with a size of 3.7 x 4.7 x 6.7 nm [38][39], often denoted as G-actin. It is expressed in nearly all types of eucaryotic cells and has an amino acid sequence which is extremely well conserved through evolution [40]. Actin is one of the most abundant proteins in human tissues. In muscle cells it constitutes 20 -25 % of all proteins [41]. It can bind one ATP molecule complexed with a divalent ion. Actin self-assembles in presence of ATP and divalent ions, like  $Mg^{2+}$ , into two-stranded, left-handed helical filaments, usually denoted as F-actin. These filaments have a thickness of 9 to 10 nm and a full helical period of 72 nm [42]. However, intermediate resolution (2 - 3 nm) electron microscopy studies have shown that the structure of F-actin does depend on the nucleotide bound and on other proteins bound to the filament [43]. Therefore actin filaments seem to be a rather dynamic structure and not only passive elements.

Atomic models show that actin monomers bind not only to their nearest neighbors in the strand but also to those in the other strand [44]. The binding of

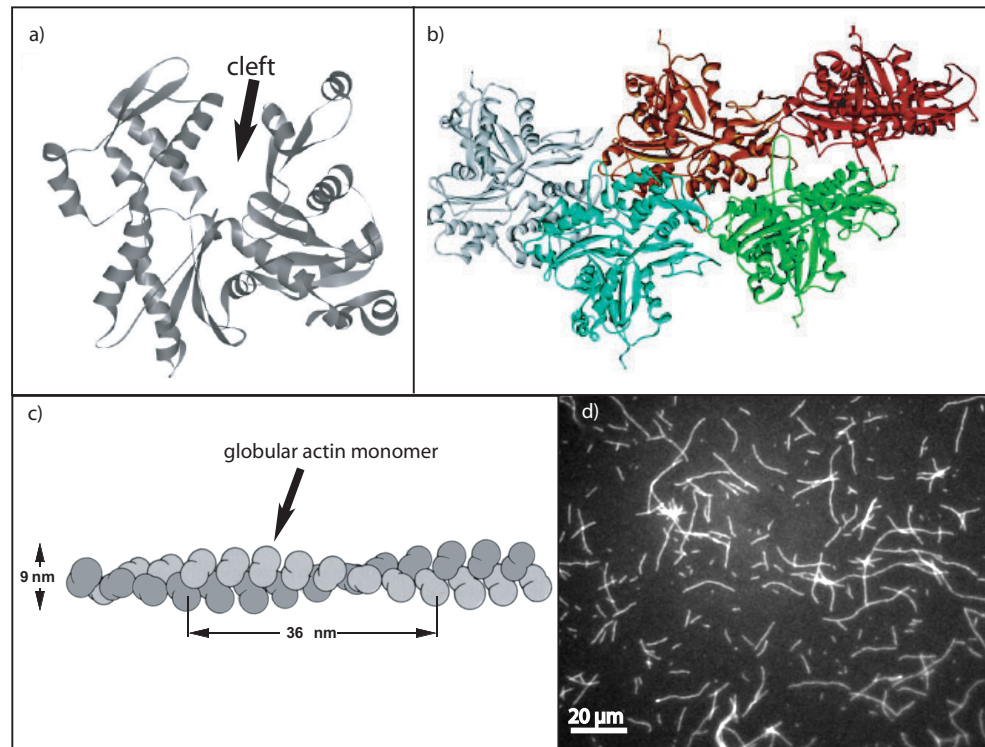


Figure 2.1: Actin

a) X-ray crystal structure of non-complexed globular actin with a resolution of 1.4 Å. The central cleft of the molecule (arrow) is the binding site of the ATP molecule. (source: Otterbein et al [38]) b) Structural model of F-actin, obtained by atomic modelling of data obtained from crystallography of DNase-complexed actin. (source Holmes et al [42]) c) Schematic geometry on an actin filament self-assembled from globular 43 kD protein units. (source: Alberts [8]) d) Fluorescently labelled actin filaments grafted onto a thin PDMS layer on a glass slide.

one monomer to all its neighbor monomers stabilizes the filament and enables actin filaments to reach lengths of up to 100  $\mu\text{m}$  [45][46]. Actin filaments have an average length of 22  $\mu\text{m}$  [47]. The persistence length of actin has been determined to values of 15 - 20  $\mu\text{m}$  [48] [49][50][51].

Along the filament axis, the monomer center to center distance is 5.5 nm, so that a full period of an actin filament contains 26 monomeric subunits [42]. Due to the asymmetry of its monomers, actin filaments have a polar structure with two structurally different ends. One, called the plus end, has a higher binding affinity for new monomers than the other, called the minus end.[45] Thus, actin filaments grow faster on the plus end than on the minus end.

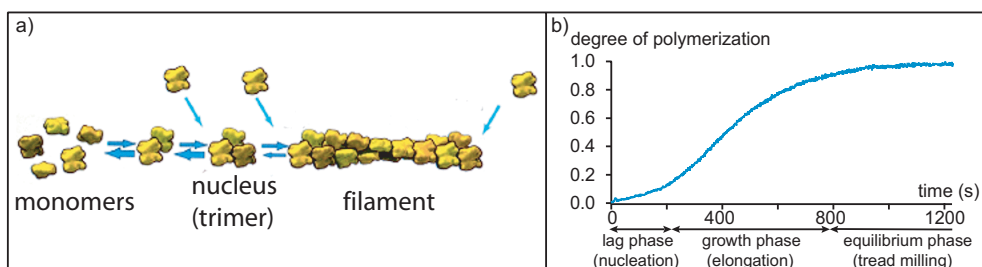


Figure 2.2: The process of actin polymerization

a) **Schematic polymerization through first, assembly of monomers into stable nuclei (trimers) and later filament growth from these nuclei.** (source Amann et al [55]) b) **Actin polymerization curve recorded with a fluorescence spectrometer (SPEX). A fluorescence dye (NBD) was covalently bound to the actin monomers. Upon the integration of a monomer into a oligomer, the fluorescence intensity of the dye is enhanced by a factor of roughly 2.3. Therefore the fluorescence intensity of the sample is a measure for its degree of polymerization.**

The polymerization speed of either end is proportional to the concentration of actin monomers in solution and can be negative, which means depolymerization. At physiological conditions, the critical concentration that separates polymerization from depolymerization is 12 to 15 times higher at the slowly growing minus end of the actin filament [52]. When polymerizing close to attractive surfaces<sup>1</sup> the critical concentration for polymerization is strongly reduced [53]. At equilibrium monomer concentration in the solution, the rates of polymerization at the plus end and depolymerization from the minus end are the same. This process of continuous polymerization and depolymerization of filaments at their different ends, while their average length stays constant, is called treadmilling [54].

Like crystallization, the polymerization of actin filaments has a minimum number of monomers, which is three, from which on filaments are thermodynamically stable. Thus, polymerization is no instantaneous process, but has a lag phase in which nuclei of three or more monomers are formed by stochastic three particle collision processes. A schematic polymerization process and a polymerization curve of actin are shown in figure 2.2. The polymerization process starts with the lag phase ( $\approx 60s$ ) during which stable nuclei of three actin

<sup>1</sup>Since actin is negatively charged, in general all positively charged surfaces are attractive.

monomers are formed. Following, these oligomers elongate until they reach their final average length and start the treadmilling dynamics. The duration of the lag phase has an inverse cubic dependence on the concentration, since three particle collision processes are represented by the cubic order of the virial expansion. Buffer conditions favorable for the polymerization of actin are neutral or slightly acidic pH, high ionic strength<sup>2</sup> and elevated temperature. In other words, physiological conditions. Actin was prepared from rabbit skeletal muscle in a procedure developed by James Spudich in 1982 [56] and further purified in a second step using gel column chromatography (Sephacryl S-300).

### Myosin V

Myosin V is a non-muscle myosin that has been shown to support polar movement of actin filaments on a single molecule level [57][19][21] and is therefore denoted as a processive molecular motor. Individual myosin V molecules with fluorescent light chains have been observed to walk along actin filaments with an average velocity of 540 nm/s for an average length of up to 2.4  $\mu\text{m}$  [57]. The tertiary structure of myosin V has been resolved recently by X-ray scattering for a kinetic state of the molecule without any nucleotide bound to it [58] with a 2 Å resolution. Additionally, images with roughly 2 nm resolution obtained by transmission electron microscopy exist, which show the form and structure of myosin V [59][60] (figure 2.3a). Myosin V is a dimeric molecule. Each monomer, that has a molecular weight of 212 kD, consists of a head, a neck and a tail domain (figure MyosinV) The terminal region of the tail is a globular domain that is thought to attach to cell organelles in order to transport them and is thus called the cargo binding domain. The  $\alpha$ -helical neck region binds six light chains, of which apparently only four are calmodulin [63]. With 23nm length, the neck is long enough for the two heads of myosin V to bind simultaneously to two actin monomers in an actin filament that are separated by the pseudorepeat (36nm) of the F-actin helix [59]. The head domain of myosin V has 41% sequence identity with the head domain of muscle myosin II [64]. To enable myosin V to processively move along actin filaments, both heads should spend most of the time of their cycle bound to actin. This pre-

---

<sup>2</sup>> 50 mM KCl

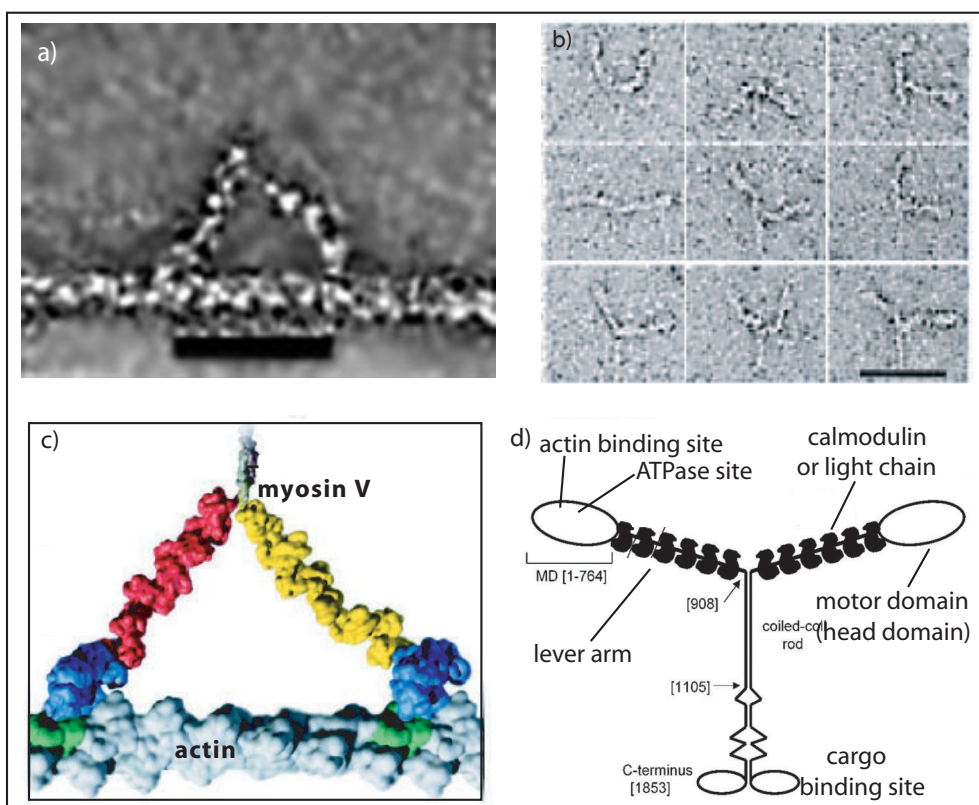


Figure 2.3: Structure of myosin V

a) Transmission electron microscope image of a truncated myosin V molecule bound to an actin filament. The scale bar is 30 nm. (source: Walker et al [59]) b) Electron micrographs of myosin V molecules adsorbed on a carbon film. The scale bar is 50 nm. (source Burgess et al [60]) c) Model for the structure of myosin V bound to an actin filament. (source Vale et al , [61]) d) Assumed structure of myosin V (source Trybus et al [62]). Numbers in brackets are the amino acid numbers.

vents the simultaneous unbinding of both heads and thus keeps the molecule from diffusing away. The duty ratio of myosin V has been measured to be 0.7 [12]. Time resolved fluorescence enhancement measurements with genetically expressed myosin V monomers indicate that ADP release (at rates between 12 and  $18\text{ s}^{-1}$ ) [65] [11] is the rate limiting step of the molecule's kinetics.

Experiments with dimeric chick brain purified myosin V molecules adsorbed to optically trapped polystyrene beads have produced dwell time distributions of a myosin molecule moving along an actin filament. Those reveal a slow rate ( $12.5 \pm 1\text{ s}^{-1}$ ), which was identified as ADP release and a fast rate ( $150 \pm 38\text{ s}^{-1}$ ), which may reflect a composite rate of other transitions [21]. The step size of myosin V has been measured in several experiment to be 30 - 40 nm [19][21]. Recent experiments investigating the step size have shown that a step of 36 nm can be separated in two sub-steps of 25 and 11 nm, where the 25 nm step is attributed to a conformational change of the molecule and the 11 nm step to rectified Brownian motion [16]. This means, that due to thermal noise, the actin binding domain of the molecule is fluctuating in its position along the filament, until it encounters its binding site. The binding of the domain to the filament could be the rectifying process and is only possible if the distance to the next binding site is smaller in direction of the molecule's movement along the filament. The question if myosin V moves in a hand over hand<sup>3</sup> or in a inchworm like manner<sup>4</sup> is settled since it was shown in experiments, with fluorescent calmodulin light chains attached to the neck domains of the molecule, that the trailing head moves around 72 nm forward during a step [66]. This shows clearly that myosin V moves hand over hand. Single molecule fluorescence polarization measurements have shown that the head domain of myosin V changes the angle with which it binds to the actin filament between the trailing and the leading position from  $40^\circ$  to  $140^\circ$  [67]. The relation between the force applied to a surface adsorbed myosin V molecule against its movement and the average dwell time ( at saturating ATP concentrations) shows no changes in dwell times up to 1.5 pN [19]. For forces exceeding 1.5 pN, dwell times increase exponentially. At a load of 2.7 pN the movement of an actin

---

<sup>3</sup>the trailing head releases the filament and binds in front of the leading head

<sup>4</sup>the trailing head moves up to the leading head, upon which the leading head moves forward

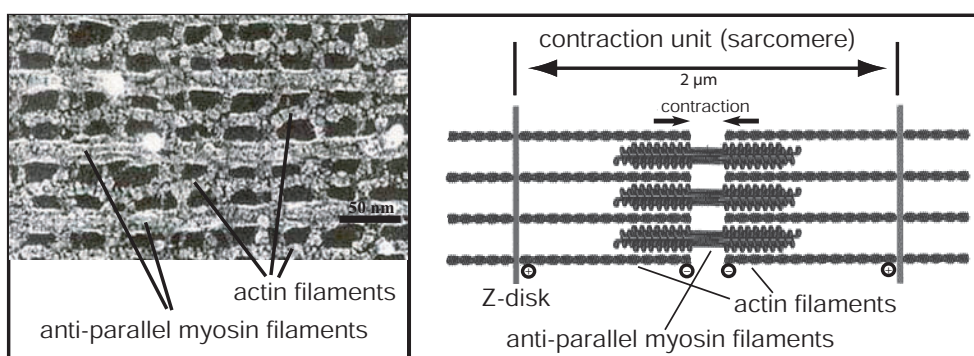


Figure 2.4: Electron micrograph and schematics of smooth muscle  
 a) **High resolution electron micrograph of the arrangement of actin and myosin filaments that form the core unit of a smooth muscle cell.** (taken from [www.ucsf.edu/cooke-research/researchframe.htm](http://www.ucsf.edu/cooke-research/researchframe.htm)) b) **The schematics of a sarcomere, the contractile unit of the muscle system. Actin filaments are arranged anti-parallelly and are contracted by myosin filaments, in which myosin II molecules are also arranged in a anti-parallel way.** (Source: [8])

filament pulled by a myosin V molecule is actually stalled [19]. The affinity of myosin V for binding ADP is ten times higher than the affinity for ATP [65]. Genetic [68], biochemical [69] and localization [70] studies support the assumption that inside cells, myosin V transports vesicles, cell organelles<sup>5</sup> and mRNA along actin filaments of the cytoskeleton [71]. This is further supported by in vitro assays in which vesicle associated myosin V molecules were capable of actin filament motility [72].

Myosin V was prepared from chick brain in a procedure developed by Richard Cheney in 1998 [73].

## Muscle Myosin II

Myosin II is, together with actin, the most important part of the contraction system in muscle cells. Anti-parallelly oriented myosin molecules pull on actin filaments to reduce the distance between them (see electron micrograph and schematics in figure 2.4).

Myosin II has a dimeric structure of two equal 130 kD motor proteins. Each monomer can be roughly divided in three functional subunits, the so

<sup>5</sup>smooth endoplasmic reticulum

called head, neck and tail domains. The head domain is of globular shape and contains the N-terminus and the actin binding as well as the ATP hydrolysis site. The short neck domain is an  $\alpha$ -helix to which two calmodulin like light chains are attached. The long tail domain is an  $\alpha$ -helix. The tails of two monomers coil together to form the dimer. In solutions of ionic strength below 300mM of monovalent ions, myosin II can assemble into filaments or even clusters of many antiparallel dimers. In solutions above 300mM ionic strength, the dimers stay individually in solution. Myosin II binds strongly to actin in absence of ATP and has been shown to act together with actin filaments as a molecular motor in the presence of ATP in muscle cells and in vitro [74][75] by moving actin filaments in the direction of their polarity. Myosin II can be cleaved by proteases in about the middle of its tail domain. The resulting part with the two actin binding sites is called HMM (Heavy Meromyosin). HMM molecules do not assemble into filaments but still show motor activity [76]. The ATPase activity of these myosin fragments can be impeded by blocking the ATPase site in the globular head domain with n-ethylmaleimide (NEM). The resulting inactivated myosin fragment binds to actin, but can not release it anymore and is called NEMHMM. The lack of the ATPase activity was tested in surface motility assays [76] of actin filaments on NEMHMM coated surfaces. Myosin II was prepared from rabbit muscle in a procedure developed by S. Lowey [77].

### **Filamin**

Filamin is an actin binding homo-dimer of a molecular weight of 250kD per monomer. Each monomer is elongated 80 nm long and contains an actin binding site as well as a binding domain to form a dimer [78]. These two binding sites are on opposite ends of the elongated structure of the monomer, such that the dimer has a V-shape and is a rather flexible molecule [78]. In its dimeric form filamin can link actin filaments either to individual bundles at low molar actin-filamin ratios or to isotropic networks at higher ratios [79][80]. The critical ratio for the transition from isotropic to anisotropic cross linking is around 140:1 for the molar actin: filamin ratio [81]. Inside cells, filamin is found in stress fibers [82], associated with the cortical actin network and near

the cell membrane. Filamin is known to bind to many other macromolecules than only filamentous actin. So far, about 20 binding partners are known [83], among which the family of Rho GTPases are the most exciting for the cellular role of filamin. Rho family proteins (Rho, Rac, Cdc42) are cellular stress sensors, which are implicated in the mechano-sensing of the cell. The activation of Rho family proteins induces the formation of stress fibers of the actin cytoskeleton [84]. Filamins bound to this stress sensing apparatus can transduce the externally imposed stress onto the actin cytoskeleton and induce a stiffening of the actin cortex by its reorganization. The filamin used in the context of this work was purified from chicken gizzard according to [85].

### **Bovine Serum Albumin (BSA)**

Bovine Serum Albumin (BSA) is a 66.4 kD Protein, that is isolated from bovine blood serum. The main biological function of BSA is to regulate the osmotic pressure of blood by binding fatty acids,  $\text{Ca}^{2+}$ ,  $\text{K}^+$  and  $\text{Na}^+$  ions. It is water soluble and has no specific interactions with most proteins and functional groups so that it is often used to passivate surfaces by adsorbing to them and thus blocking the surface from other proteins to adsorb. Denatured it forms layers that do not dissolve in water, what was used to passivate glass or polymer surfaces. Purified BSA was purchased from Sigma Aldrich Biochemicals.

### **Monoclonal immunoglobulin antibodies for myosin V**

Monoclonal antibodies with a high affinity for myosin V were expressed in mouse stem cells after the injection of myosin V molecules. These stem cells were fused with tumor cells to multiply rapidly and raised in a cell culture. Since every stem cell expresses only one kind of antibody every line of cells expressed one clone of a myosin V antibody. The antibodies from all cell lines were tested for their affinity for myosin V and the cell lines with the highest affinity selected. In total, five different kinds of antibodies with high myosin V affinity were produced. All antibodies supported the motor activity of myosin V in motility assays, when myosin V was bound to the surface through these antibodies. This leads to the assumption that these five antibodies do not bind to the globular head domain of myosin five, but somewhere along the

tail or cargo binding domain. The antibodies were used to attach myosin V to different kinds of nano or micro-beads with a reproducible binding method and affinity. The molecular weight of antibodies is approximately 156 kD [86]

### 2.1.2 Phospholipids

Phospholipids are amphiphilic molecules that have hydrophobic tails consisting of two fatty acid chains and a hydrophilic head group. Due to their amphiphilic nature lipids can self-assemble to form monolayers at interphases such as air-water or bilayers in aqueous solutions. The driving force behind the self-assembly of lipids is the minimization of interface energies due to the hydrophobic effect of the fatty acid chains interacting.

The lipids used in the context of this work were:

-DMPC, which has a zwitterionic head group that is electrostatically neutral and two 14 carbon atom fatty acid chains

-DPPE-PEG-2000, is a lipid with an zwitterionic head group, which has a PEG polymer chain of 2 kD molecular weight attached and two 16 carbon atom fatty acid chains

-DPPE-PEG-2000-amine, is a equivalent lipid which has a PEG polymer chain of 2 kD molecular weight with an amine group at the end attached. Since the amine group is positively charged at the pH conditions used (pH 7.5 - 8), the side of the lipid that faces the buffer solution carries a positive charge.

-DPPE-TexasRed, is a equivalent lipid with a TexasRed fluorescence dye attached to its head group.

-Cholesterol is not a phospholipid but a sterol. These are small hydrophobic molecules with four fused rings and a short tail. Due to its hydrophobic nature, cholesterol can be embedded into the hydrophobic core of phospholipid mono- and bilayers, where it has shown to increase the bending rigidity of Giant phospholipid vesicles. [87][88]

All lipids were purchased at Avanti Polar Lipids, Inc..

For abbreviations see Appendix.

### 2.1.3 Chemicals

#### Phalloidin

Phalloidin is a fungal toxin isolated from the mushroom *Amanita phalloides*. Phalloidin binds strongly to F-actin at the cleft between two monomers [89][90], not to G-actin, and stabilizes the filaments. The stabilization of the filaments leads to a shift in the ratio of actin bound in filaments and free monomers in a way that nearly all the actin is bound in filaments. Thus the treadmilling process of actin filaments is prevented. This determines its toxicity in muscle cells and liver because the dynamics of the cytoskeleton is suppressed. Cell culture experiments showed that growth and cell motility, two actin related processes, are inhibited when Phalloidin is injected into cells [91]. To visualize actin filaments, fluorescence dyes can be bound to phalloidin. TRITC-Phalloidin was used in the experiments because of its resistivity to photochemical bleaching. Phalloidin and TRITC-Phalloidin were purchased at Sigma Aldrich Biochemicals.

#### A23187

A23187 is a naturally occurring antibiotic that forms dimeric pore structures, complexed with divalent ions. It can be embedded into lipid membranes, where it acts as a passive transmembrane carrier for divalent ions. The A23187 can be dissolved in chloroform and mixed with lipid solutions, thus that it can be used in mixture directly for the preparation of vesicles.

#### Cellulosenitrate (Nitrocellulose)

Nitrocellulose is a cellulose polymer that has on the average 1.8 to 2.3 nitrate groups attached to each carbon ring. It is widely used as biocompatible surface to grow cell cultures or to adsorb proteins in electron microscopy or after gel electrophoresis. Since physisorption of a protein occurs through unspecific surface-surface interaction of protein and substrate, the proteins may partly denature in the contact area. Cellulosenitrate films swell to many times their thickness in contact with water. Nitrocellulose was purchased as a 2 % solution (Collodion) in amyl acetate from Sigma Aldrich Biochemicals.

### **Dithiothreitol(DTT)**

Dithiothreitol (DTT) is an agent that protects all proteins that contain thiol groups from oxidation. This is important because the thiol groups, especially Cysteins, play a crucial role in the functionality of proteins. They can form dithiol bridges which often control the tertiary structure and thus the function of proteins. In myosin II a cystein group is also present at the ATPase site of the head domain. Oxidation of thiol groups inhibits the function of many proteins . An example for this is muscle myosin II that loses its motor activity in vitro when Cystein 707, a reactive group in the head domain is treated with BMNDMB, a thiol active reagent. It regains its motor activity when BMNDMB is cleaved by UV radiation [92]. Adding DTT to a protein solution at concentrations exceeding the molar protein concentration by orders of magnitude, decreases the probability that a thiol from the protein is oxidized by decreasing the ratio of protein thiols to non-protein thiols. Also with actin solutions it was shown, that thiol oxidation leads to a monomer-monomer binding, which can cross-link actin filaments and thus form networks even without cross-linking proteins [93]. DDT was purchased at Sigma Aldrich Biochemicals.

## **2.2 Sample Preparation**

### **2.2.1 Surface coating with thin polymer layers**

For protein adsorption on soft surfaces, thin polymer layers were spin coated on microscopy glass slides. For nitrocellulose layers, a 2% collodion solution was spun for 30 seconds at 5000 rpm and subsequently dried for 2 hours at ambient temperature. For PDMS layers, a 5% PDMS and cross-linker solution in dodecane was spun for 60 seconds at 3000 rpm and subsequently annealed for 24 hours at 70°C. The quality of the surfaces done at different concentrations, rotation speeds and annealing procedures was analyzed with phase contrast and reflection interference contrast microscopy (RICM) and proved to be best at the conditions mentioned above.

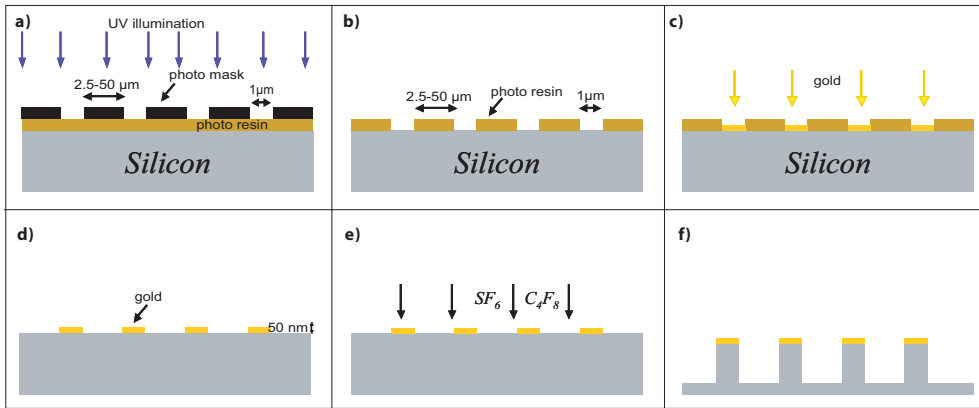


Figure 2.5: formation of pillar array substrates from silicon

a) The silicon wafer, which is coated with photo resin is illuminated through the mask pattern with UV light. b) After the removal of the mask, the resin is removed in solvent at the irradiated spots. c) Gold is deposited on the sample by vapor deposition. d) The remaining photo resin is removed together with the gold layer on top of it. The gold deposited directly on the wafer remains. e) In an anisotropic etching step, silicon is removed at the places where it is not covered by the gold dots. f) Final structure of the silicon pillar array sample.

## 2.2.2 Pillar array preparation

The pillar array structures were developed, produced and characterized by Wouter Roos in the lab of Prof. Joachim Spatz at the University of Heidelberg. First, flat silicon substrates were spin coated with a thin layer of positive lift-off photo resin (ARP-5350, All-Resist) and lithographically structured with a photo-mask. Mask patterns were round holes with a diameter of  $1\mu\text{m}$ , arranged in square arrays with spacings between 2.5 up to  $50\mu\text{m}$ . At the round areas, which had been illuminated with UV light, the resin could be dissolved and a thin gold layer was vapor deposited. After removing the rest of the resin, the silicon surface was structured with an array of round gold dots of  $1\mu\text{m}$  diameter. Subsequently an anisotropic reactive ion etching technique was applied to remove all silicon between the gold islands, down to a depth of 10-15  $\mu\text{m}$ , meanwhile leaving all material shielded by the gold islands intact. This technique produces arrays of micro-pillars with gold surfaces at a very high precision and reproducibility (image 2.6). To produce a similar array structure out of photo resin, thick negative resin layers were illuminated through similar

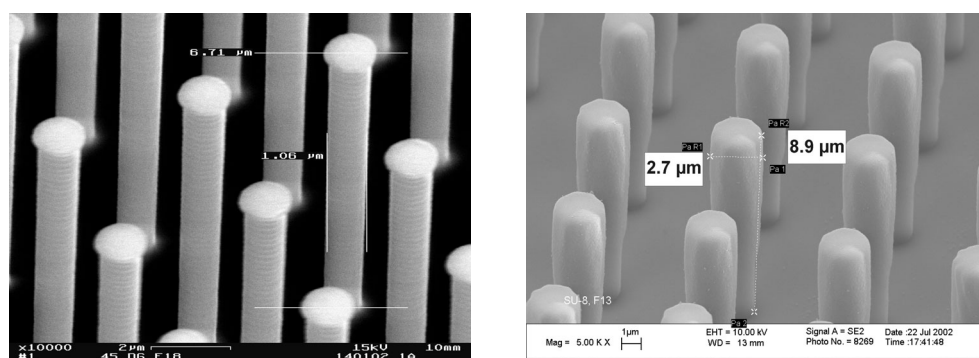


Figure 2.6: SEM images of pillar array substrates made from silicon and PDMS a) Silicon pillar array; The brighter tops of the pillars are the gold disks used in the substrate preparation process to form the pillars in an anisotropic etching process. b) PDMS pillar array; Visibly, the pillars made from PDMS do not achieve the same aspect ratio as for the silicon substrate.

photo-masks and resin between the desired pillar structures dissolved. For pillar structures from PDMS, hole structures from photo-resin were produced by using again a positive instead of a negative photo-resin. Subsequently these were used as molds for the PDMS samples. The advantage of polymer substrates is their transparency and their lower stiffness of the pillars, whereas the silicon surfaces have the advantage of higher precision and a chemical differentiation between the tops of the pillars and the bulk of the array

### 2.2.3 Giant phospholipid vesicle preparation

Electro-swelling [94] was used for the preparation of giant vesicles used in chapter 3.3 and 3.5. Lipid solution in chloroform was pipetted onto indium-tin oxide (ITO) plates, which were cleaned with Hellmanex (Hellma Inc. Germany) sonicated and washed with double purified water (Millipore). Subsequently the plates were left to dry in a vacuum chamber or blown dry with nitrogen. Subsequently the lipid solution was pipetted onto the slides and the slides left to dry in the vacuum chamber. Electro-swelling occurred at  $37^{\circ}\text{C}$ , 1 Hz and 10 V for 2 hours.

## 2.2.4 Magnetic bead functionalization

To functionalize the magnetic beads, a washing procedure, proposed by the manufacturer (Dynal, Norway), has to be performed, to suspend the beads in the appropriate buffer solution for functionalization. Subsequently the protein to be bound to the bead is added to the bead solution and incubated for usually 12 - 24 hours at 4°C at slow tilt rotation. After that, the protein was removed from the solution by magnetic separation of the beads and the exchange of the buffer solution. Finally BSA was added to the solution at 1 mM concentration to passivate the possible remaining active surface and was subsequently also removed from solution.

To attach myosin V monoclonal antibodies, protein A pre-coated M280 beads (100pM solution) were incubated with the antibodies in a 10  $\mu$ M solution to ensure a complete coating of the bead surface. Thus the binding statistics of myosin V to the beads is not affected by the antibody density on the surface of the bead.

For the attachment of NEMHMM<sup>6</sup>, the protein was first biotinylated in an amine reaction described in detail in the Avidin-Biotin Chemistry Handbook [95]. A 3 $\mu$ M solution of the biotinylated protein was incubated with a 100pM bead solution to achieve a high density of actin binding proteins at the surface.

## 2.3 Experimental Techniques

### 2.3.1 Optical Microscopy

Optical microscopy is the oldest and most common method for the observation of biological probes and processes. The first high resolution microscope was developed in 1670 by Antoni van Leeuwenhoek, who used it to observe cells for the first time. The biggest advantage of light microscopy over microscopy techniques with higher spacial resolution, such as electron microscopy or different scanning probe microscopy techniques, is that dynamic processes of a probe can be observed in real time. Samples can be imaged at room temperature in

---

<sup>6</sup>inactivated myosin fragments

a near physiological state, using only the interaction of visible light with the probe, which in most cases does not alter the sample significantly. The spacial resolution  $\delta x$  to image details of a structure observed is limited to the Bragg criterion of  $\delta x = \frac{\lambda}{2 \cdot NA}$ <sup>7</sup>, which for common applications leads to a resolution limit of around 200 nm, which for many biological processes is a large length scale. On the other hand, for the observation of many dynamic processes in biological samples, it is not necessary to exactly image a structure with a resolution equivalent to the length scale of the process, but simply to measure the displacement of an object of invariant geometry. For this purpose, the main task is to determine the position of the object in each image of a movie of the observed process. With well adjusted optics of modern microscopes, the spacial resolution of the determination of a particle position can be in the range of 1 nm [66], which is a small length scale for most biological processes.

### Microscopy Setup

The microscope used for all experiments presented in the context of this work was a Carl Zeiss Axiovert 200. The camera to record the microscopy images was a Hamamatsu ORCA-ER CCD with  $1364 \times 1024$  pixel at a image frequency of 8.5 Hz. The number of pixels used for imaging could be reduced or down to a  $4 \times 4$  pixels read out into one image point (pixel binning), which allowed higher imaging rates, of up to 100 Hz. The images of the camera were read out directly to a PC computer using a digital frame grabber card (Stemma Imaging). The image acquisition program used was Open Box, a software developed by Jörg Schilling during his PhD. thesis at the institute. By defining priorities for the display and the saving processes of the images, at the level of the Windows operating system, the software enables simultaneous storage and display of images of a movie.

### Fluorescence microscopy

Fluorescence microscopy is based on the principle that certain chromophores can be excited in their electronic bond structure with light in the visible range

---

<sup>7</sup>NA denotes the numerical aperture of the optical system, which is the incident angle of light multiplied with the optical density of the medium. For modern microscopy objectives, values for NA range from 0.2 up to 1.48.

( $\lambda_x$ ) and will subsequently emit light of longer wavelength ( $\lambda_m$ ). The reason for the different excitation and emission wavelength is that, according to the Frank-Condon principle, the transition from the ground to the excited state and vice versa can only occur via vibrational levels [96]. The excitation energy is partly converted into vibrational quanta of the excited molecule and the emitted light must have a longer wavelength. If the excitation and the emission light spectra do not significantly overlap, it is possible to separate excitation and emission light by a dichroic mirror and band pass filters. Therefore, by using an inverted microscope with a filter and mirror set (see scheme and explanation in figure 2.7), which matches the specific dye, the light emitted by fluorescence chromophores can be observed.

By linking the dye molecules to biological materials, objects, much smaller in size than the optical resolution of the microscope and even nearly the same refractive index as the surrounding medium, can be imaged. Nevertheless there are severe disadvantages in using fluorescence microscopy with biological probes. One key problem is the creation of free radicals in the solution by energy transfer from the dye molecule to other molecules in close proximity to the biological material. These can damage severely the fluorescence dye and lead to the suppression of its fluorescence with time (photochemical bleaching) or damage a protein to which it is attached. Consequently, the observation time of a fluorescence sample is limited and a possible damage of the sample with time has to be kept in mind. Especially oxygen has to be mentioned, since a very reactive oxygen singlet state can be generated with a energy transfer in the near infrared wavelength ( $\approx 1$  eV, which corresponds to a light wavelength of  $\approx 1242$  nm). Since the excitation wavelength of all fluorescence dyes is shorter, the energy transfer to an oxygen molecule is generally possible and all dye molecules show the problem of radical formation. Nevertheless, dyes with relatively long excitation wavelength, like Rhodamine or TexasRed, exhibit a reasonable stability against photochemical bleaching. To remove oxygen from the buffer solution, it was always stirred under vacuum for at least 30 minutes directly before experiments. As light source for the fluorescence microscope a Carl Zeiss AttoArc 100W mercury arc discharge lamp was used.

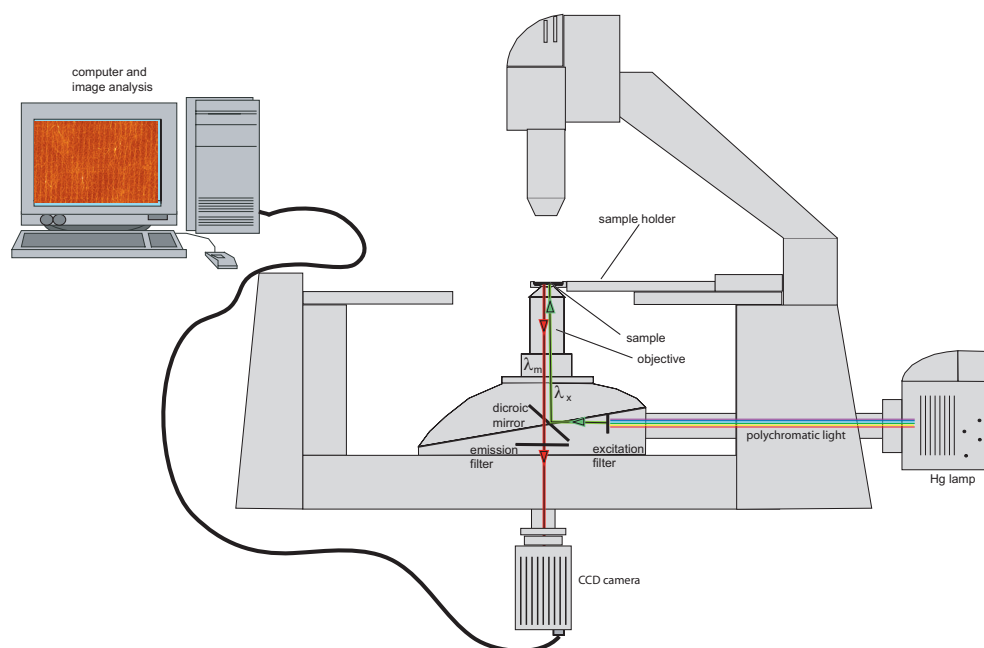


Figure 2.7: Schematics of the principle of a fluorescence microscope. The Hg arc discharge lamp emits polychromatic light with a continuous spectrum and discrete chromatic lines. The most intense line is at 546 nm and is often used for fluorescence applications. The excitation filter is a narrow bandpass, which transmits only a narrow band around  $\lambda_x$ , which has to overlap well with the excitation spectrum of the fluorescence dye. This excitation light is reflected by a dichroic mirror and focussed on the sample. The chromophore in the sample emits a spectrum, which does not substantially overlap with the excitation spectrum. This spectrum around  $\lambda_m$  passes the dichroic mirror and the emission filter and is recorded with the camera. Reflected light, which chromatically is around  $\lambda_x$  is reflected by these two optical components and does not reach the camera. This is extremely important since the intensity of the reflected light from all optical components is always much higher than the fluorescence signal.

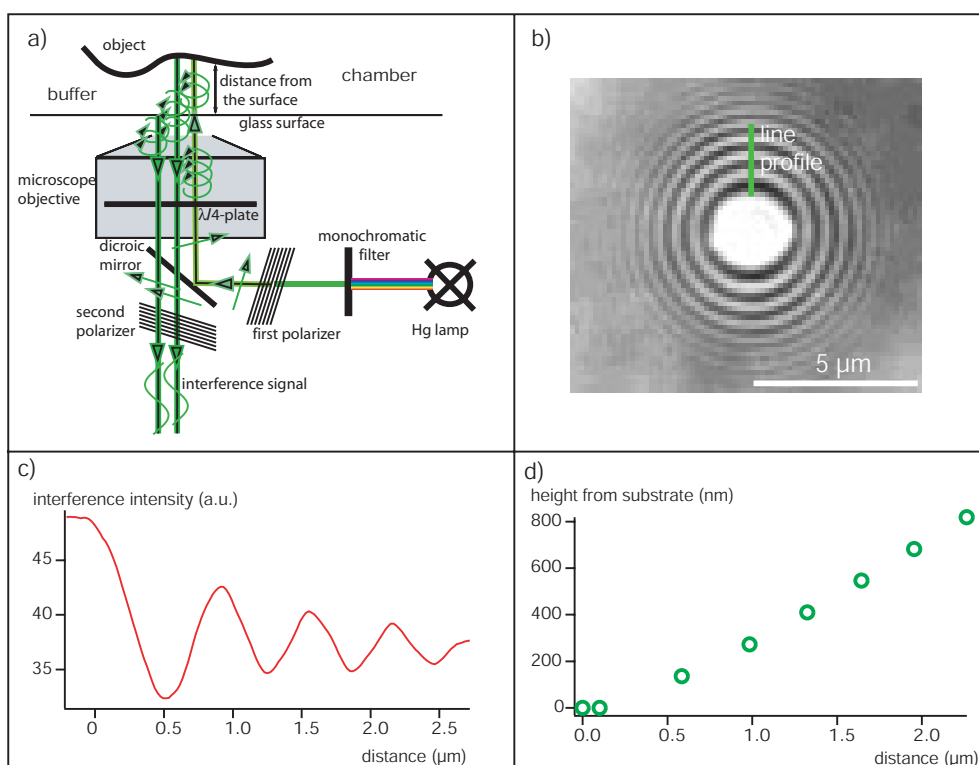


Figure 2.8: Principle of the Reflection Interference Contrast Microscope  
**a) Schematics of the RICM set up. b) RICM image of a surface adhered vesicle. c) Intensity of the line profile in the image above. d) Reconstructed height of the vesicle surface from the substrate along the line profile.**

## Reflection Interference Contrast Microscopy (RICM)

RICM is an interference microscopy technique used to reconstruct height profiles of interfaces close to the bottom glass slide of a chamber. It is commonly used to reconstruct the lower surface of vesicles [97], liquid interfaces [98], or to measure distances of beads from a glass surface [99]. It is realized with an inverted microscope setup and its scheme of function is shown in figure 2.8a.

The two light beams that form the interference pattern are the one reflected on the glass-buffer interface of the chamber and the one reflected of the buffer-object interface. An RICM image contains the three dimensional information about the form of an interface. A typical example for a quasi spherical vesicle is shown in figure 2.8b. The reflective coefficient  $r$  of an interface is

$$r = \left( \frac{n_1 - n_2}{n_1 + n_2} \right)^2 \quad (2.1)$$

where  $n_1$  and  $n_2$  are the refractive indices of the two materials. For water (and thus nearly all buffer solutions)  $n$  is 1.33 and for the glass used  $n$  is 1.51. For phospholipid membranes, the refractive index is approximately 1.4, so that the proportion of the reflected light is extremely small ( $r=6.5 \cdot 10^{-4}$ ). Since reflection intensities at the optical components inside the microscope (e.g. lens surfaces) are orders of magnitude higher, these have to be filtered out using an anti-reflex technique (figure 2.8a). To this purpose, the incoming monochromatic light beam passes first a linear polarizer and subsequently a  $\frac{\lambda}{4}$  plate inside the objective, after all lenses, so that the incident light in the probe has a circular polarization. The reflections of the light waves at both interfaces switch the polarization direction by  $180^\circ$ . Thus, after passing the  $\frac{\lambda}{4}$  plate after reflection, the interference signal of the two beams reflected from the sample will again have a linear polarization, but perpendicular to the initial one. By placing a second linear polarizer before the camera, nearly all other reflected light besides the interference signal of the two beams reflected from the sample can be filtered out. The reconstruction of the height profile of the observed object is done by analyzing its interference pattern in the image, usually using line intensity profiles taken at characteristic points of the image. For incident light, which enters the sample perpendicular to the focal plane<sup>8</sup>, the intensity of the interference signal  $I(x,y)$  depends on the intensities of the two reflected beams,  $I_1$  and  $I_2$ , and the distance  $h(x,y)$  from the surface. It is given by

$$I(x, y) = 2\sqrt{I_1 \cdot I_2} \cdot \cos\left(\frac{4\pi}{\lambda} \cdot n \cdot h(x, y)\right) \quad (2.2)$$

Since  $n$  is an integer number, the intensity of a continuously increasing distance function  $h(x,y)$  has a periodicity of  $\lambda/2$  (see intensity signal in figure 2.8c). Thus RICM images can neither give absolute heights nor tell if an interface is convex or concave with the same curvature. The problem of uncertainty of the absolute height can be overcome by introducing a second wavelength in the setup, as recently done by Sengupta et al [99]. Only if the general shape of an object is known, as it is the case for vesicles, beads or liquid drops, the

---

<sup>8</sup>this is a reasonable assumption when the object is centered at the optical axis

contour can be reconstructed. Scattering of the reflected light in the sample leads to a decay of the signal to noise ratio of the RICM image with increasing distance of the interface from the glass surface. Therefore the RICM technique is limited to near surface applications and can usually be used to reconstruct interfaces that do not extend more than  $10 \mu m$  from the glass surface.

### 2.3.2 Image analysis and processing

Microscopy techniques produce data of a visualized object in form of images or movies. To extract numerical quantities of the experiments from those, images have to be analyzed and processed to extract vector form data of the object. From these, physical properties of the object can be calculated. Images retrieved in the context of this work were matrices with matrix elements ranging from 1 to 4096 (12 bit greyscale).

#### Particle tracking

The aim of particle tracking algorithms is to determine the position of an object with a very high accuracy in every image frame of a movie to retrieve the trajectory of its motion. The most common tracking algorithm is based on fitting a Gaussian intensity distribution at the image intensity profile. This method works well with most spherical objects and objects that are smaller than the wavelength of light<sup>9</sup>. The intensity landscape of the image, is fitted by a two dimensional gaussian curve . The peak position of the fit function is taken as the center position of the object in the focal plane of the microscope (figure 2.16) . Thus the two dimensional trajectory of the center of the object can be constructed.

A new technique, developed in the framework of this thesis is a three dimensional particle tracking algorithm. For this purpose the width  $w$  of the Gaussian fit curve is taken as a measure of the position of the object perpendicular to the focal plane. When fitting the image of a spherical object that is moved perpendicular to the focal plane with a two dimensional Gaussian function, the function of the width  $w$  exhibits a minimum in the focal plane.

---

<sup>9</sup>The envelope function of the airy pattern of the point spread function is very close to a gaussian

This is due to the broadening of the optical transfer function when the object is moved out of focus. Thus if the object does not cross the focal plane, a well defined relation of the width  $w$  to the distance of the object from the focal plane  $z$  exists. By calibrating  $w(z)$  as a function of  $z$  the data retrieved in the experiment can be converted into a motion perpendicular to the focal plane. In combination with the in-plane movement of the object, three dimensional trajectories of a moving object can be established. Obviously, the technique is limited to displacements perpendicular to the focal plane that are not much larger than the size of the object, since otherwise a relation between  $w$  and  $z$  is hard to establish with sufficient precision.

For the calibration of  $w(z)$ , a stepper motor was connected to the objective drive of the microscope, by means of which, the position of the focal plane could be moved by increments of 25 nm up to 5  $\mu\text{m}$ . Using increments of 100 nm yielded the smoothest curve for  $w(z)$ , since for smaller increments, the mechanical error proved to be dominant. Figure 2.10 shows a calibration curve  $w(z)$  for a 2.8  $\mu\text{m}$  diameter magnetic bead, that was attached to a glass surface when the focal plane was moved by increments of 100 nm. The measured relations for  $w(z)$  could be well fitted with a single exponential function, which was later used as a conversion function for  $z(w)$  (figure 2.10).

Since the measured relation  $w(z)$  depends on the settings of the microscope, such as the opening of diaphragms, calibration and experiment were always done with exactly the same settings in the same chamber and mostly the calibration was performed directly after the experiment.

The resolution of particle tracking methods can be easily determined by position analysis of immobile particles. A large number of images of the immobile particle is taken and the position determined in each image. A histogram of the particle positions should give a gaussian distribution, the width of which is a measure for the resolution of the method. This method yields a resolution for the three dimensional tracking algorithm of 2 nm in the focal plane and 7 nm perpendicular to it. Nevertheless, for the perpendicular resolution one also has to account for the possible error of the calibration, since there is no exact length scaling factor as for the in plane direction. This error was taken as the average residuum of the measured calibration curve  $w(z)$  to its expo-

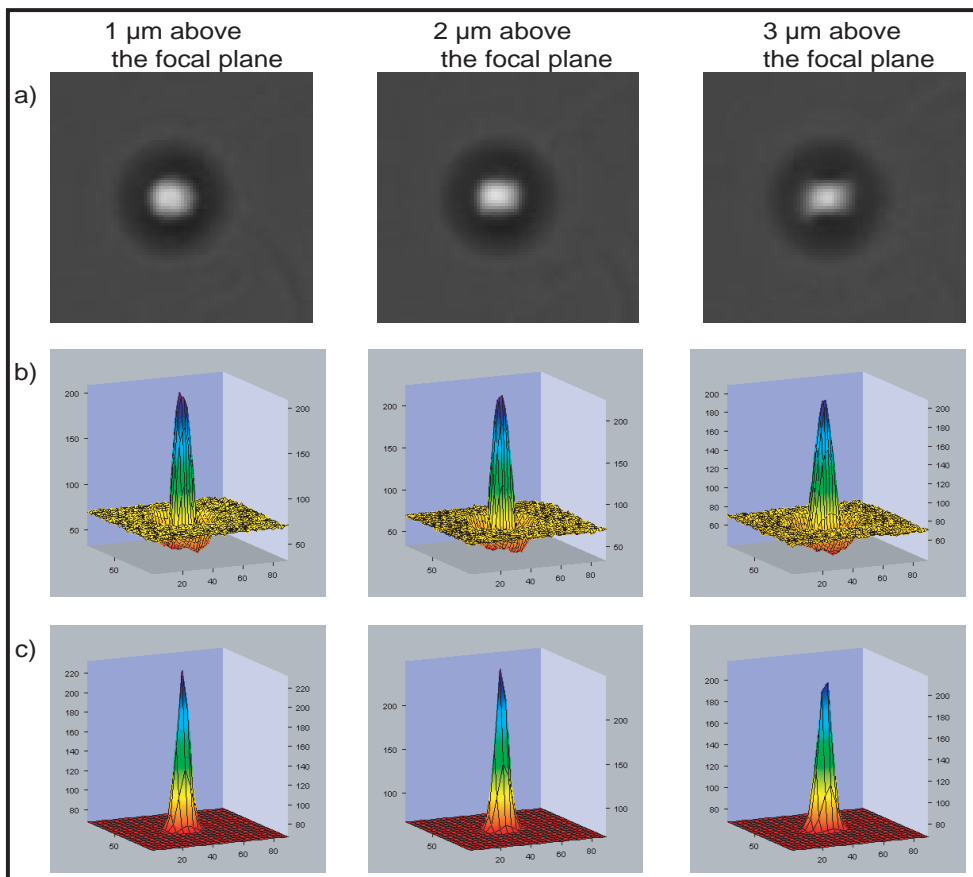


Figure 2.9: Three dimensional tracking algorithm

a) Three off focus images of a  $1.4 \mu\text{m}$  radius magnetic bead. The microscope optics were adjusted in a way to form an interference maximum in the middle of the image of the bead. This technique leads to a higher tracking precision. Between each frame, the distance of the bead to the focal plane was increased by  $1 \mu\text{m}$ . b) Intensity profiles of the images above. The units of the horizontal axis are pixels ( one pixel is  $97 \text{ nm}$ ), the units of the vertical axis is intensity in a 8 bit scale. c) Two dimensional gaussian fit curves of the intensity profiles, which are used for the calibration of the tracking of movement perpendicular to the focal plane. The width of the fit curve visibly increases as the distance of the bead from the focal plane increases.

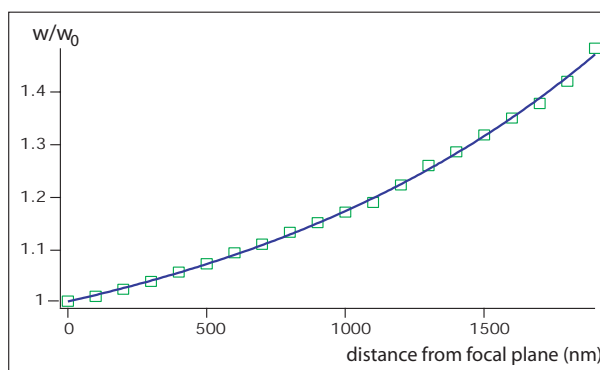


Figure 2.10: Calibration curve for the three dimensional particle tracking algorithm

The relative width  $w/w_0$  is plotted versus the distance by which the objective is moved relative to the focal plane of the microscope (squares).  $w_0$  is the initial width of the gaussian tracking function. The increase of the relative width can be well approximated with an exponential function (line), which is later used as a conversion function for the tracking algorithm.

ponential fit function, which was used to retrieve  $z(w)$  in the experiments. This error was determined to 16 nm, such that the total resolution perpendicular to the focal plane is  $r = \sqrt{(7nm)^2 + (16nm)^2} = 17.5nm$ . For moving objects the determination of a resolution of the tracking algorithm is more complex. In one movie frame of a moving object, the intensity landscape of the object is integrated over the acquisition time of the camera. Thus the resolution of the tracking algorithm will be a function of the velocity of the object and of the acquisition time of the camera. To determine the resolution of the particle tracking algorithm for moving beads the motion of magnetic beads that were pulled through a viscous solution with a constant force was analyzed. The position difference from one movie frame to the next was averaged and the standard deviation from the average value, found by this statistical analysis, is taken as a measure of the resolution for a certain velocity and acquisition time. Figure 2.11 shows the thus determined tracking resolutions for velocities parallel to the focal plane of up to more than  $60 \mu m/s$  and a acquisition time of 30 ms per image.

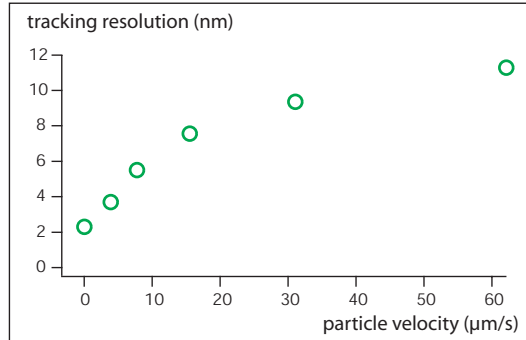


Figure 2.11: Resolution of the particle tracking algorithm as function of the velocity of the particle

### Shape tracing

Shape tracing algorithms determine the form of an object in an image due to certain recognition criteria and return a vectorized contour of the object. The two shape tracing algorithms developed in the context of this work were used for fluorescence images of actin filaments and phase contrast or fluorescence images of phospholipid vesicles. Actin filaments are seen as bright lines in fluorescence images and phase contrast images of vesicles are determined by the equatorial projection of the optical density distribution of the vesicle shell, thus a dark line closed on itself. Thus the core unit of the algorithm is to follow a contour and return its coordinates with a high precision. To start the shape tracing, two starting points have to be given in the first image of the movie, which have to be on either side of the curve that should be detected. Subsequently a line is drawn between the points and the intensity for a given number of points on this line is calculated. A strength of the algorithm is that due to an intensity weighting procedure, points and respective intensities are not limited to pixel positions of the image, but can be interpolated. The weighting procedure for the intensity  $I(x,y)$  in an arbitrary point  $(x,y)$  of the image takes into account the intensity of the closest pixel  $I(x_0, y_0)$  and its eight neighboring pixels. The weighting function is the inverse distance of the point from the pixels.

$$I(x, y) = \sum_{i=-1}^{i=1} \sum_{j=-1}^{j=1} \frac{1}{\sqrt{(x - x_{i,j})(y - y_{i,j})}} \cdot I(x_{i,j}, y_{i,j}) \quad (2.3)$$

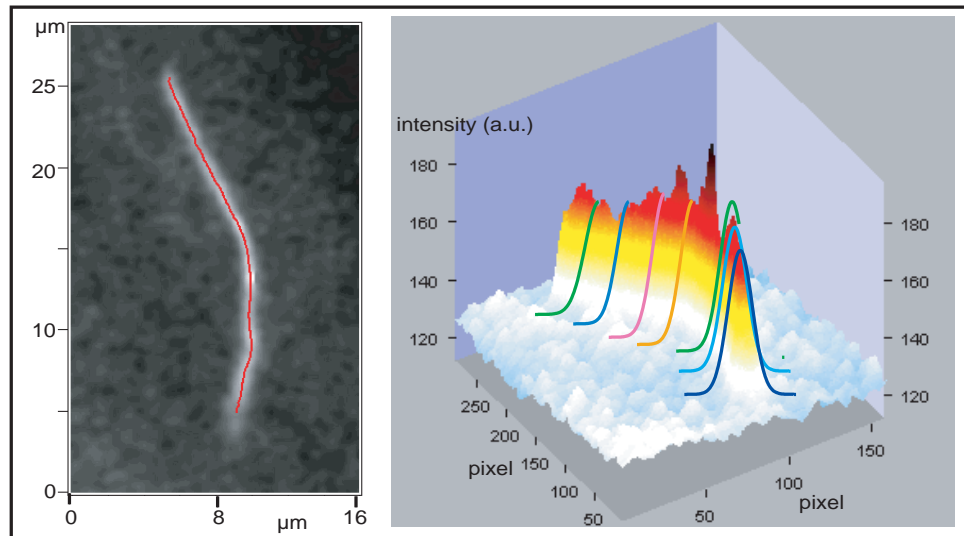


Figure 2.12: Actin filament shape tracing

a) An image of an actin filament moving in a hydrodynamic flow and its vectorized shape (red line), as determined by the shape tracing algorithm described in the text. b) Intensity profile of the filament image and, in color, several schematically put gaussian fit curves across the profile, which determine the shape tracing. All horizontal units in the graph are image pixels (97 nm) and all vertical ones intensities.

The length of the 3x3 pixel square, over which the intensity of each point is evaluated, coincides roughly with the optical resolution of the microscope and therefore is a legitimate value for the integration size. To better cope with noisy images, a feature was introduced that draws  $n$  parallel lines and takes their average as a central value. Subsequently the line intensity profile is fitted with a gaussian function and its center identified as the position of the object, the actin filament or the vesicle membrane. To acquire the second line intensity profile, the end points are simply moved a distance  $d$  perpendicular to the first line. By again fitting the profile with a Gaussian, a second point on the object is identified. To adjust the starting points to the curvature of the object, for all subsequent end points, the center points of the last two profiles are connected and a point in a distance  $d$  is chosen. From this point, the end points of the next line profile are chosen to be perpendicular to the moving direction separated by the length of the line profile.

By this way, the tracing process moves along a curve of arbitrary shape as

long as the path does not intersect with itself. The termination condition for the tracing process is given for the vesicle simply by an angular coordinate, which runs from 0 to  $2\pi$ . In the case of an actin filament the tracing process starts in about the middle of the filament and is terminated when the peak value of the gaussian fit of the line intensity profile drops below a value relative to the average of all other points. This means that the fluorescence intensity has substantially decreased, ergo the end of the filament is reached. Then the tracing is restarted from the endpoint of the filament. It moves along the entire filament contour in the appropriate direction to the other end. Thus the entire length of the filament is being captured.

For the resolution of the shape tracing algorithm, again, the resolution for stationary filaments can be determined by tracing an immobile fluorescent filament. This was analyzed with a filament unspecifically adsorbed on a hydrophobic surface (silanized glass) for fluorescence images of good quality<sup>10</sup> and taking the standard deviation from image to image as a measure of the resolution. This resolution was determined to 6.7 nm.

### Order analysis

If a structure, shown in an image, e.g. an actin network (figure 2.13a), is assembled randomly or ordered in one direction can be calculated from the image by an order analysis algorithm. Hereby, an anisotropy parameter is calculated for the image. The method used in the context of this work, was to first Fourier transform the image using a FFT algorithm (figure 2.13b). Subsequently, a radial intensity profile  $I(\omega)$  as an angular function from the center of the transformed image was computed (figure 2.13c).

For an isotropic first image, the Fourier transform of it should show a radial symmetry and its intensity profile  $I(\omega)$  should be a constant function. For an anisotropic first image, the radial symmetry is broken and the Fourier transform shows an elliptic form (see figure 2.13b). The ellipticity of the Fourier transform is a measure of the anisotropy of the image and is given by the ratio of the two ellipse axis  $R_{AB}$ . To retrieve  $R_{AB}$  from  $I(\omega)$ , this function

---

<sup>10</sup>the signal to noise ratio of the filament relative to the background should be one order of magnitude or higher

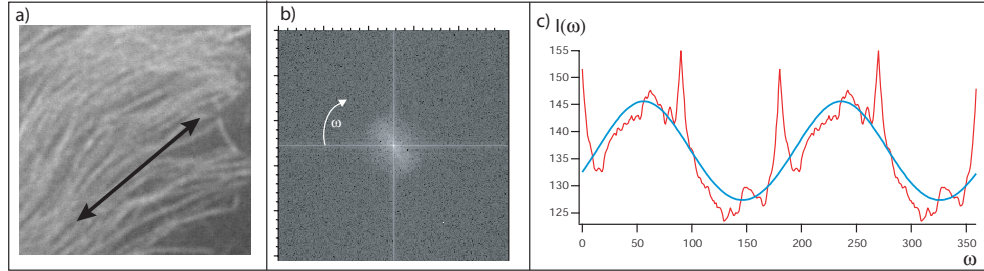


Figure 2.13: Order analysis of an actin assembly

a) Actin network in which the filaments are ordered in one direction. The arrow shows the direction retrieved through the quantitative analysis. b) Fourier transform of the image shown in a). The horizontal and vertical lines are cut-off effects of the transform, due to the finite images size. An angle  $\omega$  is defined and angular intensity line profiles are taken. c) Cumulative intensity of the line profiles as a function of the angle  $\omega$  in image b and the fit with the elliptic function of equation 2.4. Peaks are at  $55^\circ$  ( $=\omega_0$ ), which is the direction of the ordered filaments. The spiky peaks are the artifacts due to the horizontal and vertical lines.

can be fitted with

$$I(\omega) = C \cdot R_{AB} \cdot \frac{1}{\sqrt{1 + (R_{AB}^2 - 1)\cos(\omega - \omega_0)}} \quad (2.4)$$

The fit parameter C is simply an amplitude function and  $\omega_0$  is the angle at which the highest anisotropy occurs.

### 2.3.3 Magnetic colloidal force transducer (Magnetic Tweezers)

To be precise, one has to note that magnetic tweezers are not "tweezers" in the sense that a particle is trapped in a potential well, like optical tweezers. Magnetic Tweezers use the magneto-static force  $F_m$ , which acts upon a para- or ferromagnetic material, with magnetization  $\vec{M}$  and volume V in an inhomogeneous field  $\vec{B}(\vec{r})$ .

$$\vec{F}_m = -\vec{\nabla}(\vec{B}(\vec{r})\vec{M}) \cdot V \quad (2.5)$$

to pull nano or micro sized particles along the field gradient. Nevertheless, for historic reasons and because of the good sound, the name magnetic tweezers will be further used. The magnetic particles used in the context of this work were  $1.4 \mu\text{m}$  radius super-paramagnetic polystyrene-beads (M280 Dynabeads,

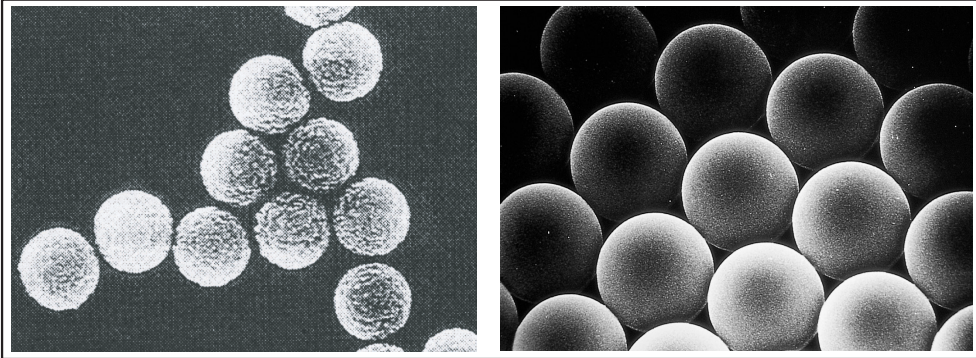


Figure 2.14: Electron micrographs of super-paramagnetic colloidal particles **The 1.4  $\mu\text{m}$  radius magnetic beads used in the context of this work (left) and larger 2.25  $\mu\text{m}$  radius magnetic beads (right) with which, due to a higher iron oxide content, seven times larger forces can be achieved.**

Dynal Inc., Norway) with encapsulated ferromagnetic iron oxide ( $\gamma\text{-Fe}_2\text{O}_3$ ) nano-particles (figure 2.14).

The iron oxide particles are about 15 nm in diameter, which is smaller than the single domain size limit [100]. Thus the magnetization of a bead depends only on the orientation of the nano-particles inside. To orient the ferromagnetic particles in the polystyrene matrix, a minimum magnetic field density is required, which then sets a lower limit for the force than can be applied to the bead. M280 Dynabeads have a mass density of  $1300\text{kg/m}^3$  and reach their saturation magnetization of 12 - 14 kA/m [100][101] in fields of about 62 mT [100].

The current source used for the magnetic tweezers setup is a custom built power amplifier which has an input channel for a function generator (Stanford Research Systems DS 354). The amplifier converts the voltage signal of the function generator into a current signal which is applied onto magnet coils of the magnetic tweezers. The current which passes through the coils is picked up with a  $1\Omega$  resistor as a voltage signal and read out with a digital input card (PI-216, Decision Computers) in a computer.

One of the major advantages of magnetic tweezers is the large force range, which depends on the geometry of the magnet core, the coil current, the distance of the core from the bead and finally the maximum magnetization of the bead. Magnetic tweezers for cell experiments can exert forces up to 10

nN [102], whereas tweezers for single molecule experiments can stably work with forces as low as 50 fN (see following section). Like optical tweezers it is a non-invasive technique, such that the probes on which the force is transduced can be manipulated from the outside of a closed chamber or compartment. Recently, setups have been developed in which beads can even be trapped in a magnetic potential and manipulated three-dimensionally [103]. For the application of forces as a function of time (constant, sinusoidal, linear etc.) magnetic tweezers have the advantage that within the linear coil current - force regime simply the coil current has to be modulated. Since the magnetic beads are reasonably uniform<sup>11</sup> in size and magnetic moment, and the chamber does not interfere with the magnetic field on the beads, not every bead has to be calibrated individually, but few calibration measurements are sufficient to determine a stable coil current - force relationship for a magnetic tweezers setup. Last but not least, it has to be said that magnetic tweezers are inexpensive, fast to design, build and mount and thus are an excellent nano-mechanics tool for adventurous experimentalists.

### Vertical force transducer

The vertical force transducer is a setup, which exerts forces perpendicular to the focal plane of the microscope. It consists of a horseshoe shaped soft iron core with two coils that magnetize the poles of the core with opposite polarities. A schematic drawing is shown in figure 2.15. The optical axis of the microscope has to be centered accurately with respect to the gap between the N and the S pole of the magnet. If this conditions are met, all force components parallel to the focal plane of the microscope cancel, and the force is oriented strictly perpendicular to the focal plane of the microscope. This was tested for standard adjustments of the setup. The test showed that the angle relative to the optical axis was always below 5 degrees, which means that the force components parallel to the focal plane were more than one order of magnitude smaller than the perpendicular ones. The force range of the transducer can be shifted by varying the distance between the magnet and the sample. For the experiments described in the context of this work, it

---

<sup>11</sup>less than 10% standard deviation

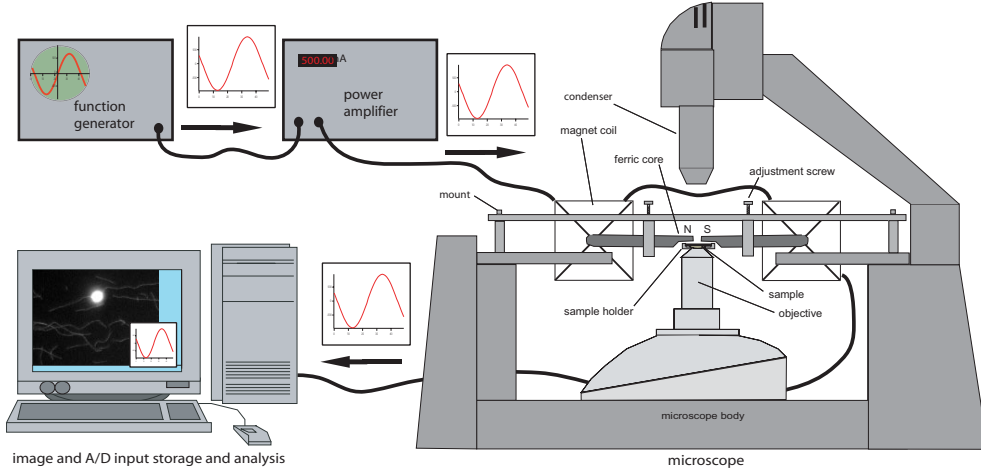


Figure 2.15: Vertical magnetic tweezers

**Schematic side view of a vertical magnetic tweezers setup installed on a Carl Zeiss Axiovert 200 microscope.**

varies from 50 fN up to 10 pN. To mount the setup on the microscope in a reproducible way, with a defined distance between magnet and sample, this distance was adjusted before each experiment. For this adjustment, first, the tip of a calibrated micrometer screw, which could be adjusted vertically with a precision of  $5 \mu\text{m}$  was brought in electric contact with the sample holder fixed on the microscope. Following, the screw position was changed by the desired distance and the vertical position of the magnet adjusted with four screws on the setup, to again come into electric contact with the micrometer screw tip. The force transducer was calibrated by pulling magnetic beads (radius  $R_{bead}$ ) through a solution of known viscosity  $\eta$  and determining the pulling force  $F_m$  by the bead velocity  $v$ .

$$F_m = 6\pi\eta v R_{bead} \quad (2.6)$$

For the calibration water - glycerol mixtures with 20-50 *mass%* water content were used. Their viscosities ranged from 5.6 to 70 *mPa · s* and were measured by falling ball viscosimetry and compared with literature values [104]. Two different ways of determining the velocities of the beads pulled through the solution were applied to calibrate the setup. In the first case, the far out-off focus image of a bead, with characteristic ring pattern was observed and a movie saving process was started. Then the focal plane was moved upwards

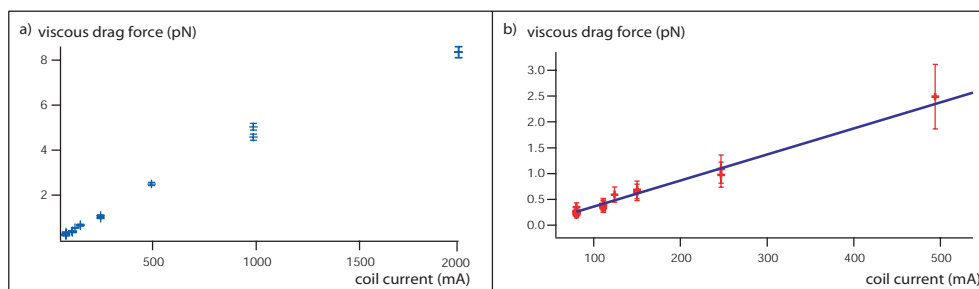


Figure 2.16: Vertical magnetic tweezers calibration

**Graph of the viscous drag force vs. the coil current of the vertical magnetic tweezers at a distance of 1.5 mm between the magnet core and the beads. Graph a) shows the entire force and current range, whereas graph b) shows only the linear range of the current force relation. Error bars are calculated from the uncertainty of the bead velocity and the solution viscosity. The line fit is the conversion function used for the experiments.**

(by usually  $40 \mu\text{m}$ ) and a constant current applied to the coils. The time required for the bead to travel the  $40 \mu\text{m}$  upwards was identified by comparison of the characteristic ring patterns. The second method used for the determination of the bead velocity was the three dimensional tracking algorithm described above. The first methods gives a calibration over larger distances, whereas the second enables a more accurate velocity determination. Reassuringly, both ways of calibration yielded the same force - coil current relation for the setup and were subsequently combined for the calibration function. One example is shown in figure 2.16. Calibration measurements were done in completely sealed chambers to avoid interference of convective movements with the calibration. Furthermore, only beads in the chamber, which were more than ten diameters off the bottom surface and more than  $50 \mu\text{m}$  away from any other bead, were taken for calibration, to avoid hydrodynamic wall effects and magnetic bead-bead interactions.

An advantage of magnetic force transducers over other colloidal force techniques is that externally controlled force - time relations  $F(t)$  can be imposed over the function generator. It must be pointed out that this is only correct as long as the force current relation is linear. From figure 2.17 it can be seen, that the magnetization of the iron core of the magnet is only a linear function up to 600 mA. Thus only this current regime was used in the experiments.

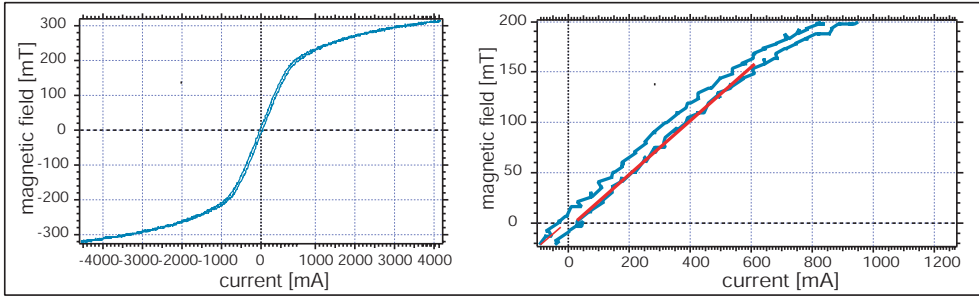


Figure 2.17: Vertical magnetic tweezers magnetization

The magnetic field between the two magnet poles of the vertical magnetic tweezers setup. Left the entire curve and right an expanded region where the magnetic field is roughly linear as a function of the applied coil current. The red line indicates the linear fit used for the magnetization function. Visibly a small hysteresis of the iron core exists. However, the forces induced by the hysteresis were absolutely negligible, even compared to the gravitational force of 35 fN of a M280 magnetic bead.

### Horizontal force transducer

The horizontal force transducer is a setup that exerts forces on magnetic beads parallel to the focal plane of the microscope. A schematic view is shown in figure 2.18. A rectangular ferric core, which is magnetized by one large coil is approached to the outside of the experiment chamber. The force exerted on the bead is determined by the distance of the core to the bead, its geometry [105] and the coil current. Figure 2.19 shows the magnetic field and its gradient for two core geometries as a function of the distance between bead and core. The calibration of the setup was also achieved by pulling magnetic beads through a viscous solution as described above. Figure 2.20 shows the magnetic field induced by two different core materials and the calibration measurement. The core material used in the experiments was a iron cobalt alloy which was a gift from the accelerator lab of Ludwig-Maximilians Universität München and has a 24 % higher magnetization than conventional soft iron. Still at large distances of the ferric core to the beads, the saturation magnetization of the beads is not completely reached and no linear force-current relation can be expected. The best function to fit the calibration curve is a power law function of the coil current, since this includes the effects of the bead magnetization. Best fits were achieved for an exponent  $\frac{5}{4}$ .

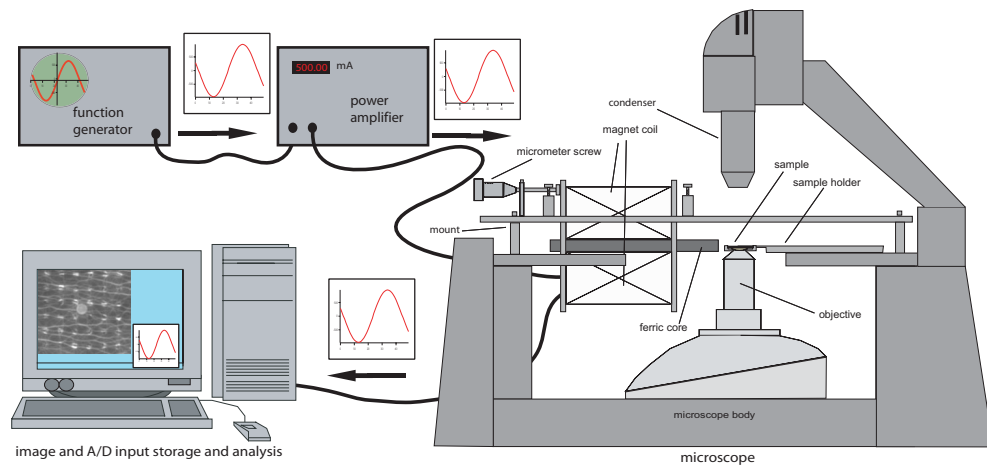


Figure 2.18: Horizontal force transducer  
Schematic side view of a horizontal magnetic tweezers setup installed on a Carl Zeiss Axiovert 200 microscope.

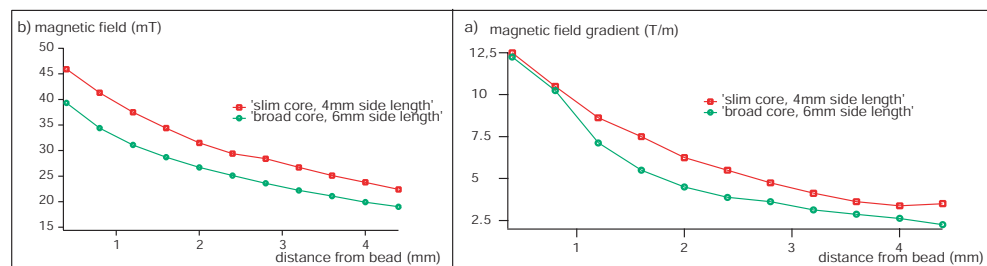


Figure 2.19: Horizontal force transducer magnetic field and field gradient  
a) Magnetic field of the force transducer as a function of the distance from the ferric core. Two different core geometries are compared. b) Magnetic field gradient of the two geometries vs. distance from the core.

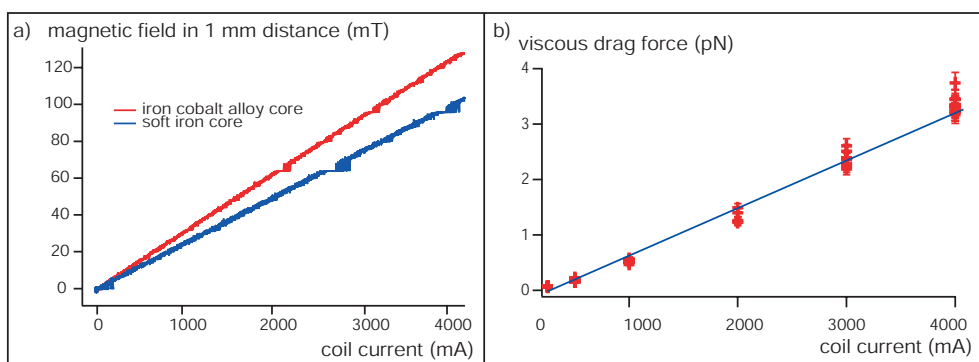


Figure 2.20: Horizontal force transducer magnetization and calibration curve  
a) Magnetic field of the horizontal magnetic tweezers in 1 mm distance from the ferric core. The iron cobalt alloy has a 24 % higher magnetization that conventional soft iron. Kinks in the magnetization curve are artifacts due to the switching of the sensitivity range of the hall sensor device used. b) Calibration curve of the magnetic tweezers retrieved from the viscous drag of magnetic beads being pulled through a solution of known viscosity.

# Chapter 3

## Results and Discussion

### 3.1 Myosin V single molecule experiments

#### 3.1.1 Particle transport by myosin V

To study transport properties of single myosin V molecules, fluorescently labelled actin filaments were grafted to soft surfaces of nitrocellulose to serve as a grid for the myosin V movement. Actin was labelled with TRITC-Phalloidin at a molar one to one ratio. Thin nitrocellulose layers were prepared as described in section 2.2.1. First, a 100 nM solution of NEMHMM<sup>1</sup> in A buffer was injected in the chamber and left to incubate for one minute. NEMHMM molecules bind to the surface by hydrophobic adsorption. Then, the chamber was rinsed twice with B buffer to remove NEMHMM from solution. Subsequently, a 50  $\mu$ M solution of BSA in B buffer was injected in the chamber and left to incubate for 3 minutes. BSA unspecifically adsorbs on nitrocellulose surfaces and passivates them against unspecific interactions with actin filaments [106]. As a next step, the chamber was rinsed three times with A buffer solution and subsequently a 20 nM actin filament solution in A buffer was injected. The solution was left in the chamber for two minutes, for the actin filaments to be bound by the surface adsorbed NEMHMM and subsequently rinsed out with A buffer. The resulting assemblies of actin filaments on the surface exhibited average distances between filaments that were large enough to prevent one bead from binding to two filaments. Myosin V coated magnetic beads were injected into the chamber at a 0.3 pM concentration in

---

<sup>1</sup>inactivated myosin fragments, which bind actin filaments

A buffer containing 2 mM ATP. The low concentration of magnetic beads was necessary since due to their gravitational force of 35 fN, the beads sink to the surface and at distances below 100  $\mu\text{m}$  they attract each other in a magnetic field and agglomerate. To prevent convection due to evaporation at the sides of the chamber, those were sealed with silicon vacuum grease. The beads could be manipulated from the outside using a hand held permanent magnet. The magnetic beads used show an intrinsic fluorescence at many wavelength, so that they could be observed simultaneously with the actin filaments in the fluorescence microscope.

### Identification of single molecule events

One goal was to study the motion of beads being pulled by only one molecule. For this purpose the density of myosin V molecules on the surface of the beads has to be controlled very accurately. To determine probabilities for beads being moved by a single myosin molecule, the statistics of binding and movement of beads on actin filaments was evaluated. Beads were placed, with the permanent magnet, onto actin filaments and the number of events, when the bead attached and moved ( $K_a$ ), relative to the number of events when the bead diffused away from the filament ( $K_n$ ) were determined. The distribution of attachment probability of myosin V molecules to the surface of the bead, can be assumed to follow a binomial distribution. This can be expanded for small numbers of molecules and a constant average value, as it is in this case, into a Poisson distribution [107]. Then the probability  $p_1$ , that an observed movement of a bead stems from only one molecule is

$$p_1 = \ln \left( \frac{K_n + K_a}{K_n} \right) \cdot \frac{K_n}{K_a} \quad (3.1)$$

The ratio of the number of myosin V molecules per bead, during the incubation, was adjusted to a value of 80:1. This yielded  $K_a = 20$  for 300 beads that were placed onto actin filaments ( $K_n=280$ ). Therefore the probability that a movement of a bead is due to only one single molecule pulling it is 96.6 %. The relatively high number of molecules needed per bead is due to the fact, that for steric reasons only a small fraction of the bead surface<sup>2</sup> can actually approach

---

<sup>2</sup>always smaller than 4 % of the entire surface for a 60 nm long linkage

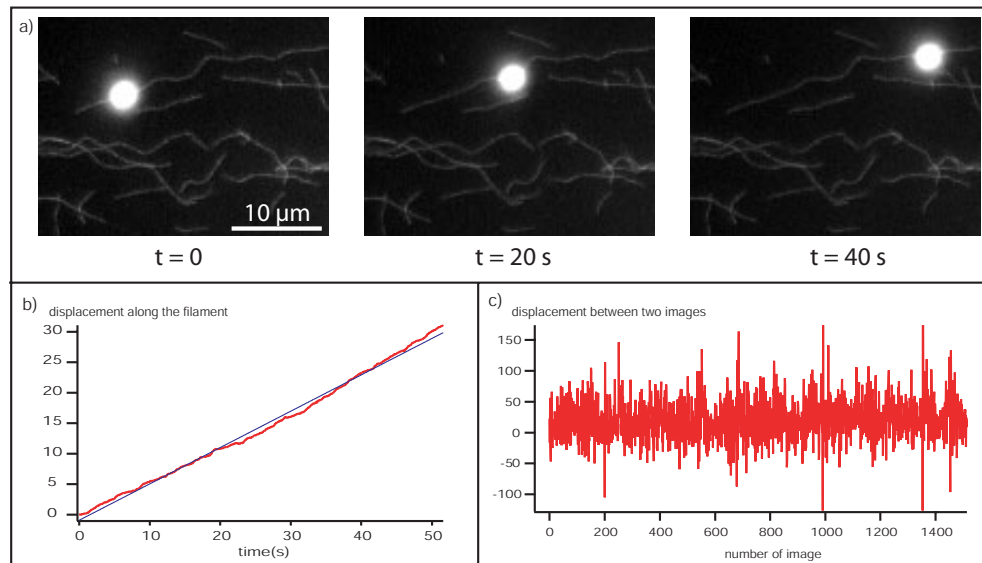


Figure 3.1: Movement of a myosin V coated bead along an actin filament  
**a) Snapshots of a magnetic bead, being moved presumably by a single myosin V molecule along a surface grafted actin filament for over  $30 \mu\text{m}$ . Such long movements of single molecules can be used for statistical analysis of the displacement to determine the average step size of the molecule during the movement. b) Displacement of the bead along the filament plotted versus time. The line is a linear fit, which determines the average velocity of the bead. ( $597 \text{ nm/s}$ ). c) Displacement of the bead from one image of the movie to the next one (1519 images).**

close enough the filament to allow a myosin V molecule, much smaller than the bead, to attach. Furthermore, the incubation time of the myosin V molecules with the bead solution was only 1 minute directly before the injection into the chamber, to account for the low stability of the molecule. Therefore it can be assumed that not all molecules bind to the beads.

### 3.1.2 Average step size

The average step size of a molecule moving along an actin filament can be evaluated directly by analyzing the trajectory of the movement along the filament. Image 3.1 shows snapshots of a moving magnetic bead, its displacement along the actin filament  $x(t)$  and the derivative  $\Delta x$  per time interval between two images, of it. The derivative, which is the displacement  $\Delta x$  from one movie frame to the next is composed from the displacement of the motor protein and

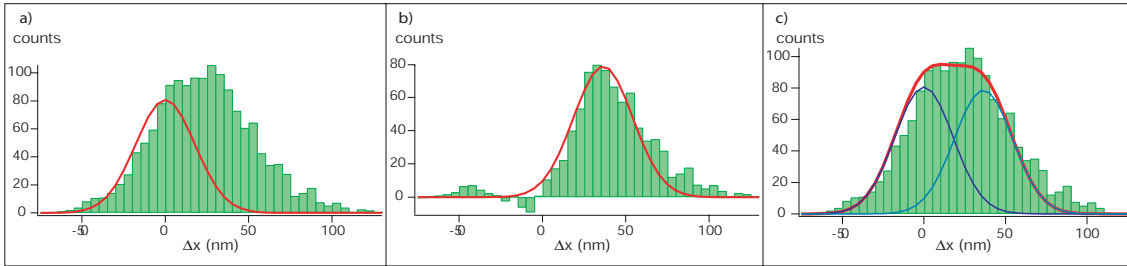


Figure 3.2: Histograms of the image to image displacement of a moving bead. **Histograms of the movement shown in image 3.1. a) Entire distribution of displacements with a fit curve centered at zero, which accounts for the time intervals when the molecule did not advance. b) Distribution in which the contributions from the fit curve of a) was subtracted and gaussian fit with equal width (centered at 36.5 nm). c) Entire distribution and both gaussian fit curves and their sum curve.**

the displacement of the bead relative to the motor protein due to thermal motion. The observed displacement also includes white noise contributions from the camera noise and fluctuations in the tracking algorithm. The combined contributions of the noise terms and the motion of the bead relative to the molecule were determined by analyzing the fluctuations of a non moving bead bound to an actin filament. Histograms of the displacements from image to image parallel to the filament can be fitted with a gaussian function. Thus if  $p(n)$  is the probability that the molecule makes  $n$  steps of equal length  $\lambda$  in the time interval between two images, the observed bead displacement from one movie frame to the next will be

$$\Delta x = \delta + \sum_n (p(n) \cdot n) \cdot \lambda \quad (3.2)$$

$\delta$  is the white noise function that determined by thermal motion and instrument noise terms. Since the contributions from all possible numbers of steps are simply added, the distribution of  $\Delta x$  will be a superposition of the gaussian distributions given by the white noise term around integer values of the step size  $\lambda$ . Figure 3.2 shows a histogram of the values for  $\Delta x$  determined by analysis of 1519 images of the movement shown in image 3.1. The bin width of the histogram was chosen to be in the range of the resolution of the tracking algorithm. To free histograms from artifacts due to the starting position of each bin, ten different histograms, in which the starting position of the bin was

always shifted by one tenth of the bin width, were averaged. The histogram should contain several gaussian curves of equal width, centered around integer numbers of the step size. The curve representing the contributions of the time intervals, when the molecule did not advance and only the white noise term contributes, should be centered at zero. To determine this contribution, the part of the histogram between -80 and 0 nm was fitted with a gaussian, which was centered at zero. Figure 3.2a shows the fit curve that should represent the time intervals in which the molecule did not advance. This curve was subtracted from the histogram and the resulting histogram again fitted with a gaussian of equal width (figure 3.2b). The fit curve is centered around  $36.5 \pm 0.8$  nm, which should represent the step size of the molecule. To exclude errors caused by the choice of the bin width of the histogram, the same procedure was used for histograms with bin width between 1 and 12 nm. The step sizes determined varied between 35.5 and 38 nm with width of the gaussian functions differing by not more than 2 nm. As a test, the average velocity  $\langle v \rangle$  of the molecule can be calculated from the fit result of the histograms. If  $A_0$  and  $A_{36.5}$  are the amplitudes of the gaussian fit functions at  $\Delta x = 0$  and  $\Delta x = 36.5nm$  respectively and  $\Delta t$  is the time between two images, the velocity should be given by

$$\langle v \rangle = \frac{A_{36.5}}{A_{36.5} + A_0} \cdot \frac{\lambda}{\Delta t} \quad (3.3)$$

This formula yields an average velocity of 530 nm/s for the molecule, which agrees reasonably well with the value of 597 nm/s, determined by fitting the displacement vs. time data with a linear function. The slightly lower velocity stems from the fact, that time intervals during which the molecule advanced two or more steps are not included. These results suggest that myosin V molecules move the beads with steps that in average have the same length as the pseudo repeat of the actin helix. This is not a very surprising result since the actin filaments are fixed to a surface and spiraling of the molecule around the filament is extremely unlikely with the bead attached. Nevertheless it shows the importance of discrete binding sites along the actin filament.

### 3.1.3 Force spectroscopy of the actin binding potential of moving myosin V molecules

Many proteins' functions are determined by specific interactions between specific domains of biological macromolecules. This holds for ligand receptor pairs, such as integrins or fibronectin, as well as for motor molecules, such as myosin V, which moves along actin filaments in a stepwise manner by cyclic binding and unbinding associated with lateral displacements. Processivity of the molecule, for example, is determined by the molecule's ability to stay firmly bound to the filament during many steps it takes. Thus it is regulated by the interaction potential between actin and the actin binding site of myosin V. The binding strength of this potential is studied by examining bond rupture forces during the movement of single myosin V molecules. A significant difference between ligand-receptor binding potentials and those for motor molecules is that the first are time invariant whereas the latter change periodically. However, myosin V has a rate limiting step in its biochemical cycle (ADP release, 12 and 18  $s^{-1}$  [65] [11]), which dominates the kinetics of the molecule. Comparison between this slow rate ( $12.5 \pm 1 s^{-1}$ , [21]) and a faster, probably composite rate of other processes ( $150 \pm 38 s^{-1}$ , [21]) shows that the molecule spends more than 90% of its cycle time in one kinetic state with ADP bound. Since for the rupture of a single bond a rupture probability per time depends on the potential, it is most likely that the potential that is probed, when the bond is broken is that of the state that dominates the kinetics of the molecule. This assumption is supported by recent experiments, which show that the distributions of run length of individual myosin V molecules show a single exponential behavior [108], which indicates a thermally activated dissociation of the molecules from the actin filament from one distinct kinetic state. Even if the binding potential of another kinetic state is very much weaker, so that bond rupture will stochastically occur during two kinetic states, each probability per time is integrated over the time the molecule spends in the state respectively and since these probabilities are linear functions with time, they simply add up. In this case, the potential probed would be a composite potential from different kinetic states of the molecule, which also is a characteristic feature. Thus the kinetic cycle of one head of the molecule can be simplified for the case of rup-

ture force analysis to a two-state model. In one state the head is bound with a binding potential which is examined, and in the other, no binding potential exists and the head is detached from the filament.

Many studies on force spectroscopy of single ligand receptor bonds have been performed with static force transducers, such as scanning force microscopes [109], micropipette techniques [110][111], or in flow chambers [112]. Yet for motor molecules, bond rupture forces of an inactive myosin II molecule from an actin filament have been measured in only one experiment with optical tweezers [113]. An experimental complication, compared to ligand-receptor force spectroscopy is, that the molecule moves while the force is exerted on the bond. Therefore static force transducers are not easily usable for this kind of experiment. The advantage of magnetic force transducers compared to optical traps is, that the induction and calibration of forces perpendicular to the focal plane of a microscope are much easier to accomplish.

As in the previously described experiment, myosin V molecules were bound with monoclonal antibodies to magnetic beads with a 96.6 % probability for single molecule events. Actin filaments were grafted to nitrocellulose coated glass surfaces in the same way and the beads were placed onto the filaments with the permanent magnet. The movement of the bead observed was permanently tracked with the three-dimensional tracking algorithm. When a bead was found to move along a filament<sup>3</sup> a linear force ramp was started and the force increased until the bead detached from the filament (see images 3.3).

The exact moment of the bond rupture was identified with the tracking data for the movement perpendicular to the focal plane, which is the width  $w$  of the 2D gaussian fit function of the tracking algorithm. As long as the bead, bound to the actin filament, moves along the surface,  $w$  should be constant, with fluctuations due to the bead hovering on a linker and image and tracking fluctuations. As soon as the bond is ruptured, the distance between bead and surface should, to first order approximation, increase linearly for the short time the bead can still be observed. Since the width  $w(z)$  as a function of

---

<sup>3</sup>the criterion for a motor-caused movement was the observation of a continuous displacement along the filament with the help of the tracking algorithm.

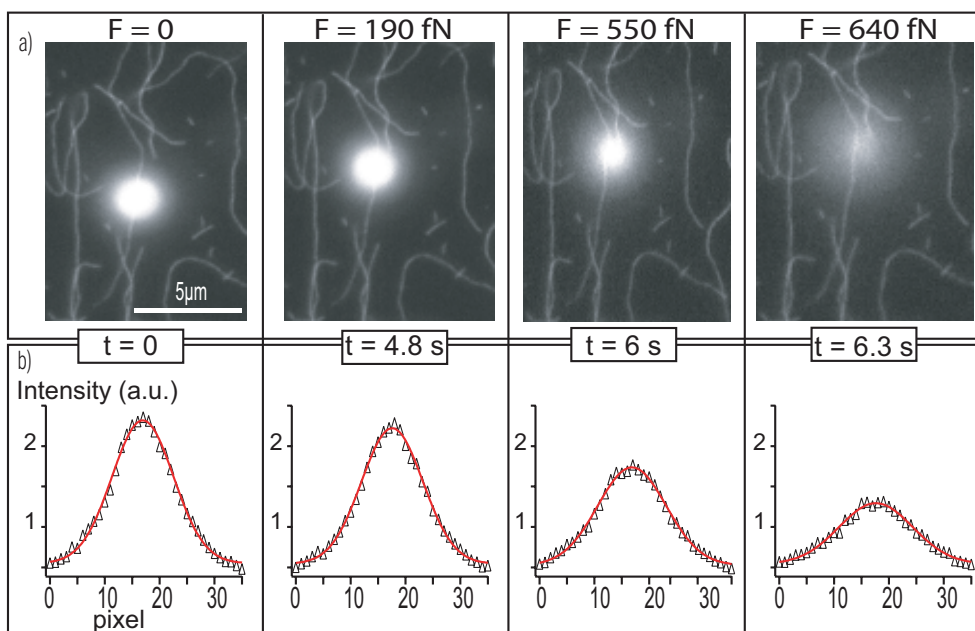


Figure 3.3: Snapshots of a force induced bond rupture of a myosin V molecule moving along an actin filament

a) Example of a fluorescent magnetic bead moved most likely by a single myosin V molecule along an actin filament while the force oriented perpendicular to the focal plane is increased at a fixed rate  $\dot{F} = 0.3$  pN/s. It finally detaches from the filament shortly before the third frame as indicated by the blurring of the fluorescence image. b) Corresponding intensity profile of snapshots of the bead in each movie frame and its gaussian fit. Note that the width of the fit curve increases as the bead leaves the focal plane.

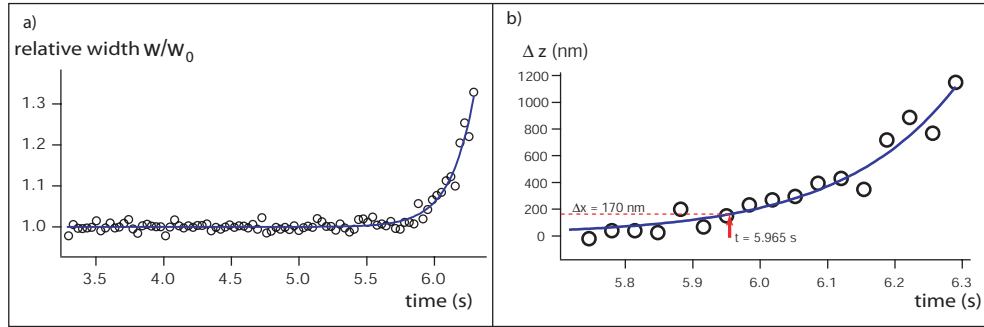


Figure 3.4: Rupture process a) of single myosin V molecule from an actin filament

**a) Circles:** time dependence of the relative width of the gaussian fit of the fluorescence intensity profile during motion of the bead and its detachment process. **Solid line:** Fit of the relative width by function  $w(t)$  of equation 3.4. The time of detachment determined for this event is  $t = 5.965 \pm 0.015s$ . **b) Expanded graph** of the distance  $\Delta z$  of the magnetic bead from the sample surface during the rupture process. The values of  $\Delta z$  were determined using the three dimensional tracking algorithm described in section 2.3.2. The arrow indicates the determined moment of the bond rupture. It occurred at a separation distance of 170 nm of the magnetic bead from the sample surface. This value seems reasonable for the length of the linkage of the bead to the actin filament plus an eventual bending of the filament.

a vertical displacement can be well fitted with an exponential function, the observed tracking parameter  $w$  should increase exponentially once the bond is ruptured. Thus the tracking parameter function  $w(t)$  was fitted with a time shifted exponential function to identify the rupture moment.

$$w(t) = w_0 \cdot (1 + e^{\frac{t-t_0}{r}}) \quad (3.4)$$

In this equation,  $w_0$  is the average value of the tracking parameter  $w$ , while the bead is moving along the filament,  $t_0$  is the time shift of the exponential increase of the function and  $r$  is a measure of the speed of the increase and therefore linked to the separation velocity and therefore also the rupture force. Before the application of the force on the bead, the measured width showed fluctuations due to a hovering of the bead, linked by the molecule to the filament, and noise in the tracking process. Statistical analysis of these fluctuations of the parameter  $w$  showed that during the rupture process, at  $t = t_0 - 3 \cdot r$  the parameter  $w$  had already increased to a value that was three

standard deviations higher than the average of fluctuations of  $w$  in the absence of force. Therefore it can be very well assumed, that at  $t = t_0 - 3 \cdot r$  the distance of the bead has increased to a value that is not due to fluctuations of the bead or a stretching of a linkage anymore, but due to a rupture of the myosin V - actin bond. Thus this value for  $t$  was taken as the rupture moment of the bond. Comparison with the applied force at this moment yielded the rupture force. Figure 3.4a shows the parameter  $w(t)$  for a typical rupture event.

This fitting procedure is an objective criterion for the determination of the moment of detachment and thus has the advantage that subjective judgement of the rupture moment by visual inspection of the images is avoided. It should be noted, that with the above analysis, a time resolution of around 10-30 ms is achieved, which is below the frame rate of the camera (59 ms) and therefore gives a more precise value of the detachment force.

To verify that in the experiments the strength of the bond between myosin V and actin<sup>4</sup> is captured, the same experiment was performed with myosin V bound to actin in its rigor state in absence of ATP. The unbinding forces were about six times higher and showed a broad distribution. The use of monoclonal antibodies ensured the reproducibility of the results, since the connection between the bead and the myosin molecule was the same for every bead used.

Rupture forces of myosin V molecules moving along actin filaments were studied at force rates  $\dot{F}$  from 27 fN/s up to 2.4 pN/s. The results can be seen in graph 3.5. Clearly, the rupture force increases with the force rate and does so in a way that seems, after a certain onset, logarithmic. To calculate the parameters  $k_0$  and  $f_0$  of equation 1.4, which characterize the binding potential, the probability  $N(F)$  (equation 3.10), that a bond which existed at zero force still exists at force  $F$ , has to be computed. For the realistic case of a force transducer experiment, equation 3.10 has to be slightly modified. All force transducers have a lower limit  $F_l$  for the force they can exert on the probe due to a minimum magnetic field for the magnetization of the beads. Thus when integrating over the force coordinate, the lower limit of any integral must

---

<sup>4</sup>and not the one between myosin V and the antibody or the antibody and protein A

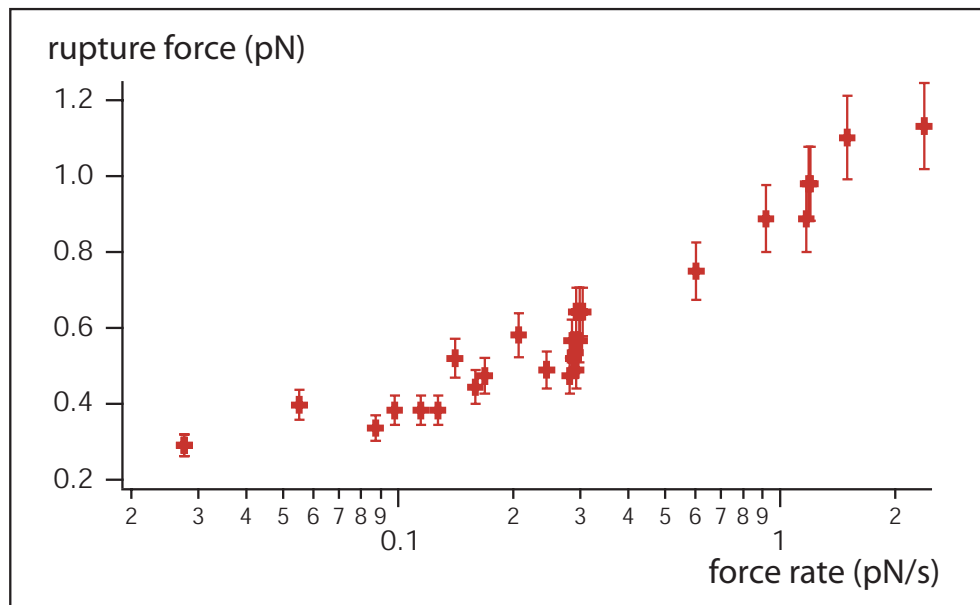


Figure 3.5: Rupture forces of single myosin V molecules from actin filaments. Rupture forces of single myosin V molecules for force rates ranging from 27 fN/s up to 2.4 pN/s. As expected for a process governed by a rupture probability per time unit, the rupture forces increase with increasing rate of force application. The increase (related to the logarithmic scale for the force rate) seems to follow a logarithmic behavior. The error bars in the graph are the cycle time ( $\tau_c \approx 60ms$ ) of myosin V multiplied with the force rate  $\dot{F}$  plus the force uncertainty from the calibration.  $\tau_c$  is the time uncertainty for the rupture process since the bond is ruptured in a particular kinetic state of the molecule and  $\tau_c \cdot \dot{F}$  is therefore the corresponding uncertainty of force.

coincide with the lower force limit of the setup.  $N(F)$  therefore becomes

$$N(F) = \exp\left(\int_{F_i}^F -k(F)\left(\frac{dt}{dF}\right)dF\right) \quad (3.5)$$

For the vertical magnetic force transducer the lower force limit depends on the distance of the magnet poles from the bead and has been determined for the experiment of myosin V rupture forces to be 250 fN.

For the calculation of  $N(F)$ , only one of the two binding sites of the molecule has to be taken into account. This one of the two binding sites (the leading one) is always bound to the actin filament until the rupture. A definite complication of the calculation comes from the fact that a moving motor molecule is alternately bound with one or two sites to the filament, so that the externally applied force has to be divided between the two sites when both are bound. For simplicity all possible geometric factors will be neglected here and it will be assumed that half the external force is acting on each of the two actin binding domains. Another simplification which will be used here is that the time intervals in which the molecule is bound with one or two heads respectively, will be assumed to have the same length  $\Delta t$ . The length of the time interval  $\Delta t$ , that in average the molecule stays bound with one or two binding sites respectively to the filament can be calculated from the average velocity of the movement ( $v \approx 600$  nm/s) and the step size of the molecule ( $\Delta x \approx 36$  nm). It is therefore assumed to be  $\Delta x/2v = \tau_c/2 = 30$  ms. Regarding the duty ratio  $r_d$  of 0.7 [12], the average time for the molecule to be bound with two heads would be 49% ( $r_d^2$ ) and to be bound with either one head 42% ( $2 \cdot r_d \cdot (1 - r_d)$ ) of the entire cycle time  $\tau_c$ . Therefore this assumption seems to be in good agreement with kinetic data of the molecule. Furthermore the introduction of additional parameters, like the ratio of time intervals when the molecule is bound with one or two heads respectively, can be avoided. Thus the force - time relation for one binding site is a discontinuous function, jumping between two values of the rate of force increase exerted on the bond (see figure 3.6). This seriously complicates the calculation of  $N(F)$ .

Since the force  $F$  is a discontinuous coordinate for the probability  $N$ , the probability  $N(t)$ , that the bond still exists at time  $t$ , is retrieved first. Thus

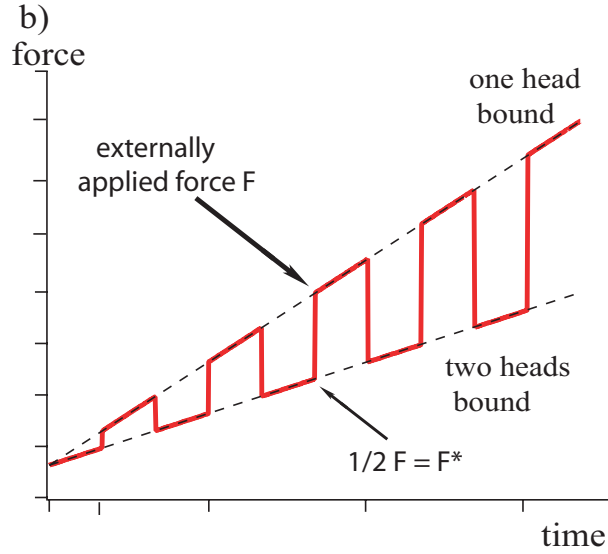


Figure 3.6: Force - time relation of a moving motor molecule  
Discontinuous force - time relationship sensed by one binding site of the motor molecule while moving along the filament (thick line). When bound with one head, the slope of the force rate equals the force rate exerted on the bead (upper slope), whereas when bound with two heads, the external force is divided between the two binding sites (lower slope).

equation 1.2 has to be solved for a discontinuous force-time dependence  $F(t)$  such as that shown in figure 3.6. It can be written as:

$$F(t) = \begin{cases} F_l + \frac{dF}{dt} \cdot t, & \text{for } 2m \cdot \Delta t < t < (2m + 1) \cdot \Delta t, \text{ (one head bound)} \\ \frac{1}{2} \cdot (F_l + \frac{dF}{dt} \cdot t), & \text{for } (2m + 1) \cdot \Delta t < t < (2m + 2) \cdot \Delta t, \text{ (two heads bound)} \end{cases} \quad (3.6)$$

where  $m$  is an integer number. Taking into account the limiting force  $F_l$  of our instrumentation, which is applied on the molecule from time  $t_l$  on, we write the solution of equation 1.2 as

$$\ln(N(t)) = \int_{t_l}^t -k(t') \cdot dt' \quad (3.7)$$

This integral can be divided up into parts of equal length  $\Delta t$ . Within these integrals,  $F(t)$  and  $k(t)$  are continuous functions. Substituting  $n = t/\Delta t - 1$  and  $l = t_l/\Delta t$  we write

$$\ln(N(t)) = \sum_{i=l}^n \int_{i\Delta t}^{(i+1)\Delta t} -k(t') \cdot dt' \quad (3.8)$$

The sum can be reordered in such a way that intervals with the same slope are put together in two separate sums. One of the sums represents the time intervals when the motor molecule is attached with two binding sites and the other the intervals when it is attached with only one.

$$\ln(N(t)) = \sum_{i=l/2}^{n/2} \int_{2i\Delta t}^{(2i+1)\Delta t} -k(t') \cdot dt' + \sum_{i=l/2}^{n/2} \int_{(2i+1)\Delta t}^{(2i+2)\Delta t} -k(t') \cdot dt' \quad (3.9)$$

We now substitute  $F^* = F/2$  and  $F_l^* = F_l/2$  and transform the probability  $N$  from the time coordinate  $t$  to the force coordinate  $F$ . We write the force coordinate  $F$  which is our externally applied force for the first sum as  $F = \dot{F}^* \cdot t$ . This represents the time intervals when the motor molecule is attached with two binding sites to the filament and the external force is divided between the binding sites. For the second sum we write  $F = 2\dot{F}^* \cdot t$ , for the time interval when the whole external force acts on one binding site.

$$\ln(N(F)) = \sum_{i=l/2}^{n/2} \int_{2i\Delta t\dot{F}^*}^{(2i+1)\Delta t\dot{F}^*} -k(F') \cdot \frac{dF'}{\dot{F}^*} + \sum_{i=l/2}^{n/2} \int_{(2i+1)\Delta t2\dot{F}^*}^{(2i+2)\Delta t2\dot{F}^*} -k(F') \cdot \frac{dF'}{2\dot{F}^*} \quad (3.10)$$

Taking the force dependence  $k(F)$  from equation 1.4, each of the integrals can be solved individually and we can write

$$\ln(N(F)) = -\frac{k_0 \cdot f_0}{\dot{F}^*} \sum_{i=l/2}^{n/2} \left[ e^{\frac{F}{f_0}} \right]_{2i\Delta t\dot{F}^*}^{(2i+1)\Delta t\dot{F}^*} + -\frac{k_0 \cdot f_0}{2\dot{F}^*} \sum_{i=l/2}^{n/2} \left[ e^{\frac{F}{f_0}} \right]_{(2i+1)\Delta t2\dot{F}^*}^{(2i+2)\Delta t2\dot{F}^*} \quad (3.11)$$

Substituting  $\kappa = \frac{\dot{F}^* \cdot \Delta t}{f_0}$ , we write

$$\ln(N(F)) = -\frac{k_0 \cdot f_0}{\dot{F}^*} \left( \sum_{i=l}^{n+1} (-e^\kappa)^i + \frac{1}{2} \cdot \sum_{i=l}^{n+1} (-e^{2\kappa})^i \right) \quad (3.12)$$

The sums are expressions of geometric series and can thus be written as

$$\ln(N(F)) = \frac{k_0 \cdot f_0}{\dot{F}^*} \left( \frac{e^{\kappa(n+2)} - e^{\kappa(l+1)}}{1 + e^\kappa} + \frac{e^{2\kappa(n+2)} - e^{2\kappa(l+1)}}{2(1 + e^{2\kappa})} \right) \quad (3.13)$$

This result can be simplified using the following assumptions:

1.)  $\kappa \ll 1$

Looking at the values for  $\Delta t = 30$  ms and the maximum value for  $\dot{F}^*$ , which is 1 pN/s, the assumption is justified for values for  $f_0$  not below 0.2 pN. Thus

$\kappa \leq 0.15$  and  $e^\kappa \leq 1.16$ . Therefore the approximation  $e^\kappa = 1$  leads even in the worst case to an error which is not decisively larger than the uncertainty of the measurement, which is around 15 %. Nevertheless the validity of the approximation has to be checked later with the fit parameter  $f_0$ .

2.)  $n \gg 1$

For our experiment this means that the motor molecule takes several steps before being detached from the filament. Writing  $n + 1 = t/\Delta t = F/(\dot{F} \cdot \Delta t)$  we see that even for the fastest detachment at the highest force rate  $n+1$  is still around 20, which justifies the approximation.

We can now write

$$\begin{aligned} \ln(N(F)) &= -\frac{k_0 \cdot f_0}{2\dot{F}^*} \left( e^{\frac{F^*}{f_0}} - e^{\frac{F_{l^*}}{f_0}} + \frac{e^{\frac{2F^*}{f_0}}}{2} - \frac{e^{\frac{2F_{l^*}}{f_0}}}{2} \right) = \\ &= -\frac{k_0 \cdot f_0}{\dot{F}} \cdot \left( e^{\frac{F^*}{f_0}} - e^{\frac{F_{l^*}}{f_0}} + \frac{\left( e^{\frac{F^*}{f_0}} \right)^2}{2} - \frac{\left( e^{\frac{F_{l^*}}{f_0}} \right)^2}{2} \right) \end{aligned} \quad (3.14)$$

$$N(F) = e^{-\frac{k_0 \cdot f_0}{\dot{F}} \cdot \left( e^{\frac{F^*}{f_0}} - e^{\frac{F_{l^*}}{f_0}} + \frac{\left( e^{\frac{F^*}{f_0}} \right)^2}{2} - \frac{\left( e^{\frac{F_{l^*}}{f_0}} \right)^2}{2} \right)} \quad (3.15)$$

The main disadvantage of the method used, compared with static bond rupture experiments like micro-pipettes or scanning force microscopes, is that continuous binding and rupture of the bond by periodically bringing the two binding partners together and pulling them apart is not possible. Once the bond ruptures, the bead is pulled away from the surface into the bulk of the sample and can not be brought back to the filament to rebind. For this reason it was not possible to measure the distribution of rupture forces ( $-\frac{d}{dF} \cdot N(F)$ ) at each force rate, but only to measure 28 isolated events of bond rupture forces at different force rates. Therefore one can not expect to retrieve the parameters, that characterize the binding potential, with the same precision as with static force transducers. The molecular parameters  $k_0$  and  $f_0$  can therefore be only evaluated by fitting the rupture force versus force rate data with a function representing a characteristic value for the theoretical rupture

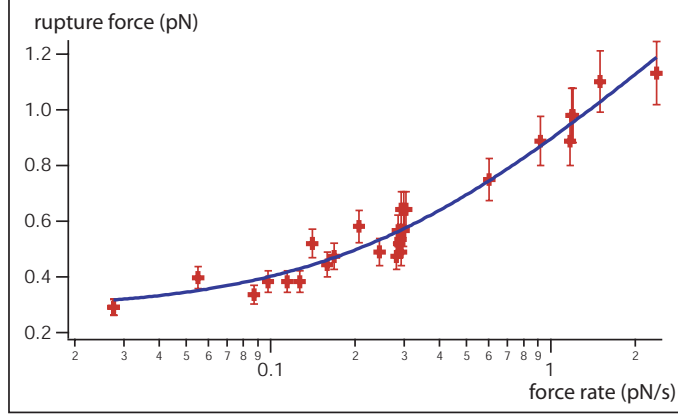


Figure 3.7: Rupture forces of single myosin V molecules with a least square fit **The measured rupture forces were fitted with the function of equation 3.16 with only  $k_0$  and  $f_0$  as adjustable fit parameters.**

force. One such characteristic value for a rupture force is the force  $F_d$ , where the probability  $N(F)$  has decayed to half its initial value, meaning that there is a 50 % probability that the bond still exists or is already ruptured at force  $F_d$ . Thus we set  $N(F_d) = 0.5$  and solve equation 3.14 for  $F_d(\dot{F})$ . This yields

$$F_d(\dot{F}) = f_0 \cdot \ln \left( 2 + 2e^{\frac{F_d}{2f_0}} + e^{\frac{F_d}{f_0}} + \frac{2 \cdot \dot{F} \cdot \ln(2)}{f_0 \cdot k_0} - 2 \cdot \sqrt{1 + 2e^{\frac{F_d}{2f_0}} + e^{\frac{F_d}{f_0}} + \frac{2 \cdot \dot{F} \cdot \ln(2)}{f_0 \cdot k_0}} \right) \quad (3.16)$$

Figure 3.7 shows the least squares fit of  $F_d(\dot{F})$  to the data set for the rupture forces. The fit values for the two parameters were  $k_0 = 0.264 \pm 0.04s^{-1}$  and  $f_0 = 0.349 \pm 0.035$  pN. For the reason mentioned above, the fit accuracy does not represent a realistic value for the uncertainty of the two parameters. Due to a asymmetry in the distribution of rupture forces (see 3.8b), even the average values of the two parameters could be different.

Therefore a Monte-Carlo-like method of randomly modifying the data set obtained and fitting the results with function 3.16 was developed. Examples for the distribution  $N(F)$  and its derivative with the parameters  $k_0 = 0.264s^{-1}$  and  $f_0 = 0.349pN$  at three different force rates are displayed in figure 3.8. As an interval of most likely rupture forces in the distribution, 68.4%<sup>5</sup> of all

<sup>5</sup>corresponding to the integral between the two values of the standard deviation of a

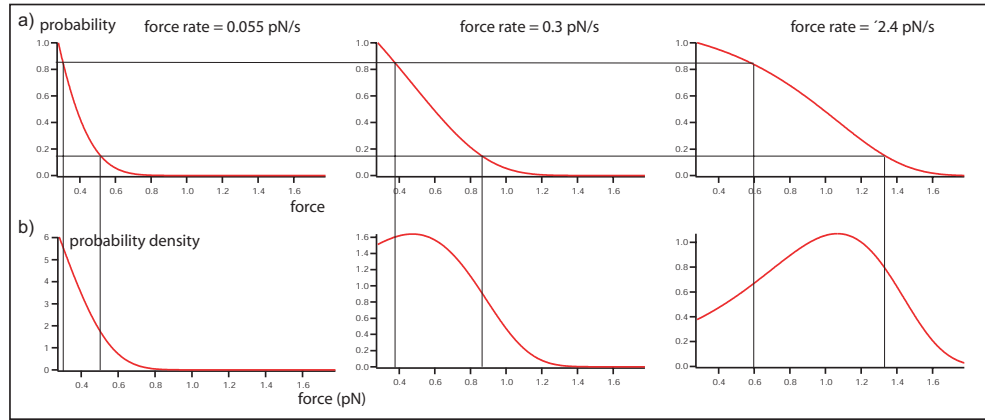


Figure 3.8: The probability  $N(F)$  of an intact bond and the bond rupture distribution  $-\frac{N(F)}{dF}$

a) Probabilities that a myosin V molecule, that was moving along an actin filament when the force was switched on, is still bound at force  $F$ , displayed for three different force rates  $\dot{F}$ . b) Distributions of the probable rupture forces.

possible rupture forces were considered, centered around the value where  $N(F)$  equals 0.5. This corresponds to all  $N(F)$  values between 0.158 and 0.842. From  $N(F)$ , the possible force interval (shown in figure 3.8) can be computed. Figure 3.9 shows this force interval for all original data points. For the fit procedure, all original data points are simultaneously, randomly moved within their force interval and the resulting data set is fitted with function 3.16. The resulting fit values of the parameters  $k_0$  and  $f_0$  are stored in a list, of which, after many repetitions of the same procedure (3000 - 10000) the average value and the standard deviation are calculated. With a binary filter, all results which produced negative fit values for any of the two parameters (11.6%) were excluded from the statistics. The average value of  $f_0$  was 0.378 pN with a standard deviation of 0.103 pN. For  $k_0$ , this procedure yielded a value of  $0.169 \text{ s}^{-1}$  with a standard deviation of  $0.058 \text{ s}^{-1}$ . The standard deviations from the individual fits are negligible compared to these values.

An alternative method for the determination of the two parameters  $k_0$  and  $f_0$  is the evaluation of the probability density  $P(F) = -\frac{N(F)}{dF}$  for a bond

---

gaussian distribution

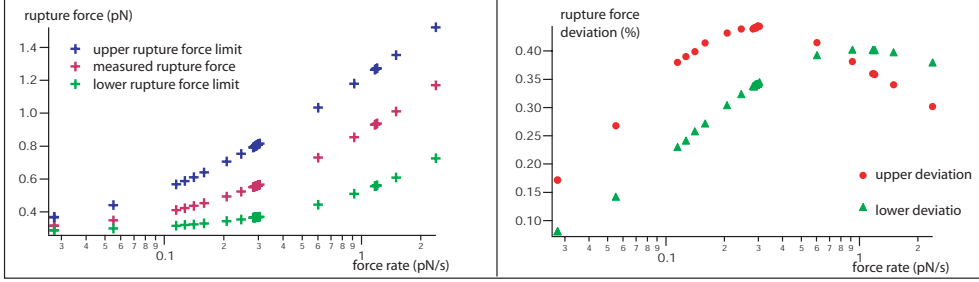


Figure 3.9: Stochastic deviations of the rupture forces

a) **The measured rupture forces with their upper and lower force limit determined from the span between 0.158 and 0.842 of the probability  $N(F)$ .** b) **Proportional deviations of the upper and lower limit from the experimentally determined value.**

rupture. From equation 3.15 it can be derived as

$$P(F) = e^{-\frac{k_0 \cdot f_0}{F}} \cdot \left( e^{\frac{F}{2f_0}} - e^{\frac{F_l}{2f_0}} + \frac{\left( e^{\frac{F}{f_0}} \right)}{2} - \frac{\left( e^{\frac{F_l}{f_0}} \right)}{2} \right) \cdot \frac{k_0 \cdot f_0}{F} \cdot \left( \frac{\left( e^{\frac{F}{f_0}} \right)}{2f_0} + \frac{\left( e^{\frac{F}{f_0}} \right)}{f_0} \right) \quad (3.17)$$

This probability density can be calculated for each rupture event for the given rupture force  $F$  and the the force rate  $\dot{F}$  as a function of the two parameters  $k_0$  and  $f_0$ . The values of the parameters  $k_0$  and  $f_0$  at the position of the maximum of the probability density  $P(f_0, k_0)$  determines the most likely values of these two parameters for the given rupture event. In this way, the probability density  $P(f_0, k_0)$  was calculated for all rupture events and all individual probability densities added up to a combined probability density  $P_g(f_0, k_0)$  for all ( $n=28$ ) rupture events.

$$P_g(f_0, k_0) = \frac{1}{N} \cdot \sum_{i=1}^n P_{F_i, \dot{F}_i}(k_0, f_0) \quad (3.18)$$

Figure 3.10 shows surface and contour plots of the calculated function  $P_g(f_0, k_0)$ . The maximum of  $P_g(f_0, k_0)$  is at  $k_0 = 0.61s^{-1}$  and  $f_0 = 0.33pN$ . Taking all rupture events into account, these are the most likely values for the two parameters.

To account for the small number of rupture events measured, again a Monte Carlo simulation method was used to randomly modify the rupture force data

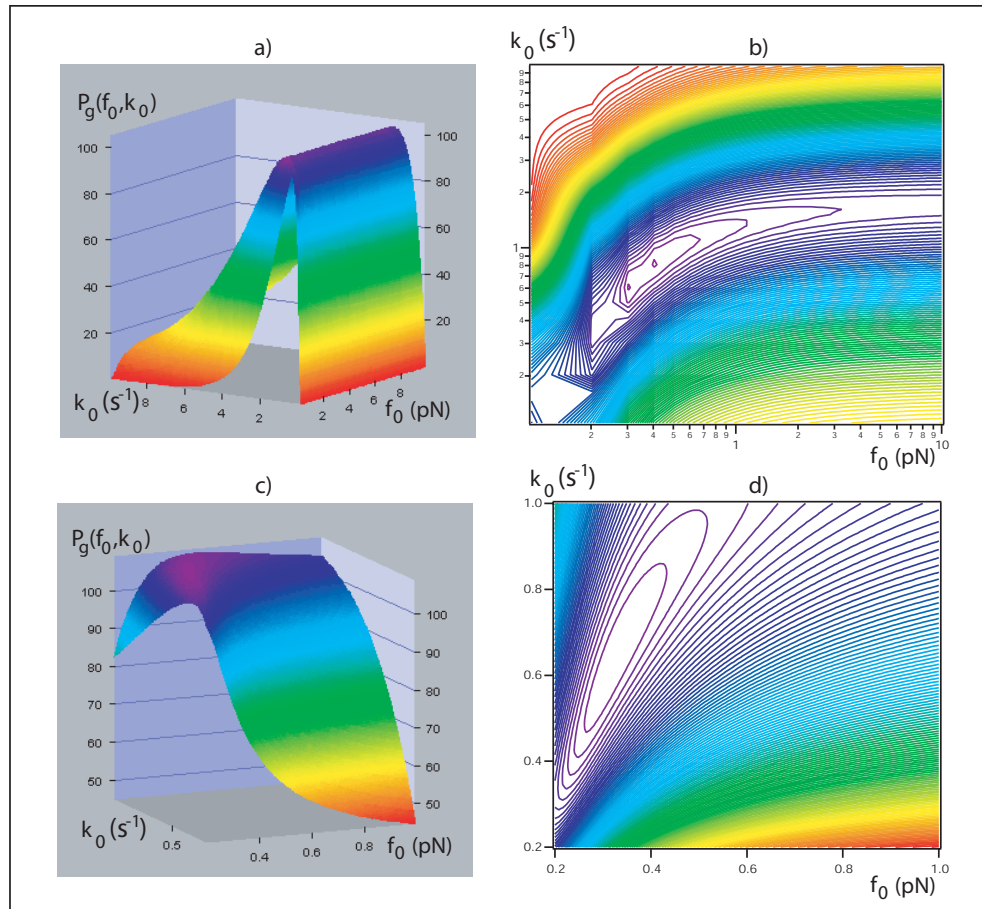


Figure 3.10: Combined probability density  $P_g(f_0, k_0)$  for a myosin V bond rupture as a function of the parameters  $k_0$  and  $f_0$ .

a) and b) as well as c) and d) are surface and density plots of the same range of the parameters  $k_0$  and  $f_0$ . In graph d) the maximum of the probability density, which determines the most likely values for the parameters, can be clearly seen.

obtained from the experiment. As before, every data point was randomly moved inside its force interval in which 68.4% of all rupture forces for a given force rate are expected. Following, each modified data set was subjected to the previously discussed procedure of finding the most likely values for  $k_0$  and  $f_0$ . This procedure was repeated for 3000 randomly modified data sets and the average value and standard deviation determined from the obtained list of individual values. This led to values of  $k_0 = 0.32 \pm 0.18 s^{-1}$  and  $f_0 = 0.33 \pm 0.1 pN$ .

The two procedures for the determination of the parameters  $k_0$  and  $f_0$  return the same value for  $f_0$ , whereas the values for  $k_0$  are slightly different. Nevertheless for the two different values for  $k_0$  their respective ranges of uncertainty overlap, thus an approximate value of 0.2 - 0.3  $s^{-1}$  can be assumed. Interestingly, this value is remarkably smaller than the value calculated from the duty ratio in chapter 1.1 (1.57  $s^{-1}$ ). Since this calculation using equation 1.1 included the assumption that the two binding domains work independently, the measured dissociation constant shows, that a stress mediated interaction between the two binding domains exists for myosin V. There seems to be a coordinated binding pattern of the two actin binding sites, which decreases the dissociation constant of the dimeric molecule during its movement along the filament and therefore increases its processivity and average run length.

The value for the rate of dissociation in the absence of an external force  $k_0$ , allows us to calculate a run length distribution  $P(l)$  for an individual myosin V molecule in the absence external force. The run length  $l$  is the distance a molecule moves along a filament before detaching. The probability  $p(\Delta t)$  that the molecule does not unbind during one time interval  $\Delta t$  (30 ms) when it is only attached with one head to the filament is:

$$p(\Delta t) = e^{-k_0 \cdot \Delta t} \quad (3.19)$$

For  $N$  time intervals, the probability  $p(N \cdot \Delta t)$  that the molecule is still bound to the filament while moving is

$$p(N \cdot \Delta t) = \prod_N e^{-k_0 \cdot \Delta t} = e^{-N \cdot k_0 \cdot \Delta t} \quad (3.20)$$

Assuming that the molecule can detach from the filament only when one head is bound, the probability that the moving molecule is still bound to the filament

after a time  $t$  is

$$p(t) = e^{-\frac{k_0 \cdot t}{2}} \quad (3.21)$$

Converting this to a probability of a length travelled  $p(l)$  and taking its derivative, the run length distribution  $P(l)$  will be

$$P(l) = \frac{1}{l_t} \cdot e^{-\frac{l}{l_t}}, l_t = \frac{\Delta x}{\Delta t \cdot k_0} \quad (3.22)$$

The parameter  $l_t$  is the average value of the distribution. For a step size  $\Delta x$  of 36 nm and the retrieved value of  $k_0$ , it is  $4 - 6 \mu m$ . This coincides well with run length statistics, obtained by observation of the motion of many individual labelled myosin V molecules [57] which were fit with parameters  $l_t$  of 2.4- 0.7  $\mu m$  for ionic strength of 150 - 400 mM KCl respectively, where one would expect shorter run length than at 25 mM KCl as in our measurements.

From the parameter  $f_0$ , for the characteristic force of bond rupture, a length  $l$  ( $l = k_b T / f_0$ ) of the reaction pathway (figure 1.3) can be determined as  $11 \pm 3$  nm. This large value indicates that the bond between myosin V and actin is rather of macromolecular than of atomic scale, as e.g. the biotin - streptavidin bond. Actually this large value can only be explained if a domain of one binding partner e.g. myosin V is inserted into a binding pocket of the other binding partner. For a binding potential between two attractive surfaces, the Debye screening length, which for the buffer used is 2 nm, is much smaller than the value of  $l$  determined and would not allow such a long range interaction. The large value measured means also a high force sensitivity of the bond. Upon force, the rupture of the bond is very much accelerated. This opens the possibility of a interaction between the two actin binding domains of myosin V mediated by internal stress in the molecule. Through internal stress, the two binding sites may communicate to coordinate their binding states with the filament and optimize the processivity of the molecule.

### 3.1.4 Myosin V movement under forward and backward forces

To study the movement of myosin V single molecules under forces parallel to the direction of movement the set up of the horizontal magnetic force transducer was designed. In previous work, a bimodal distribution of the velocities

of beads transported by myosin V molecules was observed [105]. The binding statistics for the determination of the probability of single molecule events for this experiment only showed a probability of 70.8 %. Since this number matches relatively well the percentage of observed beads with lower velocities, the assumption was that beads moved by two or more molecules could have higher transport velocities than beads being moved by a single molecule. This would be possible if two molecules interact by a stress coupling via the bead surface and the biochemistry and kinetics of a molecule were strain sensitive. This strain sensitivity was thought to be probed by inducing a positive or negative load on the molecule and observing possible differences in the movement, compared to the movement in the absence of force. Myosin V coated beads were prepared as described in the previous section, with a ratio of molecules per bead ratio adjusted in a way to yield again a probability of 96.6 % for single molecule events. Actin filaments were grafted onto the sample surface equivalently, but under hydrodynamic flow, to preferably align the filaments in the direction of the magnetic force on the beads. Beads were placed with the permanent magnet onto filaments which were rather aligned parallel to the force direction and the movement was followed in real time with a gaussian tracking algorithm. By chance, the movement of the molecule was in the direction of the force acting or opposed to it.

### **Backward forces**

When a bead was found to continuously move along the filament, the force on the bead was continuously increased until the bead detached from the filament. Figure 3.11 shows snapshots of a bead moving along a filament under an increasing force acting against the movement, until it is stalled and finally detaches from the filament and is pulled back along it.

Figure 3.12 shows the displacement of the bead along the filament together with the force acting against its movement versus time. It shows that at around 900 fN the movement is slowed down and the movement is less smooth than before. At a force of 1.3 pN the bead detaches from the filament.

The detachment force can be compared with the bond rupture forces studied in the previous section. Because of the geometry of the molecule being

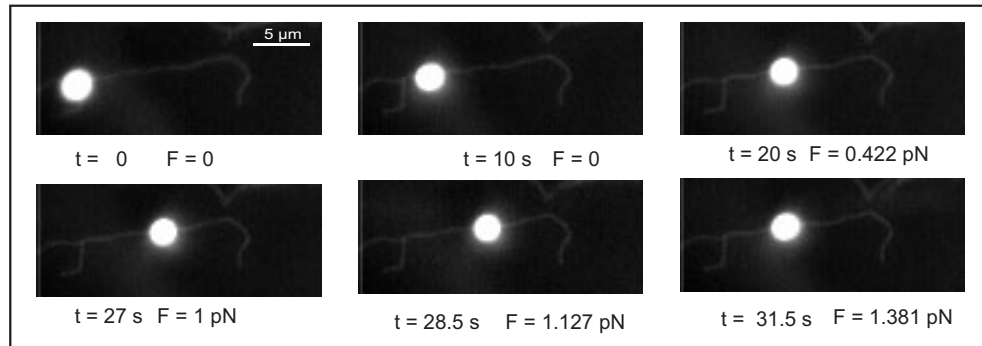


Figure 3.11: Movement of a magnetic bead transported by a single myosin V molecule under increasing backward load

The bead moves with a nearly constant velocity until the linearly increased load reaches 900 fN ( $t = 26$  s). Above this value it advances very slowly, is finally stalled and detaches from the actin filament ( $t = 30.7$  s). The bead is pulled back and rebinds to the filament ( $t = 31.5$  s).

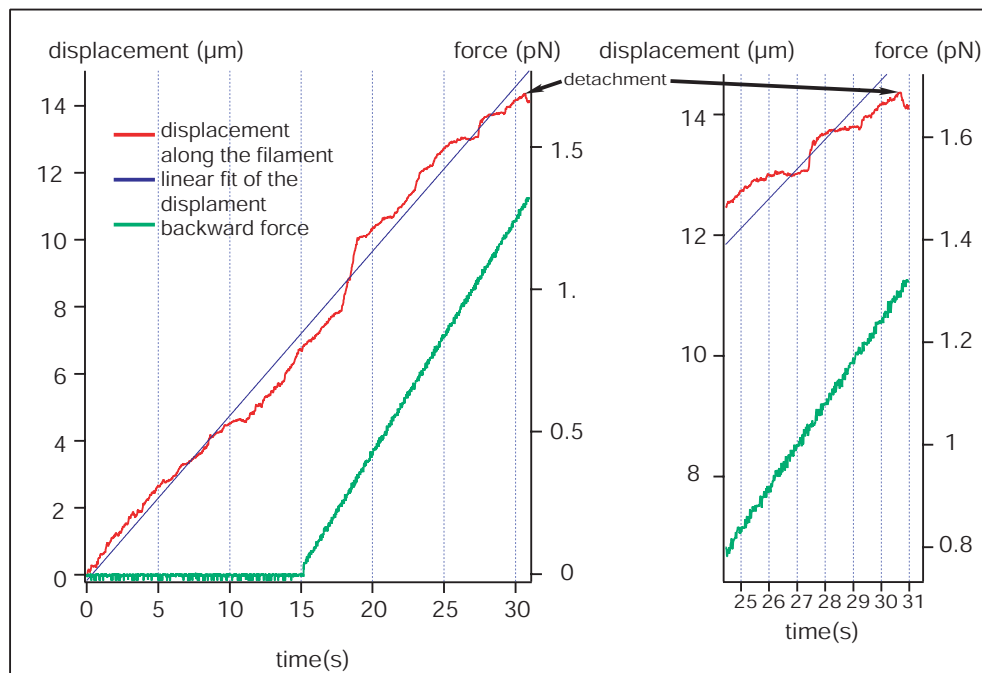


Figure 3.12: Displacement of myosin V along actin under backward load  
The displacement of the bead shown in figure 3.11 is a roughly linear function (see fit). Its velocity does not change upon the increase of the backward load until the force reaches 900 fN. At higher force, the movement is not smooth and slowed down, until the detachment from the actin filament.

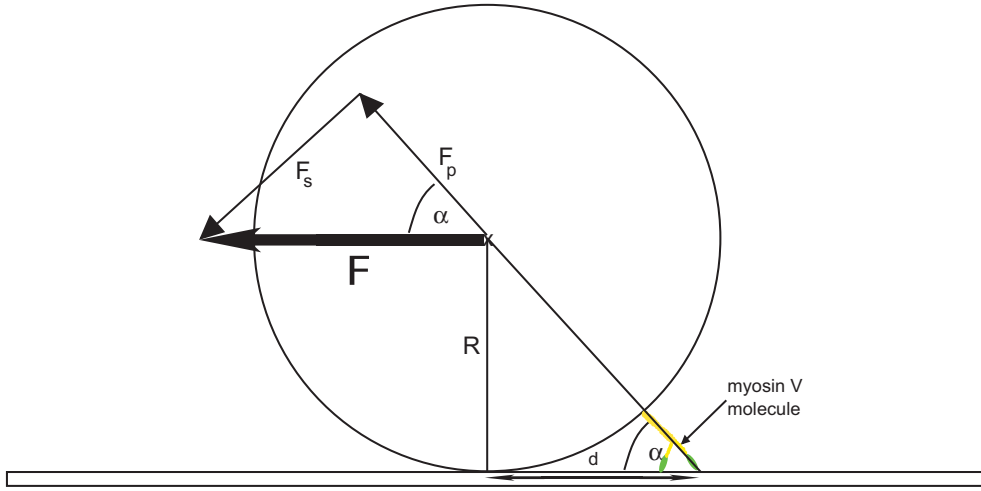


Figure 3.13: Schematics of the geometry when myosin V is examined under a load parallel to its direction of movement.

bound to the bead via a linker molecule, the force, which is transmitted to the binding site will be different from the force exerted onto the bead. A scheme of the geometry is shown in figure 3.13.

A force  $F$  acting parallel to the surface along which the molecule is moving will press the bead onto this surface and the force vector will be divided into a component  $F_p$  pulling on the linkage between bead and filament, which is essentially the bond between the myosin V molecule and the actin filament, and a component  $F_s$  perpendicular to it, pressing the bead onto the surface. The angle  $\alpha$  between the direction of the force  $F$  and the molecule orientation determines the value of  $F_p$  as  $F_p = F \cdot \cos(\alpha)$ . Since the displacement  $d$  between binding site and bead center (see figure 3.13) can be measured in a separate experiment with a non moving bead,  $F_p$  can be expressed as a function of  $d$  and the bead radius  $R$ .

$$F_p = F \cdot d \cdot \sqrt{\frac{1}{R^2 + d^2}} \quad (3.23)$$

A measurement, which produced a value of 420 nm for  $d$  showed that only 28.7% of the externally applied force is acting on the myosin - actin bond. From this a linkage length  $l$  of 61.6 nm can be calculated, which seems, regarding electron micrographs in figures 2.3 and 1.2, to be a reasonable value for a large molecule like myosin V. Taking these geometric factors into account, the rupture of the bond occurred at force of 373.5 fN, with a rate of force increase of

23.6 fN/s acting on the binding site. Using the previously determined binding potential parameters  $k_0$  and  $f_0$ , the fit function used for analysis of the rupture forces perpendicular to the movement direction (equation 3.16), returns a value of 330 fN for a force rate of 23.6 fN/s. This shows that the direction of the force vector on the actin - myosin V bond does not have a significant importance on the magnitude of the rupture force.

The observation of a near stalling of myosin V under a backward load of 900 fN coincides well with measurements on the dwell time distributions of myosin V under force. Up to a force of around 1 pN, no increase in the average dwell time was observed, whereas above 1 pN, the dwell time increased strongly [19][114]. The fact that the molecule moves smoothly with a constant velocity under an increasing backward load is a strong argument for the assumption that the forward movement is driven by a conformational change of the molecule, which provides the force for the displacement and not by a diffusive motion along the actin filament, which is rectified by its binding sites. If the forward movement of the molecule is driven by the internal force of the molecule, as it would be for a conformational change, the external force acts against the internal force of the molecule. The force which moves the molecule actively forward is thus reduced by the magnitude of the external load. Since the force which moves the molecule forward determines only the time it takes to complete the movement of one actin binding domain to its next binding site, this time is increased linearly with increasing load. The velocity of the molecule is determined by the average time of the rate limiting step of the molecule. This rate limiting step is not the forward movement of the actin binding site of the molecule, but the release of ADP [12][21]. Therefore a linear increase of the short time it takes to move the actin binding domain forward to the next binding site can probably not be observed. On the other hand, for a diffusive motion, the average time to reach the next binding site will increase exponentially with a backward load on the molecule [115]. The energy barrier  $\Delta E$  imposed by an external load of e.g. 800 fN on a thermal process like a diffusion is  $\Delta E = 36nm \cdot 800fN = 7.2 \cdot k_bT$ . Such an high value should increase the time for the forward movement of the actin binding site of myosin V so much, that it should be observed in a change of velocity [115].

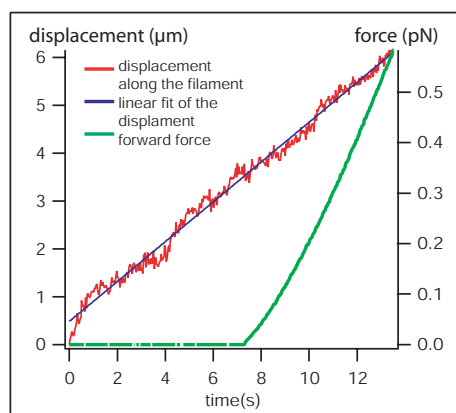


Figure 3.14: Displacement of myosin V along actin under forward load  
**The well adjusted linear fit curve for the movement without and with force indicates a constant velocity of 450 nm/s, independent from a pulling force in the direction of movement.**

Since this is not the case, a diffusive forward motion of myosin V along the actin filament seems unlikely.

### Forward forces

When a myosin V molecule was moving in direction in which the force could be applied, the movement of the myosin V under force acting in direction of its movement could be examined. The first approach was to exert rectangular force pulses with periods of a few seconds on the moving molecules. This proved not to be feasible since the beads always detached from the actin filaments immediately when the force was switched on. This may be due to a small torque which may be exerted on the bead when a magnetic field is switched on suddenly and the nano-crystals have to align with the field inside. To overcome this problem, the force exerted on the bead was increased linearly, again until the bond between myosin V and actin ruptured and the bead was pulled away from the filament. The displacement of a myosin V molecule vs. time for such an event is shown in figure 3.14.

First the bead - myosin V complex moves for 7 s and  $3.5 \mu\text{m}$  without any external force. Then the magnetic force pulling the bead forward into the direction of the movement is slowly increased up to 600 fN, upon which the bead is pulled off the filament. The linear fit curve for the displacement shows

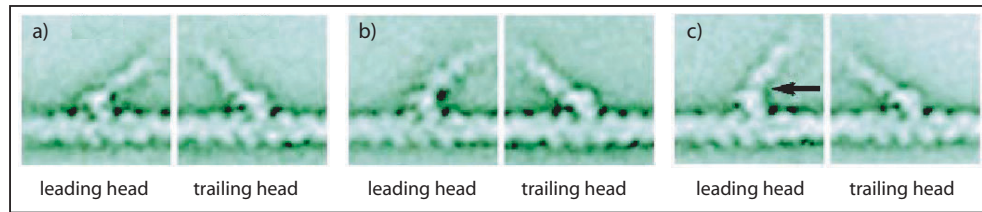


Figure 3.15: Electron micrographs of moving myosin V molecules . The images, which were taken from a sample of myosin V molecules with ATP present in solution, were classified, according to their lever arm structure, into three categories and the images averaged. a) Both leading and trailing lever arm are straight and no pliant point at the contact between lever arm and head domain exists. b) The leading lever arm is slightly bent but no clear pliant point can be observed. c) The leading lever arm is slightly bent and a pliant point (arrow) between the lever arm and the head domain can be seen. (source: Burgess et al [60])

no significant change for the movement in the absence and in the presence of a forward pulling force. This indicates, that as in the case of the force acting against the movement of the molecule, that the rate limiting kinetic step of ADP release does not depend on the external force, if the magnitude is below 600 fN. If stress mediated coupling between the two head domains of the molecule exists, as proposed from the data of the duty ratio and the average run length observed, which do not match for a model without coupling [16], it seems rather that the leading head is blocked by internal strain, than the trailing head is accelerated in its biochemical cycle. This could explain why no change in the velocity is observed, since the velocity of the molecule is determined by the biochemical cycle of the trailing head. Another hint to this view is that cryo-electron micrographs of moving myosin V molecules showed a bending of the leading lever arm and a pliant point between this lever arm and the head domain, whereas the trailing lever arm and head domain seemed rather straight (figure 3.15) [60].

Thus concluding, the entire force experiments with single myosin V molecules strongly indicate a stress mediated interaction between the two actin binding domains of the molecule. The trailing head of the molecule seems to block the release of the leading head from the actin filament to avoid an unbinding of

the molecule from its track. This new phenomenon can be denoted as super-processivity, since it increases the average length of the protein's movement beyond the value expected from its duty ratio. This example shows how internal strain in a molecule can lead to a coordination of different biochemically active sites in a motor protein to optimize its function, similar to allosteric effects like in hemoglobin.

## 3.2 Actin cortex models on micro pillar arrays

As already described in the introduction, the actin cortex is of vital importance for many processes of cell mechanics. Several studies have been performed on the structure [7] and function [116] of the actin cortex inside cells. However, the quantitative analysis of experiments done on cells is difficult, since inside cells, the actin cortex is regulated by a large number of actin binding<sup>6</sup> and regulating proteins<sup>7</sup>, which can neither be simultaneously monitored nor controlled. The theoretical interpretation of mechanical studies is hindered by the fact, that cells are non-equilibrium systems and thus actively respond to external stresses.

The strategy presented in the context of this work is to design and investigate realistic in vitro models of the actin cortex, which can be controlled quantitatively to make the results accessible to theoretical investigation. To date most in vitro models for studying mechanical properties of the actin cortex have been entangled or cross-linked solutions of actin filaments [117][118]. However, a bulk solution is not a very realistic model for a thin sheet, like the actin cortex inside cells. Pillar array substrates, represent a possibility to create quasi-two dimensional thin sheets of actin networks attached to the plane of the tops of the pillars. Additionally, by freely suspending the network in the buffer solution, only bound to the top of the pillars, the influence of surface interactions on the mechanical properties can be minimized.

Pillar array substrates were prepared as described in section 2.2.2. To impede unspecific binding of proteins, especially actin, to any other part of the substrate than the gold functionalized tops of the pillars, the silicon surface was passivated by binding PEG-750 silane<sup>8</sup> to it [49]. To specify the gold disks on top of the pillars for protein attachment, the gold surface was modified with alkanethiol mono-layers by placing the whole substrate in a 5 % alkanethiol in ethanol solution for 24 hours. After removal from the solution, substrates were shortly rinsed with ethanol to remove clusters from the surface. The substrates were attached, functional side down, with two double sided scotch tape strips

---

<sup>6</sup>filamin,  $\alpha$ -actinin

<sup>7</sup>gelsolin, fascin

<sup>8</sup>synthesized in the lab of Prof. J.P. Spatz, University of Heidelberg

on a microscopy glass slide. Buffer solutions were injected from one open side of the sample and rinsed out to the other side by slightly tilting the sample.

### 3.2.1 Self assembly of a freely suspended quasi two dimensional actin network

First a  $5\ \mu\text{M}$  solution of inactivated myosin fragments (NEMHMM) in A buffer was injected and left to incubate 5 min. The NEMHMM molecules physisorbed to the hydrophobic alkane surface, providing sites for the specific attachment of actin filaments. Subsequently, a  $250\ \mu\text{M}$  solution of BSA in B buffer was injected to passivate the remaining surface of the gold disks and left for 5 minutes to incubate. After this solution was rinsed with A buffer, a  $50\ \text{nM}$  solution of mechanically shredded, TRITC-Phalloidin labelled actin filaments was injected to bind to the tops of the pillars. Most of these short filaments had length that could not be well resolved with the fluorescence microscope, which means below  $1\ \mu\text{m}$ . After 5 minutes this solution was rinsed with F buffer and a  $1.25\ \mu\text{M}$  solution of G-actin in F buffer solution was injected.

The polymerization kinetics of G-actin solutions enabled a polymerization in form of an elongation of the short filaments already bound to the tops of the pillars. As mentioned in section 2.1.1 the kinetics of actin polymerization show a time lag for the start of filament growth due to the formation of trimers as stable nuclei. The length of the lag phase depends on the concentration in about an inverse cubic form. The kinetics of the elongation of the short filaments grafted onto the pillars has no lag phase, so that the growth of these filaments starts immediately after the injection of the buffer solution. This growth of pillar bound filaments reduces the concentration of actin monomers in the bulk solution and increases the lag phase of polymerization in the bulk. Thus, as the filaments on the pillar tops grow, the bulk is more and more depleted of monomeric actin, such that no long filaments can form in the bulk. By this way, actin filaments can be polymerized selectively from the tops of the pillar array. Due to the polarity of actin filaments, with one end growing faster than the other, this technique produces assemblies of actin filaments, which are bound with one end at the pillar tops (slowly growing end), while the other end

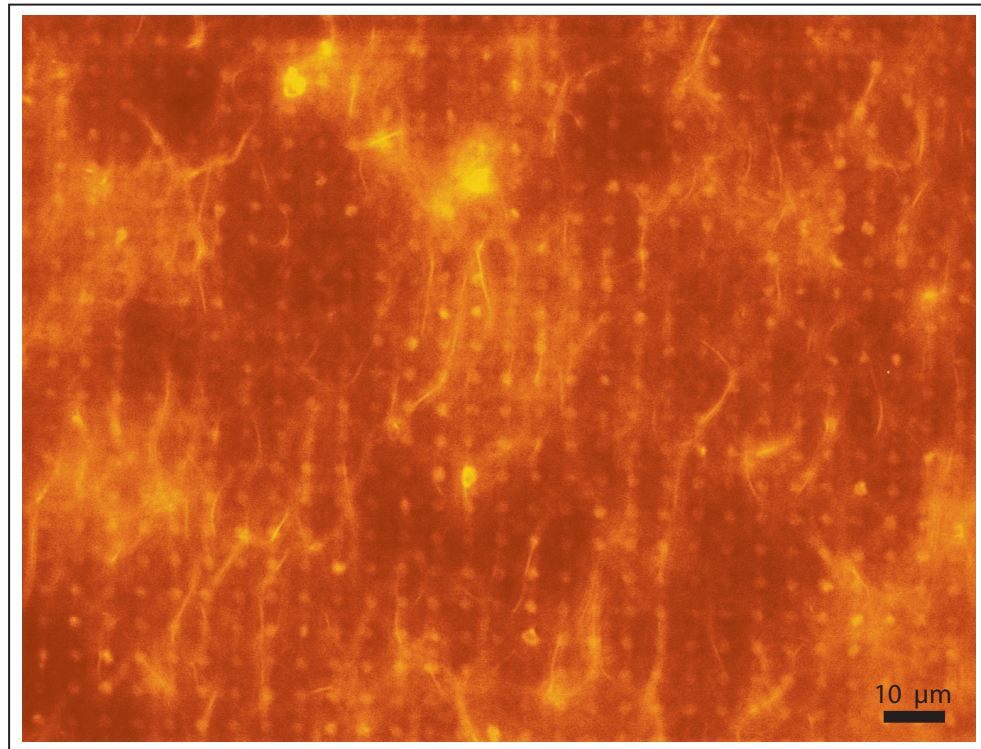


Figure 3.16: Fluorescence micrograph of actin filaments attached to a silicon pillar array substrate

**The filaments are in the focal plane at the tops of the pillar array substrate. There they appear with sharp contours. Many actin filaments seem to extend from a top of a pillar into the bulk of the sample, where their contours appear blurred.**

(fast growing end) is extending into the bulk of the sample. After 10 minutes polymerization time, the chamber was carefully rinsed and TRITC-Phalloidin injected to label the filaments. Figure 3.16 shows a fluorescence micrograph of actin filaments bound to pillar tops inside the sample. Filaments can be seen to extend from the focal plane, which is the plane of the pillar tops, out into the bulk, so that they appear blurred. This is also due to the thermal undulations of the filaments, which happen on a faster time scale than the integration time of the camera.

To generate a quasi two dimensional actin network structure on the plane of the pillar tops, a 500 nM solution of filamin in A buffer was injected into the chamber. Filamin is a dimeric actin binding protein and can thus inter-link

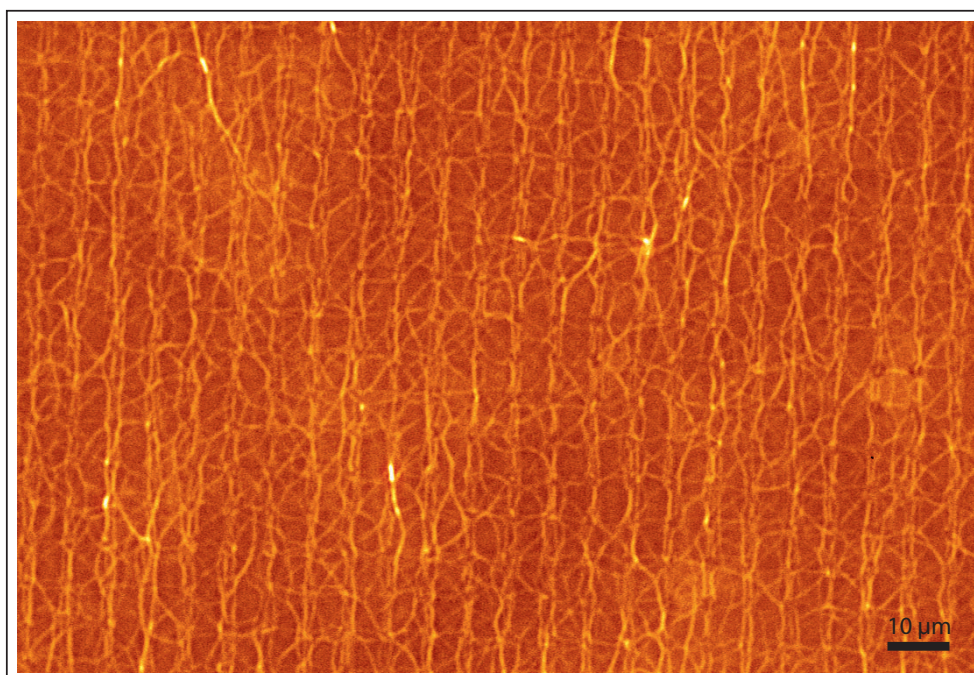


Figure 3.17: Fluorescence micrograph of a cross-linked quasi two dimensional actin network on a silicon pillar array substrate

**The network was formed after injection of filamin into the sample shown in figure 3.16. An orthogonal order of the actin structures in the network can clearly be observed. Crossing points of the network are the positions of the silicon pillars.**

actin filaments in the sample. Spontaneously<sup>9</sup> the formation of a network structure on the pillars was observed as seen in figure 3.17.

Apparently the formation of the network was initiated by cross-linking the actin filaments close to their highly mobile dangling ends in the bulk of the sample. Further binding between filaments reduces the potentiality of the filaments to extend far into the bulk and finally confines the whole network to the plane of the pillar tops. Because of the cross-linked structure, the different intensities of the inter-pillar connections and of filamin being observed to form bundles at low actin concentrations [80], it can be assumed that the whole structure consists of a inter-linked network of actin bundles. Remarkably, the geometry of the actin network resembles the orthogonal structure of the pillar array, indicating that the structure of a self-assembling actin network can be

---

<sup>9</sup>this means the time to put the sample back on the microscope and find the correct focal plane, which is about 10 - 15 sec.

imposed through the geometry of its binding sites with a substrate. That should stem from the fact that a filament will most likely bridge to its next neighboring site, thus favoring the assembly into an imposed geometry. This is especially interesting since the actin cortex inside cells is always bound to the cell membrane and this result hints to a possible correlation and induction between membrane protein organization and cortex structure.

The thickness of the structure can only be estimated with an upper limit of the depth of the focal plane ( $\approx 300$  nm) since the whole network is well focused over the entire field of view. The well defined network extended over the whole sample of several millimeters side length in a quality as shown in figure 3.17. In comparison, similar experiments were performed with substrates of orthogonally arranged gold disc arrays on silicon. The gold discs had height of 10 nm from the silicon substrate. The silicon surfaces were again passivated with PEG-750 silane to prevent protein adsorption to them. Following the same protocol as for the pillar array substrates, actin filaments were selectively polymerized from the gold disks and cross-linked with filamin. In contrast to the pillar substrates, no well defined orthogonal actin network could be formed on the flat patterned substrates (image in figure 3.18). This is attributed to the flat surface being a rigid boundary, and thus possibly impeding the structure forming process of freely dangling filaments by unspecific interaction. This is especially important since actin is a semi-flexible polymer, which has a tendency to adsorb to solid surfaces when it has more than one binding site on the substrate.

One motivation for our efforts to generate freely suspended actin networks was to study the transport behavior of the processive motor protein myosin V. Therefore, the freely suspended quasi two dimensional actin network served as a grid for the movement of the motor proteins. Myosin V was bound via monoclonal antibodies to protein A coated, fluorescent polystyrene beads of 40 nm diameter. A 15 pM solution of the myosin V coated beads in A buffer was injected into the chamber which contained the actin network bound to the pillar substrate. The bead solution was left in the chamber to bind to the actin network for 5 minutes and subsequently non-bound beads were removed by rinsing with A buffer. Finally, a 2 mM ATP solution in A buffer was injected

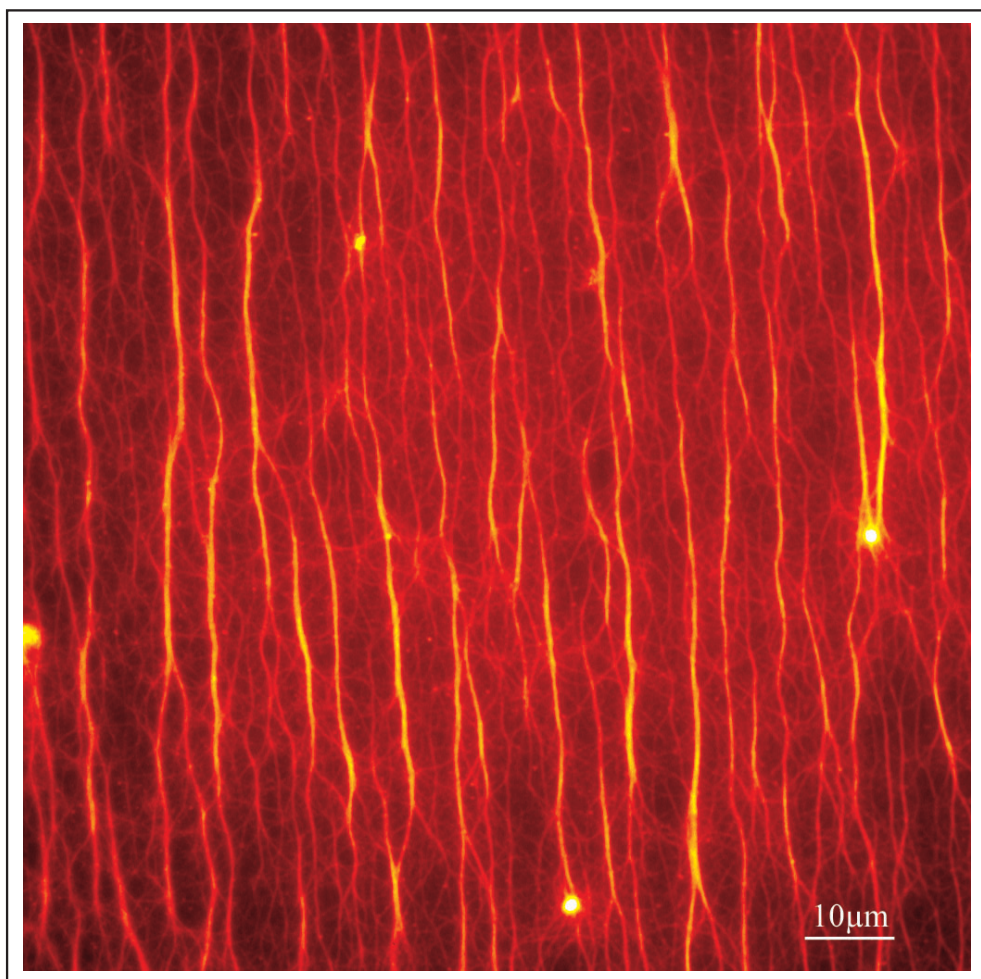


Figure 3.18: Actin network cross linked with filamin on a flat patterned substrate.

**The alignment of the thick actin bundles is due to the flow caused by the injection of the buffer solution.**

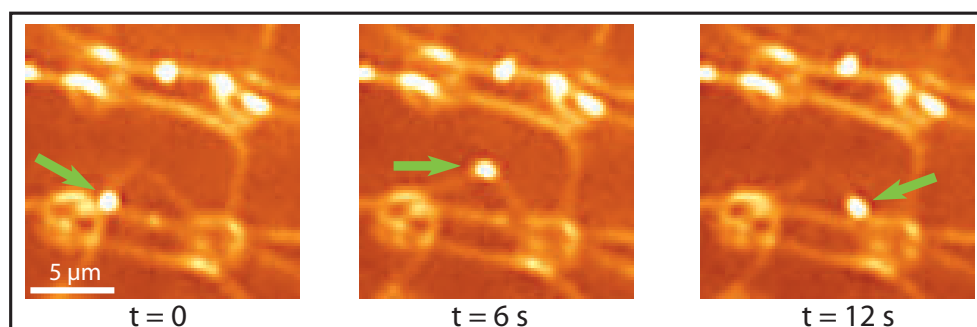


Figure 3.19: A 40 nm polystyrene bead being transported by myosin V on an quasi two dimensional actin network.

**The bead, indicated by the green arrows, is first moved diagonally up from the pillar on the left bottom side of the image. In the center of the four pillars shown, two actin filaments intersect and the bead changes the direction of its movement. This indicates, that myosin V can change its track upon the encounter of another actin filament. The average velocity of the bead was 273 nm/s.**

into the chamber and the motion of the beads was observed simultaneously with the actin network. Figure 3.19 shows snapshots of the network with beads being transported by myosin V. Many beads were immobile during the time of observation, whereas another fraction of beads moved for short distances of around 1 or 2  $\mu m$  before they stopped their movement and remained immobile, bound to the actin structure. A smaller number of beads moved for a short distance and eventually detached from the actin, diffusing away into the bulk of the sample. The first difference in comparison to movement data on myosin V coated beads moving along surface<sup>10</sup> grafted actin filaments is that both velocities and distances are lower for transport on the actin filaments on the pillar array. This may be due to the presence of filamin bound to actin, since it is known [119] that filamin and myosin bind to the same area on actin filaments and thus compete for actin binding sites. An interesting aspect of the movement of myosin V on filamin bundled actin networks is the fact, that myosin V moves along bundles although that binding sites for the motor protein on the filament are already occupied by filamin. This indicates that there could be a certain flexibility of the step size of myosin V, since it is unlikely that on an actin filament, which is decorated with filamin molecules,

<sup>10</sup>nitrocellulose and PDMS surfaces

the myosin can always find unoccupied binding sites, at a pseudo repeat of the actin helix ( $\approx 36nm$ ) apart.

### 3.2.2 Mechanical properties of the quasi two dimensional actin network

The mechanical properties of the freely suspended actin bundle network on top of the pillar array substrates are of great interest, since no thin sheet structure of actin has ever been analyzed for its mechanics. The combination of the new method of the formation of self-assembled actin networks on pillar array substrates and magnetic bead force probing could open first time possibilities to analyze mechanical properties of these structures. For this purpose, magnetic beads, coated with NEMHMM (as described in section 2.2.4) of 0.5  $\mu$ M concentration were injected into the chamber. The beads were lifted with a hand held permanent magnet onto the surface of the actin network, where they bound irreversibly, because of the high NEMHMM density on the bead surface. The horizontal magnetic force transducer was used to pull the beads in one direction and observe the deflection amplitude of the bead simultaneously with the fluorescence microscope. To reduce photochemical damage to the actin during the mechanical experiment, the observation of the bead deflection was pursued using a FITC fluorescence filter set, in order to reduce sharply the excitation of the rhodamine dye bound to actin. Since the magnetic beads are fluorescent at all wavelength of visible light, during the force probing only the magnetic bead can be observed. An image of a bead bound to the actin network and its deflection depending on the pulling force is shown in figure 3.20. No viscous response was expected for a highly cross linked network. Thus a linear pulling force function  $F(t)$  ( $F(t) = \dot{F} \cdot t$ ) with a constant and very low loading rate  $\dot{F}$  was chosen to minimize hydrodynamic artifacts. Due to the very high rigidity of the silicon pillars to which the actin network is attached, these act as rigid boundary for the actin network suspended between them. Thus only the local environment of the magnetic bead is mechanically probed. Values for the stiffness of the network varied strongly (30 - 200 nm/pN), depending on the position of the bead relative to the pillars. Also on the scale of the distance between pillars, the network is not very homogeneous, which

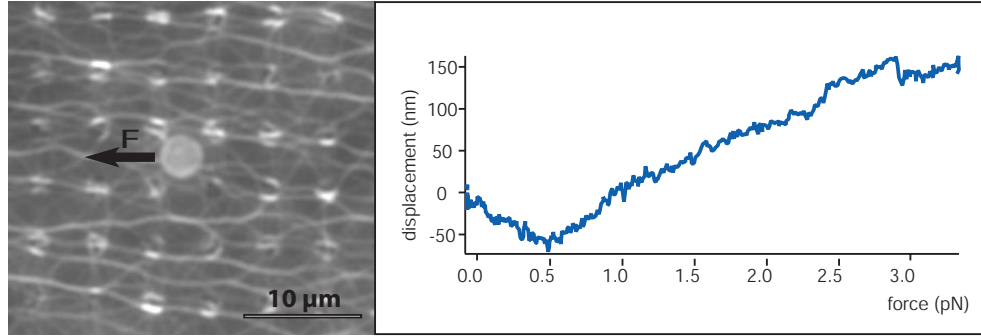


Figure 3.20: Probing the elastic properties of a freely suspended quasi two dimensional actin network on a pillar array substrate.

a) A magnetic bead, which is bound to the actin network is being pulled with the horizontal magnetic tweezers. b) The displacement of the bead in direction of the force is plotted vs the magnitude of the applied force.

again leads to strong variations in the stiffness. Thus the elastic properties of the network can only be determined to an order of magnitude. A very simplistic approach to retrieve a crude value for the Young modulus  $E$  of the actin network is to treat the deformation as a shearing of a thin sheet with thickness  $h$ . When a shearing force  $F$  is acting in  $x$  direction parallel on the surface (in the  $x$ - $y$  plane) of the thin sheet, the only existing stress component is  $\sigma_{xz}$ . For a uniform force on the surface,  $\sigma_{xz}$  is the force  $F$  divided by the surface area  $A$ . The only strain component in this geometry is the shear component  $\epsilon_{xz}$ , which for this simple case is the displacement of the bead  $\Delta x$  divided by the thickness of the sheet  $h$ . Unfortunately the thickness of the actin network is not known exactly, only estimates using a confocal scanning laser microscope indicate a thickness in the order of 100 - 300 nm. Since the displacements  $\Delta x$  were in the same order,  $\epsilon_{xz}$  should be of the order of one. Stress and strain of a homogeneous shear deformation of an elastic body of the geometry described, are linked by the equation [120]

$$\sigma_{xz} = \frac{E}{1 - \nu} \cdot \epsilon_{xz} \quad (3.24)$$

The parameter  $\nu$  in the equation is the Poisson ratio of the material, a measure for the lateral contractibility. Since it can only attain values between -1

[121][122] and  $1/2$ <sup>11</sup>, the exact value of the Poisson ratio does not influence the order of magnitude calculation. Since for many biological materials the compression modulus  $K$ <sup>12</sup> is much larger than the Young modulus  $E$ , the Poisson ratio  $p$  is often assumed to be close to 0.5. The surface area of the bead ( $2.8 \mu\text{m}$  diameter) with which it is bound to the network can roughly be estimated as  $1 \mu\text{m}^2$ . For the applied forces in the range of a few piconewtons and the displacements in the order of a few hundred nanometers, equation 3.24 yields values for the Young modulus  $E$  of around 1 Pa. This value is between one and two orders of magnitude above the value for the elastic modulus  $G'$  for entangled actin networks in the plateau regime, measured with magnetic micro-rheology methods [123]. Obviously it is not comparable with the value of the Young modulus of actin as a material parameter of a protein, which will be discussed in the following section. The elastic modulus of a network is determined by its structure<sup>13</sup>, whereas the Young modulus of an actin filament is determined by the atomic and intermolecular interactions inside the filament. In comparison, the Young moduli of the cell cytoskeleton, retrieved from *in vivo* experiments, were roughly three or four orders of magnitude higher[37][124]. In experiments with endothelial cells, in which it was shown that the actin cortex dominates the mechanical behavior of the cell, a value of 6 kPa was determined for the Young modulus of the actin cortex. This is interesting value to compare with the freely suspended actin network on the pillars array substrate, since it is thought to mimic the actin cortex inside cells. An important difference, which surely is one major reason for the much lower elastic modulus measured for the artificial actin cortex is, that the mesh size in the real cellular cortex is in the order of one to a few hundred nanometers, whereas for the actin network on the pillar array the mesh size is in the order of one micrometer. Another important difference is that the model cortex was cross-linked only by one actin binding protein (filamin), whereas in the cellular cortex many actin binding proteins are present.

---

<sup>11</sup>for conventional materials,  $p$  varies only between 0 and  $1/2$

<sup>12</sup> $K = \frac{3E}{1-2p}$

<sup>13</sup>mesh size, degree of cross-linking, etc.

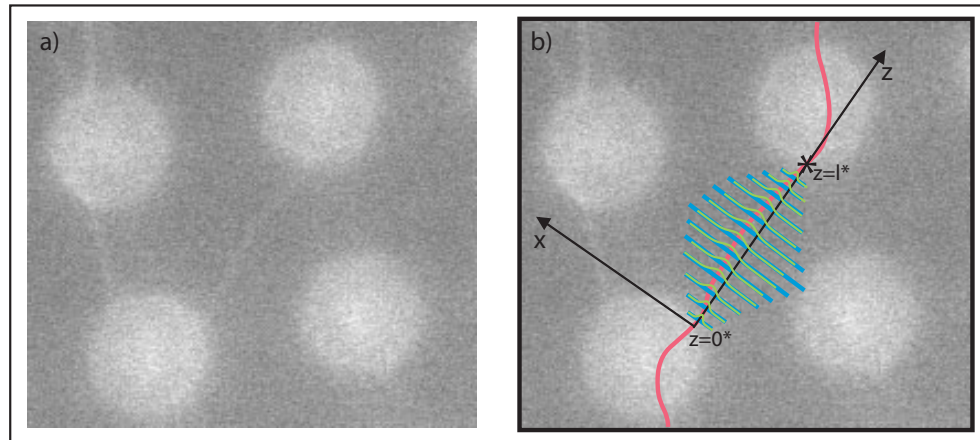


Figure 3.21: Thermally undulating filament on a photo resin pillar substrate **a) Snapshot of the filament on the pillar substrate. b) Coordinate system imposed by the shape tracing algorithm relative to which the Eigenmodes of the filament were analyzed. The contour of the filament was drawn to visualize it.**

### 3.2.3 Elastic properties of actin filaments

Because of the regular spacing of the pillars in the array, this kind of substrates offer well defined boundary conditions for the analysis of mechanical properties of filaments, bundles or probably even more complex actin structures. Pre-polymerized actin filaments can be fixed at both ends to pillar tops, which were functionalized with NEMHMM in the same way as previously described. For the analysis of the contours of fluctuating filaments by micro-fluorescence, the silicon substrates provided a too low signal to noise ratio of the fluorescence. Due to the very strong reflection of the excitation beam, off the silicon substrate, the intensity of the reflected light passing the emission filter was so high that it had a comparable intensity as the fluorescence signal. To overcome this problem, the group of Prof. J. Spatz at the University of Heidelberg developed pillar array substrates made from photo resin, that were similar in geometry. These nearly transparent samples provided a sufficient signal to noise ratio of the fluorescence images to trace the shape of a filament with a high steadiness over many hundred image frames. Figure 3.21 shows an fluorescence image of a undulating filament on photo resin pillars.

The shape of the filament was determined in each image frame for the

part of the filament which extended between the points of attachment on the pillars. The shape of the filament should be represented by a superposition of all thermal Eigenmodes according to equation 1.17.

$$X(z) = \sum_i x_{k_i}(z) \quad (3.25)$$

For the case of the experiment presented here, it can be well assumed that the filaments are bound by several NEMHMM molecules to the pillar, so that the point of attachment of the filament to the pillar will be its last possible contact point. Because of this rigid attachment to the pillar, no angular degree of freedom exists at the points of attachment, such that the first derivative of  $x_{k_i}(z)$  will be fixed at these points. This represents the boundary conditions, that have to be inserted into the general solution of equation 1.17. Accounting for this, Eigenmodes of the bending excitation are of the form

$$x_{k_i}(z) = A_i \cdot ((\sin(k_i l) - \sinh(k_i l)) \cdot (\cos(k_i z) - \cosh(k_i z)) - (\cos(k_i l) - \cosh(k_i l)) \cdot (\sin(k_i z) - \sinh(k_i z))) \quad (3.26)$$

where  $l$  is the length of the filament. In addition, the wavenumbers  $k_i$  of the Eigenmodes must fulfill the condition

$$\cos(k_i l) \cdot \cosh(k_i l) = 1 \quad (3.27)$$

which was solved numerically. A sum of the first four Eigenmodes was used as a fit function for the shape of the undulating filament while the amplitude  $A_i$  of each mode was used as a fit parameter (figure 3.22).

500 consecutive images of a filament were analyzed in this way and a set of four averaged Eigenmodes was retrieved. The bending energy of a semi-flexible polymer is determined by its bending stiffness  $\kappa$  and its contour function  $x(z)$  as

$$E_b = \frac{\kappa}{2} \cdot \int_0^l \left( \frac{\partial^2 x(z)}{\partial z^2} \right)^2 dz \quad (3.28)$$

Thus knowing the amplitude  $x_i$  of a undulation mode, it is possible to relate the thermal energy of that mode to the bending stiffness  $\kappa$ . Since the equipartition theorem states that the thermal energy for each degree of freedom, and such

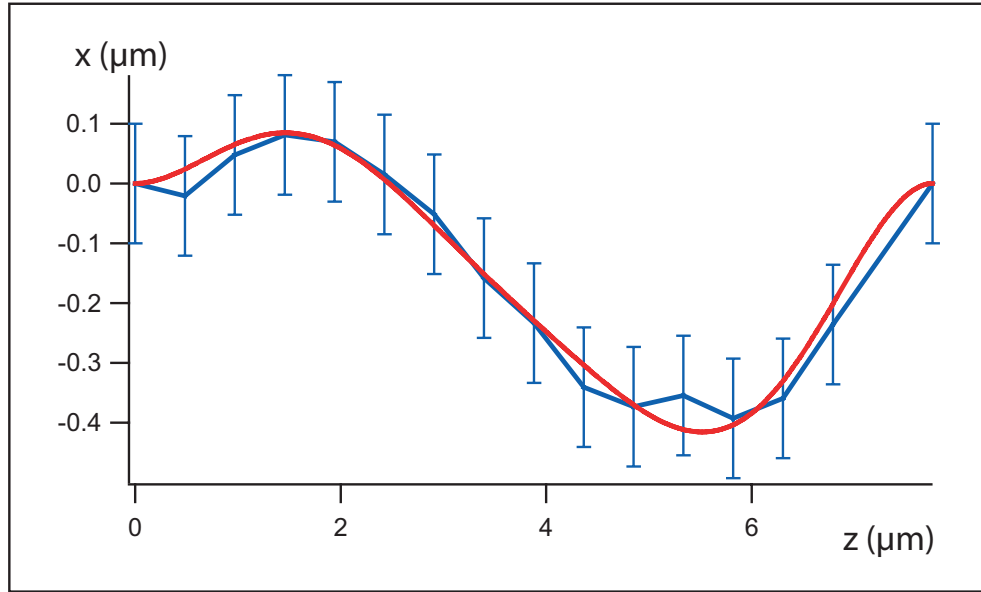


Figure 3.22: Fit of the first four Eigenmodes for the contour of an undulating actin filament

**The contour of the filament (blue, with error bars) , displayed in figure 3.21 is fitted with the function of the first four Eigenmodes determined by equation 3.26.**

each independent Eigenmode of the system, is equal to  $\frac{1}{2} \cdot k_b T$ , this energy value can be considered to be the bending energy of the filament in each mode. The bending stiffness can thus be computed by solving integral 3.28 for the value of  $\kappa$ . The bending stiffness was calculated for each of the first four Eigenmodes of the filament shown in figure 3.21 and the results for the value of  $\kappa$  are shown in figure 3.23.

The bending stiffness apparently decreases with increasing mode number, which must be due to an artifact of the measurement, since  $\kappa$  is only a function of the material and the diameter of the filament. This artifact is attributed to the noise distortion of the images. For Eigenmodes with more nodes and smaller amplitudes, (higher modes) a white noise function superimposed on the shape function of the filament will most likely not cancel when integrated over one node. Thus image noise can statistically increase the apparent amplitude of higher modes, which will manifest itself in a apparently lower bending stiffness. Therefore the most realistic value for the bending stiffness is given by the value of  $6.3 \cdot 10^{-26} J \cdot m$  for the first mode. To evaluate the uncertainty of this result,

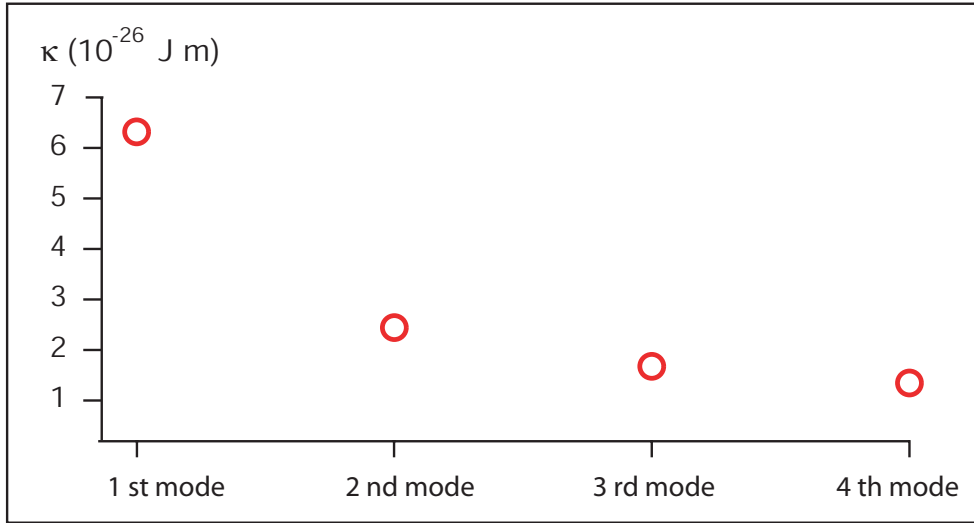


Figure 3.23: Bending stiffness of an actin filament determined from the first four undulation Eigenmodes

**The apparent decrease of the bending stiffness with increasing mode number is an artifact due to the signal to noise ratio of the images. The most reliable value is the one determined from the first mode.**

the signal to noise ratio for the first mode was determined by the ratio of the fit residual to the amplitude in each point of the filament shape. This gave a ratio of 1:2. As the amplitudes are averaged over 500 image frames the standard deviation of a average value decreases as the inverse of the square root of the number of measurements, reducing the initial value of 200% uncertainty to 8.9 % for the entire experiment. From the bending stiffness, the persistence length (see equations 1.4) of a TRITC-labelled actin filament can be calculated to  $15.1 \pm 1.3 \mu m$ . The reason to evaluate only the first 500 images of a much longer set and accept a higher inaccuracy is that the longer the filament is observed, the more photochemical damage may be done to its structure, which may alter the results. The result for the persistence length of an actin filament is in very good agreement with other experiments that arrived at values between 16 and 18  $\mu m$  [48][50]. The knowledge of the bending stiffness of an actin filament allows us to calculate the Young modulus of actin as a material parameter. As mentioned in section 1.3 the Young modulus  $E$  can be calculated from the bending stiffness  $\kappa$  and the moment of inertia  $I$  of the polymer.

$$E = \frac{\kappa}{I} \quad (3.29)$$

The moment of inertia of a cylindrical rod of radius  $R$  is

$$I = \frac{\Pi \cdot R^4}{4} \quad (3.30)$$

Because of the strong influence of the radius  $R$  on the value of the inertia of the filament, it would be too simplistic to take half the apparent diameter of an actin filament ( $R_0 = \frac{9nm}{2}$ ) as a value for  $R$  since the actin filament has a double helical structure. Thus in one dimension, the projection of the filament into a plane has to be analyzed and the effective radius of the filament varies between  $R_0$  and  $\frac{R_0}{2}$ . Along the filament, the radius, which has to be taken for the calculation of the inertia is given by  $R = \frac{R_0}{2} \cdot (1 + \sin(k \cdot x))$ . The parameter  $k$  is related to the actin helix pseudo repeat length of 36 nm by  $k = \frac{\pi}{36nm}$ . The inertia can be calculated by integrating over one pseudo repeat of the filament.

$$I = \frac{\pi}{4} \cdot \frac{1}{36nm} \int_0^{36nm} \left( \frac{R_0}{2} \cdot (1 + \sin(k \cdot x)) \right)^4 \cdot dx = 2.1 \cdot 10^{-34} m^4 \quad (3.31)$$

This leads to a Young modulus of  $3.1 \cdot 10^8 N/m^2$  for actin as a material. This is remarkably lower than the value of  $2.4 \cdot 10^9 N/m^2$  determined from stretching experiments of actin filaments [125] and  $1.8 \cdot 10^9 N/m^2$  retrieved through torsional micromanipulation [126]. This difference in the values stems from the fact that the group of Yanagida used a diameter of 5.6 nm to calculate the Young modulus. With this value, the Young modulus retrieved in the context of this work becomes  $2 \cdot 10^9 N/m^2$  and is in excellent agreement with the value of the Yanagida group. The here determined Young modulus of actin of  $3.1 \cdot 10^8 N/m^2$  is basically the same as for other bio-materials such as DNA ( $3 \cdot 10^8 N/m^2$  [127][128]) or organic polymers such as amorphous teflon [129] or plexiglas [127] and remarkably only a factor of 50 below the value of soft metals, such as lead [130].

A second approach of calculating the persistence length from a movie of a fluctuating filament was to superimpose all images of the movie and analyze the resulting image. The shape of the filament in this time averaged image represents an integration over time of all its Eigenmode undulations with functions of equation 3.26. Since the time dependence of the Eigenmodes is given by a cosine term [120], the average value over a time, which is long compared

to the undulation period of the filament, vanishes and therefore contains no accessible information. However, the standard deviation of the integral does not vanish, but gives a constant factor  $\frac{\sqrt{2}}{2}$  times the amplitude function of equation 3.26. Thus by comparing the standard deviation of the intensity profiles, perpendicular to the line connecting the attachment points of the filament, with the standard deviations of the Eigenmode functions, the bending stiffness  $\kappa$  can be retrieved. The simplest practical way to do so is to take the perpendicular line intensity profile exactly in the middle between the attachment points. At this point the first mode has its full amplitude function and the second mode has a node and therefore does not contribute to the standard deviation of the intensity. In a first order approximation, all higher modes, which have amplitudes more than one order of magnitude smaller than the first, can be neglected for their contributions. Thus the line intensity profile taken in the middle between the attachment points can be fitted with a gaussian function and the standard deviation  $\sigma_s$  of the gaussian be used to calculate  $\kappa$ . A correction term for  $\sigma_s$  has to be applied, since the intensity profile of the filament in one image frame has already a finite width  $\sigma_f$ . Since  $\sigma_f$  is included in the fit parameter value  $\sigma_s$ , but does not contribute to the fluctuation amplitude, it has to be subtracted from  $\sigma_s$  to determine the real standard deviation  $\sigma$  of the first Eigenmode undulation. Figure 3.24 shows the image, the line profile and its fit in the middle of the filament of the 500 superimposed individual images (a) and b)) and the line profile of the filament in one image frame (c)), of the filament, which was previously used to calculate its persistence length (figure 3.21). This method for the calculation of the persistence length of a fluctuating filament yielded a value of  $7.16 \cdot 10^{-26} J \cdot m$  for the bending stiffness  $\kappa$  and  $17.2 \mu m$  for the persistence length. This is in good agreement with the values retrieved from the procedure in which every image frame is fitted with the Eigenmode functions. The slightly higher value can be attributed to the fact, that even in one image frame, the intensity of the filament image is integrated over a small integration time of the camera. Thus the value for  $\sigma_f$  is slightly overestimated, leading to a slightly underestimated value for  $\sigma$  and thus to a slightly higher value for the persistence length. Nevertheless, one advantage of the method is that the same values are retrieved for a superposition of only

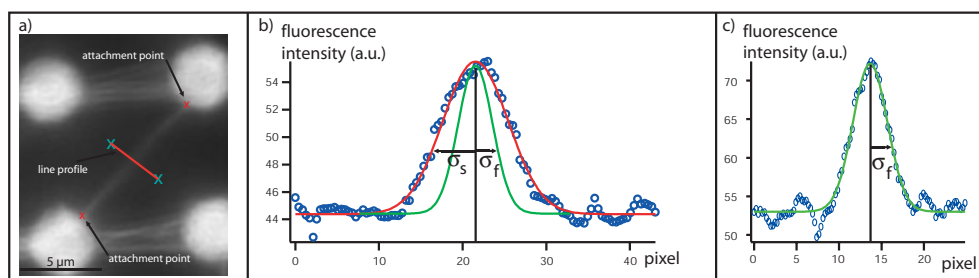


Figure 3.24: Principle of the superposition mechanism to determine the bending rigidity of an actin filament

**a) A superposition of the first 500 images of the undulating filament shown in figure 3.21. The two attachment points on the pillars and the line profile perpendicular in the middle of the undulating filament are indicated. b) Intensity plot of the line profile indicated in a) with its gaussian fit curve (red line). The green line is the line intensity profile fit of the filament in one image, which is shown in c). The width  $\sigma_s$  of the superposition line profile fit and  $\sigma_f$  of the line profile fit of one image are indicated. Fit curves and their parameters are scaled to relative values.**

100 images, so that already with a smaller number of image frames of a movie the persistence length can be calculated with a high accuracy. The largest advantage is that since the contour does not have to be analyzed exactly in each movie frame, but as an averaged superposition image, the distortion by camera noise and background light is strongly reduced and much smaller undulation amplitudes can be detected.

### 3.2.4 Elastic properties of actin - filamin bundles

In a first approach, the contour fitting method was used to determine the bending stiffness of actin-filamin bundles. Filamin bundles, immobilized by binding to NEMHMM on the tops of the pillar substrate are shown in figure 3.25a. The bundles were formed after mixing a 20 nM solution of labelled actin filaments with a 5 nM solution of filamin in A buffer for 10 minutes. Thick bundles as shown in figure 3.25a did not show a large enough thermal undulation amplitude to resolve their thermal movement. Therefore, mixing ratios and concentrations were adjusted in order to retrieve bundles with a small number of filaments in them. A mixture of 3nM actin filaments with 1.5 nM filamin produced bundles that had thermal undulations that could be

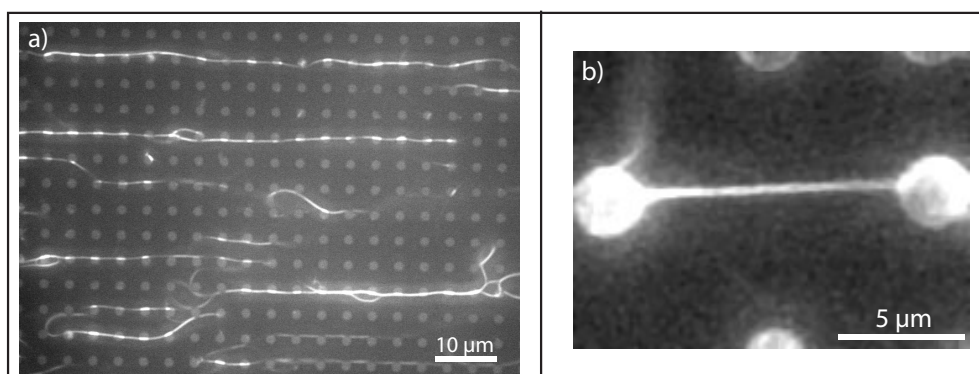


Figure 3.25: Actin - filamin bundles immobilized on pillar array substrates  
a) **Thick bundles immobilized on a silicon pillar substrate.** b) **A bundle of only a few actin filaments bound to two pillars of a PDMS substrate.**

traced when suspended between pillars that were separated by more than  $10 \mu\text{m}$ . Figure 3.25b shows a fluctuating actin-filamin bundle suspended between two pillars of a PDMS substrate. To acquire information about the number of filaments in the bundle, the fluorescence intensity of the bundles was measured at several different sites on it, by taking a line profile across the intensity landscape of the bundle image, fitting it with a gaussian function and taking the peak height as the intensity. The same was done with a number of individual filaments, which were injected into the same chamber after rinsing the bundles out. The linearity of the optical system, regarding measured intensities, was ensured by calibration for low intensities, using a filter set that transmits only 25 and 50 % of the light intensity. Using a fluorescence spectrometer, the emission intensity of an labelled actin filament solution was measured before and after the injection of filamin, with the exact concentrations as used in the bundle experiment. No significant change in fluorescence could be observed, so that a possible change of fluorescence intensity of filaments in bundles can be excluded. Thus by dividing the average intensity for a bundle by the average intensity retrieved from analysis of many individual filaments, the number of filaments in a bundle can be obtained. It should be noted that this relation has only been tested for bundles that contain less than 10 filaments. The bundle shown in figure 3.25b had a 4.93 times higher fluorescence intensity than individual filaments. Therefore it can be presumed that it was formed

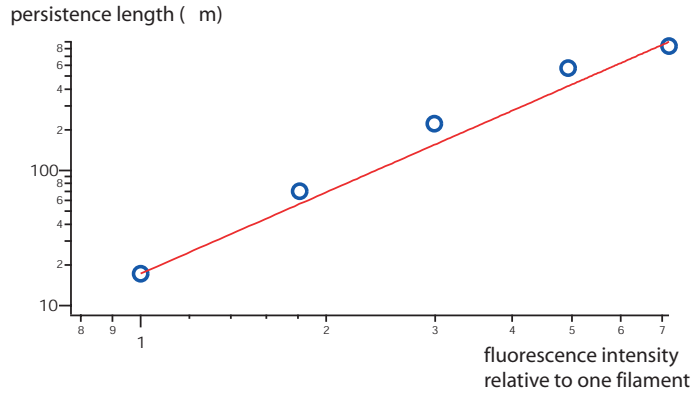


Figure 3.26: persistence length of actin-filamin bundles  
**Dependence of the measured persistence length  $l_p$  of actin-filamin bundles on the measured fluorescence intensity of the bundle relative to individual filaments. The number of filaments  $n$  in the bundle is presumably composed of has been shown to be a linear function of its fluorescence intensity.**

by bundling 5 actin filaments together. The bending stiffness  $\kappa$  calculated for the bundle by the contour fitting procedure of many individual images was  $2 \cdot 10^{-24} J \cdot m$ , which is equivalent to a persistence length of  $490 \mu m$ . This is 32.5 times the value of the persistence length retrieved with the same method for an individual filament.

Since the amplitudes of the bundle fluctuation showed to be substantially smaller than for individual filaments, the superposition method was also used to calculate the persistence length of fluctuating bundles and proved to be less error prone. For the bundle shown in figure `refbundleonpillb` this method yielded a value of  $2.38 \cdot 10^{-24} J \cdot m$  for the bending stiffness  $\kappa$  and  $571 \mu m$  for the persistence length. These values are 33.2 times the value retrieved for an individual filament with the same method. The fact that the ratio of bundle to filament persistence length retrieved with the two different methods used is practically the same, shows that values slightly differ for the two methods, but the comparability of results obtained with the same method is very good. With this method, a number of actin - filamin bundles was analyzed for their persistence length and the number of actin filaments they were composed of (results shown in figure 3.26). The dependence of the persistence length  $l_p$  on the number of filaments in a bundle  $n$  was fitted with a power law function of the type  $l_p(n) = l_{p1} \cdot n^p$ . The amplitude  $l_{p1}$  of the fit function was held constant

at  $17.2 \mu m$ , to relate the values to the persistence length found for an individual filament and only the parameter  $p$  for the power law dependence was adjusted. Least square fitting yielded a value of  $2.05 \pm 0.04$  for  $p$ . This quadratic dependence can be related to the mechanical behavior of rigid rods. The bending stiffness  $\kappa$  of a homogeneous rigid rod increases as the fourth power of its diameter  $d$  ( $\kappa \propto d^4$ ). When  $n$  actin filaments are packed into a bundle structure, the diameter  $d$  of the bundle, which is formed, will increase approximately as a square root of the number of filaments in the bundle ( $d \propto \sqrt{n}$ ). Thus if an actin filament bundle behaves mechanically like a homogeneous rigid rod, its bending stiffness and persistence length are expected to scale as a quadratic function of the number of filaments in the bundle ( $\kappa \propto n^2$ ), which is exactly the result of the experiment. This result pinpoints that actin bundles, which are linked by a very large number of filamin molecules mechanically behave like homogeneous solid rods with the same Young modulus as actin filaments.

The observed quadratic dependence shows the importance of stress fiber formation by cells in response to a mechanical stress. The actin cross-linking protein filamin, which was used to form the actin bundles, was initially identified in stress fibers inside cells [82]. When an external stress is imposed on eucaryotic cells, such as e.g. fibroblasts, the Rho GTPase family proteins, which also interact with filamin [83], are activated and induce the formation of thick actin bundle structures, so called stress fibers, in response [84]. If these stress fibers mechanically behave like solid rods, cells could dramatically stiffen their structure, by bundling actin filaments of its cortex. Thus the result that the bending modulus of actin - filamin bundles increases quadratically with the number of filaments in the bundle shows that cells can enormously stiffen their cytoskeleton simply by rearranging its structure into bundles. In fact magnetic bead micro-rheometry studies of endothelial cells showed a drastic stiffening of the cells upon stress fiber formation in response to an agent which likely activates the Ras and Cdc42<sup>14</sup> pathway [1].

Concluding, three dimensionally structured substrates, like the pillars ar-

---

<sup>14</sup>two Rho GTPase family proteins

rays, offer new possibilities to study the self-assembly of biological materials and the mechanical properties of these self-assembled structures.

### 3.3 Structure and mechanics of actin cortex vesicles

A even more realistic biomimetic system of the actin cortex of eucaryotic cells are self-assembled actin networks inside giant phospholipid vesicles. Together with the lipid bilayer of the vesicle they mimic the composite structure of the cell membrane and its associated actin cytoskeleton. By attaching magnetic beads to these actin cortex vesicles and applying a force pulse to the beads, the viscoelastic properties of the vesicles were determined.

The method of the formation of actin cortices inside vesicles was developed by Laurent Limozin<sup>15</sup> and is described in great detail in previous publications [131][132]. Giant uni-lamellar phospholipid vesicle were prepared as described in section 2.2.3. The solution used for electro-swelling was 3  $\mu\text{M}$  G-actin with equimolar TRITC-Phalloidin in G\* buffer. The molar lipid composition of the vesicles was: 78% DMPC; 17% cholesterol; 3% DPPE-PEG-amine; 2% A23187 ionophore. The G-actin containing vesicles were left sedimenting in a flow chamber for 2 hours to allow a sufficiently large number to adhere to the BSA coated glass slide at the bottom of the chamber. To remove the G-actin in solution outside the vesicle, the chamber was slowly rinsed ten times with G\* buffer of 5 times the chamber volume. To initiate the polymerization of the actin inside the vesicle, a 2 mM solution of  $\text{MgCl}_2$  in G\* buffer was injected into the chamber. The magnesium can pass the vesicle membrane through the A23187 ionophore and thus start the polymerization of actin inside the vesicle. The beads used to attach to the outer leaflet of the vesicle membrane were Tosyl-activated M-280 dynabeads, that exhibit a net negative charge on their surface. Therefore they can be coupled electrostatically to the positively charged PEG-amine lipids of the membrane. A 0.3 pM solution of beads in G\* buffer was injected into the chamber that contained the vesicles with the completely polymerized actin cortex. The beads were manipulated from the outside of the chamber with a hand held permanent magnet and placed onto vesicles that exhibited a uniform fluorescence of their actin cortex. The beads bound to the outer leaflet of the membrane, were immobile, showing only

---

<sup>15</sup>limozin@marseille.inserm.fr

small fluctuations in their position, most likely due to thermal motion of the membrane. In comparison, magnetic beads, which were placed onto vesicles without cortex, moved, due to gravity, along the vesicle surface down onto the substrate. The fact that the beads on the actin cortex vesicles stayed immobile on the spot of the vesicle where they were placed, indicates the existence of a coupling of the bead to the cortex, through the membrane.

### 3.3.1 Structure of the actin cortex

Since the vesicle membrane consisted of 3% positively charged lipids (DPPE-PEG-amine) and actin is highly negatively charged, nearly all actin bound to the surface of the lipid membrane. This assumption is justified by the observation, that in the vesicles containing G-actin, the fluorescence is homogeneously distributed over the volume of the vesicle, whereas after the polymerization, the entire fluorescence intensity was concentrated at the vesicle membrane. Vertical slices of a vesicle with polymerized actin inside and a magnetic bead attached to it are seen in figure 3.27. Since mechanical properties of complex polymer networks are a function of the structure<sup>16</sup> and the material properties of the polymer, the investigation of the structure of the artificial actin cortex bound to the vesicle membrane is of primary importance for the understanding of the mechanical properties. This structure could be observed with fluorescence microscopy, in optimal quality at the adhesion surface of the vesicle on the substrate. Only at the adhesion surface, a large area of the vesicle surface can be in the focal plane of the microscope. Figure 3.28 shows an image of the structure of polymerized actin filaments at the adhesion surface inside a vesicle. Interestingly, the actin filaments of the artificial cortex inside the vesicle do not form just a random network, in which filaments overlap and cross each other, but an ordered arrangement of parallel actin filaments, which form bundle like structures, that seem to avoid contact with each other in hairpins. On the length scale of the bead radius ( $1.4 \mu m$ ) the structure is homogeneous, but very anisotropic, which was tested with the order analysis algorithm described in section 2.3.2. The same kind of actin assembly was found on the

---

<sup>16</sup>e.g. mesh size, filament arrangement

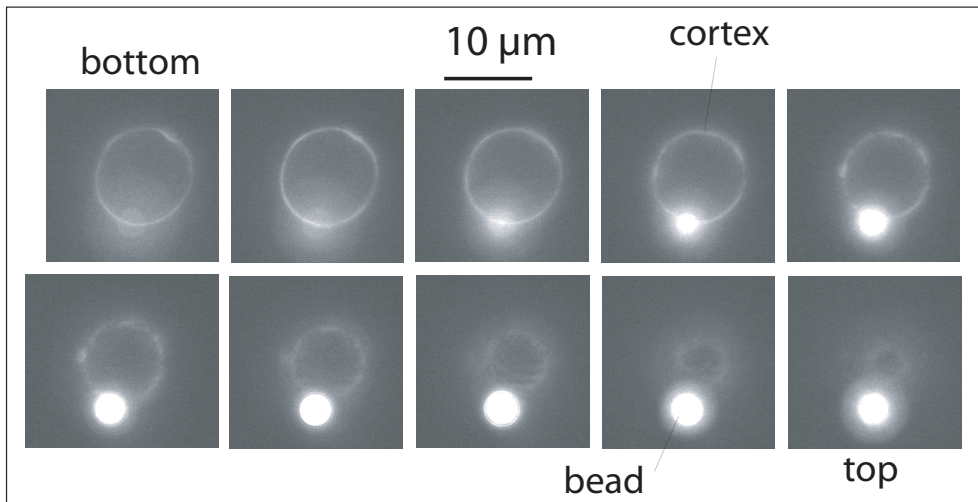


Figure 3.27: Fluorescence micrographs of an actin cortex vesicle with a magnetic bead attached

**The images are slices of the actin cortex vesicle parallel to the adhesion surface on the substrate. The vertical spacing between two images is  $1 \mu\text{m}$ . The fluorescently labelled actin is entirely bound to the membrane, forming a thin cortex structure.**

upper side of the vesicle, but the curvature of the membrane does not allow to image it with an equivalent precision. An explanation for the parallel arrangement of the actin filaments on the membrane is, that the polymerization happens along the membrane surface in a two dimensionally confined space. Since the actin is electrostatically attracted to the membrane, monomers can already bind to the membrane before polymerization. The polymerization on the membrane should start much faster than in the bulk of the vesicle, since three particle encounters, which are needed to form trimers as stable nuclei, are much more likely in two dimensions. When elongating actin filaments confined to a surface meet, they would have to align parallel to continue their growth, since a crossing is impeded in two dimensions. When two bundles structures of many parallel filaments meet during polymerization, they can not always align, since the surface of the membrane is finite. Thus they will bend and avoid each other to enable further filament growth. The assumption that actin forms mono-layers when binding to a positively charged membrane is further supported by neutron reflectivity studies [133] where a thickness of 6.9 - 8.4 nm was found for the actin layer. For the global shape of the vesicle, confocal

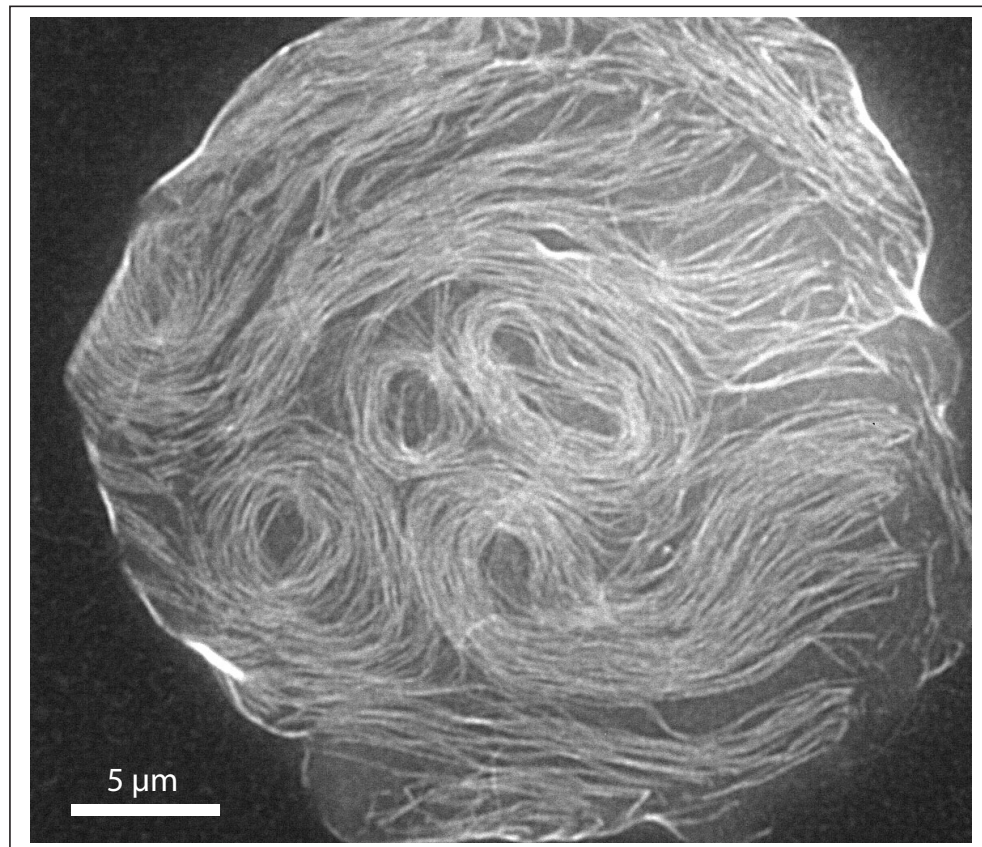


Figure 3.28: Structure of the actin cortex inside a vesicle  
Structure of the actin cortex inside a vesicle at the adhesion surface of the vesicle on the substrate. Visibly, thick parallel bundle-like filament assemblies are formed. Those assemblies end in hair pin like structures, where the filaments are bent to avoid each other. While the filament assembly is roughly homogeneous, visibly a high degree of anisotropy exists.

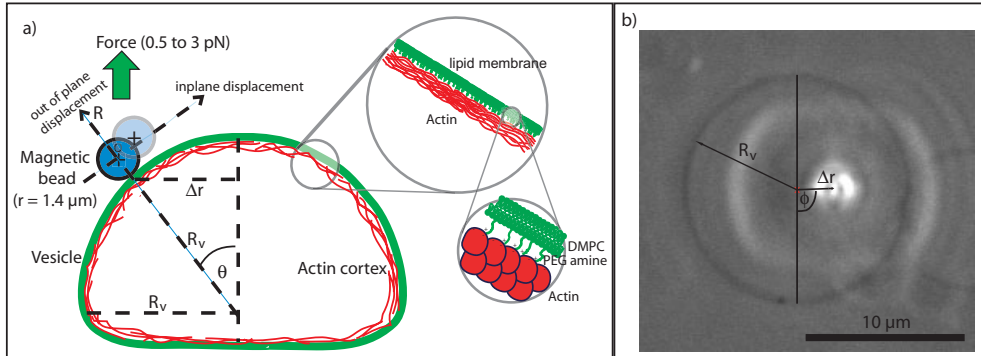


Figure 3.29: Actin cortex vesicle with a magnetic bead attached  
**a) Schematic view of the geometry of an actin cortex vesicle. b) Phase contrast image of a vesicle used to determine the center and the radius of the vesicle.**

scanning micrographs of adhered actin cortex vesicles showed that the global shape can be well described with the geometry of a spherical cap with a cutoff plane at the glass surface. This is also the expected shape for strongly adhered vesicles on a surface [134]

Taking into account the spherical cap shape of the adhered vesicle, the three dimensional position of the bead on the vesicle surface can be retrieved from the information of the center and radius  $R_v$  of the vesicle and the distance  $\Delta r$  of the bead from the center of the vesicle (see figure 3.29a). These parameters were determined using a phase contrast image of the vesicle with the bead attached (figure 3.29b) and have an accuracy of the optical resolution of the microscope, which is approximately 200 nm. The information about the position of the bead on the vesicle allows us to separate the force on, as well as the displacement of the bead, into an in-plane and an out-of-plane component relative to the vesicle surface, in the plane which is given by the vesicle's rotational symmetry axis and the bead position in the absence of force. The angular deviations from this plane ( $\Delta\phi$  in figure 3.29b), during the application of force where in nearly all cases under 0.1 rad. The in-plane components are defined as parallel to the vesicle surface directed to the top. The out-of-plane components are defined as perpendicular to the vesicle surface directed outwards (see figure 3.29a). The force components in plane  $F_i$  and out of plane

$F_o$  relative to the vesicle surface are

$$F_i = F \cdot \frac{\Delta r}{R} \quad (3.32)$$

$$F_o = F \cdot \frac{\sqrt{R^2 - (\Delta r)^2}}{R} \quad (3.33)$$

For the components of the displacement, the bead tracking data, which is given in cartesian coordinates  $(x,y,z)$  has to be transformed into spherical coordinates  $(R, \phi, \theta)$  of a coordinate system with its origin in the center of the vesicle (figure 3.29). The in-plane displacement  $x_i$  is given by  $R_v \cdot \Delta\theta$  and the out-of-plane displacement  $x_o$  simply by  $\Delta R$ .

An important parameter for the characterization of each individual vesicle is the density of the actin cortex attached to the inside of the membrane. Since the electro-swelling of the vesicles was done in solution with a constant concentration  $c_{ac}$  of  $3\mu M$  G-actin, the initial bulk concentration of actin inside the vesicles should be in about the same, although previous studies [131] showed that some variations might exist. Since the total amount of actin inside the vesicle scales with the volume of the vesicle, whereas the surface density scales inversely with the surface area, the total surface density of actin filaments  $\rho_s$  on the membrane will be a linear function of the vesicle radius  $R_v$ . Assuming a parallel assembly of the actin filaments on the membrane the average distance  $d$  between filaments can be calculated knowing that a section of 72 nm length of an actin filament contains 26 monomer (see figure 3.30a).

$$\rho_s = \frac{26}{72nm \cdot d} = \frac{\frac{4}{3}\pi R_v^3 \cdot c_{ac}}{4\pi R_v^2} \quad (3.34)$$

Solving the equation for a vesicle of 10  $\mu m$  radius, which is a typical value, yields an average distance of 60 nm between neighboring parallel filaments. Since this number is below the optical resolution of the microscope, what seems to be individual filaments in figure 3.28 should actually be small bundles of actin filaments. This assumption is confirmed by measurements of actin filament adsorption on charged mono-layers, done as a test experiment with a micro film balance device on the same microscope. In figure 3.30b the structure formed by pre-polymerized actin filaments injected into the subphase of

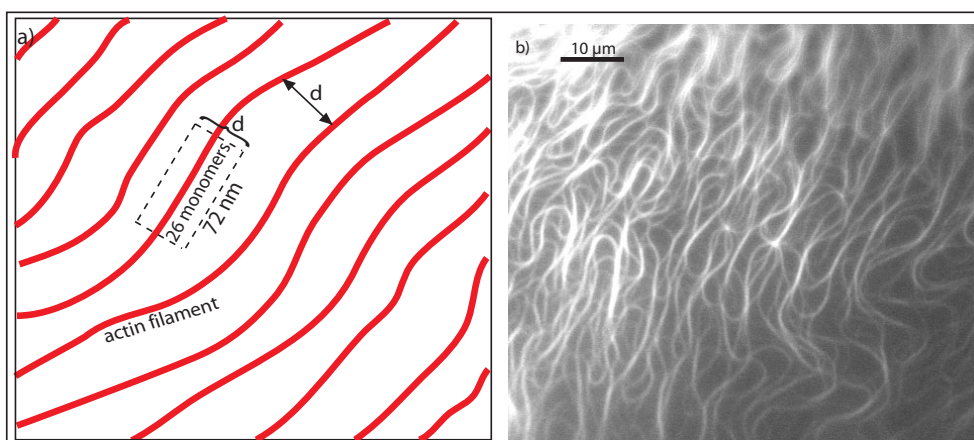


Figure 3.30: Schematics of a parallel filament arrangement and actin bundles on micro film balance

a) **Schematic representation of the average distance  $d$  between parallel filaments** b) **Actin filament structures adsorbed on a phospholipid mono-layer of equal lipid composition on a micro film balance. A bundle formation is clearly visible.**

a micro filmbalance with a lipid monolayer of equivalent composition as in the vesicles can be seen. Filaments are not parallelly assembled since they were not polymerized in situ, but a clear bundling can be seen. This can be due to the attraction between the negatively charged filaments and the positively charged lipids. This may produce an effect similar to a counter-ionic condensation [135]. Positively charged lipids can diffuse to the actin filaments and induce a net positive charge cloud around them. This cloud of positive charges in effect could attract other negatively charged filaments. A similar bundling effect has been observed in bulk solutions for divalent ions ( $Mg^{2+}$ ) on actin filaments [136]. The relation between the radius of vesicles and their actin density at the surface was verified analyzing the fluorescence intensity of the cortex. Similar as for actin bundles, the fluorescence intensity profile at the many spots at the perimeter of the vesicle was fitted with gaussian functions and product of average height and width of the gaussians was taken as a measure for the fluorescence intensity of the cortex. As a relative intensity measure for comparison and to normalize the cortex intensity, the fluorescence intensity of the magnetic bead was also measured and the cortex intensity divided by it. The resulting normalized intensity is a relative measure for the actin density of

the cortex. The observation that the normalized intensity proved to be proportional to the radius of the vesicle supports the assumption that the cortex density scales linear with the radius. The polymorphism of actin structures, that included the actin binding proteins filamin and  $\alpha$ -actinin, confined in phospholipid vesicles was discussed in a previous publication [131].

### 3.3.2 Data acquisition

All measurements were made on a Carl Zeiss Axiovert 200 microscope with a Carl Zeiss Plan-Neofluoar 100, N.A. 1.3 objective. Images were recorded with a Hamamatsu ORCA-ER CCD camera using a the acquisition software OPEN BOX developed by Jörg Schilling. The vertical magnetic force transducer was mounted on the microscope at a distance between magnet core and sample that forces in the range of 75 fN to 5 pN could be exerted in the regime where the force is a linear function of the coil current. The magnetic force as a function of the coil current was calibrated in a separate experiment. The displacements observed were in the order of  $1\mu m$ , which is about an order of magnitude smaller than the vesicle diameter, thus perturbations can be assumed to be small. To minimize chromatic effects in the images and and to prevent photochemical damage to the actin filaments when working in bright field and phase contrast mode, an optical band pass filter of 1.5 nm FWHM around 633 nm (Omega Optical) was inserted into the transmission light path before the sample. To exclude the possibility of a movement of the chamber superimposing with the movement of the bead on the vesicle, always the response of a bead, adhered somewhere on the glass surface close to the vesicle, to a strong force pulse, was monitored before starting measurements on the vesicle. Also, always a vertical stack of fluorescence images of the actin cortex vesicle, shifting the focal plane  $1\mu m$  up between each image, was taken before starting the force measurements. To measure the creep compliance of the vesicle, periodical step force pulses of usually 30 s period were exerted onto the bead attached to the vesicle. The position of the bead in three dimensions was constantly tracked using the three dimensional particle tracking algorithm described in section 2.3.2 in the bright field mode of the microscope. After the application of 20 force pulses, the force was switched off to let the vesi-

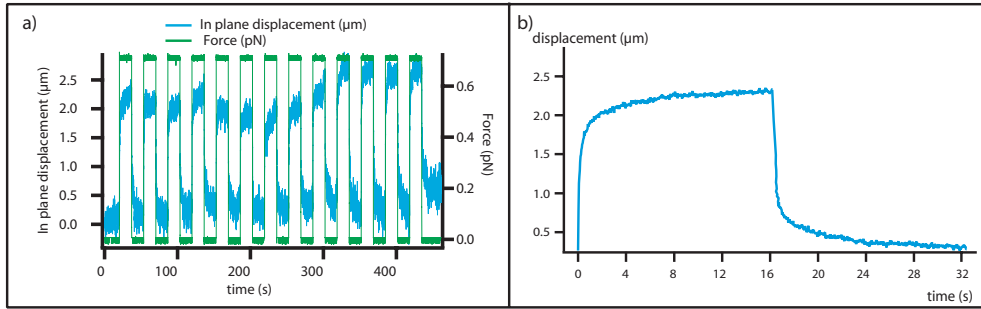


Figure 3.31: In plane force and displacement of a magnetic bead on the surface of an actin cortex vesicle.

**a) Over a period of 430 s, 13 force pulses of 0.75 pN and the related displacement of the magnetic bead along the surface of the vesicle are displayed. Visibly the bead displacement is slightly different for each force pulse. b) Displacement of the magnetic bead during one interval period of the periodic force application averaged from the 13 displacements shown on the left.**

cle relax completely into its equilibrium shape. Following the force amplitude was changed and the procedure repeated. The starting force amplitude was usually 0.5 pN and was increased in steps of 0.25 to 1 pN up to forces of 5 pN. The measured displacements of the bead and the applied forces were separated into in-plane and out-of-plane components, as given by equations 3.32 and 3.33, and averaged over all periods of each measurement. The averaging led to a drastically smoother curve, which could be analyzed more accurately than the individual displacements.

An example for the response function of the bead is shown in figure 3.31. The response function was divided into an ascending part with a non zero force present and a descending part after the end of each step force pulse. Since the vesicle is in equilibrium before and at the end of each force pulse, ascending and descending parts of the response function are mirror images of each other and can both be used to calculate the creep compliance.

### 3.3.3 Analysis of the creep compliance

The creep compliance  $J(t)$  of the vesicle can be calculated using equation 1.27 by dividing the bead displacement by the applied force for each component. For most vesicles, creep compliances were independent of the applied force.

### 3.3. STRUCTURE AND MECHANICS OF ACTIN CORTEX VESICLES<sup>121</sup>

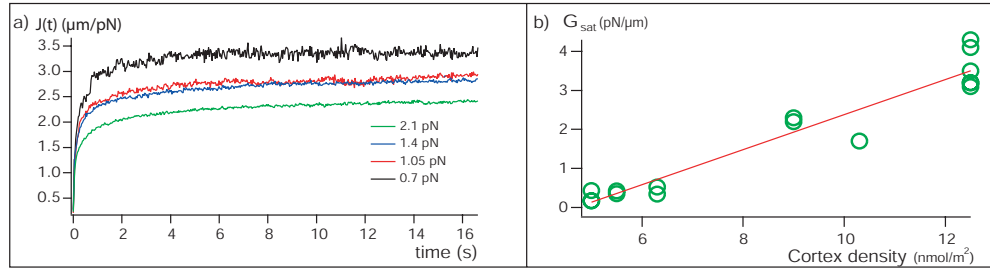


Figure 3.32: Creep compliance and zero frequency shear modulus of actin cortex vesicles

**a) Creep compliance of one vesicle determined from four different probing forces. The non linearity for the different forces can be explained with the finite surface area of the vesicle. b) Zero frequency shear modulus from many vesicles as function of the actin surface density (circles). The linear fit (line) intersects the bottom axis at a value of 4.2  $\text{nmol}/\text{m}^2$**

Nevertheless, some vesicles showed non-linear behavior between the applied force and the response function at low or high forces (see figure 3.32).

Contrary to usual non linearities, in the case of actin vesicles the higher creep compliance is observed for smaller forces. Therefore the non linearity observed will not stem from a non linear elastic behavior of the actin - membrane complex as a material, but most likely stem from the geometry of the vesicle. For higher forces the total displacement, from which the creep compliance is calculated, is larger and therefore finite size effects of the vesicle surface start playing a role for higher forces. These finite size effect can introduce an additional stalling component and therefore lead to an apparently smaller creep compliance of the material. To know if the deformations of the vesicle were of the local or the global shape, always the strongest force pulse series for which the creep compliance was measured, was repeated observing the vesicle equator in phase contrast. Since no change in the equator diameter could be observed, it can be very well assumed that the local viscoelastic properties of the actin-membrane composite sheet close to the bead position are probed. All  $J(t)$  curves show an initial rapid increase followed usually by a saturation at a level  $J_{\text{sat}}$  for long time scales. In some cases a slow creeping behavior was observed. The saturation stems most likely from the fact that a network in the finite space of the vesicle surface is probed. The inverse value  $G_{\text{sat}} = 1/J_{\text{sat}}$  is equivalent to the zero-frequency shear modulus of the system. The obtained

values of  $G_{sat}$  with their dependence on the density of the actin cortex are shown in figure 3.32b. The values seem to show a linear dependence on the density of the actin cortex, as indicated by the fit line. Interestingly, the fit curve does not pass the origin of the coordinate system, but intersects the axis of the shear modulus at a value of  $4.2 \text{ nmol}/m^2$ . This would imply that a critical onset density of the actin cortex exists below which no zero frequency shear modulus exists. This could be since the actin filaments have to interact with each other to develop an elastic shear modulus in response to an external force. If the average distance between two filaments is above a certain value ( $143 \text{ nm}$  for  $4.2 \text{ nmol}/m^2$ ), a shear interaction could possibly be impeded and the zero frequency shear modulus vanish.

The simplest way of interpreting the entire creep compliance curves obtained, is in terms of linear viscoelastic models, introduced in section 1.4.1. Since it is not straight forward to attribute parameters, and thus mechanical elements as representation, directly to each component of the actin-membrane sheet and its coupling, the most general model of a linear combination of Voigt elements was used to model the data [35]. The number of Voigt elements in series used, was determined by comparing fit quality, given by the average square residual  $\chi^2$ , for the fit of the creep compliance, increasing the number of Voigt elements.

Since most of the data points are close to the saturation level of the creep compliance for long times ( $> 3s$ ), which will be recognized by any number of Voigt elements, the  $\chi^2$  value was taken for the short and intermediate time scales ( $< 3s$ ). Fitting with a creep compliance function representing one Voigt element, yielded fit results clearly off the data set and high  $\chi^2$  values (figure 3.33). For a two Voigt element model,  $\chi^2$  decreased remarkably and the fit curves coincided well with the data sets. Adding one more Voigt element to the viscoelastic model did not improve the fit quality decisively, such that the addition of two extra fit parameters did not seem justified. Thus a two Voigt element in series model (see figure 3.34) was used to construct a fit function for the creep compliance data.

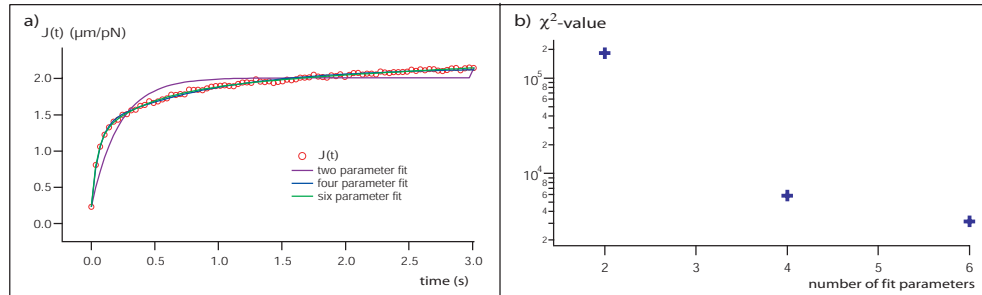


Figure 3.33: Fit functions of the creep compliance of an actin vesicle with different numbers of parameters

a) The creep compliance  $J(t)$  is fitted with three model functions with one (purple), two (blue) and three (green) Voigt elements (two, four and six parameters) respectively. Each Voigt elements has an elastic and a viscous parameter. b) The fit quality, expressed in  $\chi^2$  values of the three different fit functions.

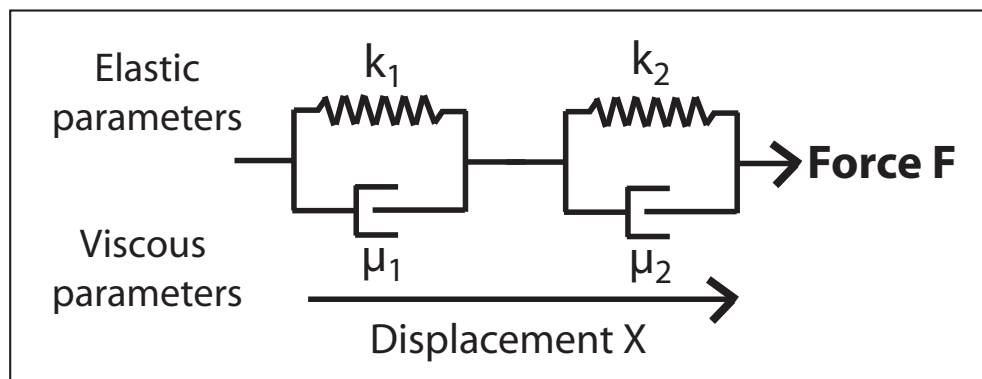


Figure 3.34: Mechanical representation model used to analyze the creep compliance of actin cortex vesicles

The function representing the model shown in figure 3.34 is

$$J(t) = \frac{1}{k_1} \cdot (1 - e^{-\frac{t \cdot k_1}{\mu_1}}) + \frac{1}{k_2} \cdot (1 - e^{-\frac{t \cdot k_2}{\mu_2}}) = A_1 \cdot (1 - e^{-\frac{t}{\tau_1}}) + A_2 \cdot (1 - e^{-\frac{t}{\tau_2}}) \quad (3.35)$$

The values  $\tau_i = \frac{k_i}{\mu_i}; i = 1, 2$  are characteristic response times of the system probed. Their values can only be retrieved with a fit procedure if they are well separated in magnitude. For the experiments presented here the two values differed usually by one order of magnitude, which is enough to identify them separately. This separation of time scales of the mechanical response of actin cortex vesicles shows that two independent mechanisms contribute to the response. Since the composite sheet probed is made up from two adjunct shells, the membrane and the actin shell, it seems straight forward to attribute one response time to each of the components. The four parameters  $k_i$  and  $\mu_i$  were retrieved separately for each force amplitude of each vesicle. For the force range where they showed to be independent of the applied force, they were averaged and taken as the values for the linear creep response of the vesicle probed. Figure 3.35 shows the dependence of the four fit parameters for the in-plane component on the density of the actin cortex inside the vesicles.

All four parameters show a roughly linear increase with the density of the actin cortex. This result can be explained if the stress in the actin cortex is distributed between all filaments close to the magnetic bead. Thus the force acting on one individual filament is inversely proportional to the density of the cortex and the entire creep compliance will be a linear function of the cortex density. For all four parameters, the linear fit function intersects the axis of the actin surface density between 4 and 5 nmol/m<sup>2</sup>, the same range as for the zero frequency shear modulus. This is a further indication that below this value the mechanical cortex properties obey a different behavior, which can not be described with the four parameter Voigt model. For the response time that is attributed to the membrane component of the composite system, which is thought to be the fast response, the electrostatic binding of actin filaments to the membrane may change the micro phase-state of the lipid bilayer and thus change the mechanical response. Separate experiments, using a continuous bleaching method of a surface supported bilayer, on a fluorescence microscope, showed, that binding of actin filaments to the bilayer reduced

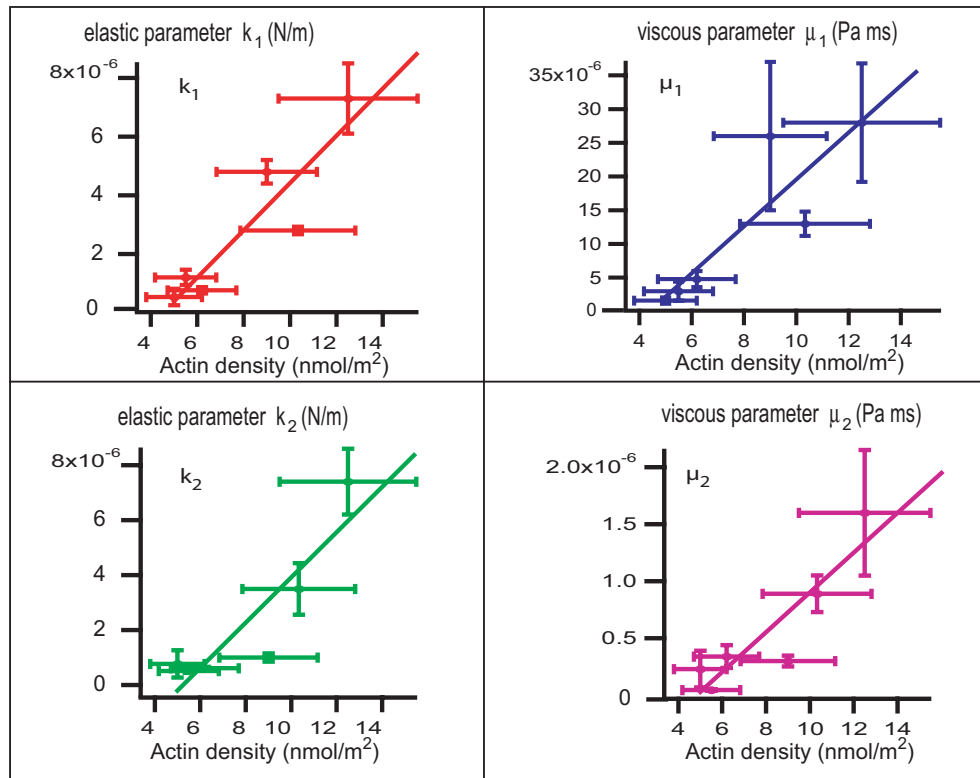


Figure 3.35: Dependence of the fit parameters of the actin vesicle creep compliance on the actin density

The four parameters  $k_1$ ,  $k_2$ ,  $\mu_1$  and  $\mu_2$  of the mechanical representation model shown in figure 3.34 and equation 3.35. Points with error bars are the data sets obtained from several vesicles with different sizes and actin cortex densities and lines in the plots are linear fit curves. While the elastic parameters are in the same range, the viscous parameters differ by one order of magnitude.

the diffusion constant of the lipid film. The characteristic response time of the vesicle membrane is proportional to the viscosity and therefore inversely proportional to the mobility of the lipids in the bilayer. The mobility itself is proportional to the diffusion constant. Additionally, studies of the mechanics of phospholipid vesicles [137] have shown that the bending modulus of the bilayer increases strongly while passing through a phase transition, induced by temperature change of the sample. The response function for the out-of-plane components showed smaller amplitudes with larger fluctuations, such that good fit results could be retrieved only for a small number of vesicles probed. The out of plane creep compliance was fitted with the same four parameter function as the in plane compliance. Of the four fit parameters three showed no visibly dependence on the actin density, only one could be well fitted with a linear function.

### 3.3.4 Calculation of the strain relaxation function $G(t)$

To retrieve the strain relaxation function  $G(t)$  for the response function measured, the convolution integral of equation 1.30 has to be solved based on the creep compliance obtained. Since no analytical solution of equation 1.30 exists, the calculation must be carried out numerically. A first approach was to use an iterative construction proposed first by Hopkins and Hamming [138]. With this method, the discrete data points of the function  $J(t)$  are taken as input and the function  $G(t)$  is assumed to be constant at each data point. Then the integral 1.30 can be solved for each data point, which leads to a recursion relation of  $G(t_i)$  from a sum of all  $G(t_{i-k}), k < i$ . The major disadvantage of this method is that the recursion can diverge if  $J(t)$  is not a monotonous function because fluctuations in the data set of  $J(t)$  are amplified by the recursion formula. Since the data sets from the experiments were not strictly monotonous, this method could not supply satisfying results for strain relaxation curves. A way of dealing with this problem, adopted by Feneberg [139] is to interpolate the  $J(t)$  values to make it a monotonous function. However this approach was rejected since the processing of the raw data material always changes the numerical results. An alternative method is a non-negative least square method to generate discrete relaxation strength for a given series

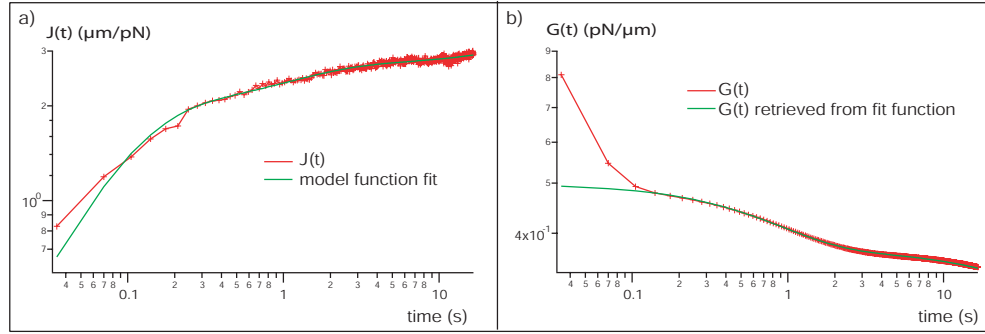


Figure 3.36: Creep compliance and stress relaxation function of an actin cortex vesicle

**a) Creep compliance and the fit function using a four parameter Voigt model series. b) The stress relaxation curves of the creep compliance data set and the fit function. Both were retrieved using the numerical procedure of the non-negative least square method to generate discrete relaxation strength.**

of relaxation times, proposed by Liu [140]. The strain relaxation function is assumed to be a discrete finite series of exponential decay processes of the imposed strain.

$$G_n(t) = \sum_{k=0}^n A_k \cdot e^{-\frac{t}{\tau_k}} \quad (3.36)$$

$\tau_k$  are relaxation times that can be chosen freely and  $A_k$  are relaxation strength for the corresponding times. A list of  $\tau_k$  must be given, usually for convenience equidistantly spaced on a logarithmic time scale;  $\tau_k = (\tau_0)^{\frac{k}{c}}$  ( $\tau_0$  is the shortest relaxation time and  $c$  a parameter for the spacing). The convolution integral of equation 1.30 is calculated for  $G_n(t)$  and the data set of  $J(t)$ , adjusting the relaxation strength values  $A_k$  to be non negative and to minimize the square of the deviation between the integral and its solution  $t$ .

$$\left( \int_0^{t_i} G_n(t) J(t_i - t) dt - t_i \right)^2 = \min \quad (3.37)$$

If the creep data contains discrete well separated response times, the result of this minimization procedure is a list of relaxation strength with only few of them being non zero. The corresponding relaxation times are characteristic for the system probed and the  $G(t)$  function can be constructed from equation 3.36.

Figure 3.36 shows a measured creep compliance function and the strain

relaxation function retrieved with the described method. To compare, the fit function from equation 3.35 for the creep compliance was also transformed to a strain relaxation function. The main difference between the  $G(t)$  function derived from the data set and the curve derived from the fit function is for short times, where the creep compliance fit curve also matches the  $J(t)$  data set not so well. Therefore care has to be taken when interpreting short time behavior of the relaxation curves. Most retrieved relaxation functions had only one or two non zero relaxation amplitudes, as expected for creep data with two or three response times [141]. Characteristic values of the strain relaxation curves are the long time strain level, which is equal to the before mentioned zero frequency shear modulus  $G_{sat}$  (figure 3.32). Since no long time flow behavior exists in the creep response curves,  $G(t)$  saturates for long times in a plateau. Two other characteristic values are the initial decrease from  $G_0 = G(t = 0)$  and the inversion point  $G_p$  of  $G(t)$  between  $G_{sat}$  and  $G_0$ . The initial decrease usually follows a power law ( $G(t) = G_0^{-\alpha t}$ ). Unfortunately, in our experiments, the parameter  $\alpha$  varied strongly from one vesicle to the next as well as from one force to another. This may not only be due to the measured system, but before all to the method to obtain  $G(t)$ , which has a definite imprecision at very short times. The inversion point  $G_p$  can be seen as a plateau value, since around  $G_p$ ,  $G(t)$  changes very slowly in magnitude. Entangled actin solutions, which are a standard model to compare the results with, also show a plateau in the same time interval of the stress relaxation curve (figure 3.37) but with a slightly higher magnitude. The plateau arises from two different relaxation mechanisms of the model system examined, which are separated on the time scale. This separation was already observed for the creep compliance data. The fact that the typical plateau in the relaxation curve of entangled actin networks also exists for the same time scales in the data for actin cortex vesicles is a strong indicator that the principal relaxation mechanisms of the biomimetic actin-vesicle model and actin filament solutions are quite similar. In actin filament solutions the two relaxation mechanisms with separated time scales are the (fast) internal dynamics of the filaments and their (slow) center of mass motion. Since the lipid bilayer, to which the filaments are attached inside the vesicle, is in a fluid state both relaxation

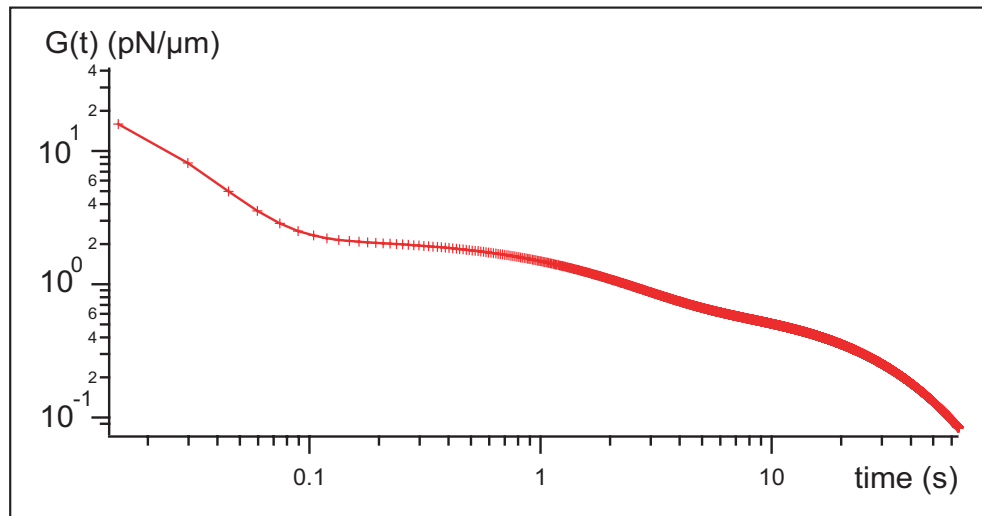


Figure 3.37: Stress relaxation curve of an entangled actin network. The stress relaxation curve was retrieved with magnetic bead micro-rheometry, initially as compliance data and subsequently converted into a relaxation curve. (Source J. Uhde, E22, TUM)

mechanisms should still be existing for the actin-vesicle model.

The behavior of  $G(t)$  for long times ( $t > 5$  s) is different for actin solutions and actin-vesicles. Whereas the stress relaxes completely in actin solutions due to a terminal flow regime of the filaments, in actin vesicles this mechanism can not exist due to the finite surface area of the vesicle.

### 3.3.5 Photochemical alternation of the actin cortex

To gain a deeper insight into the role of the actin cortex attached to the inner vesicle bilayer, it seemed desirable to be able to change the structure of the cortex after one set of measurements and following repeat the same measurements and analyze the differences. The simplest way to alternate the structure of the cortex from the outside of the vesicle is to damage fluorescently labelled actin filaments inside by strong irradiation with light in the excitation wavelength of the fluorescence dye. This effect, discussed in section 2.3.1, has been probed with actin bundles bound to the pillars array substrate, where one can observe the breaking of individual filaments in the bundle, which finally leads to the failure of the entire bundle structure. Obviously this is not a method with which the alternation of the actin cortex can be well quantified

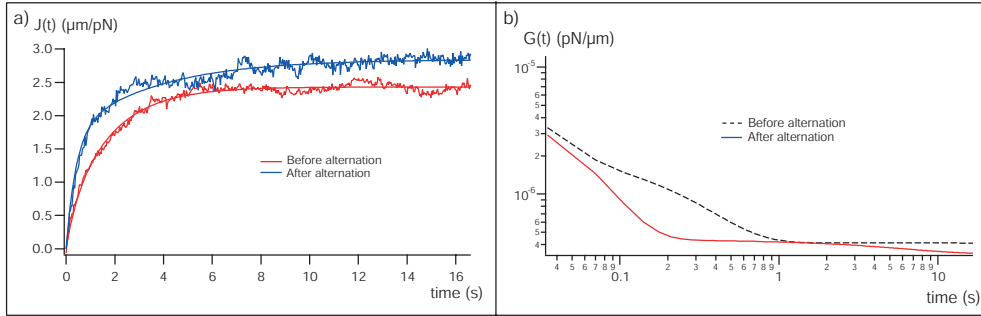


Figure 3.38: Comparison of creep compliance and stress relaxation for intact and photochemically damaged actin cortex vesicles

**a) Creep compliances and their four parameter fits before and after the photochemical alternation of the actin cortex by strong irradiation. b) Corresponding stress relaxation functions.**

or controlled. Nevertheless, to make the damage, done to the actin cortex more reproducible, all vesicles were irradiated with the same light intensity, with the focal plane at the position where the bead is bound to the vesicle for 30 seconds. When mechanically probed after the alternation of the actin cortex, most vesicles showed response and creep compliance curves, that had slightly larger amplitudes than before the alternation, but generally the same characteristic shapes, which could well be fitted with a two serial Voigt element model (see figure 3.38a). The most significant difference in the fit parameters of equation 3.35 was in the amplitudes  $A_1$  and  $A_2$ (see equation 3.35).

Before the photochemical damage of the actin cortex, the amplitude of the slower response was generally larger than one of the fast response. After the alternation, the amplitude of the slower response decreased strongly whereas the amplitude of the fast response increased. This means that the mechanism of the fast response determined more the mechanical behavior of the vesicles after the photo chemical damage. This can be easily understood if one assumes that the fast response is determined by the vesicle bilayer, which should be unaffected from the photochemical alternation. However, for large vesicles (radius  $10 \mu m$ ) the difference of the mechanical properties before and after the alternation were insignificant. This may be due to the fact that for larger vesicles, a smaller proportion of the entire structure is close to the focal plane, where the irradiation intensity is maximized. Therefore in large vesicles, more

of the entire actin cortex can be unaffected and remain basically intact. The strain relaxation function  $G(t)$  changes predominantly for intermediate times when the actin cortex is photochemically damaged. Regarding the relaxation modulus the value of the plateau for these intermediate times between 0.1 and 1 seconds is remarkably lower than for the same vesicle before the damaging of the actin cortex or even vanishes (figure 3.38b). The slower relaxation mechanism seems to play a less dominant role as for vesicles with intact actin cortex. The stress in the cortex can nearly relax to its final value through the fast internal relaxation process of the filament dynamics. The center of mass motion of the filaments, which is determined by the interaction with the surrounding filaments is much more easily possible or shorter filaments. This phenomenon also exists for entangled actin networks. The plateau value is determined by the network properties, such as the ratio of the filament length to the persistence length and mesh size, which both are changed when filaments are shortened. This has been demonstrated in oscillatory magnetic bead measurements, in which Gelsolin, an actin sequestering and capping protein was used to reduce the average length of the actin filaments in the entangled solution. The value of the storage modulus  $G'(f)$  at a frequency  $f$  of 0.3 Hz dropped from 0.3 Pa, for filaments of an average length of 10  $\mu m$  to 0.05 Pa for filaments of 1.5  $\mu m$  average length [123]. The loss modulus dropped for the two different filament lengths from 0.15 to 0.05 Pa. This comparison shows that, although the actin cortex on the vesicle membrane does not have entanglement points and exhibits a very different structure and geometry than a bulk network, basic properties of actin networks, such as a plateau modulus, which depends on the average filament length are conserved.

### 3.3.6 Work hardening

For most of the vesicles observed, the creep compliance was alike for all cycles of the step force pulse applied to them. However in a few cases, the saturation level  $J_{sat}$  of  $J(t)$  decreased during the repetition of the force pulses from an initial level to a level where it stayed constant for the rest of the force pulses applied. This phenomenon, which is known as work hardening in material science, can be explained by possible plastic deformations of the structure of

the actin cortex. By imposing an external stress on the actin cortex, local mechanical defects in the cortex structure may be formed. These defects can have strain fields, that stiffen the entire cortex and thus decrease the creep compliance. Equivalently an externally imposed stress on the cortex may release strain from the system if the cortex is prestressed by defects created during its formation. In that case  $J_{sat}$  would increase with the application of several force pulse cycles, a phenomenon which was observed in one isolated case. If the application of an external stress induces or releases internal strain in the cortex should be determined by the local structure of the cortex, relative to the imposed stress. Taking the high anisotropy of the actin cortex (see figure 3.29) into account, the differences in work hardening from one vesicle to the other can be understood.

### 3.3.7 Analysis of thermal bead fluctuations

To determine the bending rigidity of the composite actin membrane sheet, the thermal fluctuations of the vesicle were analyzed. The magnetic bead, attached to the membrane served for this purpose as a marker to visualize the membrane fluctuations. In the absence of force, the measured average amplitude  $A_m$  of the out of plane fluctuations of a magnetic bead, attached to the membrane of a vesicle with a radius of  $R = 5.5 \mu m$  was 83.4 nm. Since this value also includes the uncertainty due to the spacial resolution  $\Delta A$  of the tracking algorithm (17.5 nm), the real amplitude  $A_{ro}$  of the out of plane fluctuations is

$$A_{ro} = \sqrt{A_m^2 - (\Delta A)^2} = 81.5 nm \quad (3.38)$$

This fluctuation amplitude is linked for the case of negligible membrane tension with the surface bending stiffness  $\kappa_s$  by the relation [142]

$$A_{ro}^2 = \frac{k_b T}{16\kappa_s} \cdot (2R)^2 \quad (3.39)$$

Inserting the values determined for the observed vesicle leads to a bending stiffness of  $4.73 \cdot 10^{-18}$  J (or  $1137 k_b T$ ). This value has to be seen as an upper limit for the bending stiffness of the vesicle, since it was assumed that no tension exists in the actin membrane composite sheet. This is surely not exact since the vesicles are strongly adhered to the substrate, a process, which

always induces a certain tension in the membrane. However, for vesicles with such a high bending stiffness the tension does not play such a dominating role and will likely not lead to a large error in the value for the bending stiffness. Nevertheless, when an extra tension is induced in the membrane by pulling on it with the magnetic bead, the decrease of the fluctuation amplitude is clearly visible. With an applied force of 0.8 pN, the amplitude  $A_{r_o}$  decreases to 61 nm and with a force of 1.6 pN down to 48 nm. Concluding it can be said that a good estimate for the bending stiffness of a vesicle with an adsorbed actin cortex is roughly  $1000 k_b T$ , which is between one and two orders of magnitude more than for simple phospholipid vesicles [143][87]. Even human erythrocytes, which have an actin - spectrin cytoskeleton attached to their cell membrane and were analyzed for their bending stiffness through fluctuation analysis [144] and atomic force microscopy [145] showed lower bending rigidities  $\kappa_s$  of  $2 - 3 \cdot 10^{-19}$  J ( $48 - 72 k_b T$ ). Neutrophil cells showed in micro pipette aspiration experiments [146] bending moduli between 1 and  $2 \cdot 10^{-18}$  J. ( $250 - 500 k_b T$ ) and Dictyostelium cells showed bending moduli of 250 to  $550 k_b T$  in adhesion experiments [147], which is in the range of the value measured for the actin cortex vesicle.

The in plane fluctuations tangential to to the vesicle surface for the same vesicle had, in the absence of an external force corrected amplitudes  $A_{r_i}$  of 117.3 nm. The shear modulus  $\mu$  of a two dimensional soft solid is related to the thermal fluctuation amplitude  $A_{r_i}$  as [142][148]

$$\mu = \frac{k_b T \cdot \ln(R/a)}{4\pi \cdot A_{r_i}^2} \quad (3.40)$$

citewhoever!! The parameter  $a$  is the shortest excitable wave vector, which can be estimated to be in the order of the average distance between the filaments (109 nm). The longest excitable wave vector has the length of the radius of the vesicle  $R$ . The shear modulus  $\mu$  herewith becomes  $9.5 \cdot 10^{-8} J/m^2$ . This value is in good agreement with the stress relaxation modulus which was numerically determined from the creep experiments (see figure 3.36 b). The shear and bending modulus of an homogeneous and isotropic sheet with thickness  $d$  can

be related through [120]

$$\frac{\kappa}{\mu} \approx d^2 \quad (3.41)$$

Using this equation, the thickness of the composite vesicle shell would become  $7 \mu m$ , which is obviously not a reasonable result. The bending modulus is much larger than the value expected from the shear modulus. This discrepancy of the value of the shear and the bending modulus can be understood from the anisotropy of the material. First the actin membrane sheet is a two composite material of the actin cortex and the lipid membrane. The shear modulus is completely determined by the actin cortex, since the lipid bilayer has no shear elasticity. The bending modulus on the other hand is determined by the bending elasticity of the bilayer and of the actin cortex and therefore will be higher than expected. Even more important for the high value of the bending modulus is the anisotropy of the actin cortex itself. The shearing of the cortex has two modes, a longitudinal and a transverse mode relative to the filament orientation. Since the longitudinal mode is weaker than the transverse, the main contribution to the shear modulus comes from the longitudinal mode. The bending modulus has only a deformation mode transverse to the filament orientation and therefore will be much higher than expected from the shear data. Concluding, the shear modulus measures the longitudinal deformation modulus of the filament network and the bending modulus the transverse one, which can not be expected to be equivalent.

### 3.3.8 Strain field mapping

To measure the distribution of stress in the cortex-membrane composite sheet, the strain field on the outside of the vesicle membrane was measured. This strain field technique is a way to directly measure the Young modulus of the actin - membrane cortex without using bending or shear moduli, which are strongly determined by the geometry of the sample, which is not exactly known. For this purpose, many small (500 nm radius) non-magnetic polystyrene beads were attached to the outside of the vesicle, in addition to the magnetic bead. Polystyrene carries a negative charge, thus the small beads did not have to be surface-functionalized to bind to the positively charged membrane. To reach a sufficiently high density of non-magnetic beads on the

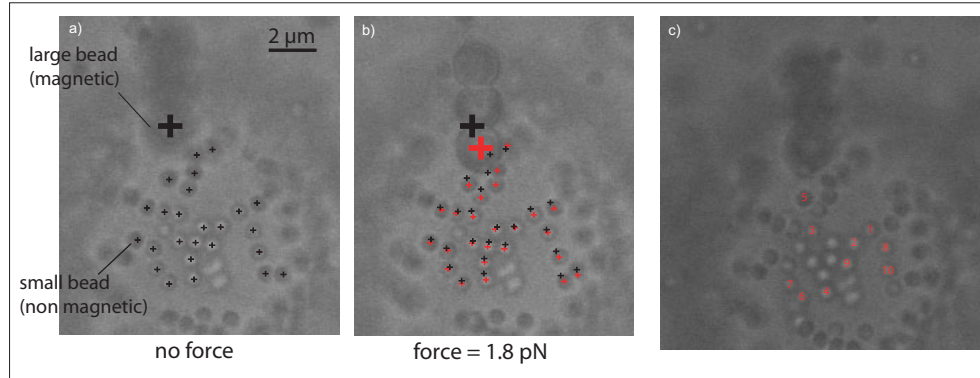


Figure 3.39: Strain field mapping on the upper half sphere of an actin cortex vesicle.

**a) Magnetic (large) and non magnetic (small) beads on an actin cortex vesicle in the absence of a force exerted on the magnetic bead. b) Same vesicle with force of 1.8 pN acting on the magnetic bead. To illustrate the displacement of the beads, the old (black) and new (red) positions of the beads have been indicated by small crosses. Already a slight tendency that small beads closer to the magnetic bead are further displaced can be seen. c) The saturation displacement  $\Delta x_{sat}$  of several beads. The numbers refer to individual beads (see figure 3.40)**

surface of the vesicles, the bulk concentration of the beads had to be very high. Because most of the non-magnetic beads did not bind to a vesicle and stayed in the bulk solution, the images of the vesicles with the beads were slightly blurred because of the background signal from the beads in the bulk. When the creep compliance of the vesicle was probed, the displacements of the small beads can be measured simultaneously with the displacement of the magnetic bead. Because of the reduced image quality, and since only the in-plane shear was thought to be probed, the movement of the beads was analyzed only in a two-dimensional coordinate system of the vesicle surface. Figure 3.39 shows a vesicle with a magnetic bead and many non-magnetic beads on it.

To analyze the strain field, the saturation displacement  $\Delta x_{sat}$  of the non-magnetic beads was measured as a function of the distance  $x_i$  to the magnetic bead. The values determined show a weak tendency to decrease with increasing distance, but no clear dependence (figure 3.40). Because of the high anisotropy of the actin cortex on the length scale of the distances analyzed, this is not

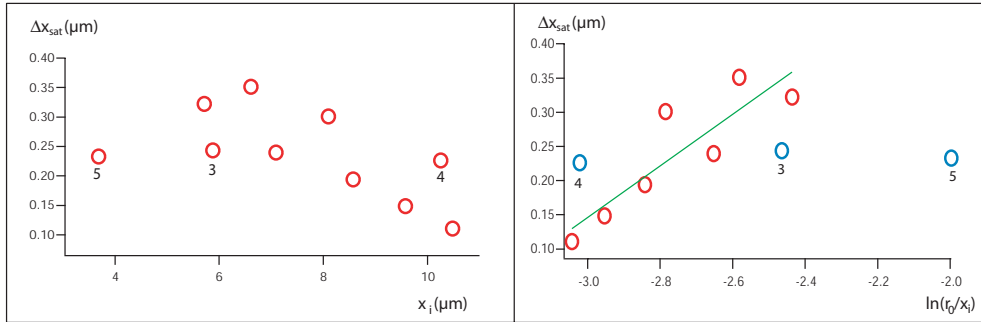


Figure 3.40: Displacements of different non magnetic beads used as strain field sensors on the outer surface of an actin cortex vesicle

**a) Saturation displacements  $\Delta x_{sat}$  of different non magnetic beads vs their distance  $x_i$  from the magnetic bead. b) The saturation displacements (circles) plotted vs the logarithm of the ratio of the bead radius  $r_0$  and the distance of the bead from the magnetic one  $x_i$ . The line is a linear fit of the relation (see equation 3.47), under exclusion of the three beads labelled 3, 4 and 5, which are assumed to be connected by a rigid structure since they are aligned and have exactly the same displacement.**

very surprising.

Nevertheless, regarding the positions of the beads, it is possible to separate them into two groups. Visibly, the beads denoted with the numbers 3 to 5, can roughly be connected with one line. The displacements for these three beads are the same within the resolution of the tracking algorithm, although their distances from the magnetic bead range from 3.7 to 10.25  $\mu\text{m}$ . This can be seen as an indicator that these three beads are connected by a straight, rigid, incompressible element, an actin filament - bundle structure in our case. Since their displacement of 230 nm is remarkably smaller than the displacement of the magnetic bead (1.15  $\mu\text{m}$ ) the actin filament structure, which presumably links the three beads is not rigidly connected to the magnetic bead. The determined displacements of all other beads show a clear tendency to decrease with increasing distance from the magnetic bead. This tendency can be analyzed regarding the in-plane shear field in a two-dimensional plane. For a two dimensional system, the in plane component of the stress tensor  $\sigma_{xx}$  is linked with the strain field components  $\epsilon_{xx}$  and  $\epsilon_{yy}$  through the equation [120]

$$\sigma_{xx} = \frac{E}{1 - p^2} (\epsilon_{xx} + p \cdot \epsilon_{yy}) \quad (3.42)$$

$E$  is the Young modulus of the membrane actin composite sheet and  $\nu$  its Poisson ratio. For the reasons mentioned in chapter 3.2.2, the Poisson ration of biological materials is generally estimated to be roughly 0.5. The strain field tensor element  $\epsilon_{yy}$  is in this case negligible compared with the value of  $\epsilon_{xx}$ , such that it does not have to be included in the calculation. For a micro mechanical experiment, contrary to a macroscopic shear measurement, the stress field is not homogeneous in the material and decays with increasing distance from the magnetic bead. In a two dimensional geometry this decay is always inverse proportional to the distance from the bead. The force from the magnetic bead is transduced to the plane of the composite membrane actin sheet through an adhesion plate of the bead on the membrane, which will be assumed to have a radius  $r_0$  of roughly  $0.5 \mu m$ . The in plane shear stress value  $\sigma_{xx}(r_0)$  at the distance  $r_0$  from the center of the adhesion plate is

$$\sigma_{xx}(r_0) = \frac{F_x}{2 \cdot r_0 \cdot d} =: \sigma_0 \quad (3.43)$$

$F_x$  is the force transduced from the bead on its adhesion plate on the membrane and  $d$  is the thickness of the membrane - actin composite sheet. Regarding the thickness measured in neutron reflectivity experiments for an actin monolayer electrostatically bound to a membrane [133] and the thickness of a phospholipid bilayer, the value of  $d$  is estimated as 10 nm. The value of  $\sigma_0$  is therefore  $180 N/m^2$  The stress field thus becomes

$$\sigma_{xx}(x) = \sigma_0 \cdot \frac{r_0}{x} \quad (3.44)$$

Since  $E$  and  $\nu$  are constant parameters, the strain field must have the same form as the stress field.

$$\epsilon_{xx}(x) = \epsilon_0 \cdot \frac{r_0}{x} \quad (3.45)$$

$\epsilon_{xx}$  is linked with the saturation displacements of the small non magnetic beads  $\Delta x_{sat}$  through

$$\epsilon_{xx} = \frac{\partial \Delta x_{sat}}{\partial x} \quad (3.46)$$

Creating a dimensionless parameter  $\tilde{x} = x/r_0$  one can write

$$\Delta x_{sat} = - \int \epsilon_{xx}(x) dx = - \int \epsilon_{xx}(\tilde{x}) d\tilde{x} \cdot \frac{dx}{d\tilde{x}} = \epsilon_0 \cdot r_0 \cdot \ln\left(\frac{r_0}{x}\right) + c \quad (3.47)$$

Thus by plotting the measured values for  $\Delta x_{sat}$  versus the value  $\ln(\frac{r_0}{x_i})$ , where  $x_i$  is the distance of the individual bead from the magnetic bead, the value of  $\epsilon_0$  can be retrieved through the slope of a linear fit (see figure 3.40). This leads to a value of 0.754 for  $\epsilon_0$  and  $179 \text{ N/m}^2$  for the Young modulus of the actin membrane composite sheet. This value is remarkably much higher than the measured value of around  $1 \text{ N/m}^2$  for the quasi two dimensional actin cortex self assembled on the silicon pillar array. The vesicle used for the strain field mapping had a radius of  $16 \mu\text{m}$ , which yields an average distance of  $37.5 \text{ nm}$  between the individual actin filaments. This is a very dense assembly of filaments, compared to the value around  $1 \mu\text{m}$  for the network on the pillar array, which could explain the strength of the cortex. Another reason for the high Young modulus could be an eventual bundling of the filaments, as suspected from images of the cortex and calculation of the average filament distance in section 3.3.1.

Giant phospholipid vesicles with internal actin cortices are to date probably the most realistic biomimetic model system to study the mechanical properties of membrane-cortex composite sheets. Although they are quite simple models, compared to the very complex cortex structures in eucaryotes, where the membrane is a mosaic of proteins, lipids, sterols and glyco-molecules and the actin cortex is regulated by many different additional proteins, the actin cortex vesicles have the definite advantage over other model systems, that they are finite size objects like cells and not bulk samples as commonly used. Regarding the persistence length of actin, determined in the previous chapter to be  $15 - 17 \mu\text{m}$ , it is obvious, that finite size effects come into play when the dimension of the model system are in the same order. As an example, a finite size effect observed for the actin cortex vesicles is the second plateau of the stress relaxation  $G(t)$ .

### 3.4 Drop evaporation of entangled actin solutions

Further insight into the dynamics of individual actin filaments can be gained by studying actin filaments subjected to a hydrodynamic flow or in confinement. Instead of setting up a complex flow system to study these dynamics, the behavior of actin filaments in evaporating entangled solutions was analyzed. For this purpose actin filament solutions of concentrations between 1 and 20  $\mu M$  (mesh sizes  $\xi$  between 1.676 and 0.375  $\mu m$ ) were prepared that contained 1nM fluorescently labelled filaments. These labelled filaments, which were observed in fluorescence mode of a microscope, serve as visible markers, representing the behavior of the entire filaments in the network. To suppress tread-milling dynamics in the network, the filaments were stabilized with Phalloidin at a molar one to one ratio. Small droplets of 10  $\mu l$  volume were pipetted onto pre-cleaned microscopy glass slides on an epi-fluorescence microscope and the dynamic behavior of the labelled filaments observed during the evaporation of the droplets. Directly after the deposition of the droplet on the glass slide, a radial spreading behavior of the solution on the hydrophilic slide is observed. After this initial dynamics, which lasts for around 15 to 30 seconds, the droplet reached an equilibrium shape which has the global shape of a spherical cap. This shape is dictated by the surface tension of the droplet, which is the dominating contribution to the free energy of the system [149]. At certain conditions for the surface of the glass slide, which were evaluated experimentally, the triple interface line at the contact between air, glass and the droplet is pinned at the position that it reaches at the end of the initial spreading phase for a time which is in the order of several minutes. Meanwhile, the evaporation of the solvent leads to a decrease in volume of the droplet.

#### 3.4.1 Reconstruction of the droplet shape

A spherical cap of volume  $V$  can be described by its contact plane radius  $a$ , its spherical radius  $R$  and a central cap height from the contact plane  $h_0$  (see figure 3.41). These parameters are linked by the relations:

$$a^2 = h_0 \cdot (2R - h_0) \quad (3.48)$$

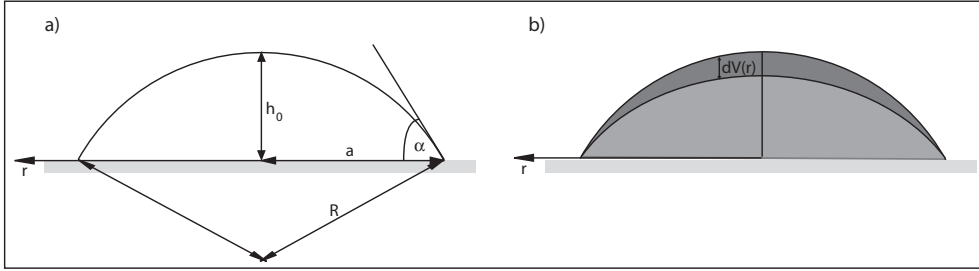


Figure 3.41: Spherical cap geometry of a droplet deposited onto a solid surface  
**a) Characteristic parameters, that determine the geometry of a spherical cap. b) Evolution of a spherical cap geometry when the triple interface line is immobile (a is invariant).**

$$V = \frac{1}{6} \cdot \pi h_0 (3a^2 + h_0^2) \quad (3.49)$$

When the triple interface line between the solvent, glass and air is pinned, the parameter  $a$  is invariant. Since the evaporating droplet has constantly to maintain its minimum energy shape of a spherical cap, equation 3.49 shows that for an invariant parameter  $a$ , the central height  $h_0$  has to decrease. On the other hand, equation 3.48 states that for a invariant parameter  $a$  and decreasing parameter  $h_0$ , the spherical radius  $R$  has to increase. For a radially symmetric body like the spherical cap, the infinitesimal volume element  $dV(r)$  as a function of the radial coordinate  $r$  is a linear function of the height of the spherical cap  $h(r)$  at the radial position  $r$  ( $dV(r) = h(r) \cdot dr$ ).

$$h(r) = \sqrt{R^2 - r^2} - \sqrt{R^2 - a^2} \quad (3.50)$$

Since for an evaporating droplet, with pinned triple line, which has to maintain a spherical cap shape the decrease of  $h(r)$  must be larger in the center ( $r \approx 0$ ) than close to the rim ( $r \approx a$ ) the decrease in volume also must be larger in the center than in the periphery of the droplet. This larger loss of volume in the center can be reached either through a larger evaporation in the center, which matches exactly the change in volume  $\frac{dV(r)}{dt}$ , or a net flow of solute radially outward. Since the evaporation is a function only of the surface element  $\frac{dh(r)}{dr}$  of the droplet and eventually its curvature, a higher evaporation rate in the center of the droplet is not possible. Contrary, since  $\frac{dh(r)}{dr}$  is larger at the rim than in the center of the droplet, the evaporation rate in the center is smaller than in the periphery of the droplet. Thus a flow has to transport

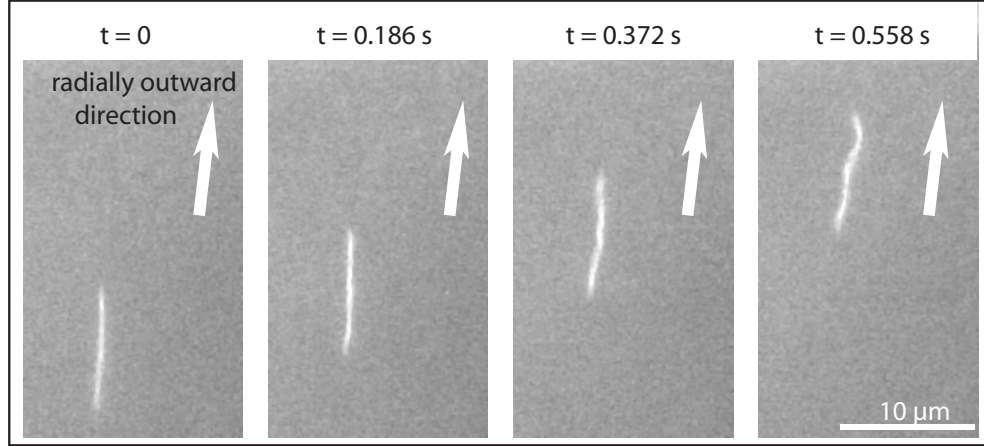


Figure 3.42: An actin filament moving radially outward in an evaporating droplet.

solvent from the central regions of the droplet radially outward to the triple line. For the droplets of entangled actin solutions this flow can be seen through the fluorescently labelled filaments, which can be observed to move towards the triple line of the droplet. Snapshots of actin filaments moving with the radial flow in an evaporating droplet are shown in figure 3.42.

The contact angle  $\alpha$  between the droplet and the glass surface can be observed during the evaporation process using the RICM mode of the microscope. Since  $\alpha$  is given by

$$\sin(\alpha) = \frac{a}{R} \quad (3.51)$$

the knowledge of the droplet radius  $a$  and the measurement of the contact angle  $\alpha$  allow us to reconstruct the evolution of the droplet shape with time. Figure 3.43 shows RICM snapshots of the contact line of a droplet, a corresponding intensity line profile and the reconstructed shapes as well as the calculated surface area and volume of the droplet.

The line intensity profile shows a periodicity that coincides well with that of a sinusoidal fit, indicating in fact a constant contact angle of the droplet, close to the glass surface. The knowledge about the droplet shape, allowed us to calculate its volume  $V$  and the surface area of the solvent- air interface  $S$  for each movie frame. The fact that the the volume of the droplet decreases linearly while the surface stays nearly constant indicates that the initial as-

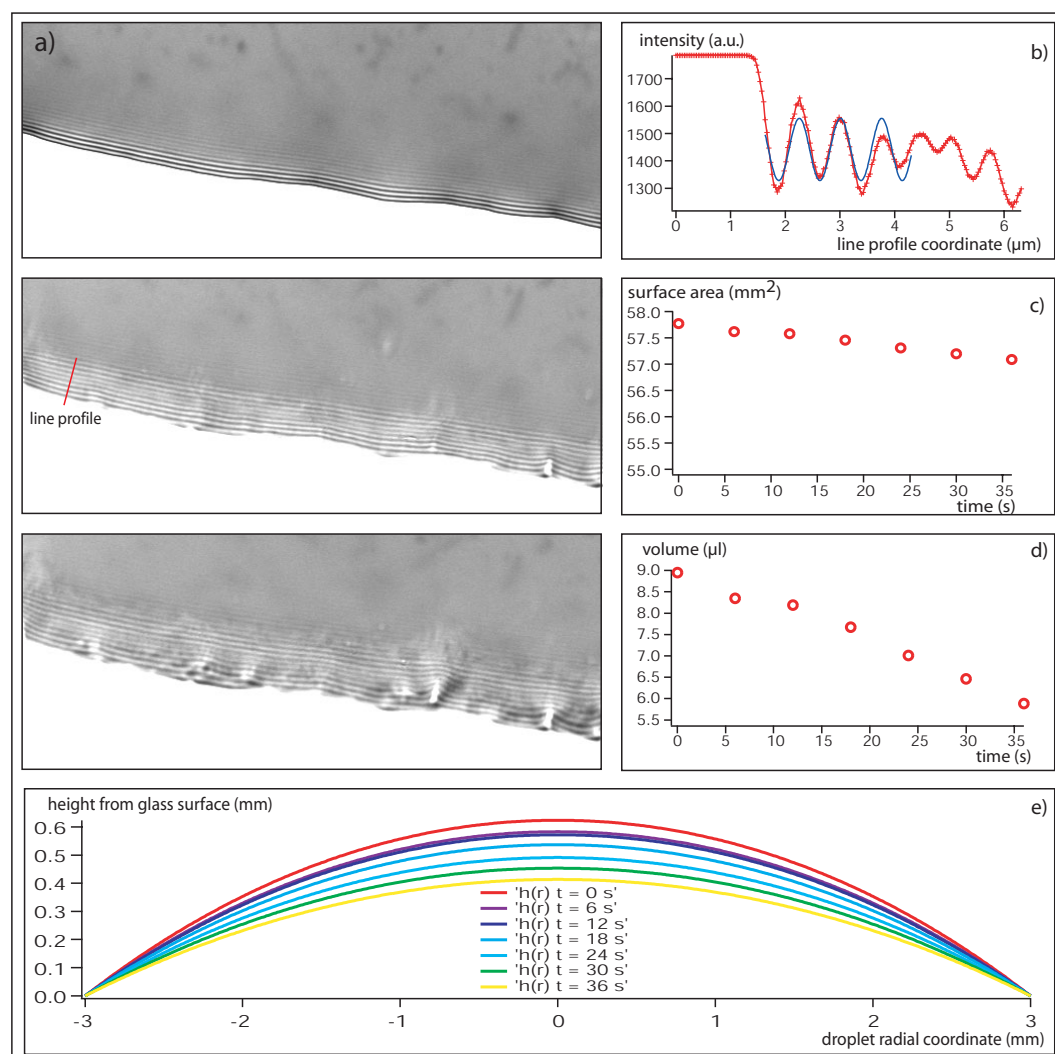


Figure 3.43: Evaporation process of an actin filament solution droplet deposited on a glass slide.

a) Three RICM snapshots of the triple interface line of the droplet taken at a wavelength of 546 nm. The time for the snapshot are 0, 18 and 36 s on a time scale that starts after the initial spreading phase of the droplet on the substrate. b) Intensity line profile (red curve) of the RICM image at  $t = 18$  s at the position indicated with the red line in the image on the left. The sinusoidal fit (blue line) shows the periodicity of the line profile. c) Time evolution of the surface area of the droplet during the evaporation process. d) Droplet volume evolution. e) Reconstructed spherical cap shapes of the droplet at time between  $t = 0$  and  $t = 36$  s.

sumption of a spherical cap shape of the droplet is correct.

### 3.4.2 Filament bending under hydrodynamic pressure

This behavior dominates for around the first minutes of the evaporation process. More and more actin filaments are deposited by the flow at the triple interface line, such that a dense structure of compressed actin filaments is built up. The same effect of radially outward particle transport leads to ring-like stains of coffee or wine drops on smooth surfaces, which every coffee drinker knows from his office table [150]. The dense actin structure can be seen in fluorescence as well as in RICM mode of the microscope. This structure acts as a barrier for newly arriving actin filaments, whereas it is permeable for the solvent. Thus newly arriving actin filaments are compressed against this structure by the hydrodynamic flow of the solvent. For mesh sizes below  $1 \mu\text{m}$ , these filaments, which were initially aligned with the flow direction, aligned parallelly with the triple interface line upon contact with the dense actin structure. For smaller mesh sizes, the filaments were strongly bent and finally folded before aligning with the triple interface line. This bending and folding process was analyzed to determine dynamic properties of actin filaments. The contour of a filament during this process was reconstructed from each image frame of a movie, that was recorded from this bending process, using the shape analysis algorithm described in chapter 2.3.2. Figure 3.44 shows snapshots of an actin filament being compressed against the dense actin structure close to the triple interface line and its reconstructed contour (in red).

At first glance, the bending and folding process described seems to be equivalent to a buckling process driven by a mechanical instability of a rigid rod upon compression.

If we assume the filament to be a stiff object, its buckling process can be described for small amplitudes by solving the differential equations for weakly bent rods under hydrodynamic forces parallel to the rod axis. The general equation for the buckling shape  $Y(z)$ , where  $z$  is the axis in which filament and

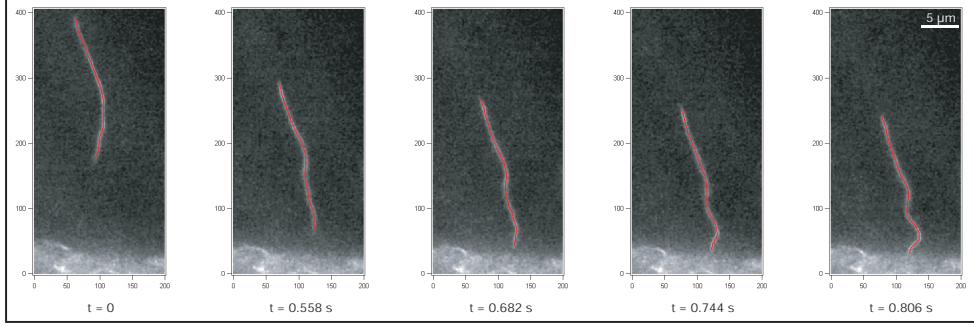


Figure 3.44: Snapshots of an actin filament being compressed against the dense actin structure close to the triple interface line of an evaporating actin droplet. **The contour of the filament during this process was reconstructed using a self developed shape tracing algorithm, discussed in chapter 2.3.2 and is shown as a red line in the images.**

force are aligned, is [120]:

$$\kappa \cdot \frac{d}{dz^4}(Y(z)) - \frac{d}{dz} \cdot (F(z) \cdot \frac{d}{dz} \cdot Y(z)) = 0 \quad (3.52)$$

$\kappa$  is the bending modulus of a TRITC labelled actin filament, which was determined in the experiments in chapter 3.2 to be  $6 \cdot 10^{-26} J \cdot m$ .  $F(z)$  is the hydrodynamic force of the surrounding flow on the filament.  $dF/dz$  can be described for a thin rod of radius  $r$  in a medium of viscosity  $\eta$  flowing with a velocity  $v$  and confined in a thin film of thickness  $d$  by: [48]

$$\frac{d}{dz} \cdot F(z) = \frac{(2 \cdot \pi \cdot \eta)}{\ln(\frac{d}{4 \cdot r} - 0.9157)} \cdot v \quad (3.53)$$

The velocity of the flow  $v$  is equivalent to the center of mass velocity of the filaments before they encounter the dense actin structure. This assumption was tested by injecting small (40 nm) fluorescent polystyrene beads into the actin filament solution. Their velocity, which should reflect the solvent velocity, was compared with the flow velocity of the filaments and found to be equivalent. Thus for each filament, the center of mass velocity can be determined from the reconstructed contour in each movie frame and used to calculate the viscous drag force on the filament, when it is stopped by the dense actin structure at the rim. The thickness  $d$  of the solvent film, in which the filaments are confined close to the triple interface line can be estimated, with an accuracy of around 500 nm, using RICM images, to be around  $3 \mu m$ . The relatively

high inaccuracy is not significant for the value of the drag force  $F(z)$ , since the film thickness determines  $F(z)$  in a logarithmic term, relative to the filament diameter, which is three orders of magnitude smaller. Since every point along the filament contributes an equal amount of force to the entire force at point  $z$ , one can write (with  $z = 0$  at the point where the filament touches the dense actin structure)

$$F(z) = \frac{d}{dz} \cdot F(z) \cdot (l - z) =: q \cdot (l - z) \quad (3.54)$$

This is equivalent to the problem of a rigid rod, buckling under its own weight in a gravitational field. Substituting

$$e = \frac{2}{3} \cdot \sqrt{\frac{q}{\kappa} \cdot (l - z)^3} \quad (3.55)$$

the derivatives  $u$  of the filament shape  $Y(z)$

$$u = \frac{d}{dz} \cdot Y(z) \quad (3.56)$$

have the general form

$$u(e) = e^{\frac{1}{3}} \cdot (A_1 \cdot J_{\frac{1}{3}}(e) + A_2 \cdot J_{-\frac{1}{3}}(e)) \quad (3.57)$$

$J_i$  are Bessel functions of the order  $i$ .

A characteristic parameter, which can be extracted from the reconstructed contours of the compressed and bent actin filaments and compared to the predicted contours of the calculated buckling process is the contour length of the filament from the point where it touches the dense actin structure and the first deflection maximum  $l_b$  (figure 3.45). Even though the calculated buckling contours were determined for small deflection amplitudes, this length should be constant for larger deflections, which are observed during the folding process of the filament, since the maximum deflection points on the contour of the filament determine the points where the filament will be folded and finally break. Comparison of the values for  $l_b$ , determined from the reconstructed filament contours during the bending process and the calculation based on the assumption of a buckling instability process differed always by at least a factor

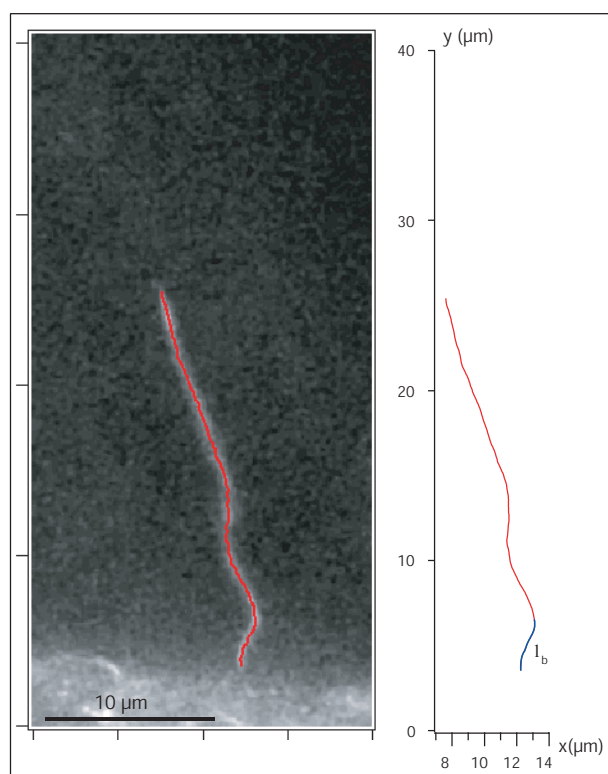


Figure 3.45: Characteristic bending length of an actin filament, which is compressed in a flow against an obstacle.

**Image and vectorized graph of the filament contour. The characteristic contour length  $l_b$  of the filament from the point where it touches the dense actin structure and the first deflection maximum is indicated in blue in the graph.**

of three. Since this discrepancy is significantly larger than the uncertainty about the parameters used and the spatial resolution of the system observed, it can be concluded that the bending and folding process of the actin filaments does not stem from a buckling instability.

The classical description of a buckling instability process takes the static properties of a rigid object into account. This picture is very likely too simplified for the bending and folding process of actin filaments compressed against a barrier as observed here in evaporating droplets. To correctly describe this process, also the dynamic properties of actin filaments have to be taken into account. Unlike a rigid rod, that exhibits a buckling instability upon compression, an actin filament is not a rigid object of initially zero curvature, which from a critical load force on has a minimum free energy at a non-zero curvature. Actin filaments exhibit bending undulations due to thermal motion, which were examined in chapter 3.2.3. Therefore these filaments are elastic objects, which always exhibit a non-zero curvature, even in the absence of an external load acting on them. These undulations are the elastic Eigenmodes of the filament, which are determined by equation 1.17 and the relevant boundary conditions. The boundary conditions which are assumed here for the filaments, are that both ends are free to move and tilt, since the filaments are only restricted in the network by the reptation tube of the surrounding filaments. The Eigenmodes  $Y_{k_i}(z)$  for a filament of length  $l$  is given by the equation

$$Y_{k_i}(z) = A_i \cdot ((\sin(k_i l) - \sinh(k_i l)) \cdot (\sin(k_i z) + \sinh(k_i z)) + (\cos(k_i l) - \cosh(k_i l)) \cdot (\cos(k_i z) + \cosh(k_i z))) \quad (3.58)$$

The wavenumbers  $k_i$  of the Eigenmodes are determined by the equation

$$\cos(k_i l) \cdot \cosh(k_i l) = 1 \quad (3.59)$$

At the moment, when the filaments encounter the dense actin structure at the triple interface line, they are vertically (here denoted as  $x$  direction) confined in a thin solvent layer of around  $3 \mu m$ . Since this is less than one fifth of their persistence length, this degree of freedom is not accessible to the filaments and a two dimensional analysis of the problem is sufficient. When a filament touches the dense actin structure at the triple interface line and is

compressed by the flow, the observed characteristic length  $l_b$  should reflect the same characteristic length of the lowest undulation mode of the filament which is accessible to the filament. Therefore the bending process of the filament at the triple interface line can be described in terms of an amplification of undulation modes upon compression. The accessibility of the individual modes is determined by spacial and temporal restrictions of the bending process. The filament is confined in a reptation tube with average diameter  $d_t$  [32].

$$d(t) \sim \frac{\xi^{\frac{6}{5}}}{l_p^{\frac{1}{5}}} \quad (3.60)$$

For a mesh size  $\xi$  of 530 nm (10  $\mu M$  actin) and a persistence length of 16  $\mu m$  the tube diameter  $d_t$  is 540 nm, thus it differs very little from the mesh size. Undulation modes with amplitudes exceeding the tube diameter will be suppressed and thus are not accessible for the filament. The spacially lowest accessible mode for the bending process will therefore be the lowest mode with an amplitude smaller than  $d_t$ . The undulation amplitudes can not be analytically calculated directly from equation 3.58, thus the whole wave function was generated and half of the peak-to-peak value taken as the undulation amplitude. For the example of the filament shown in figure 3.44 which is 21  $\mu m$  long, the first mode has an amplitude of 3.9  $\mu m$  and therefore is suppressed. The lowest mode of which the amplitude does not exceed the tube diameter is the fourth mode with an undulation amplitude of 529 nm. This mode has a characteristic length  $l_b$  of 4.45  $\mu m$ . In comparison, the filament which is bent exhibits a characteristic length  $l_b$  of 3  $\mu m$ , which is in between the values of the length of the sixth and seventh mode, and would mean a spacial confinement of the filament in a tube with a diameter of 240 or 168 nm respectively. These values differ significantly from what would be expected for a network of this concentration and no reason can be found for a eventual large decrease in mesh size. Therefore, the spacial restriction seems not to be the determining factor for the characteristic bending length  $l_b$ .

The temporal restriction of the accessible modes of a filament are given by the relaxation times  $\tau_r$  of the individual modes. These characteristic times of each

undulation mode determine the time decay function of the contour correlation.

$$\langle Y_{k_i}(z, t), Y_{k_i}(z, (t + \tau)) \rangle \propto e^{-\frac{t}{\tau_r}} \quad (3.61)$$

For a filament of known bending rigidity  $\kappa$  ( $6 \cdot 10^{-26} J \cdot m$  for TRITC-Phalloidin stabilized actin), length  $l$  and the boundary conditions given before, the relaxation time for the mode  $Y_{k_i}$  is

$$\tau_r = \frac{\zeta}{\kappa} \cdot \left( \frac{l}{k_i} \right)^4 \quad (3.62)$$

The hydrodynamic friction  $\zeta$  of the filament perpendicular to the filament axis in a solvent layer of thickness  $d$  is [48]

$$\zeta = \frac{(4 \cdot \pi \cdot \eta)}{\ln\left(\frac{d}{4r} - 0.9157\right)}. \quad (3.63)$$

For the example of the actin filament being compressed against the dense actin structure shown in figure 3.44, the characteristic bending length  $l_b$  of  $3 \mu m$  corresponds to a characteristic length between the sixth and the seventh undulation mode of the filament with a relaxation times of 85 ms ( $l_b = 3.08 \mu m$ ) and 48 ms ( $l_b = 2.67 \mu m$ ) respectively. To determine a characteristic time scale for the bending process of the actin filament, the bending energy per length unit  $E_b/l$  was calculated from the contour of the filament in each movie frame using equation 3.28. When a filament contour is numerically derived, to calculate its bending energy, the roughness of the curve, which stems from the shape tracing algorithm, introduces an extra artificial curvature, which can not stem from the actual contour, since the filament is a stiff object on length scales below one micrometer. To exclude this artifact from the calculated value of the curvature of the filament contour, the curvature was determined for short sections of the filament contour part after part. Always one section of the filament, which contained  $n$  contour points was fitted with a polynomial of second order and the quadratic coefficient taken as the curvature value of the part of the filament. Following, the next section was analyzed, by shifting the starting point of the section by one point along the contour of the filament. For short sections of the filament, the assumption that the entire curvature is given by a parabolic function is valid if the section is much shorter than

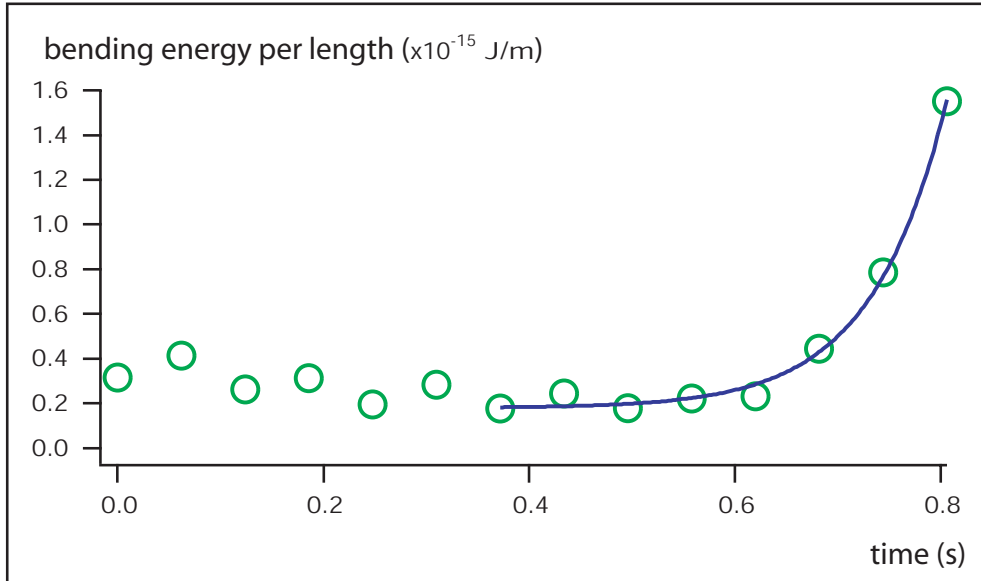


Figure 3.46: Time evolution of the bending energy per length (circles) of an actin filament, which is compressed against an obstacle

**The bending energy per length  $\Delta E_b$  of the filament displayed in figure 3.44 as it is compressed against the dense actin structure at the rim of the evaporating droplet. At the moment the filament encounters the obstacle ( $t \approx 0.682s$ ), the bending energy increases strongly. The fit curve (line) is the exponential function given in equation 3.64.**

the persistence length of the filament. Furthermore random noise artifacts are excluded with this fitting procedure. The curvature values retrieved for the curvature analysis using pieces of the length of  $n = 5$  to  $n = 11$  returned very similar values, which indicates further the correctness of the method. Figure 3.46 shows the calculated values for the contour length density of the bending energy  $E_b/l$  plotted vs time, during the bending process of the filament shown in figure 3.44, for a frame rate of 62 ms. Comparing this graph with the snapshots from the process when the filament is bent when it encounters the dense actin structure in figure 3.44, it can be seen that after the filament touches the actin structure (snapshot at  $t = 0.682$  s) its bending energy per length starts to increase strongly. The characteristic time of the increase of the bending energy per length can be taken as a characteristic time scale for the bending process of the actin filament. Therefore the bending energy per

length  $E_b/l = \Delta E_b$  was fitted with a exponential function of the type

$$\Delta E_b(t) = \Delta_0 E_b \cdot \left(1 + e^{\frac{t-t_0}{\tau_c}}\right) \quad (3.64)$$

The fit parameters are the equilibrium bending energy per length  $\Delta_0 E_b$ , the characteristic time for the increase of the bending energy  $\tau_c$  and the moment when the increase starts  $t_0$ . The retrieved value of  $t_0$  is  $0.6567 \pm 0.0054s$  and coincides well with the observed moment when the filament encounters its barrier. The fit value for the equilibrium bending energy per length  $\Delta_0 E_b$  of  $1.77 \pm 0.21 \cdot 10^{-16} J/m$  returns a total bending energy of  $3.72 \pm 0.44 \cdot 10^{-21} J$  for the entire filament, which coincides very well with the expected value of  $k_b T$  of  $4 \cdot 10^{-21} J$ . The fit value of the characteristic time  $\tau_c$  is  $72.9 \pm 5.4ms$ , which is in between the two boundary values of  $85ms$  ( $l_b = 3.08\mu m$ ) and  $48ms$  ( $l_b = 2.67\mu m$ ), expected for the observed characteristic bending length  $l_b$  of  $3\mu m$ . The same relation was found for the bending and folding process of other filaments upon their compression at the triple interface line of the droplet.

Concluding it can be stated that the compression process of an actin filament inside a network leads to a bending of the filament, which is not an instability transition as a buckling process but a mode amplification of the internal thermal undulation modes of the filament. The observed dominant mode of the bending in the case the compression of actin filaments in evaporating droplets is determined by the characteristic time of the compression and the mode relaxation time of the filament.

## 3.5 Contraction forces in active actin-myosin networks

### 3.5.1 Active actin-myosin networks

In eucaryotic cells, the actin cytoskeleton, especially actin-myosin<sup>17</sup> networks, play an important role for the active mechanical behavior of the cell such as in locomotion [14], active response to external stresses and the propagation of cellular protrusions [4]. Since the mechanics of actin-myosin networks are determined by the ATP hydrolysis and the force generation by myosin, these systems are denoted as active networks. One therefore has to distinguish between an active state of the network, when ATP is present in a high concentration<sup>18</sup> and a passive state of the network near the absence of ATP. In the active state, the diffusion time of ATP to the ATPase site on the myosin molecule is much smaller than the average dwell time of the molecule in the rate limiting kinetic step. The ATP turnover and force generation are limited by the internal kinetics of the molecule. Myosin molecules therefore exert short force pulses (power strokes) on the actin filaments in a time interval of around 1 ms [45]. This is only a small part of the entire mechanical cycle, which has a duration of roughly 50 ms [15][151]. Since for the rate limiting kinetic step the myosin molecule is not bound to the filament, most of the time a myosin molecule will be detached from the actin filaments. Obviously this will not lead to an effective cross linking of the actin network. In the passive state, the diffusion time of residual ATP molecules to the ATPase sites of myosin molecules dominates the ATP turn over time and thus the kinetics of myosin. In the absence of ATP, myosin is firmly bound to actin. Therefore the myosin molecules will spend most of the time bound to actin and thus cross link the network. The transition from the active to the passive state of the network, through ATP depletion, can be observed with magnetic bead micro-rheology [152] [118][153]. The transition can be observed in a drastic stiffening of the network due to the increased number of cross links. Both storage and loss modulus ( $G'$  and  $G''$ ), which are measures for the stored respectively the dis-

---

<sup>17</sup>In this chapter, myosin denotes the regular muscle myosin II

<sup>18</sup> $c_{ATP} \gg c_{myosin}$

sipated deformation energy, of the actin network are strongly increased during the transition [118]. This is equivalent to a sol-gel percolation transition in a polymer network [154]. Even more interesting is the observation that during this transition from the active to the passive state of the network actin filaments are transported through the network [153]. This indicates, that with an increase in the number of cross links in the network, forces are exerted on free filaments, which are then propelled through the partly cross linked network.

An approach to measure these forces inside an actin-myosin network during the percolation transition was to embed phospholipid vesicles in the actin-myosin network to act as internal force sensors. The internal forces in the network should be visualized by a deformation of the vesicles during the percolation transition. The first approach for the choice of vesicles were electrostatically neutral vesicles, which repelled the actin from their surface. The molar lipid composition was very similar as for the vesicles with actin cortex inside (79.5% DMPC; 17% cholesterol; 3% DPPE-PEG; 0.5 % fluorescently labelled lipids (TexasRed DPPE)), but with the difference that the  $PEG_{2000}$  lipids had not positively charged amine group coupled to it. The vesicles were prepared by electro-swelling in a sucrose solution of 500 mOs osmotic pressure. The buffer for the actin-myosin network contained<sup>19</sup> 250 mM KCl, 4 mM MgCl, 1 mM DDT,  $10\mu M$  G-actin, 250 nM myosin,  $100\mu M$  ATP,  $10\mu M$  phalloidin with a total osmolarity of 540 mOs. At such a high osmolarity of the solution, the possible change of the osmotic pressure due to the hydrolysis of  $100\mu M$  ATP is negligible and can be ruled out as explanation for changes in the vesicle shape. To exactly control the ATP concentration of the solution, the storage buffer of the G-actin solution was dialyzed against a ATP-free buffer solution. At the buffer conditions used, the myosin molecules should not exist as individual molecules in solution but in the form of mini-filaments, anti-parallel assemblies of a few ten myosin molecules (figure 3.47). The anti-parallel structure of these mini-filaments should enable an anti-parallel movement of actin filaments by the myosin filaments and thus a contractile motion. The entire actin-myosin solution with the embedded vesicles was pipetted into a chamber

---

<sup>19</sup>including the volume of the vesicle solution in the final buffer solution

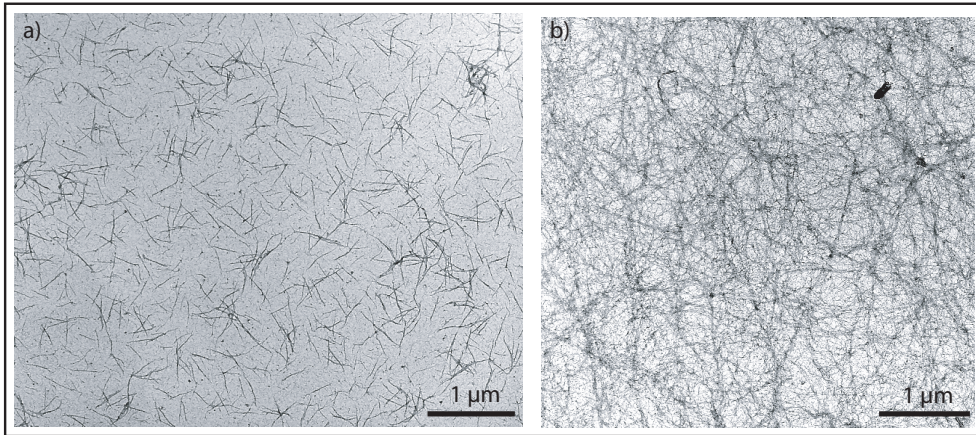


Figure 3.47: Electron micrographs of myosin mini-filaments and an actin - myosin network

**a) Filamentous muscle myosin II assemblies, prepared at 250 mM KCl concentration. b) An actin - myosin network, like the ones used in the experiments, prepared in presence of ATP. Visibly, the network is not completely homogeneous, with thicker, bundles like structures. Both samples shown were prepared with a negative staining technique.**

of the magnetic bead rheometer [152] operated by Rainer Tharmann. The magnetic rheometer was mounted on a Axiovert 200 microscope so that the sample could be observed in phase contrast and in fluorescence mode. A sinusoidal force of 1 pN amplitude and 0.3 Hz frequency was exerted on the beads in the central area of the chamber. For the observation, an area was selected in which a magnetic bead and a vesicle could be observed simultaneously. To avoid photochemical damage of the actin or myosin by radical formation at the fluorescently labelled lipids, the sample was observed before and during the transition in phase contrast at a wavelength of 633 nm where the excitation of TexasRed is extremely reduced. A problem for the observation of the vesicles in phase contrast mode was the scattering in the sample by the magnetic beads, which decreased the signal to noise ratio of the vesicle contour images.

### 3.5.2 Percolation and viscoelastic properties

The oscillation of the bead was observed until the amplitude decreased strongly and finally the bead oscillation could not be resolved anymore. Still no signif-

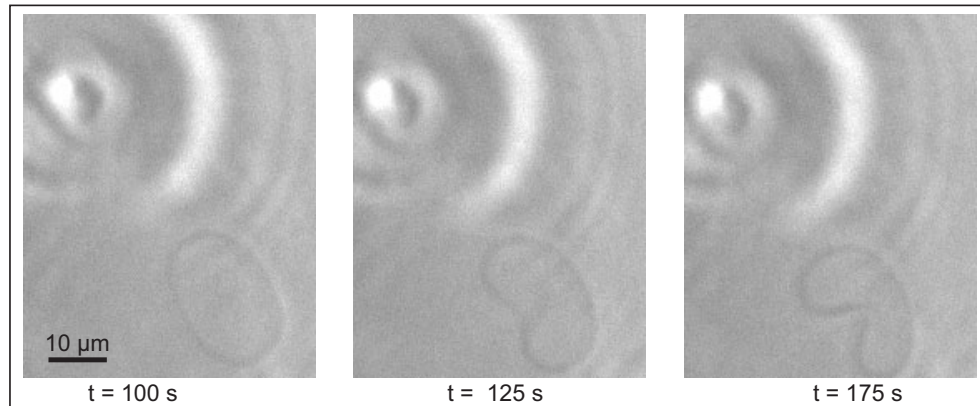


Figure 3.48: Snapshots from a movie taken during a sol-gel percolation transition in an actin myosin network

**During the transition from the active to the passive state of myosin in an actin network, forces are exerted on an embedded vesicle from a percolation structure, which strongly deform the vesicle. The origin of the time scale is set arbitrarily at a point before the transition.**

icant change in the contour of the vesicle could be observed. Thus although a percolation transition occurred no force transduction on the vesicle could be resolved. A second approach was to use vesicles, which bind to the actin network, as a force sensor. For this purpose, the  $PEG_{2000}$  – amine lipids, which were previously used for the actin cortex vesicles, were exchanged for the uncharged  $PEG_{2000}$  repeller lipids to ensure a strong coupling of the network to the vesicle surface. The same experimental procedure was applied to observe simultaneously a vesicle and a magnetic bead during the percolation transition. Figure 3.48 shows snapshots of the movie taken during the transition. The vesicle is strongly deformed during the transition. The correlation of the transition, visualized through the decreasing oscillation amplitude and the deformation of the vesicle is shown in figure 3.49. The fact that the percolation transition and the deformation of the vesicle happen at the same time indicates, that the actin myosin network contracts locally during the percolation transition. After the percolation transition, the whole sample was scanned for further examples of deformed vesicles, of which several different types were observed (see figure 3.50). Many of those show apparent invaginations as the one which was observed during the percolation transition.

From the bead oscillation amplitude  $X$ , the force  $F$  exerted on the magnetic

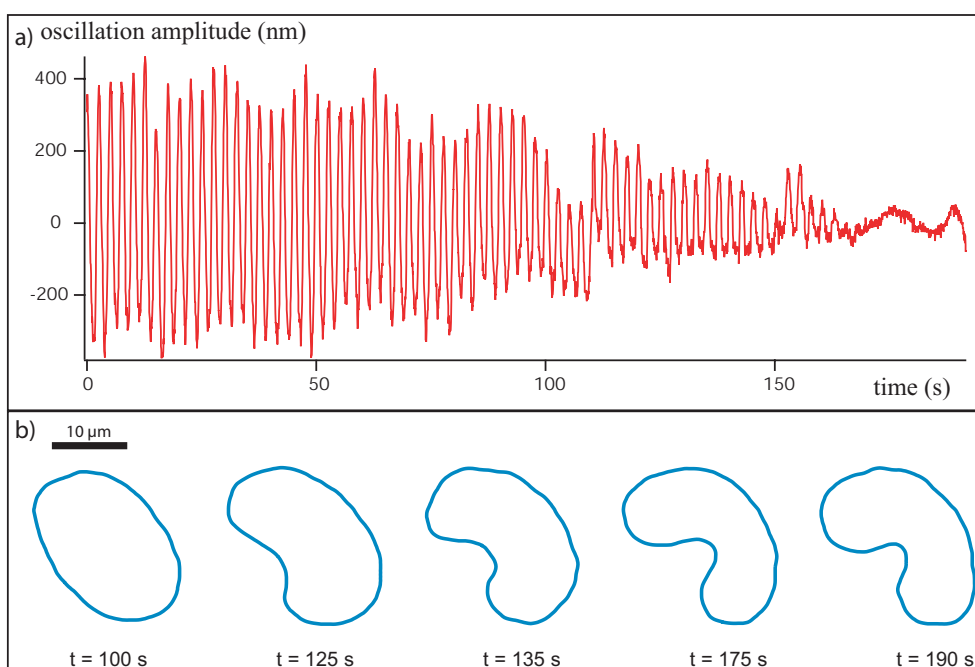


Figure 3.49: Time correlation between the damping of a magnetic bead oscillation and the deformation of an embedded vesicle in a percolating network. **a) Oscillation amplitude of a magnetic bead in an actin-myosin network during the transition from the active to the passive state of the network, induced by ATP depletion. b) The simultaneously observed contour of a vesicle embedded in a actin myosin network during the percolation transition. The contour of the vesicle was determined with the shape tracing algorithm described in in section 2.3.2**

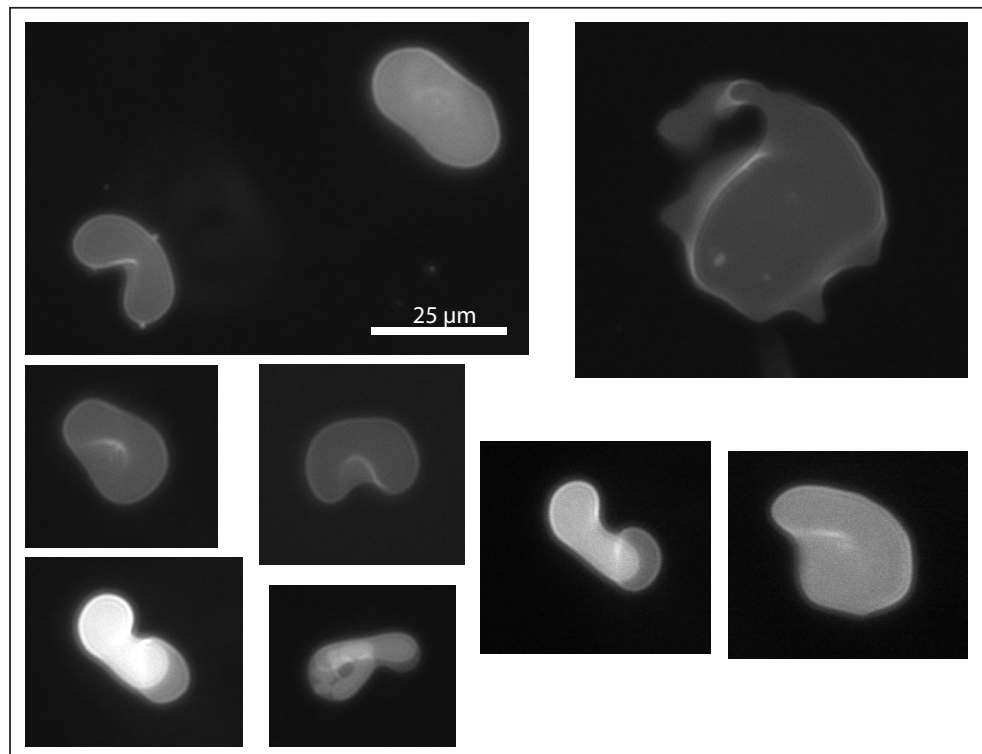


Figure 3.50: Fluorescence micrographs of deformed vesicles in an actin - myosin gel.

**Observed vesicle shapes after the complete percolation of the actin - myosin network. The vesicle seen in the top left image on the left hand side is the one which was observed during the percolation process. The scale bar is the same for all images.**

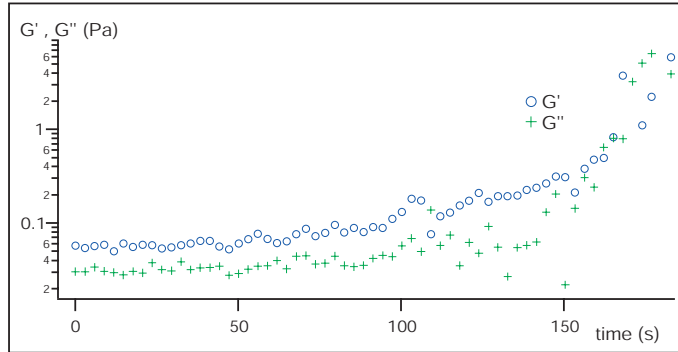


Figure 3.51: Time evolution of  $G'$  and  $G''$  of an actin-myosin network during the percolation transition.

bead and the phase shift  $\delta$  between the sinusoidal force signal and the equally sinusoidal oscillation of the bead, the storage modulus  $G'$  and the loss modulus  $G''$  of the network can be determined.

$$G' = \frac{F}{c \cdot X} \cdot \cos(\delta) \quad (3.65)$$

$$G'' = \frac{F}{c \cdot X} \cdot \sin(\delta) \quad (3.66)$$

$c$  is a constant pre-factor which describes the probe geometry. For the case of a spherical bead in a solution it is equal to the pre-factor for the viscous drag of the bead,  $6\pi R$ , where  $R$  is the radius of the bead. Since the amplitude of the bead oscillation is not constant over time, the two viscoelastic moduli were determined for each period of the bead oscillation (3 s) separately. Figure 3.51 shows the time evolution of the two moduli. The evolution of both moduli can be roughly divided into three parts of different behavior. Both moduli are nearly constant in the beginning ( $t = 0 - 50$  s), then increase slowly ( $t = 50 - 140$  s) before they increase drastically by over one order of magnitude in the short time ( $t = 140 - 170$  s) of the apparent transition. These three different time intervals can also be observed in the trajectory of the magnetic bead (figure 3.52), which is a superposition of the bead oscillation, as in figure 3.49, with the drift of the bead.

In the first time interval until approximately 50 s no drift is superimposed on the oscillation of the bead. Afterwards, a drift to the left (visible in the snapshots in figure 3.48) started which had a roughly constant velocity of 100 nm/s in the time interval between 80 and 140 s. At around 140 s the drift to

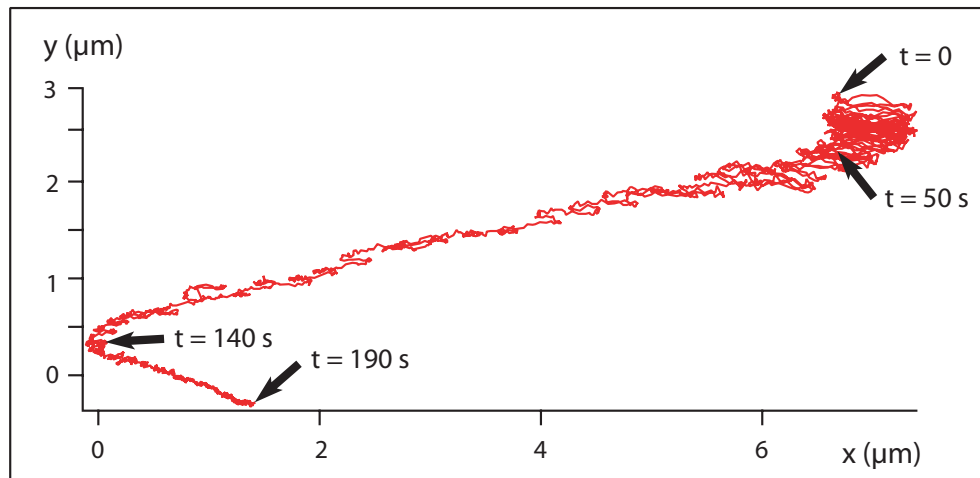


Figure 3.52: Trajectory of the oscillating magnetic bead in the percolating actin - myosin network

From a certain moment on ( $\approx 50$  s), additionally to the oscillatory movement, a large drift can be observed. The moments upon which the drift of the bead changes in magnitude or direction (50 s, 140 s) are indicated with an arrow in the trajectory. At the moment when the drift is inverted (140 s), the viscoelastic moduli drastically increase (see figure 3.51).

the left is stopped and finally nearly reversed in its direction with a velocity of approximately 40 nm/s. The drift of the bead indicates that, on the length scale of the bead, the percolation of the network does not happen homogeneously in the whole sample.

The contour of the vesicle was analyzed also during the transition (figure 3.49) using the shape tracing algorithm described in 2.3.2. As mentioned above, the image quality of the vesicle contour, acquired in phase contrast mode, was reduced due to the scattering of the beads in the sample. Therefore the shape tracing algorithm was modified in a way, that the line profiles across the contour were averaged over several parallel lines. Furthermore, the range of grey scales of the image was expanded to fill the entire available 8 bit scale. These modifications enabled the tracing algorithm to extract the vesicle contour in selected images (one every 3 s, which is the same time interval used for the sampling of the viscoelastic moduli). The curvature of the vesicle membrane along the contour in the plane of observation can be calculated with

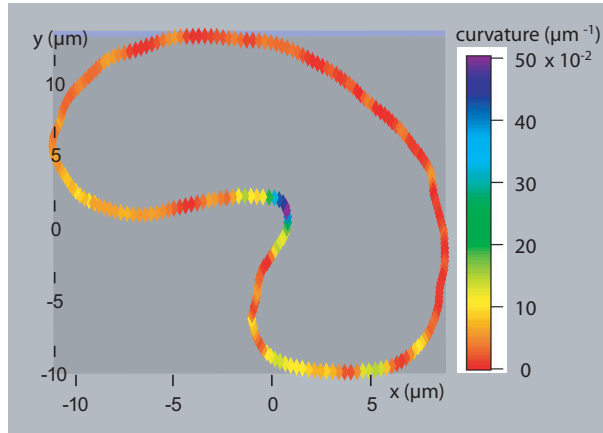


Figure 3.53: Curvature of a deformed vesicle in an actin myosin network after the percolation transition

**The color of the vesicle contour denotes the local curvature. Visibly the highest curvature of roughly  $(2\mu m)^{-1}$  exists at the invagination, which appeared during the percolation transition.**

the same parabolic fit method used for the actin filaments in section 3.4. The local curvature of the lipid membrane in the focal plane of the vesicle contour is shown for one image of a deformed vesicle in figure 3.53 in a color coded plot. The highest curvature of the membrane exists where the vesicle was deformed by the contracting actin network.

### 3.5.3 Three dimensional reconstruction of vesicles

The shape of vesicles is mainly determined by their surface area  $A$ , volume  $V$  and the spontaneous curvature of their membrane  $c_0$ . To retrieve the parameters  $A$  and  $V$  from the phase contrast images of the deformed vesicle, a three dimensional reconstruction of the vesicle is necessary. Since the contour of the vesicle, which was observed in the experiment contains only information about the form of the vesicle in the equatorial plane, certain assumptions, based on other observations have to be made. By changing the position of the focal plane it could be seen that the vesicle had a elongated, prolate form roughly given by a rotation of the equatorial contour (seen in figure 3.48 at  $t=100$  s) around its long axis. From the contour of the vesicle in the equatorial plane, this axis was determined by first calculating the distance from the center of mass for each contour point. The two opposite maxima of this distance were

fitted with a line, which was restricted to pass the center of mass. This fitted line determines the initial rotation axis of the vesicle body (see figure 3.54). This cigar like shape can be reconstructed by approximating the vesicle body by a large number of cylindrical slabs, perpendicular to the long axis (denoted as x-axis) of the vesicle. Each cylindrical slab has a diameter  $d_i$  equal to the diameter of the vesicle at the respective position  $x_i$  and a thickness  $\Delta x$ , which is the spacing of two contour points along the x-axis.

$$\Delta x = \frac{x_{i+1} - x_i}{2} + \frac{x_i - x_{i-1}}{2} = \frac{x_{i+1} - x_{i-1}}{2} \quad (3.67)$$

This reconstruction method is graphically illustrated in figure 3.54. The contour of the vesicle in the equatorial plane, which was determined with the contour tracing algorithm from the images, always contained more than 200 contour points with an average spacing of 250 nm. Thus the global shape of the vesicle was reconstructed as a body, given by more than 100 cylindrical slabs with diameters between 200 nm and 15  $\mu m$  and thicknesses  $\Delta x$  between 10 nm and 300 nm. Even though the continuous global shape of the vesicle was approximated by a number of finite cylindrical elements, the large number of elements used, allows a very accurate reconstruction. The volume  $V$  and surface area  $A$  of such a body are given by

$$V = \sum_i \left( \left( \frac{d_i}{2} \right)^2 \cdot \pi \cdot \Delta x_i \right) \quad (3.68)$$

$$A = \sum_i \left( d_i \cdot \pi \cdot \sqrt{(\Delta x)^2 + (d_{i+1} - d_i)^2} \right) \quad (3.69)$$

Using this method, the approximate volume and surface area of the vesicle were determined during the transition process when the vesicle was deformed (shown in figure 3.55). The surface area of the vesicle is constant, at around 1100  $\mu m^2$  with a standard deviation of only 3%, during the transition, which was expected, since the lipid bilayer of the vesicle is incompressible in the force range  $F$ , which can be expected from an assembly of molecular motors<sup>20</sup>.

Furthermore, the fact, that the retrieved surface area of the vesicle is constant, indicates that the method for the three dimensional reconstruction of

---

<sup>20</sup>1pN <  $F$  < 1nN

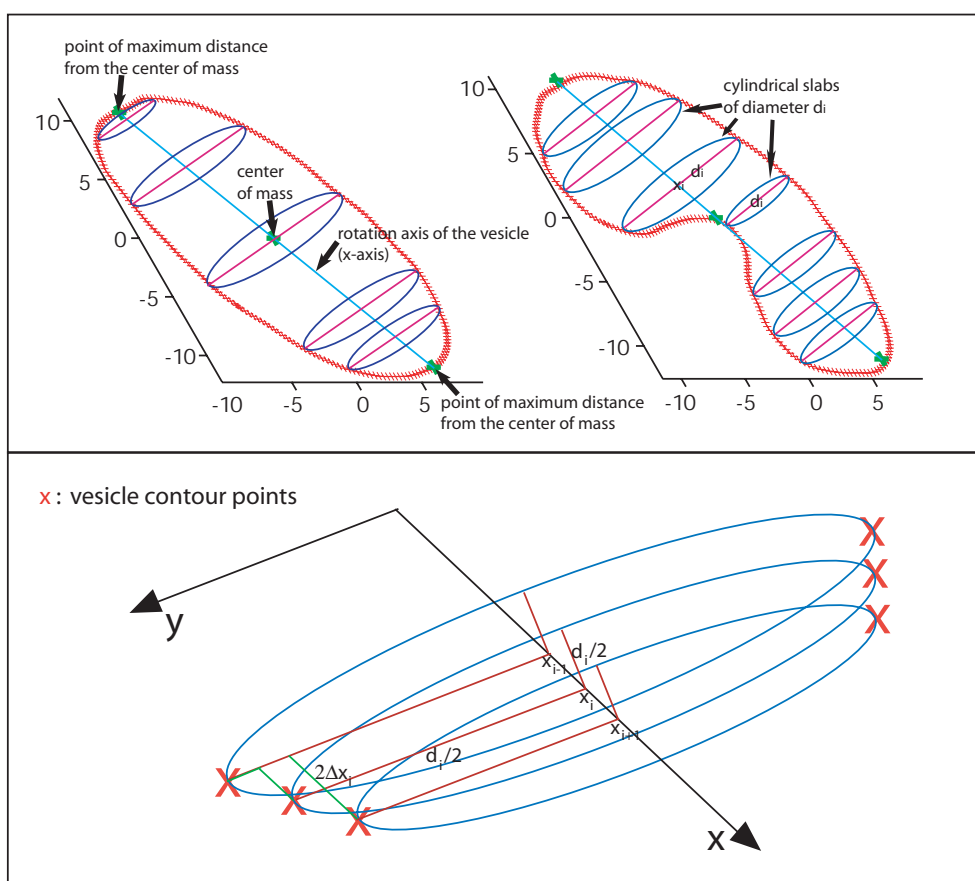


Figure 3.54: Schematics of the three dimensional shape reconstruction algorithm for a deformed vesicle

The body of the vesicle is reconstructed by a number of finite cylindrical slabs. These slabs are positioned perpendicular to the initial rotational axis of the equatorial contour of the vesicle, which was observed in phase contrast microscopy. The diameter  $d_i$  and the thickness  $\Delta x_i$  of the slabs is determined by the contour points of the vesicle projection. From the three dimensional body of the finite element reconstruction, the volume and surface area of the vesicle can be calculated using equations 3.68 and 3.69.

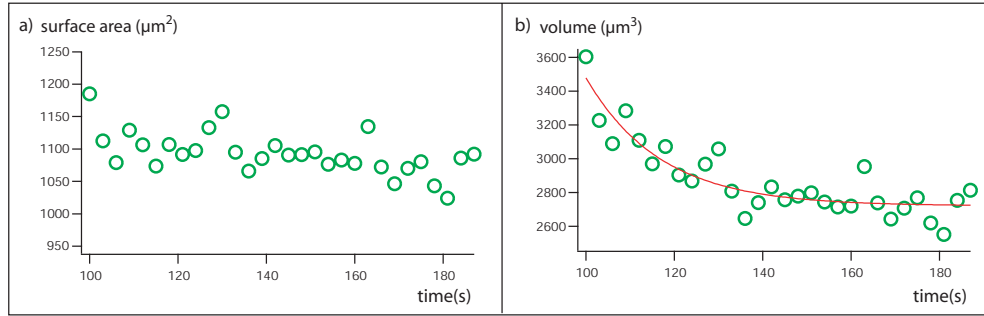


Figure 3.55: Evolution of the surface area and volume of a vesicle being deformed in a percolating actin network

**a) The surface area of the reconstructed vesicle stays constant during the deformation, which is a criterion for the validity of the reconstruction algorithm. b) The volume (circles) decreases initially fast from  $3600 \mu\text{m}^3$  to a stable final value of around  $2750 \mu\text{m}^3$ . The decrease can be approximated with an exponential decay (line).**

the vesicle shape is correct. The volume of the vesicle decreases from  $3600 \mu\text{m}^3$  before, down to roughly  $2750 \mu\text{m}^3$  after the transition, which is a decrease of nearly 25 %. This means that the contracting network induces an external pressure on the vesicle, which leads to a water transport through the membrane of the vesicle. The decrease in volume of the vesicle can be fitted with a function of the type

$$V = V_0 - \Delta V \cdot (1 - e^{-\frac{t}{\tau}}) \quad (3.70)$$

which leads to fit parameters of the initial volume  $V_0$  of  $3453 \pm 37 \mu\text{m}^3$ , of the decrease in volume  $\Delta V$  of  $752 \pm 72 \mu\text{m}^3$  and the characteristic time  $\tau$  of  $18.2 \pm 3.6\text{s}$ . The transport of water through the membrane is given by the negative time derivative of the Volume.

$$-\frac{dV}{dt} = \frac{\Delta V}{\tau} \cdot e^{-\frac{t}{\tau}} \quad (3.71)$$

### 3.5.4 Contraction forces

The integrated curvature of the membrane over the surface of the vesicle is a measure of the bending energy  $E_b$  of the vesicle. Since actin filaments are electrostatically attached to the membrane, the bending stiffness of the membrane  $\kappa$  is not known exactly. Therefore to describe the bending energy, the

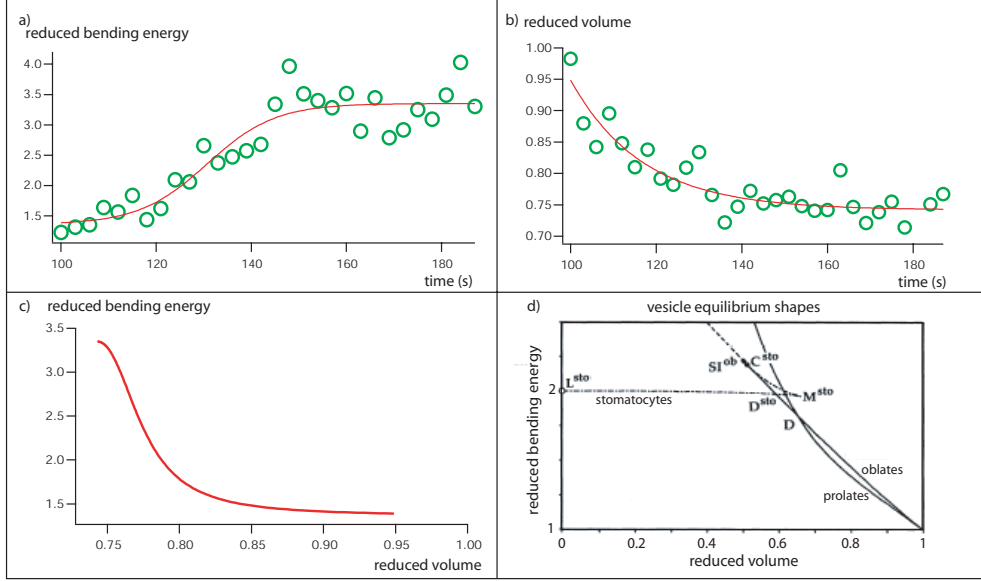


Figure 3.56: Characteristic dynamic parameters for the deformation of the vesicle in the percolating network

a) The evolution of the reduced bending energy of the vesicle during the transition (circles) and its sigmoid fit (line). b) The reduced volume of the vesicle during the transition (circles) and its exponential decay fit (line). c) The deformation process of the vesicle described by the evolution of the parameters of the reduced volume and bending energy. d) Theoretically predicted phase diagram for equilibrium shapes of phospholipid vesicles without spontaneous curvature (source: Seifert et al [155]).

reduced bending energy  $E_r$ , which is a normalized energy, relative to the spherical shape of a vesicle, is used. If  $C_1$  and  $C_2$  are the two principle curvatures of the surface, the reduced bending energy is given as

$$E_r = \frac{E_b}{8\pi\kappa} = \frac{1}{16\pi} \cdot \oint (C_1 + C_2)^2 dA \quad (3.72)$$

Equivalently the reduced volume is the volume of the vesicle normalized on the volume of a spherical vesicle of equal surface area  $A$ .

$$V_r = \frac{V}{\frac{4}{3}\pi(\sqrt{A/4\pi})^3} \quad (3.73)$$

The reduced bending energy and volume are shown in figure 3.56a) and b). The fit for the reduced bending energy is a sigmoid function of the type

$$E_r = E_{r0} + \frac{\Delta E_r}{1 + e^{\frac{(t_{1/2}-t)}{\tau}}} \quad (3.74)$$

and the the fit function for the reduced volume the same exponential used for the volume. The sigmoid function has no theoretical foundation for the bending of the vesicle and thus simply describes the transition from a initial state of reduced bending energy  $E_{r0}$  to a final state of  $E_{r0} + \Delta E_r$ . This fit function is plotted versus the fit function of the reduced volume as a line of transition of the vesicle (Figure 3.56c ). The resulting diagram describes a transition of the vesicle in the  $V_r - E_r$  plane and can be used as a comparison with phase diagrams of phospholipid vesicles equilibrium states. Equilibrium states are determined by a minimum of the bending energy of a vesicle for given surface area, volume and spontaneous curvature. The latter is a measure for the asymmetry of the lipid bilayer and will be neglected in the following for simplicity. The main shapes for vesicles without spontaneous curvature are prolates, oblates and stomatocytes. The latter are roughly spherical shapes with an invagination, a shape, which could in about describe the final shape of the vesicle in the percolating actin network. Therefore, if it is possible to relate the deformation of the vesicle to a prolate - stomatocyte transition, an isotropic external pressure can be determined from which an isotropic force of the network on the vesicle can be calculated. A phase diagram for phospholipid vesicles from Seifert et al [155] is shown in figure 3.56d as comparison with the graph determined for the vesicle in the actin network. In comparison with the vesicle shape transformation phase diagram shown in figure 3.56d, the transition line for the vesicle in the actin - myosin network first decreases in its reduced volume from 0.95 to 0.85 without significant increase in the reduced bending energy. For the phase diagram of phospholipid vesicle equilibrium shapes one sees a roughly constant increase in bending energy with decreasing volume. Between reduced volumes of 0.8 and 0.75, the bending energy of the vesicle in the actin network increases sharply by more than a factor of two. Again such a drastic increase can not be observed for vesicle equilibrium shapes. What actually makes the hypothesis of the observed deformation as a equilibrium phase transition even more unlikely, is that in the phase diagram of equilibrium shapes, the branch of the stomatocyte shape bifurcates from the oblate branch and not from the prolate as in the experiment. Therefore it can be assumed that the vesicle deformation is not an equilibrium shape caused

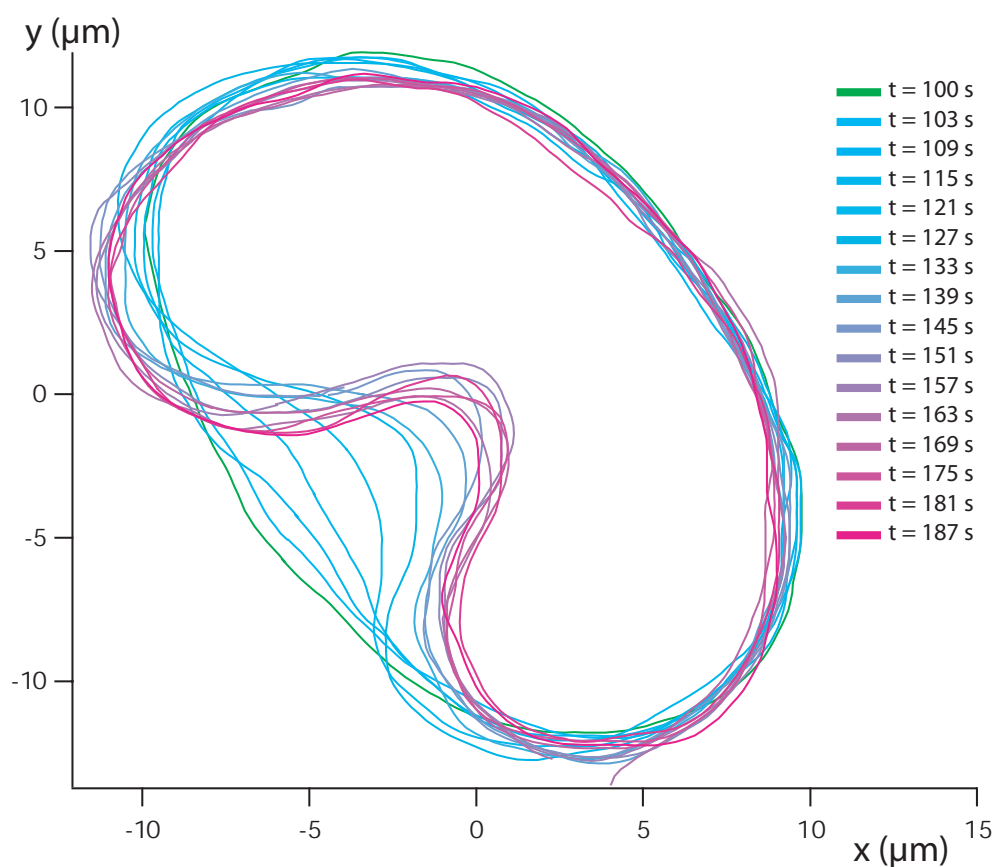


Figure 3.57: Superposition of vesicle contours at different moments during the percolation transition

**The contours of the deforming vesicle were superimposed with time intervals of 6 s. Visibly, the deformation is localized in form of a invagination on the left hand side.**

by isotropic external pressure.

Thus the only possibility to retrieve an approximation of the forces acting on the vesicle is to analyze locally the deformation and estimate local deformation forces. Figure 3.57 shows a superposition of the contours of the vesicle in its center of mass coordinate system during the percolation transition. Visibly, the deformation is restricted to its left side, where an invagination is formed.

An analysis of the three dimensionally reconstructed vesicle shapes showed that the main deformation of the vesicle concerns only 8 % of its total surface area. For simplicity one can assume that an homogeneous pressure on this

part of the surface causes the invagination of the vesicle and thus the decrease in volume. The differential change in free Energy  $dE$  is given by the change in bending energy of the vesicle and is equal to the change in pressure  $p$  on the part of the vesicle surface and the differential change in volume of the vesicle  $dV$ .

$$dE(V) = p \cdot dV \quad (3.75)$$

Thus the derivative of the bending energy  $\frac{dE(V)}{dV}$  as a function of the volume of the vesicle determines the pressure  $p$ . To determine the absolute value of the bending energy of the vesicle an estimate for the bending stiffness of  $1000 k_b T$  was used. This is a reasonable value for a vesicle with actin bound to its membrane and was determined in the experiments with vesicles with an inner actin cortex bound to their membrane in chapter 3.3. Since the pressure was assumed to be homogeneously distributed on the part of the surface of the vesicle which was strongly deformed, a multiplication of the surface area with the pressure returns the force acting locally on the vesicle. Figure 3.58 shows the evolution of the force on the vesicle during the percolation transition.

The force acting on the vesicle first increases slowly, then sharply and reaches a maximum at  $t = 137$  s during the transition. This moment of maximum force acting on the vesicle coincides with the sharp increase in the viscoelastic moduli at  $t \approx 140$  s (see figure 3.51). Furthermore, looking at the trajectory of the magnetic bead in figure 3.52, one sees, that also at this moment, the drift of the bead is inverted. This moment is probably the transition from a local to a global percolation, leading from a partly to a completely cross-linked state of the actin network. This assumption is further strengthened by the fact that actin networks are mechanically rather inhomogeneous, even on the micron scale [156] [157][158]. The structure of actin - myosin networks is shown in figure 3.47. The distribution of myosin mini-filaments does not have to be homogeneous either, such that a initially local percolation of part of the network seems plausible.

The magnitude of force exerted on the vesicle, with a maximum force of roughly 100 pN is very well in the range expected from an assembly of myosin motor molecules. Optical trap studies have shown, that one individual myosin

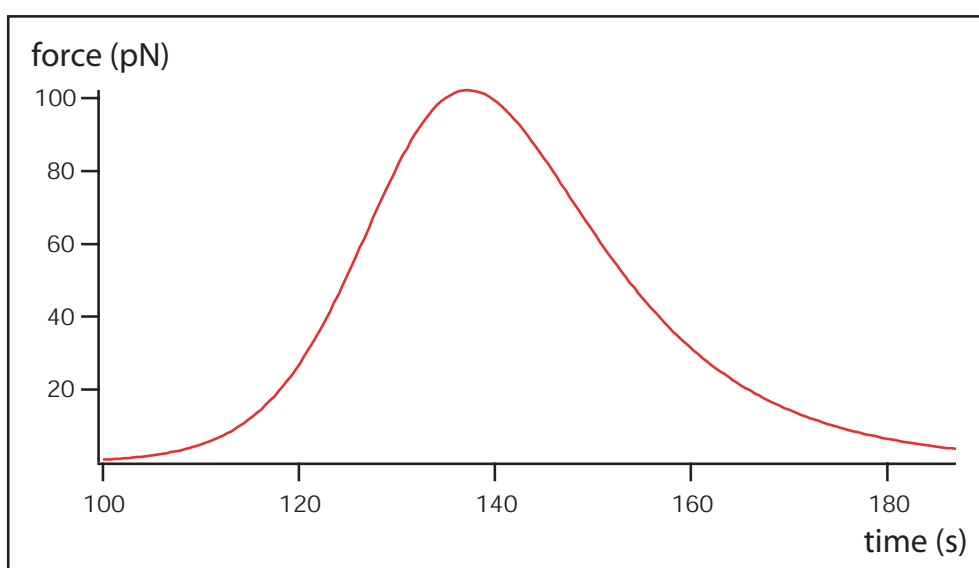


Figure 3.58: Force acting on the vesicle in the actin network during the percolation transition

The force acting on the small part of the vesicle surface area, where the invagination was formed, was calculated from the derivative of the bending energy vs. volume relation of the vesicle ( $\frac{dE(V)}{dV}$ ), shown in reduced values in figure 3.56c . The maximum deformation force of the entire process, which is a bit more than 100 pN occurs at the moment ( $t = 137$  s), when the viscoelastic moduli  $G'$  and  $G''$  increase strongly (figure 3.51).

molecule can exert forces of around 3 - 4 pN [159]. Cellular processes, which are driven by the actin - myosin cytoskeleton, exert forces of more than 5 nN at protrusion retraction of macrophages [160] and of 10 - 30 nN at the contractile motion of cardiac cells [10][161]. Therefore it seems, that in the percolating network large assemblies of myosin molecules work together to achieve higher forces. Looking at the velocity of the deformation, the vesicle bilayer is deformed at a maximum velocity of 290 nm/s. This is much slower than for example the translocation of actin filaments by surface adsorbed myosin molecules in motility assays, where velocities around 3 or 4  $\mu\text{m}/\text{s}$  are typically observed [75]. The coordination of myosin molecules in larger assemblies to achieve higher forces leads apparently to a decrease in translocation velocity, because the biochemical cycles of the molecules are not exactly in phase.

# Chapter 4

## Conclusion and Outlook

In the context of this work, many mechanical properties of biological matter, from individual molecules to complex multi-component bio-materials have been investigated. Although in the five chapters, five different systems have been investigated, a common link is the actin filament, which is a major part of every system studied. For the motor protein myosin V, actin filaments serve as rails for their movement and as binding partner. As shown in chapter 3.1, the actin filament determines the step size and the kinetics of the motor molecule. The binding potential between actin and the actively moving myosin V molecule seems to be slightly different from ligand receptor pairs. The low dissociation constant in combination with the high force sensitivity of the bond may also play a role for the function of the molecule in organelle transport processes. Due to the initially low dissociation rate, the molecule and its cargo can move for long distances along the actin cytoskeleton. However, upon a force acting on the molecule, e.g. an entanglement of the cargo in the bulk cytoskeleton, or the encounter of a cell organelle, for which the cargo is aimed, the high force sensitivity of the bond leads to a dissociation of the molecule from the actin filament. Thus, jamming or blocking of the filament for other molecules can be avoided. Thus, the experiments in which the transport and for the first time the binding properties of myosin V and actin have been studied, show not only possible molecular mechanisms of a strain induced coordination of the two actin binding domains of the motor molecule, but also indicate the role of the molecule as a very effective cellular transporter.

The bulk material properties of actin (Young modulus of  $3.1 \cdot 10^8 N/m^2$ , see

chapter 3.2.3) do not differ much from other polymeric bio-materials, such as wood<sup>1</sup>. This leads to a persistence length of actin filaments (determined to 15 - 17  $\mu m$  in chapter 3.2.3), which is in the order of the dimensions of eucaryotic cells. Therefore on these length scales, networks, which provide stability to the cells, can be formed at extremely low volume fractions of actin.

However, the elastic or viscoelastic properties of actin structures, such as bundles, or networks are primarily determined by the self-assembly of actin filaments into complex bio-materials. The examples for such complex actin structures are the actin-filamin bundles and the quasi two dimensional network in chapter 3.2 and the composite actin-lipid membrane of the cortex containing vesicles in chapter 3.3. These complex actin networks exhibit values for their Young moduli, which are first, many orders of magnitude below that of bulk actin and second very variable depending on their geometry and density. A beautiful example for the influence of the geometry of a network on its mechanical properties is the anisotropy of the actin filament assembly inside giant phospholipid vesicles. A shear deformation of the actin-membrane composite sheet, which has one deformation mode longitudinal to the filament orientation, shows a much smaller elastic modulus than a bending deformation, which has its deformation modes transverse to the filament orientation. This highlights the relation between the structure and mechanical properties of filament assemblies. Another interesting aspect is, that from an initially hard material, soft structures can arise by smart self-assembly. The variability of self-assembled composite actin structures and the differences in their mechanical properties is probably the most astonishing fact about them. When for example actin filaments are mixed in a dilute bulk solution with filamin, thick bundles are formed. When the filaments are attached to a flat patterned surface before filamin is added to the solution, a irregular bundle network is formed. Whereas when the filaments are attached to separately standing pillars in an array on the substrate, a regular network, mimicking the geometry of the array, is formed. As shown in chapter 3.2.4, highly cross-linked actin - filamin bundles exhibit the same Young modulus as actin filaments. The

---

<sup>1</sup>shear value in fiber direction

composite actin - filamin network probed, had Young moduli, which were orders of magnitude smaller. This shows that composite bio-materials, which are formed from the same components, vary not only in structure, but also in their mechanical properties, depending on their way of self assembly. The principle of a high variability of structure and function is a key principle of the cellular cytoskeleton. Cells have to adapt with their mechanical properties to changes in their environment. Only a highly dynamic and variable network can keep up its function, such as mechanical stability, cell signaling or organelle transport at a level of complexity of the cell cytoskeleton. While the dynamics of the cytoskeleton arises from constant de- and re-polymerization of the bio-polymers and the binding and unbinding of the related proteins, the experiments presented in this work highlights the possibility, that the variability of composite actin structures in eucaryotic cells arises from an interplay of active cellular signalling and a sensitive self-assembly process.

Furthermore, the biomimetic model system of the phospholipid vesicles with internal actin cortex exhibits mechanical properties, which can be attributed to the characteristic mechanical behavior of actin filament solutions. The separation of time scales, which was observed, exists in entangled actin networks as well as for cells [139]. This does not only show that the actin cortex vesicles are well suited models to mimic cytoskeleton structures of the cellular actin cortex, but also highlights the important role of general principles of the mechanics of semi-flexible polymers for cell mechanics.

The static behavior of individual actin filaments is entirely determined by its elastic properties, whereas the dynamics are determined by an interplay of hydrodynamic and elastic properties of the filament. This was shown in chapter 3.4, where actin filaments were bent and folded in a hydrodynamic flow. Since actin filaments exhibit a set of Eigenmodes, their wavelength and relaxation times are a correlated set of length and time scales that regulate the filament dynamics. Mechanical processes which happen on a certain time scale, give rise to a response on a certain length scale. This scaling behavior, which determines the frequency ( $\omega$ ) dependent storage and loss moduli of viscoelastic materials, is well known for entangled actin networks [32][162]. The high frequency response for example is determined by the density of relaxation

modes of individual filaments and shows a frequency scaling of the viscoelastic moduli as  $\omega^{\frac{3}{4}}$  [162][163]. The experiments investigating the dynamic bending and folding of actin filaments under hydrodynamic force show for the first time directly the correlation of length and time scales of individual bio-polymers and therefore establish a new foundation of the theory of semi-flexible polymer mechanics.

Active actin - myosin networks finally show contraction forces during a percolation, induced by the depletion of ATP in the system. Although the mechanism of the contraction is not clear yet, it seems that local percolation structures contract and exert forces on embedded vesicles. The magnitude of the deformation force on a vesicle of around 100 pN indicates the collective action of many myosin molecules, assembled in small filamentous structures, resembling assemblies in the cytoskeleton or in muscle cells. Contractile forces play an important role for many cellular functions. Many of those, such as cell migration are known to be determined by the actin - myosin cytoskeleton [14][164]. Another example, where actin myosin networks are implicated in cell contractions is the contraction of retinal cell for light intensity adaptation. The injection of inactivated myosin fragments into retinal cells inhibited these contractile movements [165]. Thus active actin - myosin networks seem to be well suited model systems to study basic mechanical properties of processes which occur in a similar way in cell mechanics.

The experiments presented in this doctoral thesis are all new approaches to study the mechanics of biological molecules and materials. Therefore, based on the results obtained, many following experiments could give further insight into this new and exciting field.

On the instrumentation side, the combination of a magnetic tweezers with an optical trap would enable the experimentalist to exactly position the magnetic beads on the sample. The basic problem of this approach is that the laser light scattering force of magnetic beads is much larger than for simple polystyrene beads and therefore the trapping in a simple gaussian focus profile is not a trivial task. A parallel data acquisition with a CCD camera and

a four point photo diode would push the temporal resolution of the experiments from the millisecond to the microsecond range and would open a new dynamic range for viscoelastic creep and relaxation experiments. New camera types like Peltier cooled devices and electron multiplying, back-illuminated CCD (EMCCD) cameras achieve quantum efficiencies of up to 90 % and extremely reduced read-out noise [166] [167]. In combination with total internal reflection fluorescence (TIRF) it is possible to achieve excellent signal to noise ratios, which opens the door to single molecule and quantitative fluorescence experiments with a spacial resolution in the nanometer range [66]. Thus by simultaneously observing individual steps and ATP hydrolysis events of the myosin V molecule, the chemo-mechanical coupling could be studied.

To retrieve more information about the mechanical properties of the quasi two dimensional actin networks, self-assembled on pillar array substrates, the group of Prof. J. Spatz is currently working to make the PDMS substrates less rigid, such that a force of a few piconewtons, exerted parallel to the array, would already lead to a remarkable bending of an individual pillar. Then, when pulling on a magnetic bead bound to the actin network, such as shown in figure 3.20, the neighboring pillars would be bent by the stress transmitted through the network and serve as force sensors to visualize the strain field in the network. Also for the visualization of the strain field in a percolating actin - myosin network, a softer PDMS pillar array would be an excellent force sensing tool. Therefore it was already tried to detect a bending of the individual pillars during a percolation process of an actin myosin network embedded between the pillars of the array. However, since the force constant for the deflection of the individual pillars is still around 1 N/m, and the forces are around 100 pN, it is not surprising that no deflection of the pillars could be observed.

A future direction for the research on cell model systems like the actin cortex containing vesicles are surely modifications of the actin cortex. Instead of electrostatically binding the cortex to the membrane, biotinylated actin filaments could be bound via streptavidin to biotin lipids in the membrane. This would likely lead to a different structure of the cortex, since the filaments would

be bound to discrete sites on the bilayer and not by a continuous filament - membrane surface interaction. Another interesting modification of the actin cortex structure would be to introduce different actin binding proteins into the system. Gelsolin, a capping protein could be used to modify filament length of actin and alpha - actinin as well as filamin could be used as actin filament cross linker to create different cortex structures. Furthermore, since alpha - actinin shows a temperature dependent binding behavior [168][169], the sample temperature could be used as a switch to modify the cortex structure in situ. Last, bulk samples, enclosed in giant phospholipid vesicles could be probed for their viscoelastic properties, to study finite size effects of bio-materials in confined space.

The evaporating droplets of the actin filament solution have nicely given an insight to the dynamics of individual filaments. An observation, which has not been discussed in this thesis is that, when the triple interface line was not pinned but slowly moving, the actin filaments showed a parallel aligned order in the dried regions. This can be due to the confinement in the flat edge of the droplet, where one dimension of the system is smaller than the persistence length of the filaments. The critical concentration for a isotropic - nematic phase transition, which is around 50 - 100  $\mu M$  for a bulk sample [170][171] may be lowered for a two dimensional system and could be achieved through the evaporation. Another possible explanation for the observation is a shear induced order of the polymers by the moving triple interface line. However, although evaporating solvent droplets are one of the simplest experimental samples, there are still several open questions about their internal structure formation mechanisms.

Finally, little is known about active actin - myosin networks, their internal structure and the mechanism of their contraction. Random forces inside these networks seem to change the ratio of longitudinal to transverse filament modes and the apparent persistence length of the filaments [172]. Anisotropic contractions of the network occur upon the percolation transition. To gain further knowledge about the shape of embedded vesicles in the network, three

dimensional images, taken with a fast laser scanning confocal microscope during the transition would mean one more step towards the understanding of this phenomenon. Multi particle tracking [173] inside these networks could map the anisotropic contractile forces and show local percolations. To get an insight into the structure of the percolating network and the distribution of actin and myosin, the use of new techniques of electron microscopy, such as cryo electron-tomography [174] or liquid phase electron microscopy [175][176] would further improve the understanding of the contraction process.

The broad range of experimental systems analyzed, from single motor molecules to complex composite structures, like the actin cortex containing vesicles, reflects the diverse functions of the actin cytoskeleton. As already mentioned, all experiments presented in the context of this doctoral thesis, are novel approaches to investigate the mechanical properties of biomimetic model systems of the cell cytoskeleton. New experimental setups had to be designed and new data analysis methods developed. With the exception of the determination of the persistence length of a single actin filament, all experiments described are the first of their kind. This is one of the major reasons, why in a relatively short time of two and a half years many new and exciting results could be produced and explained, whereas some observations are probably not completely understood. The other major reason is the excellent collaboration with colleagues, which became friends and the atmosphere in an institute, which should serve as a model system itself. One last thing is left to say: It was fun.

# Appendix A

## Appendix

### A.1 Chemicals

The important chemicals used for the buffer solutions are listed are shortly described. All chemicals were purchased at Sigma Aldrich.

#### A.1.1 Ascorbic acid

Ascorbic acid (vitamin C) is an anti-oxidant, which prevents the proteins in the buffer solution from oxidation by free radicals. Since in fluorescence probes a high number of free radicals are created by photochemical processes, the use of anti-oxidants is generally recommended. The molecular weight is 176.12 D.

#### A.1.2 Glucose Oxidase

Glucose oxidase is a 160 kD enzyme that catalyzes the oxidation of glucose to glucono-lactone. For this reaction one oxygen molecule is used and one hydrogen peroxide molecule produced. Thus glucose oxidase can be used to remove oxygen from aqueous solutions. This is important in applications where fluorescence dyes are used as labels, because oxygen radicals, produced in photochemical processes, damage proteins and chromophores and induce a decrease of the fluorescence intensity with time.

#### A.1.3 Catalase

Catalase is a 250 kD enzyme that activates the decomposition of hydrogen peroxide. It is a natural antioxidant which protects proteins, lipids or nucleic

acids from oxidative damage. In the experiments catalase was used to remove the hydrogen peroxide, that had been produced by the activity of glucose oxidase, from the buffer.

## A.2 Buffer composition

### A.2.1 A buffer

25 mM imidazole    pH 7.6  
25 mM KCl  
4 mM  $MgCl_2$   
1 mM DTT  
10 mM Glucose  
Glucose Oxidase + Catalase

### A.2.2 B buffer

25 mM imidazole    pH 7.6  
600 mM KCl  
4 mM MgCl  
1 mM DTT  
10 mM Glucose  
Glucose Oxidase + Catalase

### A.2.3 G\* buffer

10 mM TRIS    ph 8  
0.5 mM ATP  
0.2 mM  $CaCl_2$   
0.2 mM DTT  
0.2 mM ascorbic acid

**A.2.4 F buffer**

10 mM TRIS    ph 8

0.5 mM ATP

2 mM  $MgCl_2$

100 mM KCl

0.2 mM DTT

0.2 mM ascorbic acid

**A.3 Abbreviations**

ADP	-	Adenosine Di-Phosphate
ATP	-	Adenosine Tri-Phosphate
DMPC	-	DiMyristoylPhosphatidylCholine
DMPE	-	DiMyristoylPhosphatidylEthanolamine
DTT	-	DiThioThreitol
FITC	-	FluoreszeinIsoThioCyanat
GTP	-	Guanosine Tri-Phosphate
HMM	-	Heavy MeroMyosin
NEMHMM	-	N-EthylMaleimide(NEM)-modified Heavy MeroMyosin
PDMS	-	PolyDiMethylSiloxane
RICM	-	Reflection Interference Contrast Microscopy
TRITC	-	TetraethylRhodamine IsoThioCyanate

# Bibliography

- [1] A.R. Bausch, U. Hellerer, M. Essler, M. Aepfelbacher, and E. Sackmann. Rapid stiffening of integrin receptor-actin linkages in endothelial cells stimulated with thrombin: A magnetic bead microrheology study. *Biophys. J.*, 80:26492657, 2001.
- [2] T.D. Pollard and G.G. Borisy. Cellular motility driven by assembly and disassembly of actin filaments. *Cell*, 112:453 – 465, 2003.
- [3] A. Mogilner and G. Oster. Cell motility driven by actin polymerization. *Biophys. J.*, 71:30303045, 2003.
- [4] M.P. Sheetz, D.B. Wayne, and A.L. Pearlman. Extension of filopodia by motor-dependent actin assembly. *Cell Motility Cytoskeleton*, 22:160 – 169, 1992.
- [5] A. Mogilner and G. Oster. The physics of lamellipodial protrusion. *Eur. Biophys. J.*, 25:4753, 1996.
- [6] E.L. McNeil, D. Tacelosky, P. Basciano, B. Biallas, R. Williams, P. Damiani, S. Deacon, C. Fox, B. Stewart, N. Petruzzi, K. Osborn, C. and Klinger, J.R. Sellers, and King Smith C. Actin-dependent motility of melanosomes from fish retinal pigment epithelial (rpe) cells investigated using in vitro motility assays. *Cell Motility and the Cytoskeleton*, 58:7182, 2004.
- [7] J.V. Small, K. Rottner, P. Hahne, and K.I. Anderson. Visualising the actin cytoskeleton. *Microscopy Research and Technique*, 47:317, 1999.

- [8] B. Alberts, D. Bray, J. Lewis, M. Raff, K. Roberts, and J. D. Watson. *Molecular Biology of the Cell*. Garland Publishing, Inc., New York, 4th edition, 1994.
- [9] M.C. Wagner, B. Barylko, and J.P. Albanesi. Tissue distribution and subcellular localization of mammalian myosin i. *J. Cell Biol.*, 119:163–170, 1992.
- [10] N. Q. Balaban, U.S. Schwarz, D. Riveline, P. Goichberg, G. Tzur, I. Sabanay, D. Mahalu, S. Safran, A. Bershadsky, L. Addadi, , and B. Geiger. Force and focal adhesion assembly: a close relationship studied using elastic micropatterned substrates. *Nature Cell Biology*, 3:466–472, may 2001.
- [11] F. Wang, L. Chen, O. Arcucci, E. Harvey, B. Bowers, Y. Xu, J. Hammer, and J. Sellers. Effect of adp and ionic strength on the kinetic and motile properties of recombinant mouse myosin v. *The Journal of Biological Chemistry*, 275(6):4329–4335, 1999.
- [12] E. De La Cruz, A. Wells, S. Rosenfeld, E. Ostap, and H. Lee Sweeney. The kinetic mechanism of myosin v. *PNAS*, 96(24):13726–13731, 1999.
- [13] X. Wu, B. Bowers, K. Rao, Q. Wei, and J.A. Hammer. Visualization of melanosome dynamics within wild-type and dilute melanocytes suggests a paradigm for myosin v function in vivo. *J. Cell Biol.*, 143(7):1899–1918, 1998.
- [14] C.G. Galbraith and M.P. Sheetz. Keratocytes pull with similar forces on their dorsal and ventral surfaces. *J. Cell Biol.*, 147(6):1313–1323, 1999.
- [15] J. Howard. Molecular motors: structural adaptations to cellular functions. *Nature*, 389:561–567, 1997.
- [16] C. Veigel, F. Wang, M. L. Bartoo, J.R. Sellers, and J.E. Molloy. The gated gait of the processive molecular motor, myosin v. *Nature Cell Biology*, 4(1):59–65, Jan. 2002.

- [17] K. Svoboda, C. F. Schmidt, B. J. Schnapp, and S. M. Block. Direct observation of kinesin stepping by optical trapping interferometry. *Nature*, 365:721727, 1993.
- [18] T. Yanagida, S. Esaki, A. Hikikoshi Iwane, Y. Inoue, A. Ishijima, K. Kitamura, H. Tanka, and M. Tokunnga. Single motor mechanics and models of the myosin motor. *Phil. Trans. R. Soc. London B*, 355:441 – 447, 2000.
- [19] A. Mehta, R. Rock, M. Rief, J. Spudich, M. Mooseker, and R. Cheney. Myosin v is a processive actin-based motor. *Nature*, 400:590–593, 1999.
- [20] M.J. Schnitzer and Block S.M. Kinesin hydrolyse one atp per 8 nm step. *Nature*, 388:386 – 390, 1997.
- [21] M. Rief, R. Rock, A. Mehta, M. Mooseker, R. Cheney, and J. Spudich. Myosin v stepping kinetics: A molecular model for processivity. *PNAS*, 97(17):9482–9486, 2000.
- [22] C. M. Coppin, J. T. Finer, J. A. Spudich, and R. D. Vale. Detection of sub-8-nm movements of kinesin by high-resolution optical-trap microscopy. *PNAS*, 93:19131917, 1996.
- [23] M. J. Schnitzer, K. Visscher, and S. M. Block. Force production by single kinesin motors. *Nature Cell Biology*, 2:718–723, Oct. 2000.
- [24] M. Strigl, D.A. Simson, C.M. Kacher, and R. Merkel. Force-induced dissociation of single protein a-igg bonds. *Langmuir*, 15:7316–7324, 1999.
- [25] S.P. Tha, J. Suster, and H.L. Goldsmith. Interaction forces between red cells agglutinated by antibody. ii. measurement of hydrodynamic force of breakup. *Biophys. J.*, 50:1117 – 1126, 1986.
- [26] M. Grandbois, M. Beyer, M. Rief, H. Clausen-Schaumann, and H.E. Gaub. How strong is a covalent bond? *Science*, 283:1727 – 1730, 1999.
- [27] G.I. Bell. Models for specific adhesion of cells to cells. *Science*, 200:618–627, 1978.

- [28] R. Merkel. Force spectroscopy on single passive biomolecules and single biomolecular bonds. *Phys. Rep.*, 346(5):344–385, jun 2001.
- [29] E. Evans and K. Ritchie. Dynamic strength of molecular adhesion bonds. *Biophys. J.*, 72(4):1541–1555, 1997.
- [30] Y.L. Klimontovich. *Statistical Physics*. Harwood Academic Publishers, Chur, 1986.
- [31] C. F. Schmidt, M. Bärmann, G. Isenberg, and E. Sackmann. Chain dynamics, mesh size, and diffusive transport in networks of polymerized actin. A quasielastic light scattering and micrfluorescence study. *Macromolecules*, 22:3638–3649, 1989.
- [32] H. Isambert and A.C. Maggs. Dynamics and rheology of actin solutions. *Macromolecules*, 29:1036–1040, 1996.
- [33] B. Hinner, M. Tempel, E. Sackmann, K. Kroy, and E. Frey. Entanglement, elasticity, and viscous relaxation of actin solutions. *Phys. Rev. Lett.*, 81(12):2614–2617, 1998.
- [34] P. G. deGennes. Dynamics of entangled polymer solutions. i. the rouse model. *Macromolecules*, 9:587–593, 1976.
- [35] J. D. Ferry. *Viscoelastic properties of polymers*. John Wiley & Sons, New York, 3. edition, 1980.
- [36] M. Sato, D. P. T. L. T. Wheeler, N. Ohshima, and R. M. Nerem. Application of the micropipette technique to the measurement of cultured porcine aortic endothelial cell viscoelastic properties. *Journal of Biomechanical Engineering*, 112:263268, 1990.
- [37] A. R. Bausch, F. Ziemann, A. Boulbitch, K. Jacobson, and E. Sackmann. Local measurements of viscoelastic parameters of adherent cell membranes by magnetic bead microrheometry. *Biophysical Journal*, 75:20382049, 1998.
- [38] L. Otterbein, P. Graceffa, and R. Dominguez. The crystal structure of uncomplexed actin in the adp state. *Science*, 293:708711, 2001.

- [39] W. Kabsch, H. G. Mannherz, D. Suck, E. F. Pai, and K. C. Holmes. Atomic structure of the actin:DNase I complex. *Nature*, 347(6288):37–44, 1990.
- [40] P. Sheterline and Sparrow. Actin. *Protein Profile*, 1:1–121, 1994.
- [41] T. D. Pollard. Cytoplasmic contractile proteins. *J. Cell Biol.*, 91(156s–165s), 1981.
- [42] K.C. Holmes, D. Popp, W. Gebhard, and W. Kabsch. Atomic model of the actin filament. *Nature*, 347:4449, 1990.
- [43] A. McGough, B. Pope, W. Chiu, and Weeds A. Cofilin changes the twist of f-actin: implications for actin filament dynamics and cellular function. *J. Cell Biol.*, 138:771781, 1997.
- [44] M. Lorenz, D. Popp, and K. Holmes. Refinement of the f-actin model against x-ray fiber diffraction data by the use of a directed mutation algorithm. *J. Mol. Biol.*, 234:826–836, 1993.
- [45] J. Howard. *Mechanics of motor proteins and the cytoskeleton*. Sinauer Associates, Inc., Sunderland, MA, first edition, 2001.
- [46] S. Burlacu, P. Janmey, and J. Borejdo. Distribution of actin filament lengths measured by fluorescence microscopy. *Am. J. Physiol. Cell. Physiol.*, 262:C569–C577, 1992.
- [47] S. Kaufmann, J. Käs, W. H. Goldmann, E. Sackmann, and G. Isenberg. Talin anchors and nucleates actin filaments at lipid membranes. *FEBS Letters*, 314:203–205, 1992.
- [48] L. Le Goff, O. Hallatschek, E. Frey, and F. Amblard. Tracer studies on f-actin fluctuations. *Phys Rev Lett.*, 89(25):258101, 2002.
- [49] A. Roth, W.H. Roos, J. Konle, H. Presting, E. Sackmann, and J.P. Spatz. Freely suspended actin cortex models on arrays of microfabricated pillars. *Chemphyschem.*, 4(8):872–827, 2003.

- [50] F. Gittes, B. Mickey, J. Nettleton, and J. Howard. Flexural rigidity of microtubules and actin filaments measured from thermal fluctuations in shape. *The Journal of Cell Biology*, 120:923 – 934, 1993.
- [51] A. Ott, M. Magnasco, A. Simon, and A. Libchaber. Measurement of the persistence length of polymerized actin using fluorescence microscopy. *Phys. Rev. E*, 48(3):R1642 – R1645, 1993.
- [52] A. Wegner and Isenberg G. Twelfefold difference between the critical concentrations of the two ends of actin filaments in physiological salt conditions. *PNAS*, 80:4922 – 4925, 1983.
- [53] A. Renault, P. Lenne, C. Zakri, A. Aradian, C. Venien-Bryan, and F. Amblard. Surface-induced polymerization of actin. *Biophys. J.*, 76:1580 – 1590, 1999.
- [54] A. Wegner. Head to tail polymerization of actin. *J. Mol. Biol.*, 108(1):139–150, 1976.
- [55] K.J. Amann and Pollard T.D. Cellular regulation of actin network assembly. *Current Biology*, 20(10):728 – 730, 2003.
- [56] J.D. Pardee and J.A. Spudich. Purification of muscle actin. *Methods in Enzymology*, 85:164–181, 1982.
- [57] T. Sakamoto, I. Amitani, E. Yokota, and T. Ando. Direct observation of processive movement by individual myosin v molecules. *Biochemical and Biophysical Research Communications*, 272:586–590, 2000.
- [58] P. Coureux, A.L. Wells, J. Menetrey, C. Yengo, C.a. Morris, H.L. Sweeney, and a. Houdusse. A structural state of the myosin v motor without bound nucleotide. *Nature*, 425:419 – 423, 2003.
- [59] M. Walker, S. Burgess, J. Sellers, F. Wang, J. Hammer, and P. Tinick, J. and Knight. Two-headed binding of a processive myosin to f-actin. *Nature*, 405:804–807, 2000.

- [60] S. Burgess, M. Walker, F. Wang, Selers J.R., White H.D., Knight P.J., and Trinick J. The prepower stroke conformation of myosin v. *J. Cell Biol.*, 159:983 – 991, 2002.
- [61] R. D. Vale and R.A. Milligan. The way things move: Looking under the hood of molecular motor proteins. *Science*, 288:88 – 95, 2000.
- [62] K. Trybus, E. Kremetsowa, and Y. Freyzon. Kinetic characterization of a monomeric unconventional myosin v construct. *The Journal of Biological Chemistry*, 274(39):27448–27456, 1999.
- [63] R. Cheney, M. OShea, J. Heuser, M. Coelho, J. Wolenski, E. Espreafico, P. Forscher, R. Larson, and M. Mooseker. Brain myosin v is a two headed unconventional myosin with motor activity. *Cell*, 75:13–23, 1993.
- [64] E. Espreafico, R. Cheney, M. Matteoli, A. Nascimento, P. De Camilli, R. Larson, and Mooseker M. Primary structure and localization of chicken brain myosin v. *J. Cell Biol.*, 119:1541–1557, 1992.
- [65] E. De La Cruz, A. Wells, S. Rosenfeld, E. Ostap, and H. Lee Sweeney. The kinetic mechanism of myosin v. *PNAS*, 96(24):13726–13731, 1999.
- [66] A. Yildiz, J.N. Forkey, S.A. McKinney, T. Ha, Y.E. Goldman, and P.R. Selvin. Myosin v walks hand-over-hand: Single fluorophore imaging with 1.5-nm localization. *SCIENCE*, 300(27):2061–2065, june 2003.
- [67] J.N. Forkey, M.E. Quinlan, M.A. Shaw, J.E. Corrie, and Goldmann Y.E. Three dimensional structural dynamics of myosin v by single-molecule fluorescence polarization. *Nature*, 404:399 – 404, 2003.
- [68] E. Pastural, F. J. Barrat, R. Dufourcq-Lagelouse, S. Certain, O Sanal, N. Jabado, R. Seger, C. Griscelli, A. Fischer, and G. de Saint Basile. Griscelli disease maps to chromosome 15q21 and is associated with mutations in the myosin-va gene. *Nature Genetics*, 16:289–292, 1997.
- [69] Rogers S. L. and Gelfand V. I. Myosin cooperates with microtubule motors during organelle transport in melanophores. *Curr. Biol.*, 8:161–164, 1998.

- [70] R. Prekeris and D. M. Terrian. Brain myosin v is a synaptic vesicle-associated motor protein: evidence for a  $ca^{2+}$ -dependent interaction with the synaptobrevin-synaptophysin complex. *J. Cell Biol.*, 7:1589–1601, 1997.
- [71] V. Mermall, P. L. Post, and M. S. Mooseker. Unconventional myosins in cell movement, membrane traffic, and signal transduction. *Science*, 279:527–533, 1998.
- [72] L. L. Evans, A. J. Lee, P. C. Bridgman, and M. S. Mooseker. Vesicle-associated brain myosin-v can be activated to catalyze actin-based transport. *Journal of Cell Science*, 111:2055–2066, june 1998.
- [73] R.E. Cheney. Purification and assay of myosin v. *METHODS IN ENZYMOLOGY*, 298(B):3–18, 1998.
- [74] J.A. Spudich, S.J. Kron, and M.P. Sheetz. Movement of myosin-coated beads on oriented filaments reconstituted from purified actin. *Nature*, 315:584 – 586, 1985.
- [75] S. Kron and J. Spudich. Fluorescent actin filaments move on myosin fixed to a glass surface. *PNAS*, 83:6272–6276, 1986.
- [76] S. J. Kron, Y. Y. Toyoshima, T. Q. Uyeda, and J. Spudich. Assays for actin sliding movement over myosin-coated surfaces. *Meth. Enzymol.*, 196:399–416, 1991.
- [77] S.S. Margossian and S. Lowey. Preparation of myosin and its subfragments from rabbit skeletal muscle. *Methods in Enzymology*, 85:55 – 71, 1982.
- [78] J.M. Tyler, J.M. Anderson, and D. Branton. Structural comparison of several actin-binding macromolecules. *J. Cell Biol.*, 85:489 – 495, 1980.
- [79] M. Tempel. *Aktinbindende Proteine als Membran/Zytoskelle-Koppler und als Modulatoren der Viskoelastizität von Aktinnetzwerken*. Phd thesis, TUM, 1993.

- [80] E.A. Brotschi, J.H. Hartwig, and T.P. Stossel. The gelation of actin by actin-binding protein. *J. Biol. Chem.*, 253:8988 – 8993, 1978.
- [81] L. Hou, K. Luby-Phelps, and F. Lanni. Brownian motion of inert tracer macromolecules in polymerized and spontaneously bundled mixtures of actin and filamin. *J. Cell Biol.*, 110:1645–1654, 1990.
- [82] K. Wang, J.F. Ash, and S.J. Singer. Filamin, a new high-molecular-weight protein found in smooth muscle and non-muscle cells. *PNAS*, 72:4483 – 4486, 1975.
- [83] T.P. Stossel, J. Condeelis, L. Cooley, J.H. Hartwig, A. Noegel, M. Schleicher, and S. Shapiro. Filamins as integrators of cell mechanics and signalling. *Nature Reviews Mol. Cell Biol.*, 2:138–146, 2001.
- [84] A. Hall. Rho gtpases and the actin cytoskeleton. *Science*, 279:509 – 514, 1998.
- [85] Y. Shizuta, H. Shizuta, M. Gallo, Davies P., and Pastan I. Purification and properties of filamin, an actin binding protein from chicken gizzard. *J. Biol. Chem.*, 251(21):6562 – 6567, 1976.
- [86] H. Lodish, A. Berk, S.L. Zipursky, P. Matsudaira, D. Baltimore, and J.E. Darnell. *Molecular Cell Biology*. W.H. Freeman and Co., New York, 4th edition, 2001.
- [87] H.P. Duwe, J. Käs, and E. Sackmann. Bending elastic moduli of lipid bilayers: modulation by solutes. *J. Phys. France*, 51(10):945 – 962, 1990.
- [88] J. Henriksen, A.C. Rowat, and J.H. Ipsen. Vesicle fluctuation analysis of the effects of sterols on membrane bending rigidity. *Eur. Biophys. J.*, Epub ahead of print, june 2004.
- [89] V. Zhukarev, J. M. Sanger, J. W. Sanger, Y. E. Goldman, and H. Shuman. Distribution and orientation of rhodamine-phalloidin bound to thin filaments in skeletal and cardiac myofibrils. *Cell Motility and the Cytoskeleton*, 37:363–377, 1997.

- [90] M. Pfuhl, S.J. Winder, and A. Pastore. Nebulin, a helical actin binding protein. *EMBO J.*, 13:17921789, 1994.
- [91] J. Wehland, M. Osborn, and K. Weber. Phalloidin-induced actin polymerization in the cytoplasm of cultured cells interferes with cell locomotion and growth. *PNAS*, 74:56135617, 1977.
- [92] G. Marriott and M. Heidecker. Light-directed generation of the actin-activated atpase activity of caged heavy meromyosin. *American Chemical Society*, 35(3170-3174), 1995.
- [93] J. X. Tang, P. A. Janmey, T. P. Stossel, and T. Ito. Thiol oxidation of actin produces dimers that enhance the elasticity of the F-actin network. *Biophys. J.*, 76(4):2208–2215, 1999.
- [94] D. Dimitrov and M. Angelova. Lipid swelling and liposome formation mediated by electric fields. *Bioelchem*, 19(2):323 – 336, 1988.
- [95] M.D. Savage, G. Mattson, G.W. Nielander, S. Morgensen, and E.J. Conklin. *Avidin-Biotin Chemistry: A Handbook*. Pierce Chemical Co., Rockford, Ill., 1 edition, 1992.
- [96] N. Turro. *Modern Molecular Photochemistry*. University Science Books, Sausalito, CA, 1991.
- [97] A. Albersdorfer, T. Feder, and E. Sackmann. Adhesion-induced domain formation by interplay of long-range repulsion and short-range attraction force: a model membrane study. *Biophys. J.*, 73(1):245–257, 1997.
- [98] G. Wiegand, T. Jaworek, G. Wegner, and E. Sackmann. Studies of structure and local wetting properties on heterogeneous, micropatterned solid surfaces by microinterferometry. *J. Colloid Interface Sci.*, 196(2):299–312, 1997.
- [99] K. Sengupta, Schilling J., S. Goennenwein, Bausch A., and E. Sackmann. Absolute interfacial distance measurements by dual-wavelength reflection interference contrast microscopy. *Phys. Rev. E*, 69:021901–1 – 021901 –9, 2004.

- [100] F. Amblard, B. Yurke, A. Pargellis, and S. Leibler. A magnetic manipulator for studying local rheology and micromechanical properties of biological systems. *Rev. Sci. Instrum.*, 67(3):818–827, 1995.
- [101] U. O. Hafeli, R. Ciocan, and J.P. Dailey. Characterization of magnetic particles and microspheres and their magnetophoretic mobility using a digital microscopy method. *European Cells and Materials*, 3(Suppl. 2):24–27, 2002.
- [102] Ziemann Florian. *Untersuchung der lokalen viskoelastischen Eigenschaften von Zellen und Zellmodellen mit einem Magnetkugel-Mikrorheometer*. Phd thesis, TUM, june 1997.
- [103] C. Gosse and V. Croquette. Magnetic tweezers: Micromanipulation and force measurement at the molecular level. *Biophys. J.*, 82:3314–3329, 2002.
- [104] R. Poerschke. *Landoldt-Börnstein*, volume 18 of IV. Springer, Heidelberg, 1999.
- [105] A. Roth. Molecular motors on biostructured solid body surfaces. Diploma thesis, TUM, 2001.
- [106] Nitrocellulose surfaces passivated with the same methods showed no attachment of actin filaments and no actin was left in the chamber after rinsing.
- [107] S.M. Block, L.S.B. Goldstein, and B.J. Schnapp. Bead movement by single kinesin molecules studied with optical tweezers. *Nature*, 348:348–352, 1990.
- [108] J.E. Baker, E.B. Kremetsowa, G.G. Kennedy, A. Armstrong, K.M. Trybus, and D.M. Warshaw. Myosin v processivity: Multiple kinetic pathways for head-to-head coordination. *PNAS*, 101(15):5542–5546, Apr. 2004.
- [109] E.L. Florin, V.T. Moy, and H.E. Gaub. Adhesion forces between individual ligand receptor pairs. *Science*, 264:415–417, 1994.

- [110] E. Evans, D Berk, and A. Leung. Detachment of agglutinin-bonded red-blood-cells .1. forces to rupture molecular-point attachments. *Biophys. J.*, 59(4):849–860, APR 1991.
- [111] E. Evans, K. Ritchie, and R. Merkel. Sensitive force technique to probe molecular adhesion and structural linkages at biological interfaces. *Biophys. J.*, 68(6):2580–2587, JUN 1995.
- [112] a. Pierres, A. Benoliel, and P. Bongrand. Measuring the lifetime of bonds made between surface-linked molecules. *The Journal of Biological Chemistry*, 270(44):26586–26592, 1995.
- [113] T. Nishizaka, H. Miyata, H. Yoshikawa, S. Ishiwata, and K. Kinoshita Jr. Unbinding force of a single motor molecule of muscle measured using optical tweezers. *Nature*, 377:251–254, 1995.
- [114] A. Mehta. Myosin learns to walk. *J. Cell Sci.*, 114:1981–1998, 2001.
- [115] M.E. Fisher and A.B. Kolomeisky. The force exerted by a molecular motor. *PNAS*, 96:6597 – 6602, 1999.
- [116] A.A. Noegel and M. Schleicher. The actin cytoskeleton of dictyostelium: a story told by mutants. *J. Cell Sci.*, 113:759–766, 2000.
- [117] P.A. Janmey, S. Hvidt, J. Käs, Lerche D., A. Maggs, E. Sackmann, M. Schliwa, and T.P. Stossel. The mechanical properties of actin gels. *J. Biol Chem.*, 269(51):32503–32513, 1994.
- [118] M. Keller, R. Tharmann, M. A. Dichtl, A. R. Bausch, and E. Sackmann. Slow filament dynamics and viscoelasticity in entangled and active actin networks. *Philosophical Transactions: Mathematical, Physical & Engineering Sciences*, page Submitted, 2003.
- [119] A. McGough. F-actin-binding proteins. *Curr. Opin. Struct. Biol.*, 8:166 – 176, 1998.
- [120] L. D. Landau and E. M. Lifschitz. *Lehrbuch der theoretischen Physik: Elastizitätstheorie (Band VII)*. Akademie-Verlag, Berlin, 1970.

- [121] R. Lakes. A broader view on membranes. *Nature*, 414:503–504, Nov. 2001.
- [122] E. Bowick, M. Gutter and G. Thorleifsson. The poisson ratio of crystalline surfaces. *Europhys. Lett.*, 38(1), 1997.
- [123] Schmidt Frank. *Mikroheologie von Netzwerken flexibler Biopolymere*. Phd thesis, TUM, march 1999.
- [124] F. Braet, C. Rotsch, E. Wisse, and M. Radmacher. Comparison of fixed and living liver endothelial cells by atomic force microscopy. *Applied Physics A*, 66(575578), 1998.
- [125] H. Kojima, A. Ishijima, and T. Yanagida. Direct measurement of stiffness of single actin filaments with and without tropomyosin by in vitro nanomanipulation. *PNAS*, 91:12962–12966, 1994.
- [126] Y. Tsuda, H. Yasutake, A. Ishijima, and T. Yanagida. Torsional rigidity of single actin filaments and actinactin bond breaking force under torsion measured directly by in vitro micromanipulation. *PNAS*, 93:1293712942, 1996.
- [127] J. Marko and Cocco S. The micromechanics of dna. *Physics World*, 3:1 – 4, march 2003.
- [128] T. Stricka, J. Allemanda, V. Croquette, and D. Bensimon. Twisting and stretching single dna molecules. *Prog. Biophys. Mol. Biol.*, 74:115 – 140, 2000.
- [129] S. Goßler, G. Cagnoli, D.R.M. Crooks, H.L. Lck, S. Rowan, Smith J.R., K.A. Strain, J. Hough, and K. Danzmann. Damping and tuning of the fibre violin modes in monolithic silica suspensions. *Class. Quantum Grav.*, 21:923 – 933, 2004.
- [130] H. Vogel. *Physik*. Springer, Berlin-Heidelberg, 19 edition, 1997.
- [131] L. Limozin and E. Sackmann. Polymorphism of cross-linked actin networks in giant vesicles. *Phys. Rev. Lett.*, 89(16):168103–1 – 168103–4, 2002.

- [132] L. Limozin, M. Bärmann, and Sackmann E. On the organization of self-assembled actin networks in giant vesicles. *Eur. Phys. J. E*, 10(4):319 – 330, 2003.
- [133] B. Deme, D. Hess, M. Tristl, L. Lee, and E. Sackmann. Binding of actin filaments to charged lipid monolayers: Film balance experiments combined with neutron reflectivity. *Eur. Phys. J. E*, 2:125 – 136, 2000.
- [134] U. Seifert. Configurations of fluid membranes and vesicles. *Adv. Phys.*, 46:13 – 137, 1997.
- [135] G. S. Manning. The molecular theory of polyelectrolyte solutions with applications to the electrostatic properties of polynucleotides. *Quarterly Reviews of Biophysics*, II:179–246, 1978.
- [136] J. Tang and P. Janmey. The polyelectrolyte nature of f-actin and the mechanism of actin bundle formation. *J. Biol. Chemistry*, 271(15):8556–8563, Apr. 1996.
- [137] R. Dimova, B. Pouligny, and C. Dietrich. Pretransitional effects in dimyristoylphosphatidylcholine vesicle membranes: Optical dynamometry study. *Biophys. J.*, 79:340356, 2000.
- [138] I. L. Hopkins and R. W. Hamming. On creep and relaxation. *Journal of Applied Physics*, 28:906–909, 1957.
- [139] Feneberg Wolfgang. *Viskoelastische Mikroskopie der Zellhülle von humanen Endothelzellen*. Phd thesis, TUM, Apr. 2003.
- [140] Y. Liu. A direct method for obtaining discrete relaxation spectra from creep data. *Rheol. Acta*, 40:256–260, 2000.
- [141] N.W. Tschoegl. *The phenomenological theory of linear viscoelastic behavior*. Springer, Berlin - Heidelberg, 1989.
- [142] L. Peliti. *Fluctuating Geometries in Statistical Mechanics and Field Theory*, chapter Amphiphilic Membranes, pages 195–285. Elsevier, Amsterdam, 1996.

- [143] H. Döbereiner, G. Gomper, C.K. Haluka, D.M. Kroll, P.G. Petrov, and K.A. Riske. Advanced flicker spectroscopy of fluid membranes. *Phys. Rev. Lett.*, 91(4):048301–1 – 048301–4, 2003.
- [144] K. Zeman, H. Engelhard, and E. Sackmann. Bending undulations and elasticity of the erythrocyte membrane: effects of cell shape and membrane organization. *Eur. Biophys. J.*, 18(4):203–219, 1990.
- [145] L. Scheffer, A. Bider, E. Ben-Jakob, and R. Korenstein. Atomic force pulling: probing the local elasticity of the cell membrane. *Eur. Biophys. J.*, 30:83 – 90, 2001.
- [146] D. V. Zhelev, D. Needham, and R.M. Hochmuth. Role of the membrane cortex in neutrophil deformation in small pipets. *Biophys. J.*, 67(2):696–705, 1994.
- [147] R. Simson, E. Wallraff, J. Faix, J. Niewöhner, Gerisch G., and E. Sackmann. Membrane bending modulus and adhesion energy of wild-type and mutant cells of dictyostelium lacking talin or cortexillins. *Biophys. J.*, 74:514522, 1998.
- [148] P.M. Chaikin and T.C. Lubensky. *Principles of condensed matter physics*. Cambridge Univ. Press, Cambridge UK, 1 edition, 1995.
- [149] R. D. Deegan, O Bakajin, T. F. Dupont, G. Huber, S. R. Nagel, and Witten T. A. Capillary flow as the cause of ring stains from dried liquid drops. *Nature*, 389:827–829, Oct. 1997.
- [150] R.D. Deegan, O. Bakajin, T.F. Dupont, G. Hube, S.R. Nagel, and Witten T.A. Contact line deposits in an evaporating drop. *Phys. Rev. E*, 62(1):756 – 765, 2000.
- [151] Y. Y. Toyoshima, S. J. Kron, E. M. McNally, K. R. Niebling, C. Toyoshima, and J. A. Spudich. Myosin subfragment-1 is sufficient to move actin filaments in vitro. *Nature*, 328:536 – 539, 1987.

- [152] M. Keller, J. Schilling, and E. Sackmann. Oscillatory magnetic bead rheometer for complex fluid microrheometry. *Rev. Sci. Inst.*, 72(9):3626–3634, 2001.
- [153] J. Uhde, M. Keller, Sackmann E., Parmeggiani A., and Frey E. Internal motility in sti.ening actin-myosin networks. *Phys. Rev. Lett.*, *in review*, may 2004.
- [154] D. Stauffer and A. Aharony. *Perkolationstheorie*. VCH, Weinheim, New York, Basel, Cambridge, Tokyo, 1995.
- [155] U. Seifert, K. Berndl, and R. Lipowsky. Shape transformations of vesicles: Phase diagrams for spontaneous curvature and lipid-coupling models. *Phys. Rev. A*, 44(2):1182 – 1202, 1991.
- [156] I.Y. Wong, M. L. Gardel, D. R. Reichman, E. R. Weeks, M.T. Valentine, A. R. Bausch, and D. A. Weitz. Anomalous diffusion probes microstructure dynamics of entangled f-actin networks. *Phys. Rev. Lett.*, 92(17):178101–1 – 178101–4, 2004.
- [157] Dr. Manfred Keller. During microrheology experiments with an oscillating bead rheometer, the viscoelastic moduli measured can differ strongly from bead to bead. private communication.
- [158] M. T. Valentine, P. D. Kaplan, D. Thota, J. C. Crocker, T. Gisler, R. K. Prudhomme, M. Beck, and D. A. Weitz. Investigating the microenvironments of inhomogeneous soft materials with multiple particle tracking. *Phys. Rev. E*, 64:061506–1 – 061506–9, 2001.
- [159] J. T. Finer, R. M. Simmons, and J. A. Spudich. Single myosin molecule mechanics: piconewton forces and nanometre steps. *Nature*, 368:113 – 119, 1994.
- [160] L. Vonna, A. Wiedemann, M. Aepfelbacher, and E. Sackmann. Local force induced conical protrusions of phagocytic cells. *Journal of Cell Science*, 116(5):785 – 790, 2003.

- [161] U. S. Schwarz, N. Q. Balaban, D. Riveline, A. Bershadsky, B. Geiger, and S. A. Safran. Calculation of forces at focal adhesions from elastic substrate data: The effect of localized force and the need for regularization. *Biophys. J.*, 83:1380-1394, 2002.
- [162] T. Gisler and D.A. Weitz. Scaling of the microrheology of semidilute f-actin solutions. *Phys. Rev. Lett.*, 82:1606 – 1609, 1999.
- [163] A. Palmer, Mason T.G., J. Xu, S.C. Kuo, and D. Wirtz. Diffusing wave spectroscopy microrheology of actin filament networks. *Biophys. J.*, 76:1063 – 1071, 1999.
- [164] K.S.K. Uchida, T. Kitanishi-Yumura, and S. Yumura. Myosin ii contributes to the posterior contraction and the anterior extension during the retraction phase in migrating dictyostelium cells. *J. Cell Sci.*, 116:51 – 60, 2003.
- [165] K. Porello and Z. Cande. N-ethylmaleimide-modified subfragment-1 and heavy meromyosin inhibit reactivated contraction in motile models of retinal cones. *J. Cell Biol.*, 96:449–454, 1983.
- [166] C. Coates. Making sense of ultra sensitivity. *G.I.T. Imaging and Microscopy*, 3:2 – 3, 2003.
- [167] C. Coates, D.J. Denvira, N.G. McHleb, K.D. Thornbury, and M.A. Hollywood. Ultra-sensitivity, speed and resolution: Optimizing low-light microscopy with the back-illuminated electron multiplying ccd. *Andor Technologies*, [www.andor-tech.com](http://www.andor-tech.com), 2004.
- [168] M. Tempel, G. Isenberg, and E. Sackmann. Temperature induced sol-gel transition and microgel formation in  $\alpha$ -actinin cross-linked networks: A rheological study. *Phys. Rev. E*, 54(2):1802 – 1810, 1996.
- [169] W. H. Goldmann and Z. Guttenberg. Examination of temperature-induced 'gel-sol' transformation of  $\alpha$ -actinin/cross-linked actin networks by static light scattering. *FEBS Lett.*, 426(2):255–259, 1998.

- [170] A. Suzuki, M. Yamazaki, and T. Ito. Polymorphism of f-actin assembly. 1. a quantitative phase diagram of f-actin. *Biochem.*, 35:5238–5244, 1996.
- [171] J. Käs, H. Strey, J.X. Tang, D. Finger, R. Ezzell, E. Sackmann, and P.A. Janmey. F-actin, a model polymer for semiflexible chains in dilute, semidilute, and liquid crystalline solutions. *Biophys. J.*, 70(2):609–25, 1996.
- [172] L. Le Goff, F. Amblard, and E.M. Furst. Motor-driven dynamics in actin-myosin networks. *Phys. Rev. Lett.*, 88(1):018101–1 – 018101–4, 2002.
- [173] T.G. Mason, K. Ganesan, J.H.V. Zanten, D. Wirtz, and S.C. Kuo. Particle tracking microrheology of complex fluids. *Phys. Rev. Lett.*, 79:3282–3285, 1997.
- [174] A.C. Steven and U. Aebi. The next ice age: cryo-electron tomography of intact cells. *Trends in Cell Biology*, 13(3):107 – 110, 2003.
- [175] E.F. Fullam. A closed wet cell for the electron microscope. *Rev. Sci. Instr.*, 43(2):245–247, 1972.
- [176] S. Thiberge, O. Zik, and E. Moses. An apparatus for imaging liquids, cells, and other wet samples in the scanning electron microscopy. *Rev. Sci. Instr.*, 75(7):2280–2289, 2004.